ISSN: 2150-4091 Volume 2, Number 10, October 2010

Scientific Research

Natural Science

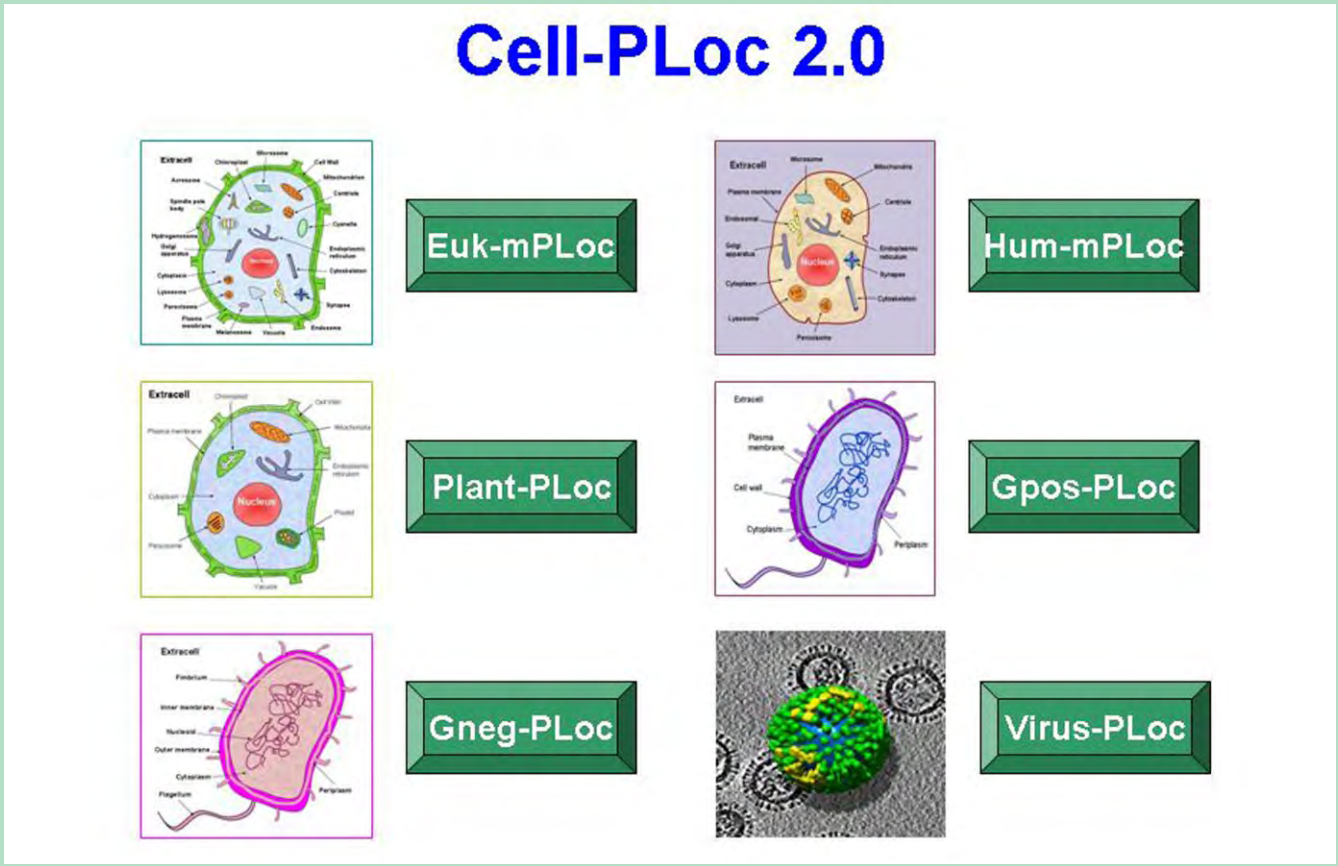

ISSN: 2150-4091

Journal Editorial Board

ISSN: 2150-4091 (Print) ISSN: 2150-4105 (Online)
http://www.scirp.org/journal/ns/

Vol.2, No.10, 1057-1179 (2010) NS

TABLE OF CONTENTS
Volume 2, Number 10, October 2010

The figure on the front cover shows the **Cell-PLoc 2.0** web-page at http://www.csbio.sjtu.edu.cn/bioinf/Cell-PLoc-2/. See the article published in Natural Science, 2010, Vol. 2, No. 10, pp. 1090-1103 by Kuo-Chen Chou and Hong-Bin Shen.

Natural Science

Journal Information

SUBSCRIPTIONS

The *Natural Science* (Online at Scientific Research Publishing, www.SciRP.org) is published monthly by Scientific Research Publishing, Inc., USA.

Subscription rates:

Print: $50 per copy.
To subscribe, please contact Journals Subscriptions Department, E-mail: sub@scirp.org

SERVICES

Advertisements
Advertisement Sales Department, E-mail: service@scirp.org

Reprints (minimum quantity 100 copies)
Reprints Co-ordinator, Scientific Research Publishing, Inc., USA.
E-mail: sub@scirp.org

COPYRIGHT

PRODUCTION INFORMATION

For manuscripts that have been accepted for publication, please contact:
E-mail: ns@scirp.org

Vol.2, No.10, 1057-1060 (2010)
doi:10.4236/ns.2010.210130

Natural Science

High sensitive and rapid responsive n-type Si: Au sensor for monitoring breath rate

Xuelan Hu[1], Jiachang Liang[2*], Xing Li[3], Yue Chen[4], Chao Zou[5], Sheng Liu[6], Xin Chen[2]

[1]Sino-European Institute of Aviation Engineering, Civil Aviation University of China, Tianjin, China;
[2]College of Science, Civil Aviation University of China, Tianjin, China; *Corresponding Author: jch_liang@yahoo.com;
[3]Department of Automation, Tianjin Technical Normal Institute, Tianjin, China;
[4]College of Aeronautical Engineering, Civil Aviation University of China, Tianjin, China;
[5]China Electronic Standardization Institute, Beijing, China;
[6]Sino-European Institute of Aviation Engineering, Civil Aviation University of China, Tianjin, China.

Received 23 May 2010; revised 18 July 2010; accepted 24 July 2010.

ABSTRACT

125 μm-breath sensor with high sensitivity and rapid response was prepared by using n-type Si: Au material. Its sensitivity coefficient and time constant were 4 V.sec/L and 38 msec, respectively. Its working principle was based on anomalous resistance effect, which not only increased the sensitivity, but also reduced its time constant greatly. Its signal processing system can select the breath signals and work stably. Therefore, the small changes of breath system can be measured and, especially, patient's breath rate can be monitored at a distance.

Keywords: Breath sensor; Signal processing system; Deep impurity; Anomalous resistance effect

1. INTRODUCTION

For semiconductors containing shallow impurities, including n-type silicon, the variation of its resistance R_s with temperature obeys $T^{-3/2}$ rule, *i.e.*

$$R_s = CT^{-3/2} \tag{1}$$

where C is proportional constant. For single crystal n-type silicon doped with deep impurities, near room temperature, the relationship between its resistance R_d and temperature T satisfies [1-3]

$$R_d = C \exp\left[-(E_F - E_A)/kT\right] \tag{2}$$

where k is Boltzmann constant, E_F Fermi level and E_A the deep acceptor level in the band gap of silicon containing deep acceptor impurities. For n-type Si: Au (n-type silicon containing deep acceptor impurities of gold), the anomalous resistance effect of exponential term in **Eq.2** can increase the sensitivity greatly. To compare the effects of $T^{-3/2}$ and $\exp[-(E_F - E_A)/kT]$, we take

$$\left|\frac{dR_d}{dR_s}\right| = \left|\frac{dR_d/dT}{dR_s/dT}\right| = 2T^{1/2}(E_F - E_A)B(T) \tag{3}$$
$$B(T) = \exp[-(E_F - E_A)/kT]/3k$$

Fermi level and the deep acceptor level of gold impurity are equal to 0.57 eV and 0.54 eV, respectively, below the conduction band in the band gap of our n-type Si: Au material and, thus, $E_F - E_A = 0.03$ eV. At room temperature (T = 300 K), we have

$$\left|\frac{dR_d}{dR_s}\right| = 1.3\times10^3 \tag{4}$$

Our experimental measuring value is 1.5×10^3. Therefore, the sensitivity of 125 μm-breath sensor, made by Wheatstone bridge using n-type Si: Au material as bridge arms, can be increased by 10^3 times, comparing with containing shallow impurities [4].

Our 125 μm-breath sensor can be used to monitor different breath flux and frequencies. In the Wheatstone bridge of our 125 μm-breath sensor, the variation of the offset voltage will play a vital role to the circuit. Generally speaking, the offset voltage is not a constant, but rather a function containing several unknown parameters. It varies according with the changes of ambient temperature and brightness, service voltage and current, even the technical defects during manufacturing. Another factor affecting the offset voltage is the asymmetry between the bridge arms, especially the relevant resistors' temperature coefficient, which depends on the deep impurity. If the offset voltage remains constant, the voltage output of 125 μm-breath sensor only depends on its flux. In order to eliminate the offset voltage drift, some compensation methods and auto-adjusting circuits are adopted. Thus, the sensor with such signal processing system can be used as

the breath sensor to monitor the patient's breath rate.

2. EXPERIMENTS

In n-type Si, the concentration of doped phosphorus (shallow donor impurity) was equal to 1.0×10^{15} cm^{-3} and in n-type Si: Au material the concentration of gold (deep acceptor impurity) was equal to 1.1×10^{15} cm^{-3}. The doped Au element was diffused in Si substrate by deep doping method [5]. The main part of 125 μm-breath sensor, made of n-type Si: Au material, was a Wheatstone bridge using anisotropic etching n-type Si: Au resistors. The length of each bridge arm was 125 μm. In terms of electrostatic method, the bridge was bonded to a borosilicate grass substrate, which had high thermal isolation capacity. The structure and photograph of the integrated fabrication of the 125 μm-breath sensor were shown in **Figures 1** and **2**, respectively.

The schematic diagram of monitoring system of 125 μm-breath sensor was shown in **Figure 3**. A resistor R was connected in series with the power supply circuit to protect the sensor. The measurement was carried out in a 6 mm-radius tube with the measuring range from 0 to 27 L/min. Before measuring, the circuit should be supplied with power to preheat for 30 minutes. The static and transient characteristics of 125 μm-breath sensor were measured, including the output voltage as well as time constant of 125 μm-breath sensor.

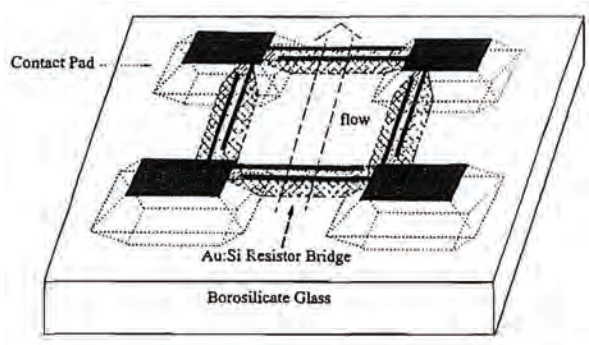

Figure 1. The structure of the 125 μm-breath sensor.

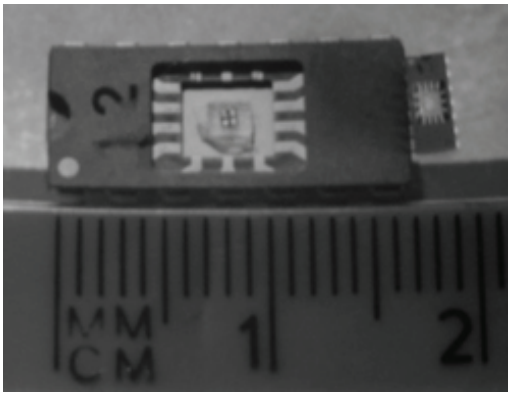

Figure 2. Photograph of integrated fabrication of 125 μm-breath sensor.

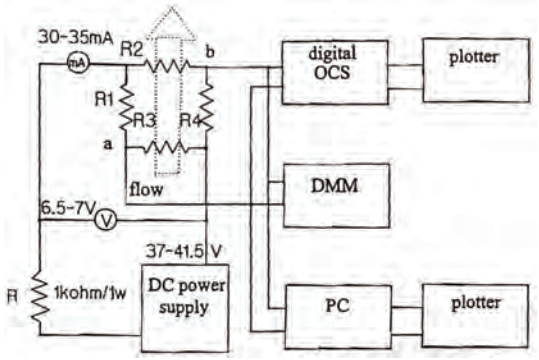

Figure 3. The schematic diagram of monitoring system of the 125 μm-breath sensor.

3. RESULTS AND DISCUSSION

3.1. Working Principle of 125 μm-breath Sensor

Except for using n-type Si: Au material instead of hot wires to form the electric bridge arms, this 125 μm-breath sensor shares the same principle with the hot wire flow meter. When air flows through the electric bridge, the temperature variation between the two arms perpendicular to the air flow direction is much more than that between the two arms parallel with the air flow direction. Thus, the temperature difference lead to the resistance change of each bridge arm, and then lead to the change of output voltage related with the flux at the output ends. The sensitivity of the sensor depends on the resistance variation of the electric bridge arms when air flows through the sensor. The more the resistance varies, the higher the sensor's sensitivity is. When the sensor size decreases to micro dimensions, the contact area between the air and bridge arms is also largely reduced. So selecting materials which have high sensitivity toward temperature is the key problem. The sensitivity of 125 μm-breath sensor was increased greatly by using n-type Si: Au material, because deep doping method can increase the temperature sensitivity of the electric bridge's single arm resistance, as shown in **Eq.3** and **Eq.4**.

3.2. The Static Characteristics of the Monitoring System of 125 μm-breath Sensor

Suppose the measurand is x, output is y and the response time is zero, the function between the measurand and the output should be

$$y = f(x) + C, \quad (5)$$

where C is a constant.

If the measurand varies dx, then the output's variation should be

$$dy = [df(x)/dx]dx = K(x)dx, \quad (6)$$

where $K(x)$ is the sensitivity coefficient. Took x and y as flux and output voltage of 125 μm-breath sensor, respectively, their relation was measured, as shown in **Figure 4**. When the flux was more than 8 L/min, it had the linear relation with the output voltage. In other words, their slop could be used to represent the sensitivity coefficient of 125 μm-breath sensor. The sensitivity coefficient $K \approx 4V \cdot \sec/L$ was obtained when we took the stable supply voltage across bridge to be equal to 7 V and the stable total supply current to be equal to 30 mA.

3.3. The Transient Characteristics of the Monitoring System of 125 μm-breath Sensor

Suppose the output voltage of breath sensor's electric bridge is V_{ab}, the relation between V_{ab} and time can be measured by the digital oscillograph (for example, HP 54501). The horizontal scanning time base of such oscillograph could varies from 50 ns to 5 s. The relation between V_{ab} and time can be represented

$$V_{ab} = \sum_m V_m [1 - \exp(-t/\tau m)], m = 1.2.3...n..., \quad (7)$$

where $V_1, V_2, ...V_n$ are the amplitudes of output voltage variations caused by different factors. $\tau_1, \tau_2, ...\tau_n$ are the time constants. Usually when $m > 2$ and V_m is too small to negligible, the **Eq.7** can be simplified to:

$$V_{ab} \approx V_1[1 - \exp(-t/\tau_1)] + V_2[1 - \exp(-t/\tau_2)], \quad (8)$$

where τ_1 is the time constant depending on electric bridge arms and τ_2 the time constant depending on the substrate. The measuring result was shown in **Figure 5**, which indicated that the time constant $(\tau_1 + \tau_2)$ of our 125 μm-breath sensor can be as small as 38 ms.

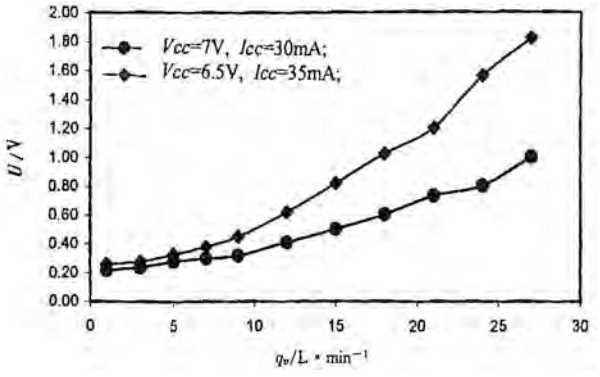

Figure 4. The relation between the sensor's flux and the output voltage of the 125 μm-breath sensor.

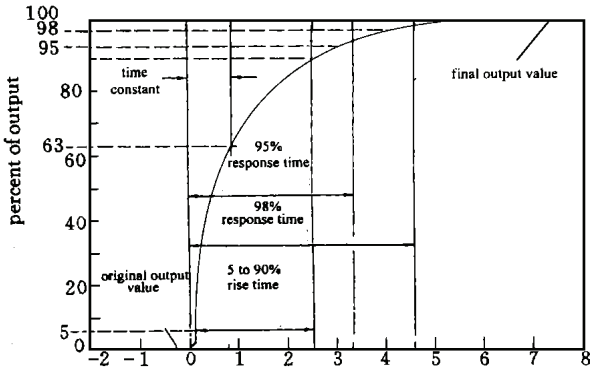

Figure 5(a). Definitions of the time constant and the response time for 125 μm-breath sensor.

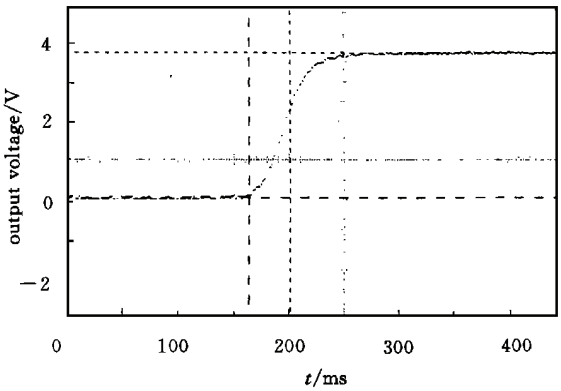

Figure 5(b). The response of output voltage versus time for 125 μm-breath sensor.

3.4. Signal Processing Circuit

The breath monitoring system can display the flux from 1 to 27 L/min and the frequency from 1 to 200 /min. Their normal values vary against different people. For example, infants breathe about 44 times per minute and adults breathe about 18 times per minute. So the system must be adjustable, which could enable the doctors and nurses to adjust the critical values to serve different people. The critical adjusting parameters include the minimal and maximal flux per minute, and the minimal and maximal flow frequency per minute. When the system detects breath state parameters exceeding the critical values, the alarming circuit of the system starts to work by lightening a red LED and sounding a buzzer to inform doctors and nurses. Due to its micro-size, this sensor is very easily to install in the tubes which are used to monitor the breath state.

The input signal from breath sensor is divided into two paths after going through the buffering section of the signal processing circuit. One is sent to the opera-

tional amplifier 1; and the other is sent to operational amplifier 2. The signal through operational amplifier 2 is also divided into two paths. One is fed to the A/D converter to display breath flow speed; and the other is fed to the Schmidt circuit to calculate the breath frequency. The breath flux matrix and frequency matrix are used to identify the breath state. If the breath flux or frequency is either too high or too low, those circuits will send corresponding signals to the alarming circuit. Then the alarming circuit will sound the piezoelectric ceramic speaker and lighten the LED to notify doctors and nurses to set those critical parameters.

Because other interfering signals, including doctors or nurses' walking, will destabilize the interface circuit, the control circuit of interfering signals is necessarily installed to eliminate their effects. The operational amplifier 1 is used to amplify those interfering signals. When the input signal is small ($<$ 10 mV), the potentiometer in amplifier will let the Schmidt flip-flop to output a up lever which can then let the A/D converter and the counter to output null. In such case, even the small interfering signal exists, the value shown on the flux and breath frequency display will be null. When normal breath signals input ($>$ 10 mV), they will be sent to the amplifier 2 after buffering. Then the signals will be sent to the A/D converter to detect the flux and to the counter to calculate the breath frequency.

The interfering signals, including doctors and nurses' walking, will be sent to amplifier 1 and then fed to the control circuit of interfering signals. After being digitized, the characteristics of those signals will be stored in storage systems. Some possible interfering waveforms can also be prestored. When the system works, the input signal will be compared with those already stored ones. If they have the same characteristics, the control circuit will send another signal to stop the breath flux and frequency circuits working.

Sometimes the offset variation and drift might lead to the whole system breakdown, especially when the monitoring system has worked in a long time (usually more then 10 hours). So the auto adjusting circuit should be installed to maintain the offset voltage constant. The operational amplifier 1 is used to amplify the interfering signal and the offset voltage drift signal. The period of breath signal is usually less than 6 s, whereas the time duration, in which the offset voltage changes obviously, is always more than 60 s. In such case, an offset voltage timing circuit can be introduced to monitor the signal's duration. Because the duration of input signal is always more than 60 s, the offset voltage timing circuit can send another signal to the auto zeroing control switch and output the compensating offset voltage from the auto zeroing voltage sampling circuit to the operational amplifier 2 to eliminate the effects caused by the offset voltage drift.

4. CONCLUSIONS

The 125 μm-breath sensor, made of n-type Si: Au material, not only has a high sensitivity ($4V \cdot \sec / L$) and short time constant (38 ms), but also its fabrication technology is simpler than others [6,7]. So, it can be widely applied.

The experiment indicates that its signal processing circuit can eliminate the voltage drift and other interfering signals. The whole circuit can work stably to process all breath signals. Therefore, patient's breath rate can be monitored at a distance. If continuing to reduce the size of electric bridge arms and improve the thermal insulation between the electric bridge and substrate, it is possible to make the time response even faster.

5. ACKNOWLEDGEMENTS

We would like to express our thanks to Dr H. J. Ma at the Institute of Heavy Ion Physics of Peking University for his assistance and discussion on the experiments and Ms jing Liang for her typesetting. This work was supported by Basic Research Project of High Education (ZXH2009C004) and Foundation of CAUC (09QD 06X).

REFERENCES

[1] Liang, J.C., Jiang, J. and Zhao, J. (1996) Studies on 0.96 and 0.84 eV photoluminescence emission in GaAs epilayers grown on Si. *Journal of Applied Physics*, **79**, 7173-7176.

[2] Li, X. (1999) Ultra large scale integration technology. Beijing Publish House of Electronics Industry, Beijing.

[3] Li, X., Liang, J.C. and Li, M. (2003) Anomalous resistance effect of Si containing deep impurities and its application to sensor. *Proceeding of Conference on Semiconductor Devices*, Montreal, 2003, 39-42.

[4] Van Putten, A.F.P. (1983) An integrated silicon double bridge anemometer. *Proceeding of Conference on Solid-State Sensors and Actuators*, Delft University of Technology, 1983, 5-6.

[5] Kapoor, A.K. and Henderson, H.T. (1980) A new planar injection-gated bulk switching system based on deep impurity trapping. *IEEE Transactions Electronic Devices*, **27**, 1256-1274.

[6] Li, Q., Hein, S. and Obermeier, E. (1996) Macro-gas-flow-sensor with integrated heat sink and flow guide. *Sensors and Actuators*, **54**, 547-551.

[7] Jonsson, A., Hok, B. and Ekstron, M. (2009) Development of a breath alcohol analyzer for use on patients in emergency care. *International Federation for Medical and Biological Engineering Proceedings*, **25(11)**, 84-87.

Vol.2, No.10, 1061-1065 (2010)
doi:10.4236/ns.2010.210131

Natural Science

Preparation and characterization of genipin-cross-linked chitosan microparticles by water-in-oil emulsion solvent diffusion method

Jesada Karnchanajindanun, Mangkorn Srisa-ard, Prasong Srihanam, Yodthong Baimark*

Department of Chemistry and Center of Excellence for Innovation in Chemistry, Faculty of Science, Mahasarakham University, Mahasarakham, Thailand; *Corresponding Author: yodthong.b@msu.ac.th.

Received 23 May 2010; revised 18 July 2010; accepted 24 July 2010.

ABSTRACT

Chitosan (CS) microparticles with and without cross-linking were prepared by a water-in-oil emulsion solvent diffusion method without any surfactants. Aqueous CS solution and ethyl acetate were used as water and oil phases, respectively. Genipin was used as a cross-linker. Influences of genipin ratios and cross-linking times on CS microparticle characteristics were investigated. Non-cross-linked and cross-linked CS microparticles were spherical in shape and rough in surface. Microparticle matrices showed porous structures. Surface roughness, mean particle sizes and bulk density of CS microparticles increased and their dissolutions in acetic acid solution decreased when genipin ratio and cross-linking time increased.

Keywords: Chitosan microparticles; Porous structure; Genipin; Cross-linking; Morphology

1. INTRODUCTION

Chitosan is a copolymer of 2-glucosamine and *N*-acetyl-2-glucosamine prepared by alkaline deacetylation of chitin that has received great attention for its possible uses in medical, pharmaceutical and metal ion treatment applications because of its biodegradability, biocompatibility and high concentration of amine functional groups [1-4]. Chitosan microparticles have usually been fabricated by precipitation, spray drying and water-in-oil (W/O) emulsification-cross-linking methods [5]. The current study describes an alternative method for preparation of cross-linked and non-cross-linked CS microparticles by the W/O emulsion solvent diffusion method.

Genipin was selected as a biocompatible cross-linker. Genipin is a natural water-soluble bi-functional cross-linker. It is obtained from geniposide, a component of traditional Chinese medicine and is isolated from the fruits of the plant, *Gardenial jasminoides* Ellis [6]. Genipin is a fully biocompatible reagent about 10,000 times less cytotoxic than glutaraldehyde [7]. The CS device matrices were successfully cross-linked with genipin [8-10].

In this work, a novel approach to the preparation of genipin-cross-linked chitosan microparticles by the simple W/O emulsion solvent diffusion method is reported. Cross-linked chitosan microparticles were solidified and formed after diffusion out of water from emulsion droplets of chiosan solution to external continuous phase, ethyl acetate. The influences of cross-linker ratio and cross-linking time on CS microparticle characteristics including morphology, particle size, dissolution and bulk density were investigated and discussed.

2. EXPERIMENTAL

2.1. Materials

Chitosan with degree of de-acetylation and average molecular weight of 90% and 100 kDa, respectively was purchased from Seafresh Chitosan Lab Co., Ltd. (Thailand). Genipin (Challenge Bioproducts Co. Ltd., Taiwan) and analytical grade ethyl acetate (Lab Scan) were used without further purification.

2.2. Preparation of Chitosan Microparticles

Chitosan solution with 1% w/v was prepared by using a 2% (v/v) acetic acid aqueous solution as a solvent. Chitosan microparticles were prepared by the water-in-oil emulsion solvent diffusion method. The 0.5 mL of 0.5% w/v chitosan solution was added drop-wise to 200 mL of ethyl acetate with a stirring speed of 900 rpm for 1 h. The beaker was tightly sealed with aluminum foil during the emulsification-diffusion process to prevent ethyl acetate evaporation. The chitosan microparticles suspended in ethyl acetate were collected by centrifuga-

tion before drying in a vacuum oven at room temperature for 6 h.

Genipin-cross-linked chitosan microparticles were produced by the same method. The chitosan and genipin solutions were mixed together under constant stirring at room temperature for cross-linking before microparticle preparation. The final chitosan concentration was 0.5% w/v after cross-linking. The different genipin concentrations (5%, 10% and 20% w/w) and cross-linking times (1.5, 3 and 6 h) were investigated.

2.3. Characterization of Chitosan Microparticles

Morphology of the chitosan microparticles was determined by scanning electron microscopy (SEM) using a JEOL JSM-6460LV SEM. The microparticles were coated with gold for enhancing conductivity before scan. Mean microparicle size and the coefficient of variation (CV) were calculated for each on SEM images by counting a minimum of 100 particles using smile view software (version 1.02). The CV value was calculated from the following equation:

$$\mathrm{CV} = \frac{\sigma}{D_p} \times 100 \qquad (1)$$

where σ is a standard deviation, and D_p is a mean microparticle diameter measured from SEM images. Lower CV values indicate high microparticle monodispersity in size.

Percentage of dissolution of the chitosan microparticles was investigated by shaking 50 mg of the chitosan microparticles in 1.5 mL of 2% w/v acetic acid aqueous solution at room temperature for 24 h. The residue microparticles were recovered by centrifugation before drying in a vacuum oven at 50°C until its weight remained constant. The percentage of dissolution of the chitosan microparticles was then calculated by following the equation. Each average percentage of dissolution value was calculated from a mean of three measurements (see **Eq.2**).

where initial and remaining CS microparticles are the weights of chitosan microparticles before and after dissolution test, respectively.

Bulk density of the chitosan microparticles was measured by gas displacement method using an ultrapycnometer 1000 (Quantachrom, USA) under helium gas. Each average density value was calculated from a mean of five determinations.

3. RESULTS AND DISCUSSIONS

Here, the water-in-oil (W/O) emulsion solvent diffusion method without any surfactant was used to prepare chitosan (CS) microparticles. The maximum water solubility in ethyl acetate is 3.30% (CAS No. 141-78-6). Then the polymer particles should form, if the less than 3.3 mL of aqueous polymer solution (W phase) was added drop-wise into 100 mL of ethyl acetate (O phase) with stirring. The water in dispersed emulsion droplets of CS solution diffused out to the continuous phase, ethyl acetate. It was found in our cases that the CS microparticles were successfully prepared using this method. In our preliminary test, the magnetic stirring speed of 900 rpm is found the most appropriate for microparticle preparation. The almost aqueous CS solution could not be broken to form uniform droplets when the stirring speed was lower than 900 rpm. Meanwhile, almost all particles were stuck at the wall of glassware during emulsification-diffusion process when higher stirring speed than 900 rpm was applied. The chitosan microparticles could not be completely solidified when the stirring time was shorter than 1 h. The CS aggregates were found when higher 0.5 mL of CS solution was used due to its high viscosity of CS solution.

3.1. Morphology and Sizes of CS Microparticles

Figure 1 shows SEM images of non-cross-linked and cross-linked CS microparticles prepared with different genipin ratios. They were nearly spherical in shape suggested that the genipin ratios did not effect on the particle shape. Surfaces of these CS microparticles are illustrated in **Figure 2**. The non-cross-linked CS microparticles in **Figure 2(a)** showed rough surfaces. This may occur from diffusion out of water from dispersed droplets of CS solution to continuous ethyl acetate phase during particle solidification. The surface roughness increased with the genipin ratio as shown in **Figures 2(b)-2(d)**. The results may be explained that the cross- linking can increase viscosity of CS solution. The diffusion out of water from cross-linked CS solution droplets was difficult.

The cross-linked CS microparticles prepared with different cross-linking times also showed the spherical-like shape, as illustrated in **Figures 3(b)-3(d)**. This indicates that cross-linking times did not effect on the particle shape. The CS microparticles prepared with longer cross-linking time showed rougher surface than the shorter cross-linking time, as shown in **Figure 4**. This may be due to increasing of the viscosity of CS solution when the cross-linking time increased.

$$\%\ \text{dissolution} = \frac{[\text{initial CS microparticles (mg)} - \text{remaining CS microparticles (mg)}]}{\text{initial CS microparticles (mg)}} \times 100 \qquad (2)$$

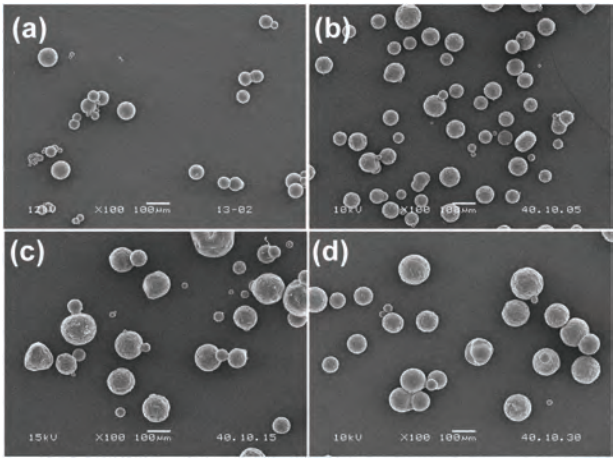

Figure 1. SEM micrographs of (a) non-cross-linked chitosan microparticles and cross-linked chitosan microparticles with genipin ratios of (b) 5%, (c) 10% and (d) 20% w/w for cross-linking time of 6 h. All bars = 100 μm.

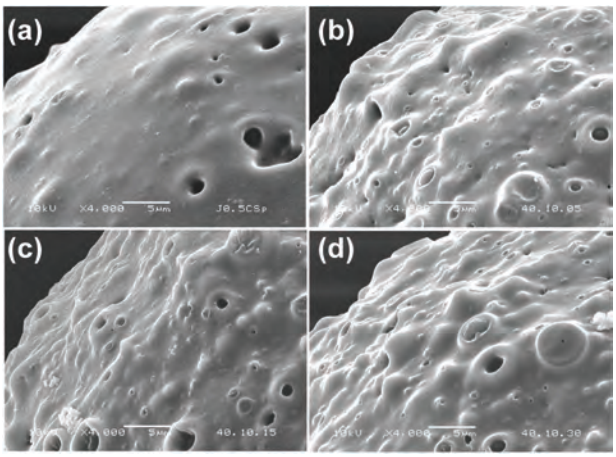

Figure 2. Expanded SEM micrographs of surfaces of (a) non-cross-linked chitosan microparticles and cross-linked chitosan microparticles with genipin ratios of (b) 5%, (c) 10% and (d) 20% w/w for cross-linking time of 6 h. All bars = 5 μm.

Internal morphology of the CS microparticle matrix was examined through their broken surfaces (**Figure 5**). It can be seen that the microparticle matrices contained porous structure, resembling a sponge. These sponge-like particles were presumably created by rapid solidification of the chitosan matrix during diffusion out of the water from emulsion droplets. However, the porous structures were completely covered with a continuous outer particle surface. The matrix of cross-linked CS micro-particles was denser than that of the non-cross-linked microparticles. As example of which is shown in **Figure 5(b)** for the cross-linked CS microparticles prepared with 20% w/w genipin ratio compared with the non-cross-linked CS microparticles in **Figure 5(a)**.

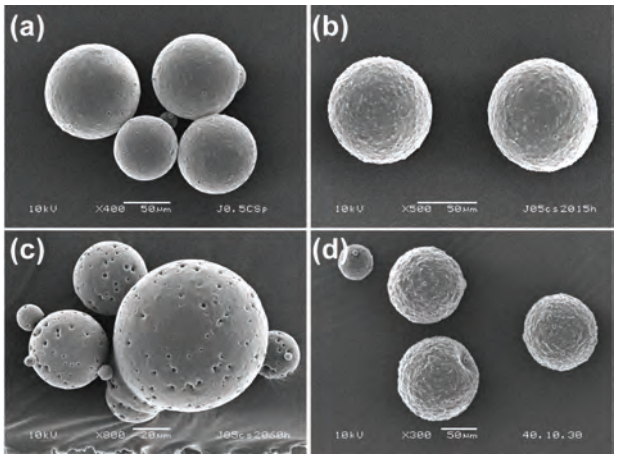

Figure 3. SEM micrographs of (a) non-cross-linked chitosan microparticles and cross-linked chitosan microparticles with cross-linking times of (b) 1.5, (c) 3 and (d) 6 h for genipin ratio of 20% w/w. All bars = 50 μm.

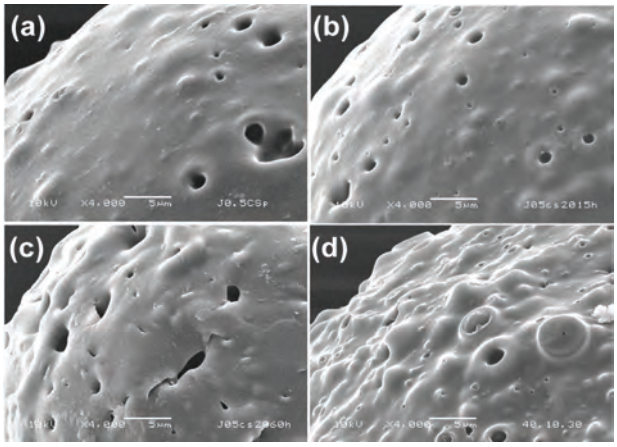

Figure 4. Expanded SEM micrographs of surfaces of (a) non-cross-linked chitosan microparticles and cross-linked chitosan microparticles with cross-linking times of (b) 1.5, (c) 3 and (d) 6 h for genipin ratio of 20% w/w. All bars = 5 μm.

Mean particle sizes of the CS microparticles were determined from several SEM images instead of scattering method (suspension in water) because of the partial swelling and dissolution of microparticles. The mean particle sizes and CV of the CS microparticles are summarized in **Table 1**. It was found that the particle sizes increased when the genipin ratio and the cross-linking time were increased. The CV for every sample is below 30% indicated the CS microparticles with low dispersity in size were formed. The results suggest that the CV of microparticles did not appear to affect the genipin ratio and cross-linking time.

3.2. Dissolution of CS Microparticles

Dissolution behavior of the CS microparticles indi-

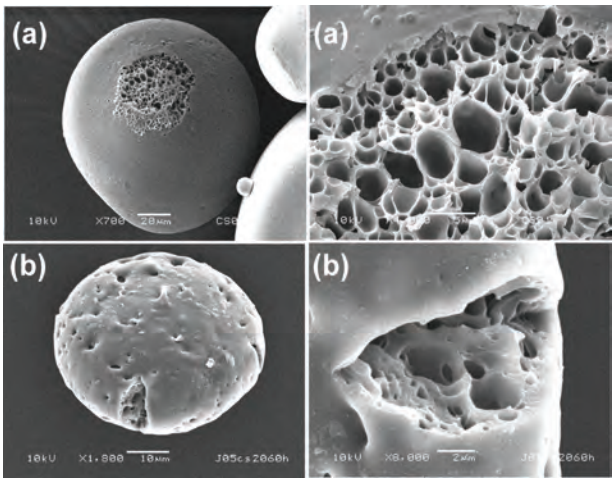

Figure 5. Low-magnification (left column) and high-magnification (right column) SEM micrographs of broken surfaces of (a) non-cross-linked chitosan microparticles and (b) cross-linked chitosan microparticles with 20% w/w genipin ratio for cross-linking time of 6 h. Bars = 20 and 10 μm for (a) and (b), respectively in left column. Bars = 5 and 2 μm for (a) and (b), respectively in right column.

rectly related to the degree of cross-linking. The higher dissolution of CS microparticles related to lower degree of cross-linking. **Figure 6** shows dissolution of the CS microparticles in acetic acid solution for 24 h. The non-cross-linked CS microparticles were completely dissolved. This due to the weak acid solution such as acetic acid solution is a good solvent for CS. The dissolution of mi croparticles was decreased when the CS was cross-linked and increasing the genipin ratio and cross-linking time. The results suggest that the degree of cross-linking increased as the genipin ratio and cross-linking time increased, according to the literatures [8,9]. This is an important advantage for application in drug delivery with controllable drug release rate. Thus the drug release rates can be tailored by varying the degree of cross-linking.

3.3. Bulk Density of CS microparticles

The porous structures of CS microparticel matrices with and without cross-linking can be clearly determined from their density values, as shown in **Figure 7**. It was found that the density values increased with the genipin

Table 1. Conditions for preparing chitosan microparticles and their particle sizes.

Process parameter	Sample No.					
	1	2	3	4	5	6
Genipin ratio (% w/w)	0	5	10	20	20	20
Cross-linking time (h)	0	6	6	6	1.5	3
Mean particle size (μm)	85	98	110	112	92	104
CV (%)	24%	27%	25%	29%	28%	29%

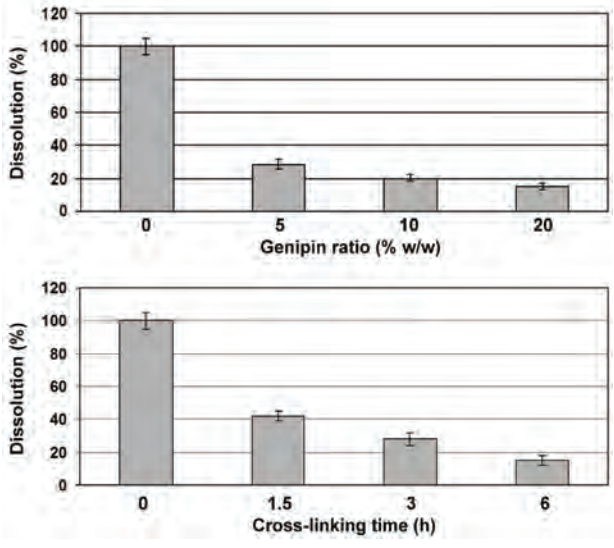

Figure 6. Dissolution of chitosan microparticles in 2% w/v acetic acid solution for 24 h prepared with different genipin ratios for cross-linking time of 6 h (above) and different cross-linking times for genipin ratio of 20% w/w (bottom).

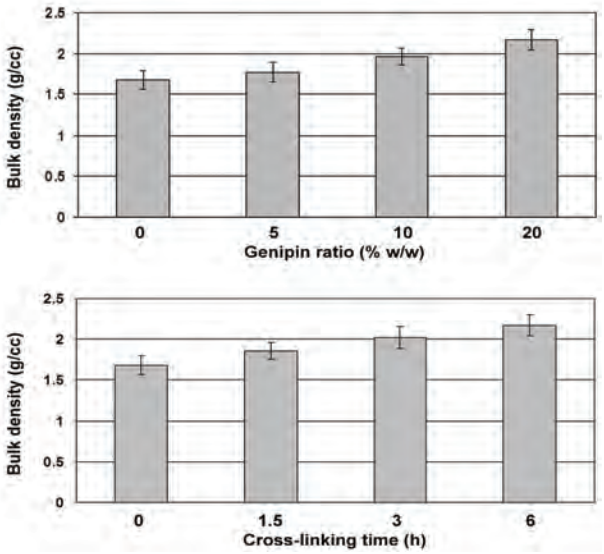

Figure 7. Bulk density of chitosan microparticles prepared with different genipin ratios for cross-linking time of 6 h (above) and different cross-linking times for genipin ratio of 20% w/w (bottom).

ratio and cross-linking time. This can be explained that the CS molecules were closer together when the higher genipin ratio and cross-linking time were used. Therefore, the denser microparticles were obtained. The bulk density change after cross-linking corresponded to the microparticle matrices of the broken CS microparticles from the SEM images in **Figure 5**.

4. CONCLUSIONS

Non-cross-linked and genipin-cross-linked chitosan microparticles with spherical-like shapes have been successfully prepared using the simple and rapid W/O emulsion solvent diffusion method. The surface roughness of microparticles increased with genipin ratio and cross-linking time but the particle shape did not change. All chitosan microparticle matricess contained porous structures. The cross-linked microparticles showed denser matrices than that of non-cross-linked microparticles. The mean particle sizes and bulk density of microparticles slightly increased as increasing the genipin ratio and the cross-linking time.

This simple W/O emulsion solvent diffusion method is promising for the preparation of drug-loaded chitosan microparticles with and without cross-linking, especially water-soluble drugs. Drug release rates from microparticles might be controlled by adjusting the genipin ratio and/or cross-linking time.

5. ACKNOWLEDGEMENTS

This work was supported by Mahasarakham University (fiscal year 2011), the National Metal and Materials Technology Center (MTEC), National Science and Technology Development Agency (NSTDA), Ministry of Science and Technology, Thailand (MT-B-52-BMD-68-180-G) and the Center of Excellence for Innovation in Chemistry (PERCH-CIC), Commission on Higher Education, Ministry of Education, Thailand.

REFERENCES

[1] Kumar, M.N.V.R., Muzzarelli, R.A.A., Muzzarelli, C., Sashiwa, H. and Domb, A.J. (2004) Chitosan chemistry and pharmaceutical perspectives. *Chemical Review*, **104**, 6017-6084.

[2] Muzzarelli, R.A.A. and Muzzarelli, C. (2005) Chitosan chemistry: Relevance to the biomedical sciences. *Advances in Polymer Science*, **186**, 151-209.

[3] Crini, G. (2005) Recent developments in polysaccharide-based materials used as adsorbents in wastewater treatment. *Progress in Polymer Science*, **30**, 38-70.

[4] Learoyd, T.P., Burrows, J.L., French, E. and Seville, P.C. (2008) Modified release of beclometasone dipropionate from chitosan-based spray-dried respirable powders. *Powder Technology*, **187**, 231-238.

[5] Agnihotri, S.A., Mallikarjuna, N.N. and Aminabhavi, T. M. (2004) Recent advances on chitosan-based micro- and nanoparticles in drug delivery. *Journal of Controlled Release*, **100**, 5-28.

[6] Mi, F.L., Shyu, S.S. and Peng, C.K. (2005) Characterization of ring-opening Polymerization of genipin and pH-dependent cross-linking reactions between chitosan and genipin, *Journal of Polymer Science, Part A*: *Polymer Chemistry*, **43**, 1985-2000.

[7] Nishi, C., Nakajima, N. and Ikada, Y. (1995) In vitro evaluation of cytotoxicity of diepoxy compounds used for biomaterial modification. *Journal of Biomedical Material Research*, **29**, 829-834.

[8] Yuan, Y., Chesnutt, B.M., Utturkarr, G., Haggard, W.O., Yang, Y., Ong, J.L. and Bumgardner, J.D. (2007) The effect of cross-linking of chitosan microspheres with genipin on protein release. *Carbohydrate Polymers*, **68**, 561-567.

[9] Silva, S.S., Motta, A., Rodrigues, M.T., Pinheiro, A.F.M., Gomes, M.E., Mano, J.F., Reis, R.L. and Migliaresi, C. (2008) Novel genipin-cross-linked chitosan/silk fibroin sponges for cartilage engineering strategies. *Biomacromolecules*, **9**, 2764-2774.

[10] Muzzarelli, R.A.A. (2009) Genipin-crosslinked chitosan hydrogels as biomedical and pharmaceutical aids. *Carbohydrate Polymers*, **77**, 1-9.

Vol.2, No.10, 1066-1072 (2010)
doi:10.4236/ns.2010.210132

Natural Science

Adsorption studies of cyanide onto activated carbon and γ-alumina impregnated with cooper ions

Liliana Giraldo[1], J.C. Moreno-Piraján[2]

[1]Facultad de Ciencias, Departamento de Química, Universidad Nacional de Colombia; lgiraldogu@bt.unal.edu.co;
[2]Facultad de Ciencias, Departamento de Química, Grupo de Investigación en Sólidos Porosos y Calorimetría, Universidad de los Andes, Colombia; jumoreno@uniandes.edu.co.

Received 5 May 2010; revised 17 June 2010; accepted 20 June 2010.

ABSTRACT

In this research, adsorption of cyanide onto catalyst synthesized with activated carbon and γ-alumina used supported and cooper has been studied by means of batch technique. Percentage adsorption was determined for this catalyst in function of pH, adsorbate concentration and temperature. Adsorption data has been interpreted in terms of Freundlich and Langmuir equations. Thermodynamics parameters for the adsorption system have been determined at three different temperatures.

Keywords: Activated carbon; Alumina; Cyanide; Isotherms; Thermodynamic

1. INTRODUCTION

Waste water discharged by industrial activities is often contaminated by a variety of toxic or otherwise harmful substances which have negative effects on the water environment. For example, of metal finishing industry and electroplating units is one of the major sources of heavy metals such as (Zn, Cu, Cr, Pb etc.) and cyanide pollutants which contribute greatly to the pollution load of the receiving water bodies and therefore increase the environmental risk [1-4].Cyanide present in effluent water of several industries. Cyanidation has dominated the gold mining industry. In view of the toxicity of cyanide, and the fact that cyanide is fatal in small dosages, authorities have been forced to tighten up plant discharge regulations. It is therefore vital to recover as much cyanide as possible, not only to meet standard requirements, but to strive towards obtaining lower levels of free cyanide (CN-) in tailing and plant effluent [4-8]. The solubility of gold in cyanide solution was recognized as early as 1783 by Scheel (Sweden) and was studied in the 1840s and 1850 s by Elkington and Bagration (Russia), Elsner (German) and Faraday (England) [9]. Elkington also had a patent for the use of potassium cyanide solutions for electroplating of gold and silver [9]. Cyanide is a singly-charged anion containing unimolar amounts of carbon and nitrogen atoms triply-bounded together. It is a strong ligand, capable of complexing at low concentrations with virtually any heavy metal. Because the health and survival of plants and animals are dependent on the transport of these heavy metals through their tissues, cyanide is very toxic. Several systems have been adopted for the reduction of cyanide in mill discharges. There are SO_2 assisted oxidation, natural degradation, acidification volatilization-reneutralization, oxidation and biological treatment. However, in the first three processes, cyanide reduction does not appear to meet the strict regulatory requirements, and as for the fourth process, it is limited to certain climate conditions. The next best process used, is the oxidation with hydrogen peroxide where the cyanide concentration is reduced to low enough levels, but this process requires an expensive reagent which cannot be reused [10-16]. Activated carbon was used for the removal of free cyanide from solution, but observed that copper-impregnated carbon yielded far better cyanide removal [17]. However, did not test other metal impregnated carbons or different metal loadings on the carbon. The use of a metal impregnated carbon system would therefore be more effective in reducing cyanide concentrations in solution. Due to the problem mentioned above, the study on using activated carbon in the removal of free cyanide is being done in our laboratory [18,19]. The adsorption onto activated carbon has found increasing application in the treatment of wastewater, as well as for the recovery of metals from cyanide leached pulps. Activated carbon has a great potential for cyanide waste treatment both in gold extraction plants and effluent from metal finishing plants and hence, it forms a subject studied in the present work. Characterization of activated carbon shows that surface area has an effect although the reactivity of the surface as a result of oxygenated functional groups, e.g.

carboxylate and phenolate is thought to be significant in the sorption of metal cations. Pore size distribution has been used to describe the internal structures and adsorption capacities of activated carbons [20]. The highly active surface properties of the activated carbon are attributed to the chemical functional groups and the internal surface areas, which typically range from 500 to 3000 m^2/g [21]. The effect of copper was studied in the adsorption of cyanide onto activated carbon. It was found that the removal capacity was highly improved by the presence of copper [18-21]. It is the aim of this research to use of activated carbon (obtained from cassava peel) [22,23] and alumina impregnated with cooper for obtain catalyst for the removal of cyanide for dilute solutions. The pertinent parameters that influence adsorption such as initial cyanide (CN^-) concentration, agitation time, pH and temperature were investigated. Adsorption isotherms at three different temperatures (*i.e.* 283 K, 313 K, 323 K) have been studied. The adsorption data have been interpreted using Freundlich and Langmuir isotherms. Various thermodynamic parameters including the mean energy of adsorption have been calculated.

2. EXPERIMENTAL

All reagents used in the experimental work were of analytical grade (E.MERCK)® Argentmetric (largely $AgNO_3$) titrations were employed for CN- determination [8]. Stock solution of cyanide (1000 $mg.L^{-1}$) was prepared by dissolving Sodium cyanide in distilled water. The concentration range of cyanide prepared from stock solution varied between 10 to 80 $mg.L^{-1}$.

2.1. Preparation of Catalysts

The activated carbon used in this study was prepared for by pyrolysis of cassava peel in presence of chloride zinc (chemical activities) by our research group. Cassava peel from Colombian Cassava cultives were impregnated with aqueous solutions of $ZnCl_2$ following a variant of the incipient wetness method [22,23] with a specific surface area of 1567 $m^2.g^{-1}$.

One of them was obtained commercial (Sasol™) sample of γ-alúmina.

2.1.1. Impregnation

Catalysts (activated carbon with cooper was labeled Cu-AC and γ-alúmina with cooper was labeled Cu-A) were formulated using a solution of $Cu(NO_3)_2.3H_2O$ (5 wt.(%) Cu) as a precursor of the active agent because of its water solubility, lower cost, and lack of poisonous elements. Activated carbons from cassava peel and γ-alúmina were used as supports. There are two well known methods of loading the metal precursor on the support: incipient wetness impregnation and soaking method. In this case, the second one was used; the activated carbon and γ-alúmina were soaked in a copper nitrate solution for 8 days under agitation until the equilibrium was reached. The ratio solid/solution (weight base) was equal to 6. The impregnated solids were filtered and scurried during 24 hours. Then, they were dried at 378 K for 24 hours 12.

2.1.2. Thermal Treatment

The objective of this step is to transform the copper salt (cupric nitrate) in copper oxides, which are the active catalytic agents. The high temperature used descomposes the nitrate releasing nitrogen oxides. The reactor must work in a nitrogen atmosphere to avoid the combustion of the support. The catalysts were treated in the activation reactor, at 830 K for 24 hours. After that, a nitrogen flow was maintained until the reactor reached room temperature 12.

2.2. Characterization

Nitrogen adsorption-desorption isotherms were performed using an Autosorb-3B (Quantachrome) equipment. Samples of 0.100 g were oven-dried at 378 K during 24 hours and outgassed at 473 K under vacuum for 10 hours. The final pressure was less than 10^{-4} mbar. Textural parameters were derived from adsorption data. The specific BET surface area was estimated 15. The specific total pore volume (V_T) was determined from the adsorption isotherm at the relative pressure of 0.99, converted to liquid volume assuming a nitrogen density of 0.808 $g.cm^{-3}$. The specific micropore volume (V_{DR}) was determined using the Dubinin-Radushkevich mode l16. The pore size distribution (PSD) was analyzed using the BJH method [17,21,22,23,24].

Acidity and basicity determinations of the support were made by titrating the acid sites with a strong basic solution and the basic sites with a strong acid solution, following the protocol detailed by Giraldo *et al*. [22,23].

The point of charge zero (PZC) of the catalyst were determined for a procedure very similar [24], which are described here. In a beaker were added 0.1 g of finely ground catalyst in an agate mortar and 20 mL of a 0.01 M KCl-0.004 M KOH. The solution was kept under constant stirring for 48 h. Then, titration was performed with a 0.1 M HCl solution using a burette and a stream of nitrogen to prevent carbon dioxide from the air is absorbed into the solution and the formation of CO_3^{-2} and HCO_3^{-1}. The titrant solution was added slowly 0.1 mL and was recorded by adding the aggregate volume and pH of the solution. Furthermore, the evaluation was carried 0.01 M solution of KCl -0004 KOH under the same conditions but without catalyst. The PCC of the catalyst was determined by plotting the pH of the solution against the volume of titrant solution to the solution without

catalyst and the catalyst solution, the pH where these two curves intersect corresponds to the PZC. Another way interpret experimental data is to calculate the burden of surface of the catalyst using the equations reported in literature [24], in this case the pH at which the burden of surface is zero corresponds to the PZC.

Studies of X ray diffraction (XRD) patterns were recorded at room temperature using a Rigaku diffractometer operated at 30 kV and 20 mA, employing Ni-filtered Cu Kα radiation (λ = 0.15418 nm). The crystalline phases were identified employing standard spectra software.

2.3. Adsorption Studies

The adsorption of CN^- on activated carbon and γ-Alumina impregnated with Cu was studied by batch-technique [9]. The general method used for these studies is described below: A known weight (*i.e.*, 0.5 g of the Cu-AC or Cu-A) was equilibrated with 25 cm^3 of the spiked cyanide solution of known concentrations in Pyrex glass flasks at a fixed temperature in a thermostated shaker water bath for a known period of time (*i.e.* 30 minutes). After equilibrium the suspension was centrifuged in a stoppered tube for 5 minutes at 4500 rpm, was then filtered through Whatman 41 filter paper. All adsorption experiments except where the pH was varied were done at pH 7.20, which was obtained naturally at solution to adsorbent ratio of 50:1. To study the effect of pH, in one set of experiments the pH of the suspensions was adjusted by using $NaOH/NH_4OH$ and HNO_3. The pH of solutions was in the range of 3.0-12. The amount of cyanide adsorbed, "X" and the equilibrium cyanide concentration in the solution, "C_e" was always determined volumetrically with standard silver Nitrate solution. Adsorption of cyanide on Cu-AC and Cu-A was determined in terms of percentage extraction. Amount adsorbed per unit weight of the Cu-AC or Cu-A, X/m was calculated from the initial and final concentration of the solution, Adsorption capacity for the adsorption of cyanide species has been evaluated from the Freundlich and Langmuir adsorption isotherms were studied at three different temperatures (*i.e.* 283 K, 313 K, 323 K). The cyanide concentration studied was in the range of 10 pmm to 80 ppm for 50:1 solution to the catalyst.

3. RESULTS AND DISCUSSIONS

3.1. Characterization

Nitrogen adsorption-desorption isotherms for the supports and catalysts are shown in **Figures 1** and **2**. The textural parameters modeled from the adsorption data are summarized in **Table 1**.

Both catalysts present lower surface area and pore volume compared to that of the corresponding support. This is mainly due to a pore blocking effect, especially micropores, which is evident from the analysis of the uptake at low relative pressures in the adsorption-desorption isotherms for the catalysts compared to the supports. The micropore volume and surface area using activated carbon is higher than that obtained from γ-alumina, as the total pore volume for both materials.

The isotherms corresponding to both catalysts present

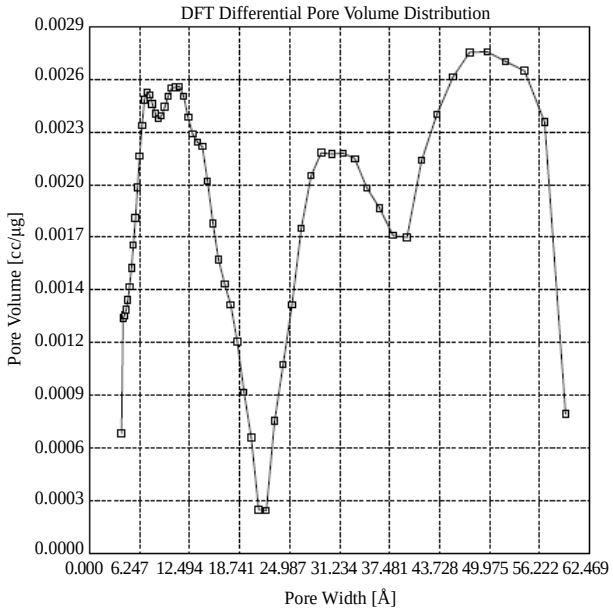

Figure 1. Pore distribution for Cu-AC.

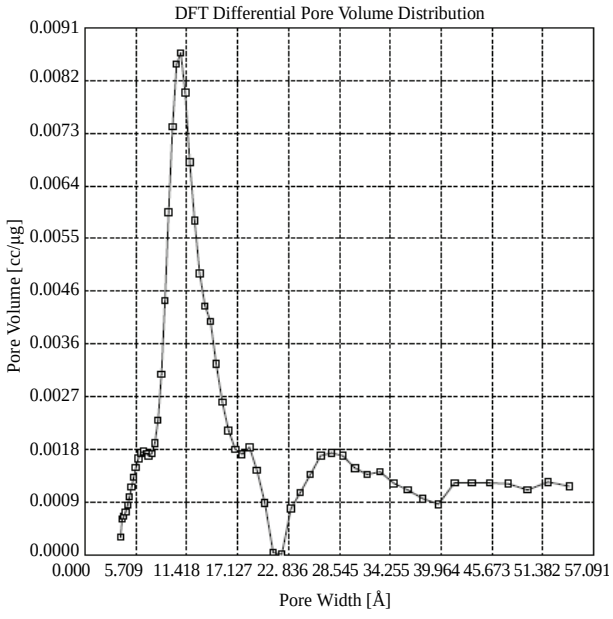

Figure 2. Pore distribution for Cu-A.

Table 1. Textural parameters of catalyst.

Sample	BET surface area ($m^2.g^{-1}$)	Pore volume (V_T) ($cm^3.g^{-1}$)	Specific micropore volume (V_{DR}) ($cm^3.g^{-1}$)
AC	1567	0.6641	0.6245
Cu-AC	1245	0.5478	0.6042
γ-Alúmina	245	0.2454	-
Cu-A	207	0.2087	-

a hysteresis loop. The uptake at high pressure rises significantly for Cu-A, which indicates a considerable presence of mesoporous. The BJH pore size distribution (**Figures 1** and **2**) shows important mesoporosity in the range of 40-90 Å for both catalysts, especially in Cu-AC, in agreement with its hysteresis loop.

Figures 3 and **4** show the curves obtained in the point of zero charge determinations using the mass titration method. All these results, pH, acidity, basicity and pzc, demonstrate that the surface of both supports are strongly basic (**Table 2**).

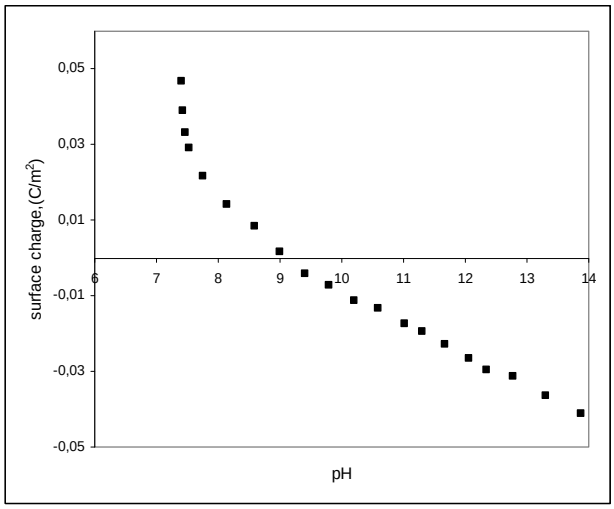

Figure 3. PZC for Cu-A catalyst.

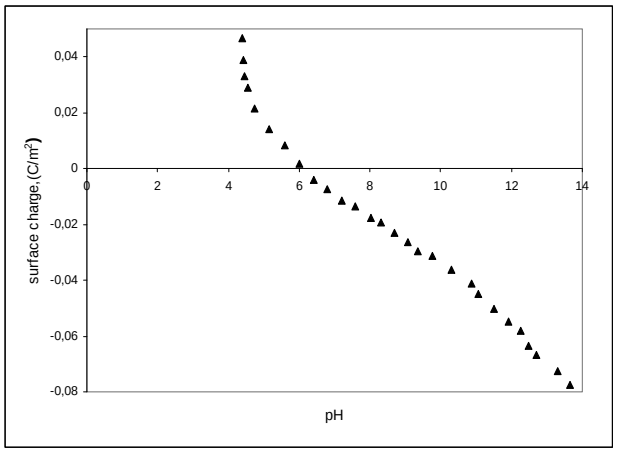

Figure 4. PZC for Cu-AC catalyst.

The X Ray diffraction patterns for both catalysts, Cu-AC and Cu-A respectively are shown in **Figures 5** and **6**. The profiles obtained show that the main oxidized metal compound corresponds to CuO. The signals of Cu_2O and Cu are also present in the spectra, specially the last one. The presence of CuO was expected because the metal appears as divalent ion in the precursor salt. The reduced species (Cu^+ and CuO) could be produced by the reducing action of the carbon surface during the thermal treatment at high temperatures.

The adsorption of cyanide on the catalyst Cu-AC and Cu-A were studied as a function of shaking time in water Bath shaker (Labconco 3535 US), pH, adsorbate concentration and temperature for known cyanide concentration at 313 K. The results are interpreted in terms of percentage adsorption. The variation of % adsorption with different intervals of time ranging from 2 minutes to 48 hours is illustrated by **Figure 7** which shows that the adsorption of cyanide at 25 ppm as well as 50 ppm concentration on Cu-AC and Cu-A is rapid at 313 K and equilibrium reached instantaneously after mixing cya-

Table 2. Physicochemical characteristics of the catalyst.

Support	pH	Acidity ($mmol.g^{-1}$)	Basicity ($mmol.g^{-1}$)	pH_{PZC}
Cu-AC	8.6	0.27	0.81	9.0
Cu-A	5.8	0.20	0.45	6.0

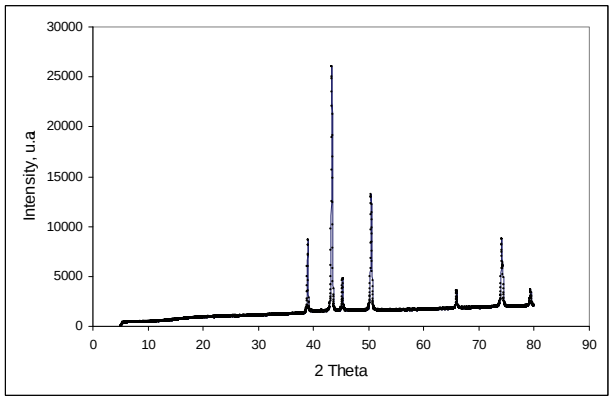

Figure 5. DRX for Cu-AC catalys.

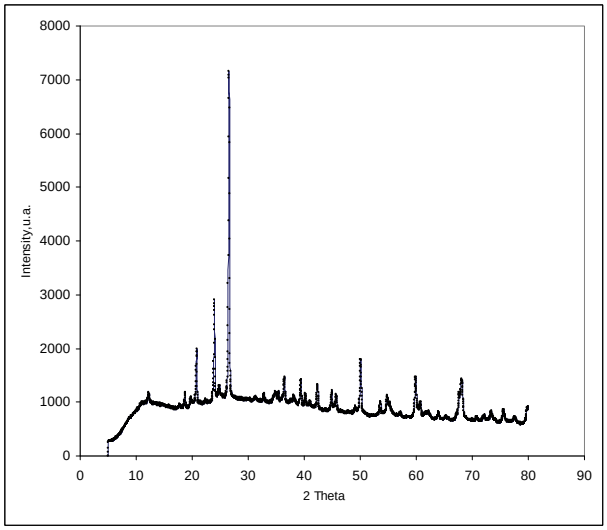

Figure 6. DRX Cu-A catalyst.

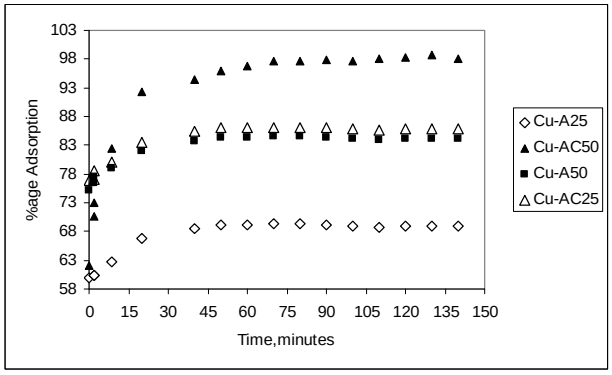

Figure 7. Effect of shaking time % age Adsorption at 25 ppm and 50 ppm for the synthesized catalyst.

nide solution with the catalyst. However, an equilibriumis reached faster with the catalyst of Cu-AC than with Cu-A; that is associated with the greatest amount of copper that is achieved on the activated carbon adsorb taking into account their surface properties and specific chemical the PZC allowing CN ions adsorb more rapidly on the catalyst surface Cu-AC on the Cu-A.

No significant change in % adsorption values was observed up to 48 hours, which indicates that surface precipitation as well as ion exchange may be the possible adsorption mechanism. Therefore, equilibrium time of 20 minutes was selected for all further studies. The adsorption is pH dependent, a much greater adsorptive capacity for cyanide was observed in neutral solution for both catalyst; moreover it is more higher adsorption capacity for Cu-AC, *i.e.*, pH 7- 8.0 (**Table 3** and **Table 4)**.

Because when the pH is reduced, surface charge of the particles becomes increasingly positive and because of the competition of the hydrogen ions for the binding sites,

Table 3. Dependence of absorbance concentration relative to CN- on Cu-A catalyst at 293 K.

pH	Amount of CN^- in taken	Amount of CN- in sol. At equilibrium	Amount of CN^- Adsorbed	Adsorption
	(ppm)	(ppm)	(ppm)	(%)
2,06	20	6,48	13,52	67,60
4,57	20	5,44	14,56	72,80
6,54	20	4,11	15,89	79,45
7,28	20	2,13	17,87	89,35
9,14	20	4,11	15,89	79,45
11,34	20	6,55	13,45	67,45
12,75	20	7,76	12,24	61,20

Table 4. Dependence of absorbance concentration relative to CN- on Cu-AC catalyst at 293 K.

pH	Amount of CN^- in taken	Amount of CN- in sol. At equilibrium	Amount of CN^- Adsorbed	Adsorption
	(ppm)	(ppm)	(ppm)	(%)
2,06	20	5,35	14,65	73,25
4,57	20	3,34	16,66	83,30
6,54	20	1,23	18,77	93,85
7,28	20	0,99	19,01	95,05
9,14	20	2,02	17,98	89,90
11,34	20	4,66	15,34	75,70
12,75	20	5,55	14,45	72,25

metal ions tend to desorbs at low pH region, as well a small decrease in cyanide adsorption was observed at pH higher than 9.0. This behavior may be due to the formation of soluble cyanide complexes, which remain in solution as dissolved component. Similarly adsorption of cyanide as a function of its concentration was studied by varying the metal concentration from 10ppm to 80 pmm, % age adsorption values decreases with increasing metal concentration (**Table 5)**, which suggest that at least two types of phenomena (*i.e.* adsorption as well ion-exchange) taking place in the range of metal concentration studied, in addition less favorable lattice positions or exchange sites become involved with increasing metal concentration.

The adsorption in aqueous solutions and adsorption isotherms at three different temperatures (*i.e.* 278 K, 298 K, 323 K) were obtained by plotting the amount of cya

Table 5. Dependence of adsorbate concentration relative to CN- on Cu-AC (this catalyst present major adsorption).

Amount of Adsorbent CN^- in taken	Amount of CN- taken	Amount of CN^- in soln. at Equilibrium	Amount of CN^- Adsorbed	Adsorption
(mg	(ppm)	(ppm)	(ppm)	(%)
500	5,00	2,42	2,58	51,60
500	10,00	3,12	6,88	68,00
500	20,00	1,41	18,52	92,60
500	40,00	15,65	30,35	75,88
500	60,00	37,98	38,44	64,06
500	80,00	41,09	38,91	48,63
500	100,00	54,58	45,42	45,42

nide adsorbed on Cu-A and Cu-AC (mg/g) against metal at equilibrium concentration "Ce" (mg/l). Adsorption of cyanide decreases with increasing temperature. Two models, Langmuir and Freundlich equations, were used to describe experimental data for adsorption isotherms.

The linear form of the Freundlich isotherm model is given by the following relation:

$$\text{Log } x / m = \log K_F + 1 / n \log Ce \quad (1)$$

where x / m is the amount adsorbed at equilibrium (mg/g), Ce is the equilibrium concentration of the adsorbate (mg/l), and K_F and 1 / n are the Freundlich constants related to adsorption capacity and adsorption intensity respectively, of the sorbent. The values of K_F and 1/n can be obtained from the intercept and slope respectively, of the linear plot of experimental data of log X / m versus logCe. The linear form of the Langmuir isotherm model can be represented by the following relation:

$$Ce / x / m = 1 / K_L Vm + Ce / Vm \quad (2)$$

where Vm and K_L are the Langmuir constants related to the maximum adsorption capacity and the energy of adsorption, respectively. These constants can be evaluated from the intercept and slope of the linear plot of experimental data of Ce / X / m versus Ce. The Freundlich and Langmuir adsorption isotherms are shown in **Figure 3** and **Figure 4** (the isotherms linearizated not shown here). The related parameters of Langmuir and Freundlich models are summarized in **Table 6**. The results reveal that both the Langmuir isotherm model adequately describes better the adsorption data (See **Figure 8**).

Calculations of thermodynamic parameters:

Thermodynamic parameters such as Gibbs free energy ΔG° (kJ/mol), change in enthalpy ΔH° (kJ/mol) and change in entropy ΔS° ($J.K^{-1}mol^{-1}$) for cyanide adsorption were calculated from the distribution constant K [10] by using the following relations:

$$\Delta G° = - RT\ln K \quad (3)$$

$$\Delta G° = \Delta H° - \quad (4)$$

and

$$K = - \Delta H° / RT + \text{Constant} \quad (5)$$

Tables 7 and **8** show the values of thermodynamics parameters ΔH°, ΔS°, ΔG° for Cu-AC and Cu-A catalyst synthesized. The positive value of ΔH° = 6.234 kJ/mole for Cu-AC and 4.897 kJ/mole, which is calculated from **Eq.5** and **Figure 5**, confirms the endothermic nature of the overall adsorption process. The positive value of ΔS° suggests increased randomness at the solid/solution interface with some structural change in the adsorbate and adsorbent and also affinity of the Cu-AC and Cu-A towards CN^-; the values more highest of entropy indicate spontaneous process. A negative value of ΔG° indicates the feasibility and spontaneity of the adsorption process, where higher negative value reflects a more energetically favorable adsorption process. The process of adsorption Cu-AC is more favorable.

Table 6. Parameters of Lagmuir and Freundlich for adsorption of cyanide.

	Langmuir			Freundlich		
	Q_o	K	R^2	K_f	n	R^2
Alumina	221,9725	0,018648	0,99835	7,431714	1,477998	0,99653
Activated Carbon	226,7673	0,029620	0,99781	11,98697	1,628459	0,99330
Cu-A	317,2252	0,041956	0,99700	22,77397	1,759936	0,98713
Cu-Ac	297,2679	0,164927	0,99646	58,15241	2,573350	0,97419

Table 7. Values of thermodynamic data for Adsorption of CN- on Cu-AC.

Temperature K	ΔH° kJ/mol	ΔG° kJ/mol	ΔS° J/K.mol
278	6.234	-8.856	0.0543
298	6.234	-6.636	0.0432
323	6.234	-12.666	0.0585

Table 8. Values of thermodynamic data for Adsorption of CN- on Cu-A.

Temperature K	ΔH° kJ/mol	ΔG° kJ/mol	ΔS° J/K.mol
278	4.897	-6.863	0.0423
298	4.897	-6.963	0.0398
323	4.897	-10.183	0.0467

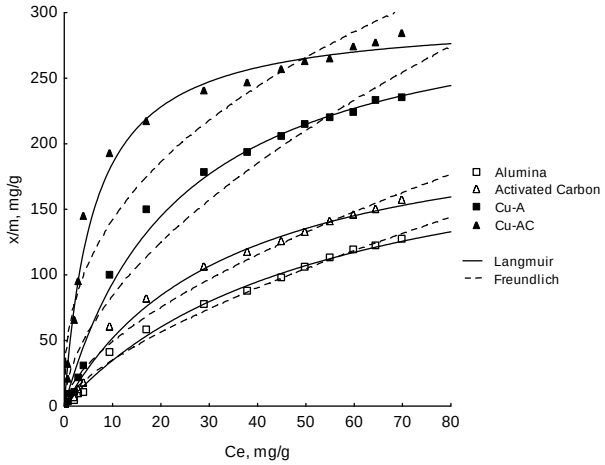

Figure 8. Langmuir and Freundlich models adjustment at 298 K.

4. CONCLUSIONS

Keeping the adsorptive nature of Cu-AC and Cu-A in view it is felt desirable to select batch adsorption process for removal of Cyanide from the industrial wastewater using activated carbon and γ-alumina. The main advantages of the procedure are:

1) The cost of starting materials for obtaining the catalyst is low and easily available in country.
2) Ease and simplicity of preparation of the catalyst due to non-corrosive and non-poisonous nature of activated carbon and alumina.
3) Rapid attainment of phase equilibration and good enrichment as well fitting of adsorption data with Langmuir isotherms.
4) The positive value of ΔH° and negative values of ΔG° indicate the endothermic and spontaneous nature of the adsorption process.

5. ACKNOWLEDGEMENTS

The authors wish to thank the Master Agreement established between Universidad de los Andes and Universidad Nacional de Colombia, and the Memorandum of Understanding between Departments of Chemistry of both Universities. Additionally, special thanks to Fondo Especial de la Facultad de Ciencias and Proyecto Semilla of Universidad de los Andes for the partial financial of this research.

REFERENCES

[1] Abell, M.L. and Barselton, P.J. (1974) The maple V handbook. AP Professional, New York.
[2] Contescu, C., Jagiello, J. and Schwarz, J.A. (1995) Proton affinity distributions: A scientific basis for the design and construction of supported metal catalysts. *Preparation of Catalysts VI, Scientific Bases for the Preparation of Heterogeneous Catalysts*, Elsevier Science, New York.
[3] Cooper, D. and Plane, A.R. (1966) Cyanide complexes of copper with ammonia and ethylenediamine. *Inorganic Chemistry*, **5**, 1677-1681.
[4] Gupta, A., Johnson, E.F. and Schlossel, R.H. (1987) Investigation into the ion exchange of the cyanide complexes of Zinc(II), Cadmium(II), and Copper(I) Ions. *Industrial Engineering Chemistry Research*, **26,** 588-597.
[5] Hogfeldt, E. (1982) Stability constants of metal-ion complexes: part A: inorganic ligands, Pergamon Press, Oxford.
[6] Riley, T.C. and Semmens, J.M. (1994) Recovery of cadmium and cyanide using a combination of ion exchange and membrane extraction. *Plating and Surface Finishing*, **81**, 46-54.
[7] Tan, T.C. and Teo, W.K. (1987) Destruction of cyanides by thermal hydrolysis. *Plating and Surface Finishing*, **74**, 70-76.
[8] Tien, C. (1994) Adsorption calculations and modeling. Butterworth-heinemann series in chemical engineering, Butterworth Heinemann, Boston.
[9] Wedl, A.G. and Fulk, J.D. (1991) Cyanide destruction in plating sludges by hot alkaline chlorination. *Metal Finish*, **89**, 33-38.
[10] Gupta, C.G. and Murkherjee, T.K. (2001) Hydrometallurgy in extraction process, CRC press, Florida.
[11] Zhou, C.D. and Chin, D.T. (1994) Continuous electrolytic treatment of complex metal cyanides with a rotating barrel plater as the cathode and a packed bed as the anode. *Plating and Surface Finishing*, **81**, 70-81.
[12] Gill, J.B., Gans, P., Dougal, J.C. and Johnson, L.H. (1991) Cyano and thiocyano complexation in solutions of noble metals, *Reviews in Inorganic Chemistry*, **11**, 177-182.
[13] Bhakta, D., Shukla, S.S. and Margrave, L.J. (1992) A novel photocatalytic method for detoxification of cyanide wastes. *Environmental Science & Technology*, **26**, 625-634.
[14] Bhargava, S., Tardío, J., Prasad, J., Föger, K., Akolekar, D. and Grocott, S. (2006) Wet oxidation and catalytic wet oxidation. *Industrial & Engineering Chemical Research*, **45**, 1221-1234.
[15] Lei, L., Hu, X., Chen, G., Porter, J.F. and Yue, P.L. (2000) Wet air oxidation of desizing wastewater from textile industry. *Industrial & Engineering Chemical Research*, **39**, 2896-2905.
[16] Mantzavinos, D., Hellenbrand, R., Livingston, A.G. and Metcalfe, I.S. (1996) Catalytic wet air oxidation of polyethylene glycol. *Applied Catalysis B*: *Environmental*, **11**, 99-107.
[17] Kolaczkowski, S.T., Plucinski, P., Beltran, F.J., Rivas, F. J., and Mc Lurgh, D.B. (1999) Wet air oxidation: A review of process technologies and aspects in reactor design, *Chemical Engineering Journal*, **73**, 143-152.
[18] Luck, F. (1999) Wet air oxidation: Past, present and future. *Catalysis Today*, **53**, 81-89.
[19] Pintar, A. (2003) Catalytic process for the purification of drinking water and industrial effluents. *Catalysis Today*, **77**, 451-462.
[20] Fortuny, A., Bengoa, C., Font, J., Catells, F. and Fabregat, A. (1999) Water pollution abatement by catalytic wet air oxidation in a trickle bed reactor, *Catalysis Today*, **53**, 107-112.
[21] Deiana, A.C., Granados, D., Petkovic, L.M., Sardella, M. F. and Silva, H.S. (2004) Use of grape must binder to obtain activated carbon briquettes. *Brazilian Journal of Chemical Engineering*, **21**, 585-592.
[22] Moreno-Piraján, J.C. and Giraldo, L. (2010) Study of activated carbons by pyrolysis of cassava peel in the presence of chloride zinc. *Journal of Analytical and Applied and Pyrolysis*, **87(2),** 288-290.
[23] Moreno-Piraján, J.C. and Giraldo, L. (2010) Adsorption of copper from aqueous solution by activated carbons obtained by pyrolysis of cassava peel. *Journal of Analytical Applied and Pyrolysis*, **7(2)**, 188-193.
[24] Rodríguez-Reinoso F. (1998) The role of carbon materials in heterogeneous catalysis, *Carbon*, **36**, 159-164.

Vol.2, No.10, 1073-1078 (2010)
doi:10.4236/ns.2010.210133

Natural Science

Structural and electrical characterization of $Bi_2VO_{5.5}$ / $Bi_4Ti_3O_{12}$ bilayer thin films deposited by pulsed laser ablation technique

Neelam Kumari, Saluru Baba Krupanidhi, Kalidhindi Balakrishna Raju Varma*

Materials Research Centre, Indian Institute of science, Bangalore, India; *Corresponding Author: kbrvarma@mrc.iisc.ernet.in.

Received 10 June 2010; revised 13 July 2010; accepted 18 July 2010.

ABSTRACT

The pulsed laser ablation technique has been employed to fabricate bilayer thin films consisting of layered structure ferroelectric bismuth vanadate ($Bi_2VO_{5.5}$) and bismuth titanate ($Bi_4Ti_3O_{12}$) on platinized silicon substrate. The phase formation of these films was confirmed by X-ray diffraction (XRD) studies and the crystallites in these bilayers were randomly oriented as indicated by diffraction pattern consisting of the peaks corresponding to both the materials. The homogeneous distribution of grains (~300 nm) in these films was confirmed by atomic force microscopy. The cross-sectional scanning electron microscopy indicated the thickness of these films to be around 350 nm. The film exhibited P-E hysteresis loops with P_r ~ 11 μC/cm^2 and E_c ~ 115 kV/cm at room temperature. The dielectric constant of the bilayer was ~ 225 at 100 kHz which was higher than that of homogeneous $Bi_2VO_{5.5}$ film.

Keywords: Thin Films; Ferroelectric; Dielectric; Laser ablation

1. INTRODUCTION

Fabrication and stabilization of materials that do not occur naturally has been the subject of great interest of current materials research [1]. Recently the investigations of ferroelectric multilayer and superlattices have received considerable attention due to the fact that these kinds of engineered materials have been identified as possessing functional properties in a sense superior to their single phase constituent films [2-4]. The control of properties could be achieved by tailoring the lattices [5] e.g. by lattice mismatch induced strain at the interface-strain engineering, polarization mismatch enhancing polarization, chemical heterogeneity, which in turn may enhance the physical properties or in many cases may give rise to new properties which were not exhibited by the starting materials.The Aurivillius family of layered bismuth oxides is a class of ferroelectrics whose properties have been widely studied [6]. More recently, there is a renewed interest because of the discovery of fatigue-free behavior in thin films for nonvolatile memory applications [7]. More importantly, Bismuth Titanate [$Bi_4Ti_3O_{12}$ (BTO)], which is an n = 3 member of this family has been reported to be a very good ferroelectric and electro-optic with small amount of the substitution of impurities, such as La, Sm and Nd for Bi and V, W and Nb for Ti in the pseudoperovskite $(Bi_2Ti_3O_{10})^{2-}$ layers of BTO to improve the remnant polarization and fatigue endurance. [8-11]. Bismuth Vanadate [$Bi_2VO_{5.5}$ (BVO)] is a vanadium analog of the n = 1 member of the Aurivillius family which has a Curie temperature of 720 K [12-14]. It has been reported in the literature that the composite of BVO and BTO solid solution possesses better physical properties and low leakage current than that of BVO [15]. The single phase BVO thin films have been prepared on platinum coated Si substrates and studied their ferroelectric and dielectric properties [16]. It has been found that these films possess non-negligible ionic conductivity attributed to the presence of oxide ion vacancies in the perovskite layer. Also the contribution of oxygen ion vacancies to the ferroelectric properties was quite high as established through fatigue characteristics.

In this article we report the structural and electrical properties of bilayer stacking of $Bi_2VO_{5.5}$ (BVO) and $Bi_4Ti_3O_{12}$ (BTO). We have fabricated bilayer thin films consisting of alternating BVO and BTO layers henceforth mentioned as BVBT. The presence of a BTO layer along with the BVO layer effectively suppressed the high electrical conductivity of BVO which is commonly observed in the laser ablated BVO thin films deposited on Pt / TiO_2 / SiO_2 / Si substrates. The BVBT bilayer thin films showed a fair increase in remnant polarization (P_r), and more interestingly a significant reduction in coercive field (E_c), as compared to the homogeneous BVO films

of the same thickness. The details pertaining to the structural, dielectric and ferroelectric properties of BV BT bilayers fabricated on platinized silicon in metal insulator metal (MIM) configuration are illustrated in the following sections.

2. EXPERIMENTAL

The bilayer structures consisting of BVO and BTO were fabricated by a multitarget-pulsed laser deposition (PLD) technique on platinized silicon substrate in the configuration Au / BVO / BTO / Pt (111) / TiO_2 / SiO_2 / Si (100). A 248 nm excimer laser (Lambda Physik Compex 201) operated at 5 Hz was alternately focused onto the well-sintered freshly polished BVO and BTO rotating targets with an energy density of 2 Jcm^{-2} at an angle of 45° by a UV lens. The substrates were placed parallel to the target at a distance of 3.5 cm and heated to 650℃ by a resistance heater. The chamber was first pumped down to 1×10^{-6} m bar, and then high purity oxygen was introduced using a mass flow controller to get oxygen partial pressure of 100 m Torr. After deposition of both the layers, the samples were cooled down to room temperature under an oxygen pressure of 1 mbar to minimize the oxygen ion vacancies. In these cases, the bilayer thin films were prepared with BTO as the first layer and BVO as the final layer with equal layer thickness.

The X-ray diffraction (XRD) studies were carried out to characterize the phase and crystallographic structure of the bilayer films using Cu K_α ~ 1.541 Å radiation (Scintag XR 2000 Diffractometer). Scanning electron microscope (SEM) (Sirion 200) and atomic force microscope (AFM) (Veeco CP II) were employed to monitor the microstructure of the films.

For electrical measurements, gold dots of 1.96×10^{-3} cm^2 area were deposited on the top surface of the films through a shadow mask using thermal evaporation technique. The electrode dots were annealed at 250℃ for 30 min. The Pt surface was used as the bottom electrode for capacitance measurements. The dielectric constant and C-V measurements were performed at a signal strength of 0.5 V using impedance analyzer (HP4294A). The polarization-electric field (P-E) hysteresis was recorded using a Precision Workstation (Radiant Technologies, Inc.) ferroelectric test system in virtual ground mode.

3. RESULTS AND DISCUSSIONS

Bilayered thin films of BVO and BTO were fabricated on platinized silicon substrates by pulsed laser ablation using the optimized deposition conditions for BVO and BTO layers. A schematic diagram of the bilayer thin film grown in this work is shown in **Figure 1**. Equal thickness (~ 175 nm) of the individual layers was maintained in bilayer films. The BTO layer was grown first on platinized silicon substrate and then immediately followed by the growth of BVO layer without any delay in order to maintain the sharp interface between the two layers. The sequence of the layers was also reversed, but not much difference in terms of physical properties was observed, hence the one bilayer structure *i.e.* BVBT bilayer is discussed as a symbolic representative one.

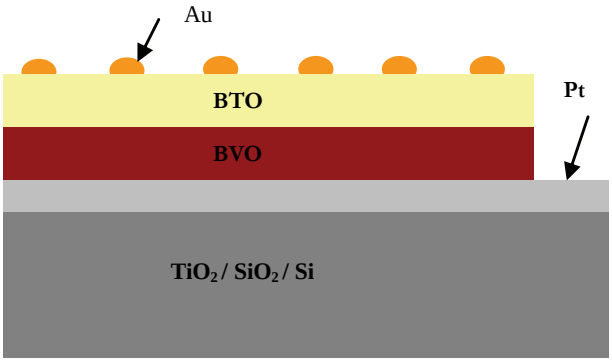

Figure 1. Schematic diagram of a BVBT bilayer thin film.

Figure 2(a) shows the representative XRD pattern of BVBT bilayer film deposited by PLD. The XRD diffraction peaks corresponding to both the BVO and BTO phases were observed and these were indexed on the basis of orthorhombic structure of BVO [JCPDS 42-0135] and BTO [JCPDS 72-1019]. It is observed that the film is polycrystalline in nature and main diffraction peaks of both BVO (113) and BTO (117) appear with higher intensities along with the other low intensity peaks. Also, the (002) reflection of BVO along with (004) of BTO appear so close that they overlap giving only one visible peak. The bilayer film possessed an interface between the two individual layers and this interface does influence the physical properties due to the lattice strain at the interface. **Figure 2(b)** shows the (002) diffraction peak corresponding to BVO of the bilayer thin film. The c-axis lattice parameter calculated for BVO from the (002) peak was found to increase from 15.42 Å for BVO layer [17] to 15.50 Å in BVBT bilayer. This increase in out-of-plane lattice parameter might be due to the in plane compressive stress on BVO in BVBT bilayer in the present case in order to keep the cell volume unchanged. Therefore, it is required to grow these films epitaxially and measure the in-plane lattice parameters along with the residual stress in these bilayer films in order to achieve the lattice driven effects in these films.

The surface morphology of the BVBT BL thin film was investigated by contact mode atomic force microscope (AFM). **Figure 3** shows the surface morphology of BVBT bilayer thin film over a 5 μm x 5 μm scan area as two-dimensional (a) and three-dimensional (b) mi-

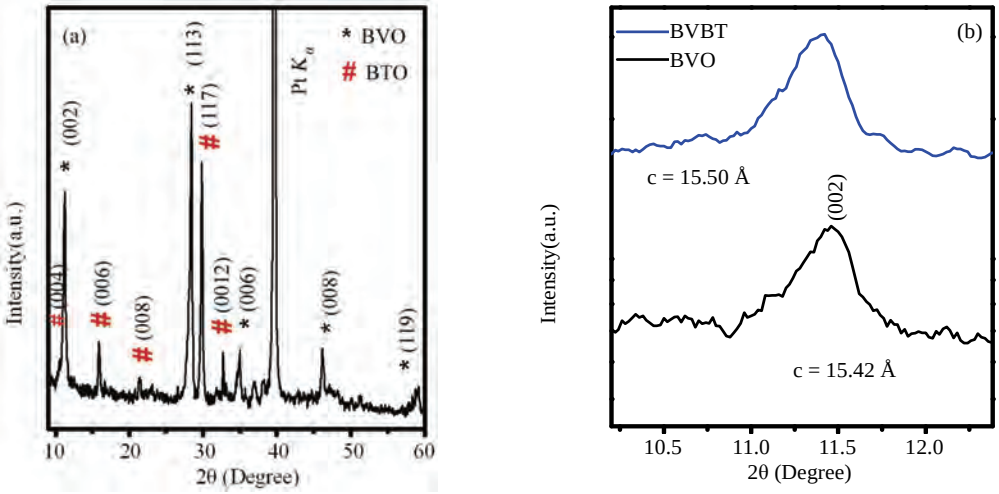

Figure 2. (a) X-ray diffraction pattern of BVBT bilayer thin film. **(b)** Comparison of BVO and BVBT bilayer diffraction pattern along (002) plane of BVO.

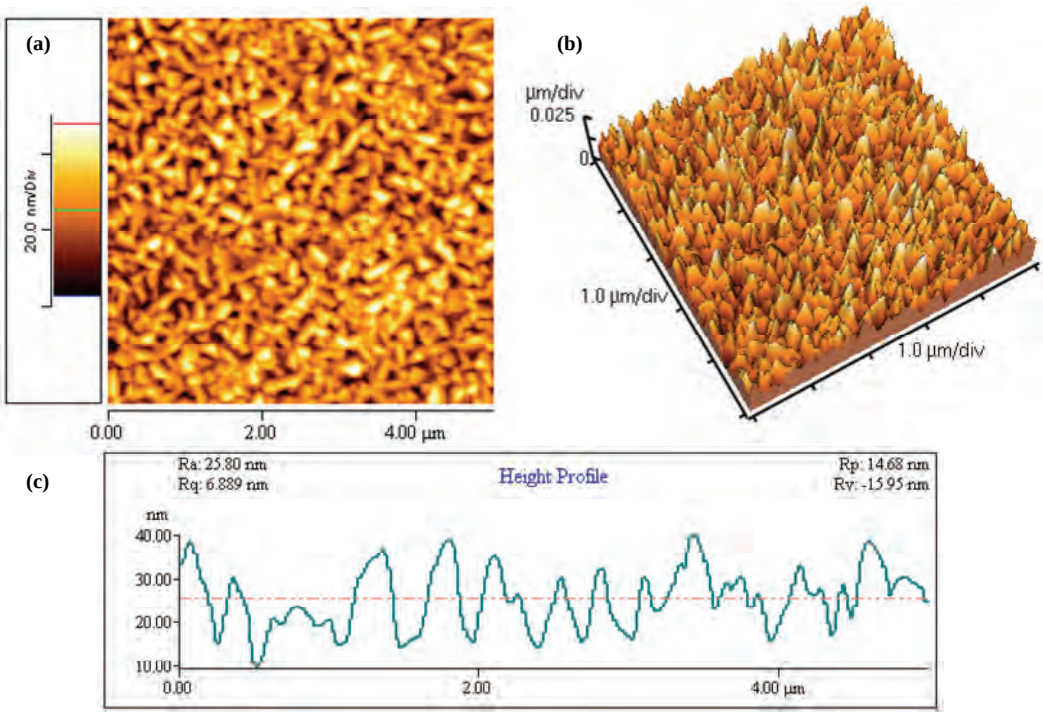

Figure 3. (a) AFM micrograph showing surface topography, **(b)** 3D image of BVBT bilayer thin film and **(c)** line profile.

crographs with the roughness profile mapped using line scan depicted in (c) The BVBT bilayer films exhibited dense surface morphology consisting of distinct grains. Further the homogeneous distribution of grains was observed with an average grain size of 0.3 µm. The root mean square of the surface roughness (R_a) was around 7 nm as observed from the roughness profile. It indicated a good quality of the deposited bilayer films.

The cross sectional microstructure of BVBT bilayer was studied by SEM and is depicted in **Figure 4** which indicated dense bilayer growth with sharp interface with Pt. A columnar like structure was observed for this sample and the thickness of the sample bilayer film was around 300 nm. It is noteworthy here that we could not distinguish between the top BVO and bottom BTO layer in this bilayer structure. This might be due to the very little difference in the atoms constituting the BVO and BTO layers which scatter the electrons almost with the

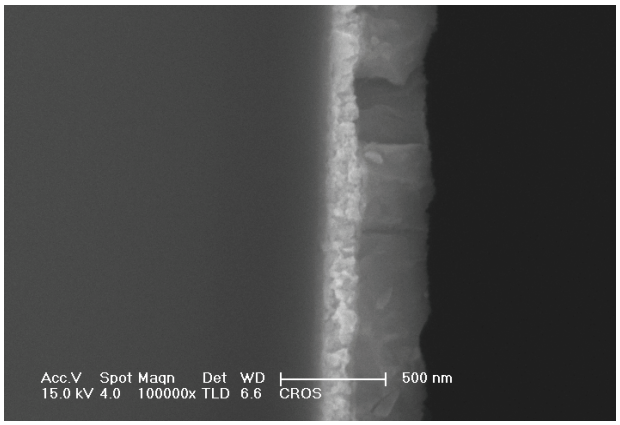

Figure 4. Cross sectional scanning electron micrograph of a representative BVBT bilayer film.

same intensity during and as a result the contrast between the two layers is poor.

In the present study we have further focused on the ferroelectric (FE) properties of these BVBT bilayer thin films deposited on platinized silicon substrate. Polarization measurements were carried out using a Precision Workstation operating in the virtual ground mode as explained earlier. A simple triangular pulse of voltage is applied across the electrodes of the sample which was fabricated in Metal-Insulator-Metal (MIM) configuration and the polarization response of the sample is observed under an integrator circuit. **Figure 5(a)** shows a typical P-E loop obtained for a BVBT bilayer thin film at room temperature. At the applied voltage of 12 V, the measured values of remnant polarization (P_r) and coercive field (E_c) for ~ 350 nm thick BVBT bilayer film were around 11 μC/cm^2 and 115 kV/cm, respectively. The non zero switchable polarization observed at zero applied field is a general characteristic of a FE material [18-19]. It showed two key characteristics of a ferroelectric which are, polarization is reversible by an application of an electric field and polarization remains at a finite value even after the removal of the electric field [20].The value of remnant polarization observed for these bilayer films is higher than that of the homogeneous BVO thin films of similar thickness [16]. Further the asymmetric nature of the P-E loops with respect to electric field axis indicates interface dominated behavior.

The capacitance voltage (C-V) characteristics of a BVBT bilayer thin film measured at 100 kHz as probing frequency is shown **Figure 5(b)**. The C-V measurements were carried out by applying a small ac signal of 0.5 V amplitude, with a varying dc electric field. The dc voltage was swept from negative bias (-8 V) to positive (8 V) in steps of 0.1 V with a sweep rate of 0.1 V/s and back again. The butterfly shape of the curve confirmed the ferroelectric nature of the BVBT BL film and the capacitance shows strong voltage dependence. The two maxima of the loop correspond to the domain switching voltage in forward and reverse directions where the polarization reversal takes place. The asymmetry that is observed in C-V curve suggests that the electrodes are asymmetric and the film contains mobile ions or charges accumulated at the interface between the film and the electrode. In addition there is a difference between the capacitance values of the two peaks, which may be due to some defect energy levels in the film.

The dielectric dispersion studies were carried out on BVBT bilayer thin film at room temperature in the frequency range of 1 kHz to 1 MHz. **Figure 6** shows the variation of dielectric constant (ε_r') and the dissipation factor (D) as a function of frequency measured at room temperature. The dielectric constant as well as dissipation factor was found to decrease abruptly in the low frequency region. The variation in dielectric constant is not significant at higher frequencies. Similar trend has been observed at lower frequencies for BVO films grown on platinized silicon substrate [16]. The small

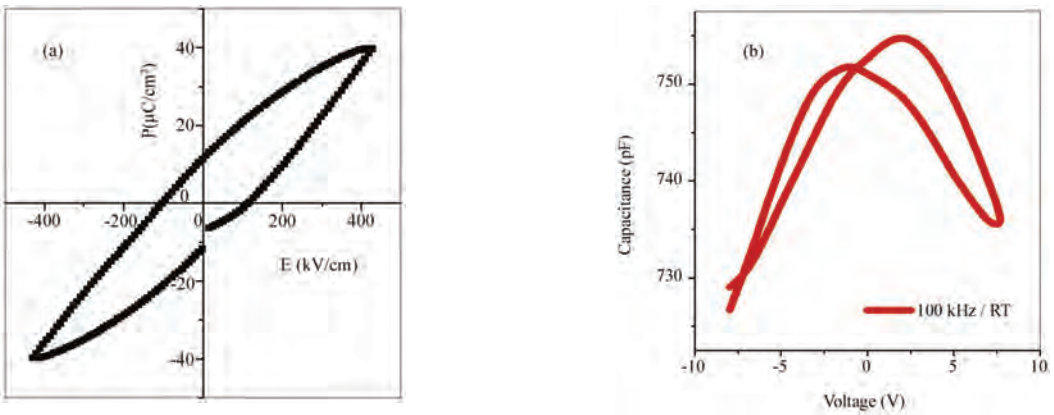

Figure 5. (a) The P-E hysteresis loop and **(b)** Capacitance- Voltage characteristics of a BVBT BL thin film measured at room temperature.

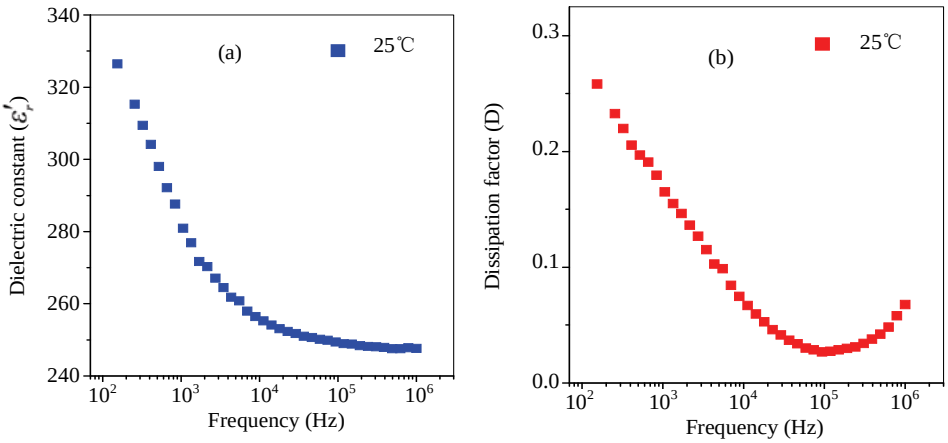

Figure 6. (a) Variation of dielectric constant and **(b)** dissipation factor of a BVBT BL thin film as a function of frequency.

dispersion observed at higher frequency has its contribution from the response of the grains, while at lower frequencies grain boundaries, free charges etc. would contribute significantly. However the dielectric loss for BVBT bilayer thin film shows an increasing trend subsequent to 100 kHz. The dissipation factor has the minimum value (~ 0.03) around 100 kHz, where the dielectric constant is ~ 252.

The comparison of the observed dielectric constant of BVBT bilayer with that of the single layer BVO and BTO films is shown in **Figure 7**. The dielectric constant of BVBT bilayer film shows less dispersion as compared to that of homogeneous BVO film. This might be due to the reduced number of defect states in bilayer films due to the presence of BTO layer. Further the observed dielectric constant of bilayer film is higher(e.g. ~ 225 at 1 M Hz) than that of single layer BVO film.

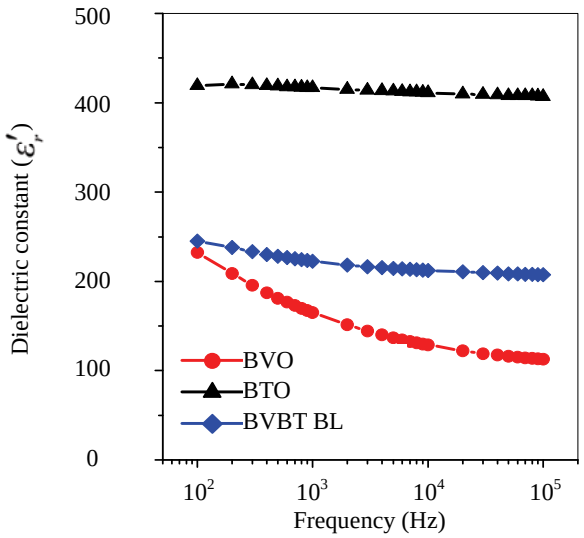

Figure 7. Comparison of dielectric constant of BTO, BTO and BVBT bilayer films.

4. CONCLUSIONS

Bilayer thin film structures consisting of ferroelectric Bismuth vanadate ($Bi_2VO_{5.5}$) and Bismuth titanate ($Bi_4Ti_3O_{12}$) individual layers were fabricated on platinized silicon substrate (Pt(111) / Ti / SiO_2 / Si) using pulsed laser ablation technique and investigated systematically their structural and electrical properties. The X-ray diffraction (XRD) studies indicated that bilayer is randomly oriented and the diffraction pattern consists of diffraction peaks from both starting materials. The Atomic force microscopy of the films indicates that there is a homogeneous distribution of grains in these films. The cross-sectional scanning electron microscopy established the dense nature of these films. The polarization hysteresis and C-V studies established the ferroelectric nature of these films. The observed dielectric constant of these bilayer films was higher than that of single layer BVO films.

REFERENCES

[1] Rijnders, G. and Blank, D.H.A. (2005) Materials science: Build your own superlattice. *Nature*, **433**, 369-370.

[2] Shimuta, T., Nakagawara, O., Makino, T., Arai, S., Tabata, H. and Kawai, T. (2002) Enhancement of remanent polarization in epitaxial $BaTiO_3$ / $SrTiO_3$ superlattices with “asymmetric” structure. *Journal of Applied Physics*, **91**, 2290-2294.

[3] Pontes, F.M., Longo, E., Leite, E.R. and Varela, J.A. (2004) Improvement of the dielectric and ferroelectric properties in superlattice structure of $Pb(Zr,Ti)O_3$ thin films grown by a chemical solution route. *Applied Physic Letters*, **84**, 5470-5472.

[4] Lee, H.N., Christen, H.M., Chisholm, M.F., Rouleau, C. M. and Lowndes, D.H., (2005) Strong polarization enhancement in asymmetric three-component ferroelectric superlattices, *Nature*, **433**, 395-399.

[5] Neaton, J.B. and Rabe, K.M. (2003) Theory of polarization enhancement in epitaxial $BaTiO_3$ / $SrTiO_3$ superlattices, *Applied Physic Letters*, **82**, 1586-1588.

[6] Aurivillius, B. (1949) Mixed bismuth oxides with layer lattices. II. Structure of $Bi_4Ti_3O_{12}$. *Arkiv for Kemi*, **1(54)** 463-480.

[7] Araujo, C.A.P. de, Cuchiaro, J.D., McMillan, L.D., Scott, M.C. and Scott, J.F. (1995) Fatigue-free ferroelectric capacitors with platinum electrodes, *Nature*, **374**, 627-629.

[8] Park, B.H., Kang, B.S., Bu, S.D., Noh, T.W., Lee, J. and Jo, W., (1999) Lanthanum-substituted bismuth titanate for use in non-volatile memories, *Nature*, **401**, 682-684.

[9] Maiwa, H., Lizawa, N., Togawa, D., Hayashi, T., Sakamoto, W., Yamada, M. and Hirano, S. (2003) Electromechanical properties of Nd-doped Bi4Ti3O12 films: A candidate for lead-free thin-film piezoelectrics. *Applied Physic Letters*, **82**, 1760-1762.

[10] Watanabe, T., Funakubo, H., Osada, M., Noguchiand, Y. and Miyayama, M. (2002) Preparation and characterization of a- and b-axis-oriented epitaxially grown Bi4Ti 3O12-based thin films with long-range lattice matching, *Applied Physic Letters*, **81**, 1660-1662.

[11] Rae, A.D., Thompson, J.G., Withers, R.L. and Willis, A. C. (1990) Structure refinement of commensurately modulated bismuth titanate, $Bi_4Ti_3O_{12}$. *Acta Crystallogr*, **46,** 474-487.

[12] Borisov, V.N., Poplavko, Y.M, Avakyan, P.B. and Osipyan, V.G. (1988) Phase transition in bismuth vanadate, *Soviet Physics - Solid State*, **30**, 904-905.

[13] Osipian, V.G., Savchenk, L.M., Elbakyan, V.L. and Avakyan, P.B. (1987) Layered boismuth vanadate ferroelctrics, *Inorganic Materials*, **23,** 467-469.

[14] Prasad, K.V.R. and Varma, K.B.R. (1994) Dielectric, thermal and pyroelectric properties of ferroelectric bismuth vanadate single crystals, *Materials Chemistry and Physics*, **38,** 406-410.

[15] Prasad, K.V.R. (1994) Investigations into the structural, dielectric and ferroelectric properties of ceramics and single crystal of parent and substituted bismuth vanadate. Ph. D. Thesis, Indian Institute of Science, Bangalore.

[16] Kumari, N., Krupanidhi, S.B. and Varma, K.B.R. (2007) Dielectric, impedance and ferroelectric characteristics of c-oriented Bismuth vanadate films grown by pulsed laser deposition. *Materials Science and Engineering B*, **138,** 22-30.

[17] Kumari, N. (2009) Structural, optical and electrical studies on Aurivillius oxide thin films. Ph. D. Thesis, Indian Institute of Science, Bangalore.

[18] Lines, M.E. and Glass, A.M. (1979) Principles and applications of ferroelectrics and related materials, Claredon Press, Oxford.

[19] Dawber, M., Rabe, K.M. and Scott, J.F. (2005) Physics of thin-film ferroelectric oxides. *Reviews of Modern Physics*, **77**, 1083-1130.

[20] Richerson, D.W. (1992) Modern ceramic engineering: Properties, processing and use in design, Marcel Dekker Inc., New York.

Vol.2, No.10, 1079-1084 (2010)
doi:10.4236/ns.2010.210134

Natural Science

Secular evolution of continental crust: recorded from massif-type charnockites of Eastern Ghats belt, India

Samarendra Bhattacharya[1], Ashwini Kumar Chaudhary[2*]

[1]Indian Statistical Institute, Kolkata, India;
[2]Indian Institute of Technology, Roorkee, India; *Corresponding Author: samar.bhattacharya@gmail.com.

Received 15 July 2010; revised 18 August 2010; accepted 23 August 2010.

ABSTRACT

It is reasonably well established that the Earth has substantially cooled from the Archean to the present and hence the sites, rates and processes of crust formation must have changed through geologic time. Archean and Proterozoic granitic rocks are the principal record of such changes. Massif-type charnockites in the Eastern Ghats granulite belt, India, of Archean and Proterozoic ages mirror the changing conditions and/or processes of continental crust formation. Though both can be explained by dehydration melting of mafic rocks, the conditions differ. Potasium and rubidium rich Proterozoic charnockites have significant negative Eu anomaly indicating melting at shallow depths in the stability field of plagioclase. In contrast, sodium and strontium rich Archean charnockites with less LREE enrichment and less depletion in Eu indicate melting at greater depths in the stability field of garnet or amphibole.

Keywords: Secular changes; Continental crust; Massif-charnockites; Eastern Ghats

1. INTRODUCTION

The continental crust comprising byouant quartzofeldspathic materials are difficult to destroy by subduction and hence can be considered as the principal record of crustal evolution through geologic time. New continental crust may form magmatically from underlying mantle. However, mantle melting products are predominantly basaltic, whereas continental crust is andesitic which can not be extracted directly from melting of mantle-peridotite. Continental crust formation therefore requires a second stage/or event of fractional crystallization [1] or remelting of basaltic magma [2]. Although there remains considerable debate on the processes of crust formation in the Archean compared to those operating in the later period (post-Archean), significant differences in key geochemical features have been documented between Archean and later granitic rocks [3-5]. Moreover, tectonic setting for Archean magmatism as exemplified by TTG remains unresolved. Partial melting may have taken place in subducted slabs [6,7] or in underplated basalt beneath thickened crust or oceanic plateau [8]. TTG suites of Archean greenstone belts are taken as the Archean continental crust, while large varieties of Proterozoic granitic plutons represent the Proterozoic continental crust (cf. Table 3 in [2]). These authors have presented extensive discussion on these differences from a Granitic perspective and their possible implications on the changing processes and or conditions of crust formation from Archean to Proterozoic times.

Eastern Ghats granulite belt, India, comprises massif-type charnockite as a major component in the regional granulite terrane, and there is unambiguous evidence of different generation of such charnockites. Archaean charnockites have been described from northern margin against Singhbhum craton and western margin against Bastar craton [9-11]. Some of the massif-type charnockite suites in the central part of the granulite belt record only Proterozoic ages [12,13]. Although, some workers have described magmatic charnockites from the Eastern Ghats, presumably as mantle-derived melt [14], it is difficult to postulate silicic melts directly from mantle-melting. On the other hand, some workers consider enderbitic charnockites of the Eastern Ghats belt as metamorphosed igneous precursors and commonly describe them as "now enderbite" [15]. Here again, the question of felsic igneous rocks directly derived from mantle remains unresolved. Dehydration melting experiments have demonstrated that silicic melts of tonalitic, granodioritic and granitic compositions are produced at 8-10 Kbar, and $\geq$ 850℃ from mafic rocks [16-18]. The massif-type charnockites in the Eastern Ghats belt are of variable composition and P-T conditions of granulite facies metamorphism are comparable to the experimental constraints as mentioned above [19, 20]. Thus a remelting of mantle-

derived melt or hydrated amphibolite under granulite facies conditions could be the favored model for the massif-type charnockites of the Eastern Ghats belt [20-22].

Considering charnockite-massifs as products of partial melting in the deep crust under granulite facies conditions, U-Pb ages of zircons in them can be taken as representing this deep crustal anatexis, while the Nd-model ages could provide the mantle-derivation ages of their protoliths.

In this communiqué, we present selected geochemical and isotopic data for two sets of massif-type charnockites of the Eastern Ghats belt, of Archean and Proterozoic ages respectively. These data could mirror the differences in some key geochemical features of the continental crust. These distinctive features may also provide some useful constraints on changing processes of crust formation from Archean to Proterozoic.

2. GEOLOGICAL SETTING

The Eastern Ghats granulite belt skirting the eastern coast of India is bounded by granite-greenstone belts of Singhbhum and Bastar cratons to the north and west respectively (**Figure 1**). The granulite lithologies record polyphase deformation and possible multiple granulite facies imprints [23-26]. Massif-type charnockite is a

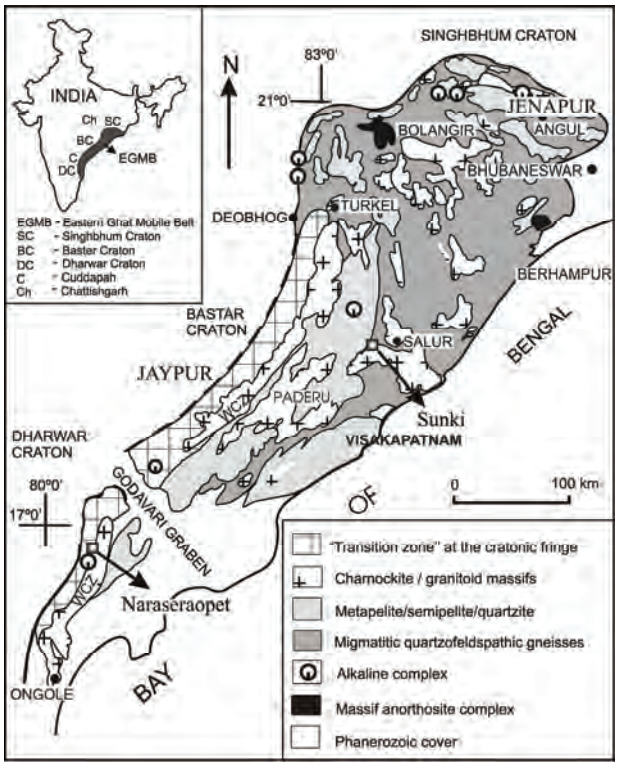

Figure 1. Generalized geological map of the Eastern Ghats Granulite belt, India.

major component in this regional granulite terrane and occurs in different crustal domains [10]. The charnockite-massifs considered here occur in the Archean domains around Jenapore & Jaypur and Proterozoic domains around Sunki, Paderu and Naraseraopet (see locations in **Figure 1**).

3. GEOCHEMICAL SIGNATURES

Bulk composition was determined by XRF spectrometry at National Geophysical Research Institute, Hyderabad and Operating condition for XRF machine was 20/40 KV for Major oxides, nominal analysis time was 300 seconds for all major oxides. For the XRF analysis the overall accuracy (% relative standard deviation) for major and minor oxides are given as less than 5%. The average precision is reported as better than 1.5%. For ICP–MS analysis at Institute Instrumentation Centre, Indian Institute of Technology, Roorkee, the average precision were 4.1% RSD.

The analytical data are given in **Table 1**. Compared to the Archean charnockites the Proterozoic charnockites are potash-rich, with high K_2O / Na_2O ratios (**Figure 2**) and this is consistent with the compositions of granitic rocks of the two periods, as described in Kemp and Hawkesworth, 2004 [2]. Compared with the Archean charnockites the Proterozoic charnockites are rubidium-rich with high Rb / Sr ratios (average 1.01, n = 11: Proterozoic and average 0.18, n = 7: Archean). The lower Rb / Sr ratios in the Archean charnockites reflect elevated Sr in the Archean than in the Proterozoic charnockites (**Figure 3**). However, Sr / Nd and Nb / La ratios are variable in both sets (**Figure 4**); though lower Nb / La ratios in many samples from Archean could reflect different processes in the Archean [2]. Greater fractionation of HREE, extending to higher $(Gd / Yb)_N$ ratios in the Archean charnockites is consistent with those in Archean greenstone belts (**Figure 5**). REE patterns are distinctive, primarily in the significant Eu depletion in the Proterozoic charnockites and much less Eu depletion in the Archean charnockites. Significant Eu-depletion coupled with Sr-depletion is characteristic of the Proterozoic charnockites compared with those of the Archean charnockites (**Figure 6**). Archean charnockites show relatively less enrichment in LREE, much less Eu-depletion and greater fractionation of HREE, compared to those in the Proterozoic charnockites.

4. ISOTOPIC SIGNATURES

Mantle-derivation ages for the charnockite suites were determined by Sm-Nd isotopic analysis of whole rocks by Thermal Ionisation Mass Spectrometry at Indian Institute of Technology, Roorkee. Detail analytical proce-

Table 1. Selected oxides, trace element and isotopic data of massif-type charnockites in EGB.

	Naraseraopet			Paderu				Sunki				Jenapore			Jaypur			
Sample	A 5/2	D 5/2	F 4/2	PD 4/4	PD 5/2	PD A1/2	PD A2/3	B4/1/S3	SK 6/5/05	SK 7/1/05	S3/1/S3	JN 2/3	JN 3/3	JN 5/3	JP 10/1	JP 5/1	JP 3/1	JP 2/1
Na2O	3.98	1.98		1.85	1.98	2.41	2.53	1.92	1.38	1.82	2.2	5.36	4.08	3.36	4.6	3.24	4.19	3.89
K2O	3.56	4.34		4.91	4.34	4.41	5.8	2.07	6.16	3.59	5.75	1.03	0.86	3.79	2.2	3.6	3.07	1.78
Rb	43.2	8.2	14.9	327.8	278.8	228.6	323.7	59.9	293	115.6	404.8	5.56	3.63	60.55	12.14	82.07	59.23	11.54
Sr	185.4	388.8	521.1	137.3	131.1	138.1	207.7	145.3	111.2	78.4	94.3	265.23	250.76	121.1	367.05	204.5	234.17	171.2
Y	6.4	36.6	20.4	35	34.6	45.8	35.4	52.1	17.209	48.5	179.7	38.65	7.19	39.12	11.64	3.5	3.38	2.69
Nb	7.6	17.6	10.2	8.3	13.8	15.9	33	35.6	19.2	35.9	5.8	13.02	13.49	10.35	11.49	1.86	5.68	0.84
La	22.2	73.4	36.5	137.2	87.1	120.8	173.8	59.3	65.5	79.4	155.9	28.24	13.27	54.26	71.81	35.1	24.77	26.93
Ce	40.3	133.2	65.8	253.6	153.8	225.9	686.8	108.9	108.8	175	387.3	51.51	24.62	99.27	108.28	47.96	39.36	33.54
Sm	2.8	13.2	6.5	15.4	10.9	15.1	16.8	11.1	8	15.1	49.1	6.49	2.11	9.66	5.24	1.57	1.88	0.78
Nd	15.6	62.6	30.6	97.8	62.3	91.9	119.6	49.7	41.8	83	221.2	25.64	10.14	43.12	32.79	11.95	12.27	7.04
Eu	0.8	4	2	3	2.8	3.1	4	3.7	2.5	1.5	2.8	2.28	0.76	3.2	1.49	0.98	0.93	0.85
Gd	4.3	13.2	6.5	16.3	11.8	16.2	18.6	12.3	5.6	11.8	40.4	6.3	3.01	11.85	6.38	2.2	2.28	1.34
Dy	1.3	7.8	4	8.2	7.6	9.6	7.9	9.5	3.7	9.6	36.7	6.93	1.34	7.33	2.3	0.6	0.65	0.42
Er	0.6	3.6	6.5	2.9	2.7	4.1	3.4	5.5	1.2	3.2	10.7	3.91	0.65	3.66	0.91	0.34	0.29	0.24
Yd	0.6	3.1	2.2	2	2.1	4.4	3.7	6.2	1.3	3.3	8.9	5.4	0.86	4.56	0.87	0.46	0.28	0.34
Lu	0.1	0.4	0.3	0.3	0.3	0.6	0.5	0.7	0.2	0.5	1.3	0.57	0.08	0.42	0.12	0.08	0.05	0.05
Isotopic	data																	
	A 5/2	C 6/9				PD A1/2	PD A2/3			SK 7/1/05	S3/1/S3		JN 3/3	JN 5/3		JP 5/1	JP 3/1	
Sm	5.11	6.3				16.94	19.34			14.44	42.32		2.64	12.1		1.78	2.22	
Nd	33.32	38.46				95.93	123.97			77.12	181.56		15.01	61.98		14.96	15.55	
$^{147}Sm/^{143}Nd$	0.0926	0.099				0.1068	0.0943			0.1132	0.1409		0.1063	0.118		0.0721	0.0863	
$^{144}Nd/^{143}Nd$	0.51078	0.5113				0.51136	0.51123			0.511672	0.511566		0.51072	0.51091		0.50986	0.51027	
$T_{DM\ Ga}$	2.8	2.3				2.4	2.3			2.8	3.1		3.3	3.5		3.5	3.4	
U-Pb Zircon	1.6 Ga [27]			0.9 to 1.1 Ga [29]				0.9 Ga [27]				3.0 Ga [9]			2.8 Ga [11]			

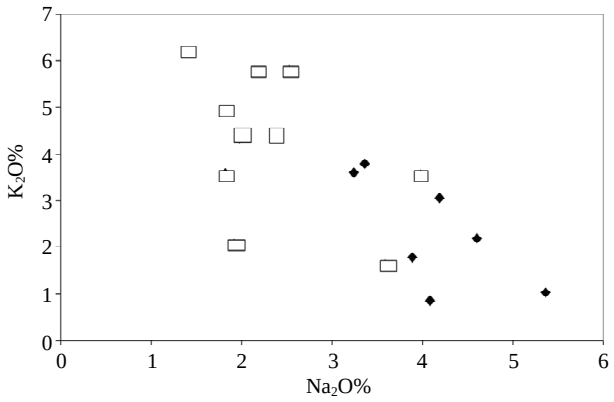

Figure 2. K_2O versus Na_2O plot of the charnockites in the Eastern Ghats Granulite belt. Archean charnockites: solid symbols; Proterozoic charnockites: open symbols.

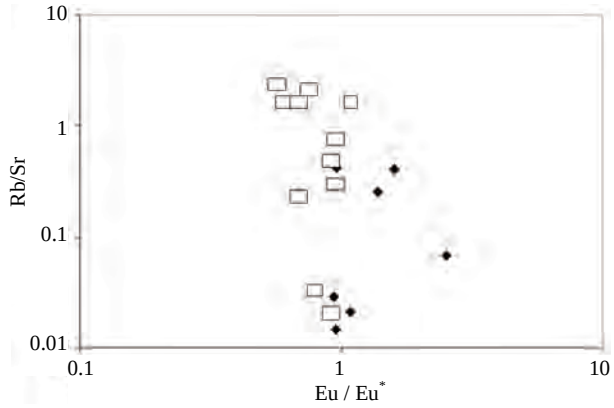

Figure 3. Rb / Sr versus Eu / Eu* plot of the charnockites in the Eastern Ghats Granulite belt. Symbols as in **Figure 2**.

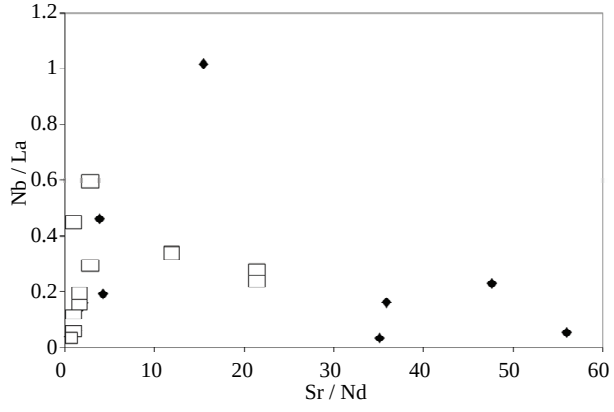

Figure 4. Nb / La versus Sr / Nd plot of the charnockites in the Eastern Ghats Granulite belt. Symbols as in **Figure 2**.

dure is given in Bhattacharya *et al.*, 2010 [27]. Measured ratios for isotopic composition are normalized to ^{146}Nd / ^{144}Nd = 0.7219 for Nd. The measured ratio of ^{143}Nd / ^{144}Nd for Ames Nd Standard was 0.512138 ± 4 (quoted

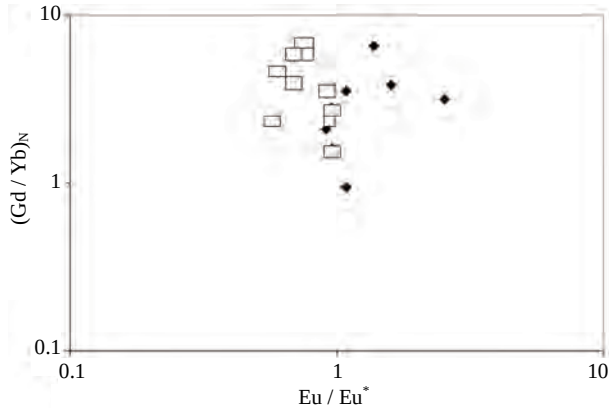

Figure 5. $(Gd / Yb)_N$ versus Eu / Eu* plot of the charnockites in the Eastern Ghats Granulite belt. Symbols as in **Figure 2**.

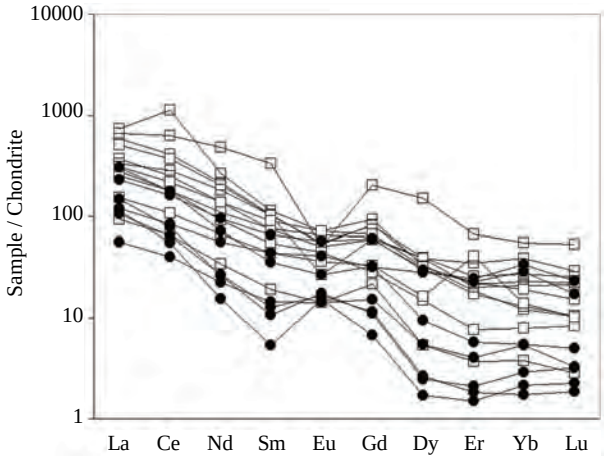

Figure 6. Chondrite normalized REE plot of the charnockites in the Eastern Ghats Granulite belt.

value 0.512138).

Mantle-derivation ages (T_{DM}) for the Proterozoic charnockites vary between 2.3 and 2.8 Ga (Naraseraopet), between 2.3 and 2.4 Ga (Paderu) and between 2.8 and 3.1 Ga (Sunki) and those for the Archean charnockites vary between 3.3 and 3.5 Ga (Jenapore) and between 3.4 and 3.5 Ga (Jaypur) respectively (**Table 1**).

5. DISCUSSIONS

High Rb / Sr ratios and significant negative Eu-anomalies in the Proterozoic charnockites indicate residual plagioclase. The implication is that intracrustal melting occurred at shallow depths, in the stability field of plagioclase. In contrast, low Rb / Sr ratios, indicating elevated Sr, and lack of significant negative Eu-anomalies in the Archean charnockites are indicative of intracrustal melting at greater depths in the stability field of garnet or amphibole [2].

Large discrepancies between crystallization ages (of anatectic charnockitic melt), given by U-Pb zircon ages reported in the literature (**Table 1**) and mantle derivation ages given by T_{DM} for the Proterozoic charnockites confirm that older crustal material was present within the source regions of the charnockitic magma [28]. This is in contrast to the relatively little time gap between crystallization ages and Nd-model ages for the Archean charnockites, similar to those observed in Archean TTGs.

6. CONCLUSIONS

These differences in the geochemical and isotopic signatures between Archean and Proterozoic charnockites reflect different conditions of crust formation rather than different processes: both can be explained by dehydration melting of hydrated basalt or amphibolite under granulite facies conditions; but Proterozoic charnockites at shallower depths (in plagioclase-stability field) than Archean charnockites (in garnet or amphibole-stability field).

7. ACKNOWLEDGEMENTS

Indian Statistical Institute, Kolkata provided the infrastructural facilities. Financial support was provided by the Department of Science and Technology, Government of India, in the form of a research project.

REFERENCES

[1] Soesoo, A. (2000) Fractional crystallization of mantle-derived melts as a mechanism for some I-type granite petrogenesis: An example from the Lachlan Fold Belt, Australia. *Journal of Geological Society*, **157**, 135-149.

[2] Kemp, A.I.S. and Hawkesworth, C.J. (2004) Granitic perspectives on the Generation and secular evolution of the continental crust. *Treatise on Geochemistry*, **3**, 349-411.

[3] Taylor, S.R. and McLennan, S.M. (1985) The continental crust: Its composition and evolution. Blackwell Publishing, Oxford.

[4] Taylor, S.R. and McLennan, S.M. (1995) The geochemical evolution of the continental crust. *Reviews of Geophysics*, **33**, 241-265.

[5] Rudnick, R.L. and Gao, S. (2004) Composition of the continental crust. *Treatise on Geochemistry*, **3**, 1-65.

[6] Condie, K.C. (1998) Episodic continental growth and supercontinents: A mantle avalanche connection? *Earth and Planetary Science Letters*, **163**, 97-108.

[7] Martin, H. (1995) Archean grey gneisses and genesis of continental crust. In: Condie, K.C. Ed., *Archean crustal evolution*, Elsevier, Netherlands, 205-260.

[8] Whalen, J.B., Percival, J.A., McNiccol, V.J. and Longstaffe, F.J. (2002) A mainly crustal origin for tonalitic granitoid rocks, superior province, Canada: Implications for late archean tectonomagmatic processes. *Journal of Petrology*, **43**, 1551-1570.

[9] Bhattacharya, S., Kar, R., Misra, S. and Teixeira, W. (2001) Early Archaean continental crust in the Eastern Ghats granulite belt, India: Isotopic evidence from a charnockite suite. *Geological Magazine*, **138**, 609-618.

[10] Rickers, K., Mezger, K. and Raith, M. (2001) Evolution of the continental crust in the Proterozoic Eastern Ghats belt, India and new constraints for Rodinia reconstruction: Implications from Sm-Nd, Rb-Sr and Pb-Pb isotopes. *Precambrian Research*, **112**, 183-210.

[11] Kovach, V.P., Simmat, R., Rickers, K., Berezhnaya, N.G., Salnikova, E.B., Dobmeier, C., Raith, M.M., Yakovleva, S.Z. and Kotov, A.B. (2001) The western charnockite zone of the Eastern Ghats belt, India: An independent crustal province of late Archean (2.8 Ga) and Paleoproterozoic (1.7-1.6 Ga) terrains. *Gond Research*, **4**, 666-667.

[12] Mezger, K. and Cosca, M.A. (1999) The thermal history of the Eastern Ghats belt (India) as revealed by U-Pb and ^{40}Ar / ^{39}Ar dating of metamorphic and magmatic minerals: Implications for the SWEAT correlation. *Precambrian Research*, **94**, 251-271.

[13] Simmat, R. and Raith, M.M. (2008) U-Th-Pb monazite geochronometry of the Eastern Ghats Belt, India: Timing and spatial disposition of poly-metamorphism. *Precambrian Research*, **162**, 16-39.

[14] Subba Rao, M.V. and Divakara Rao, V. (1988) Chemical constraints on the origin of the charnockites in the Eastern Ghat Mobile belt, India. *Chemical Geology*, **69**, 37-48.

[15] Bhui, U.K., Sengupta, P. and Sengupta, P. (2007) Phase relations in mafic dykes and their host rocks from Kondapalle, Andhra Pradesh, India: Implications for the time-depth trajectory of the Paleoproterozoic (late Archean?) granulites from southern Eastern Ghats belt. *Precambrian Research*, **156**, 153-174.

[16] Wolf, M.B. and Wyllie, P.J. (1994) Dehydration melting of amphibolite at 10 Kbar: Effects of temperature and time. *Contributions to Mineralogy and Petrology*, **115**, 369-383.

[17] Patino Douce, A.E. and Beard, J.S. (1995) Dehydration melting of biotite gneiss and quartz amphibolite from 3 to 15 Kbar. *Journal of Petrology*, **36**, 707-738.

[18] V`ielzeuf, D. and Schmidt, M.W. (2001) Melting relations in hydrous systems revisited: Application to metapelites, metagreywackes and metabasalts. *Contributions to Mineralogy and Petrology*, **141**, 251-267.

[19] Bhattacharya, S. (2003) Dehydration melting in mafic rocks in the Eastern Ghats Belt, India: Implications for variable composition of charnockitic melt and heterogeneity of source rocks. *Geological Society of India*, **52**, 131-144.

[20] Kar, R., Bhattacharya, S. and Sheraton, J.W. (2003) Hornblende dehydration melting in mafic rocks and the link between massif-type charnockite and associated granulites, Eastern Ghats Granulite Belt, India. *Contributions to Mineralogy and Petrology*, **145**, 707-729.

[21] Foley, S., Tiepolo, M. and Vannucci, R. (2002) Growth of early continental crust in subduction zones controlled by melting of amphibolite. *Nature*, **417**, 837-840.

[22] Bhattacharya, S. (2010) Review: The charnockite problem: A twenty-first century perspective. *Natural Science*, **2**, 402-408.

[23] Halden, N.M., Bowes, D.R. and Dash, B. (1982) Struc-

tural evolution of migmatites in a granulite facies terrane: Precambrian crystalline complex of Angul, Orissa, India. *Transactions of the Royal Society*, **73**, 109-118.

[24] Bhattacharya, S. (1997) Evolution of Eastern Ghats granulite belt of India in a compressional tectonic regime and juxtaposition against Iron Ore craton of singhbhum by oblique collision-transpression. *Proceedings of Indian Academy of Sciences*, **106**, 65-75.

[25] Sen, S.K., Bhattacharya, S. and Acharyya, A. (1995) A multi-stage pressure-temperature record in the Chilka Lake granulites: The epitome of the metamorphic evolution of Eastern Ghats, *journal of metamorphic geology*, **13**, 287-298.

[26] Dasgupta, S. and Sengupta, P. (2003) Indo-Antarctic correlation: A perspective from the Eastern Ghats Granulite belt, India. *Geological Society*, **206**, 131-144.

[27] Bhattacharya, S., Das, P., Chaudhary, A.K. and Saw, A.K. (2010) Mafic granulite xenoliths in the Eastern Ghats Granulite belt: Implications for lower crustal processes in the southeastern Indian Peninsula. *Indian Journal of Geology*, **80**, 55-69.

[28] McCulloch, M.T. and Chappel, B.W. (1982) Nd isotopic characteristics of S- and I-type granites. *Earth and Planetary Science Letters*, **58**, 51-64.

[29] Bhattacharya, S., Kar, R., Teixeira, W. and Basei, M. (2003) High-temperature crustal anatexis in a clockwise P-T path: Isotopic evidence from a granulite-granitoid suite in the Eastern Ghats belt, India. *Journal of the Geological Society*, **160**, 39-46.

Vol.2, No.10, 1085-1089 (2010)
doi:10.4236/ns.2010.210135

Natural Science

New experimental constraints: implications for petrogenesis of charnockite of dioritic composition

Rajib Kar[1], Samarendra Bhattacharya[2]*

[1]J.K.College, Purulia, India;
[2]Indian Statistical Institute, Kolkata, India; *Corresponding Author: samar.bhattacharya@gmail.com.

Received 13 August 2010; revised 16 September 2010; accepted 21 September 2010.

ABSTRACT

Hornblende-dehydration melting experiments at high temperatures (> 950°C) indicate change of melt composition from tonalite/granodiorite to quartz-diorite; clinopyroxene instead of hornblende as the residual phase and change in melting reaction from peritectic hornblende-dehydration to eutectic clinopyroxene-orthopyroxene-plagioclase. In the light of these experimental results, petrogenesis of a charnockite pluton of homogeneous dioritic composition in the Eastern Ghats Belt, India, can be explained as melting at high-temperatures (> 950°C). Negative Sr and Eu anomalies further indicate plagioclase as a major residual phase, consistent with melting at high-temperatures (> 950°C).

Keywords: Dioritic charnockite; Residual clinopyroxene; Residual plagioclase; Eutectic melting

1. INTRODUCTION

It is quite common that large-scale charnockitic bodies are of variable composition from tonalite to granodiorite, and sometimes even dioritic composition is reported [1]. On the other hand, petrogenesis of massif-type charnockites have been variously described: a) mantle-derived and differentiated melt [2]; b) high-temperature melting of dry granulite facies rocks [3]; c) more mafic varieties as mantle-derived melts [4]; d) product of hornblende-dehydration melting in the deep crust [5]. New melting experiments provide constraints on the petrogenesis of charnockitic rocks of dioritic composition. From the Jenapore area in the Eastern Ghats Belt, India, charnockite-massif was described as the product of hornblende-dehydration melting under granulite facies conditions, and with residual hornblende. There the two-pyroxene granulites occur as minor patches and bands and were explained as peritectic segregates [5]. A stock-like body of charnockite (pluton) occurs in the same locale, a few kilometer to the south (Lat: 20°46' N; Long: 86°05' E). In contrast to the charnockite-massif, it is of more mafic and homogeneous composition at the outcrop-scale and commonly has both orthopyroxene and clinopyroxene.

In the present communication we present geochemical data from the charnockite pluton and in the light of new experimental constraints explain its origin by melting at high-temperatures (≥ 950°C).

2. EXPERIMENTAL CONSTRAINTS

The selected results of the hornblende-dehydration melting experiments is presented in **Figure 1**. The melts of 900°C and 925°C are tonalitic (normative Qtz / Plag > 0.25) and those above 950°C are quartz dioritic (normative Qtz / Plag < 0.25) in composition. The melt composition changes from corundum normative to diopside normative when temperature increases from 925°C to 950°C. Also there is gradual decrease of plagioclase proportion with temperature rise. Moreover, the orthopyroxene and clinopyroxene are subequal in proportion at 900°C, and orthopyroxene gradually decreases in proportion to a trace amount at 1100°C. These results suggest that the nature of melting reaction changes from hornblende breakdown reaction at 925°C to eutectic clinopyroxene-orthopyroxene-plagioclase melting reaction at 950°C [6].

3. CHARNOCKITE PLUTON

The charnockite pluton at Jenapore is a relatively homogeneous body of two-pyroxene granulite, unlike those occurring as minor bands and patches within the massif-type charnockite described from the area to the north [5]. Also as distinct from those within massif-type charnockite garnet is absent, while clinopyroxene is much more abundant than orthopyroxene (**Table 1**).

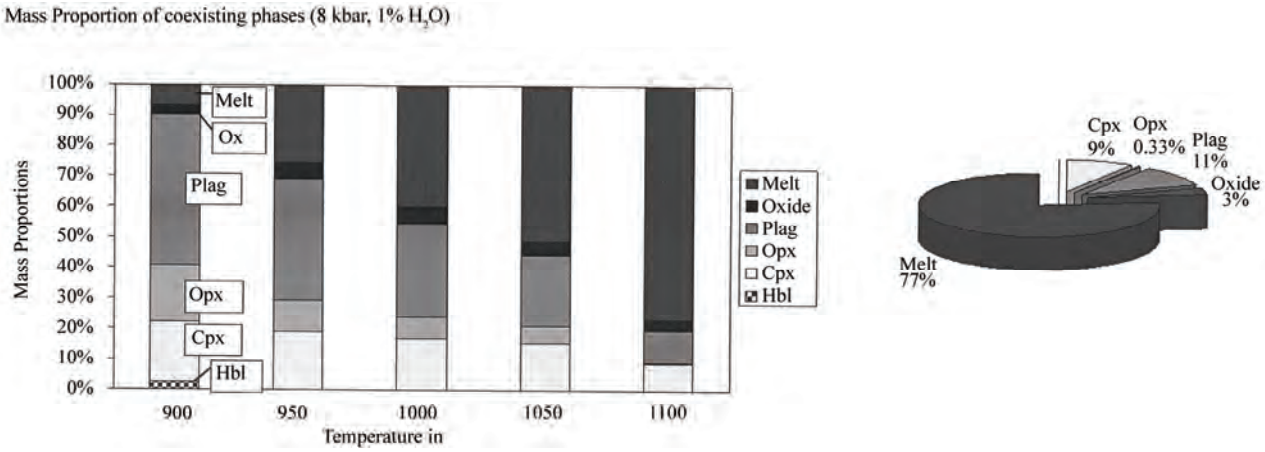

Figure 1. Mass proportions in melting experiments at 8 kbar.

Table 1. Modal mineralogy of the Charnockite pluton at Jenapore, Eastern Ghats Belt.

Sample	JN35A	2.J.95	2.J.82	2.J.90A	JN 194A	2.J.50A	JN 35F
Quartz	4.3	6.2	10.4	6.3	5.7	8.1	8.5
K-feldspar	4.2	3.1	2.5	3.2	2.7	1.8	2.1
Plagioclase	25	24.3	22.4	22.6	23.4	21.5	23
Orthopyroxene	13.3	14.5	16.4	18.3	17.4	14.6	15.3
Clinopyroxene	41.2	42	38.5	38.6	39.2	41	39.3
Hornblende	2.5	3.1	1.5	1.7	3.4	4.2	3.8
Biotite	5.4	3.7	5.2	4.6	3.9	4.5	5.3
Opaque	2.2	3.1	1.5	3.4	2.7	3.2	2.5
Accessory	1.2	Trace	1.1	0.7	1.4	0.4	0.3

3.1. Geochemistry

3.1.1. Analytical Procedure

Both major and minor oxides as well as trace elements were analyzed by ICP-MS at the Australian Geological Survey Organization, Canberra. At AGSO the sample preparation for ICP-MS has been based on a method outlined in Jenner *et al*., 1990 [7]. However, some refractory elements like Zr have been problematic and to overcome this problem, a new method has been introduced. The new method involves digesting pieces of the lithium tetraborate/lithium metaborate fusions that have been prepared and run for XRF major element analysis. Approximately 100 micrograms of chips from the smashed discs are weighed accurately into Savillex Teflon vessels. Five milliliters of internal standard, one milliliter of HF and five milliliters of HNO_3 are then added. The vessels are sealed and heated for twelve hours at 120°C on a timed hotplate, such that cooled samples are ready the following morning. The digests are then transferred to volumetric flasks and made up to volume ready for the ICP-MS. The precision can be assessed from the Zr analysis (**Table 2**).

3.1.2. Results

The analytical data for the seven samples from the charnockite-pluton is presented in **Table 3**. In the Qz-Or-Pl diagram six (6) of the seven (7) analyzed samples plot in the field of Qz-diorite, while one sample plots in the field of Qz-monzodiorite (**Figure 2**). Normative quartz: plagioclase ratios vary between 0.02 and 0.15 and all the samples are diopside normative, varying between 6.4 and 11.7. All these features are compatible with the new experimental constraints indicating high temperature melting ($\geq 950^{o}$ C) in mafic rocks. Moreover, these compositional characteristics (homogeneous) suggest a change of melting reaction from peritectic to eutectic, as in the recent melting experiment [6].

The incompatible elements like K, Rb & Ba are enriched, while Ti and base metals like Cr & Ni are depleted

Table 2. Comparative Zr analysis in ppm.

Standards	ICP-MS old	ICP-MS new	AGSO XRF	Recommended [8]
W-2	78	95	93	94
BIR-1	15	15	15	15.5
DNC-1	36	37	36	41
QLO-1	171	189	188	185
BHVO-1	151	176	175	179
AGV-1	205	235	235	227

Vol.2, No.10, 1085-1089 (2010)
doi:10.4236/ns.2010.210135

Table 3. Composition of the charnockite pluton of Jenapore, Eastern Ghats, India.

Area	Jenapore						
Sample	JN35A	2.J.95	2.J.82	2.J.90A	JN 194A	2.J.50A	JN 35F
SiO_2	49.69	52.03	54.42	52.19	52.74	52.87	53.05
TiO_2	2.9	1.72	1.53	1.34	0.97	1.11	1.71
Al_2O_3	13.85	15.53	15.09	15.74	16.58	16.63	15.29
Fe_2O_3	2.38	1.36	1.75	1.08	1.46	0.75	1.71
FeO	13.64	9.44	9.18	8.85	8.01	7.78	8.8
MnO	0.22	0.16	0.16	0.15	0.14	0.13	0.15
MgO	3.75	5.5	4.75	6.46	6.94	6.07	5.16
CaO	7.9	8.19	7.28	8.48	8.51	8.68	8.05
Na_2O	1.14	2.78	2.96	2.73	2.3	2.26	2.97
K_2O	2.07	1.51	1.56	1.26	1.06	1.87	1.79
P_2O_5	0.75	0.42	0.37	0.28	0.21	0.3	0.41
LOI	1.54	1.28	0.86	1.37	0.98	1.47	0.81
Total	99.83	99.92	99.91	99.93	99.9	99.92	99.9
			Trace elements in ppm				
Cr	9	119	105	185	98	205	78
Ni	8	50.5	33.5	37.5	20	49	24
Ni	8	50.5	33.5	37.5	20	49	24
Sc	45	31.5	31.5	33.5	32	31	34
V	263	193	162	170	167	160	184
Cu	36	26	26	20	22	22	19
Zn	176	120	127	104	97	89	114
Zn	176	120	127	104	97	89	114
Ti	17400	10320	9180	8040	5820	1660	10260
K	8588	6265	6472	5228	4338	7759	7427
Rb	48	54	54.5	34	40	56	49
Ba	1527	727	734	736	376	1066	1076
Sr	341	327	296	325	314	376	324
Zr	329	255	226	177	117	197	257
Nb	35.3	25.3	24.8	15.5	11.6	17	24.1
Th	2.46	1.98	1.51	2.83	8.84	1.49	3.72
U	0.41	0.3	0.48	0.32	0.56	0.27	0.5
La	92.7	55.3	44.9	47.5	56	56.2	64.2
Ce	234	120	97.2	97	115	115	135
Pr	22.7	13.1	11	10.4	11.8	12.2	14.8
Nd	87.7	50.3	43	39.4	42.8	45.2	55.7
Sm	15.5	9.45	8.23	7.06	7.55	7.29	9.85
Eu	3.87	2.26	2.13	1.99	1.6	2.21	2.58
Gd	15	8.92	8.33	7.05	6.96	7.14	9.2
Tb	2.28	1.37	1.32	1.11	1.06	1.07	1.43
Dy	12.9	7.83	7.5	6.32	5.98	5.96	8.01
Ho	2.8	1.69	1.64	1.4	1.29	1.28	1.76
Er	8.11	4.74	4.74	4.09	3.63	3.64	5.07
Yb	6.88	4.07	3.99	3.57	3.2	3.22	4.33
Lu	1.01	0.59	0.59	0.52	0.47	0.46	0.65
∑ REE	505.45	279.62	234.57	227.41	257.34	260.87	312.58
$(La/Sm)_N$	3.76	3.68	3.43	4.23	4.67	4.85	4.10
$(Gd/Lu)_N$	1.85	1.88	1.76	1.69	1.84	1.93	1.76
Eu/Eu*	0.19	0.19	0.19	0.21	0.17	0.23	0.20

(**Figure 3**). These features suggest a melt character for these dioritic charnockites. However, Zn is significantly

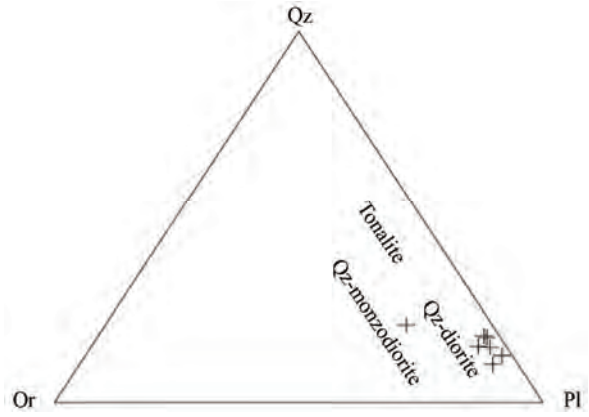

Figure 2. Normative Qz-Or-Pl diagram for the charnockites.

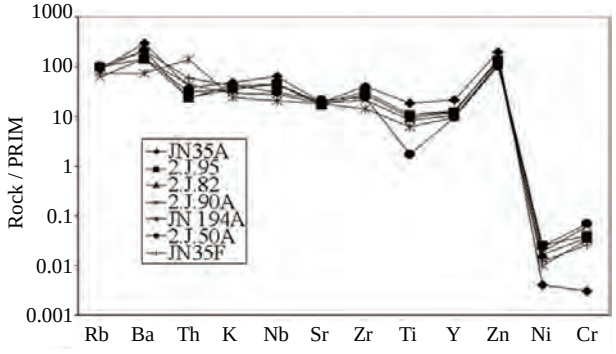

Figure 3. Multi-element spider diagram for the charnockites. Normalizing values from Taylor and McLennan, 1985 [23].

enriched and could be related to clinopyroxene as a major phase, which commonly contains trace amounts of Zn. Similar degrees of enrichment in Rb & Sr relative to primitive mantle is consistent with partial melting in mafic rocks involved in the break down of hornblende and plagioclase. However, unlike the tonalitic charnockites (cf. Figure 9 in [5]), negative Sr anomaly in the dioritic charnockites here implies plagioclase as a major residual phase [9]. Zr contents between 117 & 329 are variable, but most of the samples have near saturation concentration. This and relatively high Th (between 1.49 & 8.84 ppm) and U (between 0.27 & 0.56 ppm) suggest interaction between melt and restitic zircon. Also unlike the tonalitic charnockites, total REE contents are high, between 227 & 505 ppm, suggests near saturation concentration. Relatively less HREE fractionation $(Gd / Yb)_N$, between 1.69 & 1.88 than LREE fractionation, $(La / Sm)_N$, between 3.43 & 4.85, suggests melt-pyroxene coexistence. Significant negative Eu anomaly is characteristic of these charnockites of quartz-dioritic composition unlike those in the tonalitic charnockites and Archaean tonalites [5,10] suggests major residual plagioclase (**Figure 4**). This is also consistent with the signature

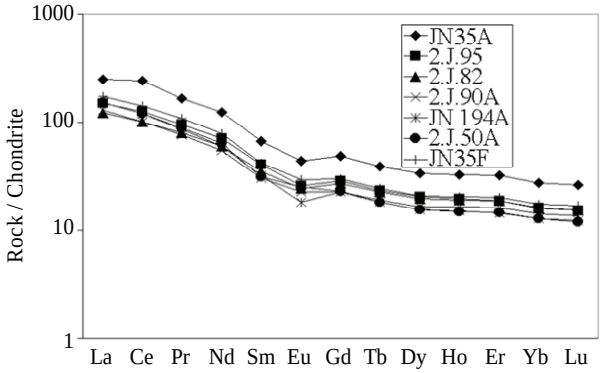

Figure 4. Chondrite normalized REE diagram for the charnockites. Normalizing values from Taylor and McLennan, 1985 [23].

of negative Sr anomaly.

4. DISCUSSIONS

The Eastern Ghats Mobile Belt, along the east coast of-peninsular India, is commonly described as a collisional orogen [11]. Extremely high temperatures (> 900°C) have been recorded from different granulite lithologies and from different parts of this regional granulite terrain [12-16]. On the other hand, dehydration melting experiments provided important constraints on the petrogenesis of massif-type charnockitic rocks of tonalitic and granodioritic compositions [17-20]. The latest experiments of hornblende-dehydration melting at high-temperatures (≥ 950°C), indicate changing melt composition from tonalite /granodiorite to quartz-diorite, along with residual clinopyroxene instead of hornblende [6]. In this context it is important to note that this is the first report of charnockite pluton of dioritic composition in the Eastern Ghats Belt. Erstwhile magmatic charnockite or their protoliths are described as enderbite, of tonalitic composition [21-22]. The tonalitic to granodioritic charnockite-massif of Jenapore was described as the product of hornblende-dehydration melting with residual hornblende & or garnet by Kar *et al*. [5]. In the same locale a stock-like body of charnockite, its quartz-dioritic composition with residual clinopyroxene and plagioclase provide evidence of high-temperatures (> 950°C). This is also consistent with the proposed change in the melting reaction from peritectic hornblende-dehydration melting to eutectic clinopyroxene-orthopyroxene-plagioclase melting.

5. CONCLUSIONS

1) This is the first report of dioritic charnockite pluton in the Eastern Ghats Belt.
2) Yet another evidence of Ultra-high temperature crustal metamorphism in the Eastern Ghats Belt.

3) Negative Sr and Eu anomalies, unlike those of tonalitic charnockites and Archaean tonalites, imply plagioclase as a major residual phase.

6. ACKNOWLEDGEMENTS

Melting experiments at the Petrological Laboratory of the Zurich Institute was supported by a Swiss Federal Fellowship to RK. Analytical data by ICP-MS were acquired by courtesy Dr. J.W. Sheraton.

REFERENCES

[1] Young, D.N., Zhao, J.X., Ellis, D.J. and McCulloch, M.T. (1997) Geochemical and Sr–Nd isotopic mapping of source provinces for the Mawson charnockites, east Antarctica: Implications for Proterozoic tectonics and Gondwana reconstruction. *Precambrian Research*, **86**, 1-19.

[2] Subba Rao, M.V. and Divakara Rao, V. (1988) Chemical constraints on the origin of the charnockites in the Eastern Ghat Mobile Belt, India. *Chemical Geology*, **69**, 37-48.

[3] Zhao J., Ellis D.J., Kilpatrick, J.A. and McCulloch, M.T. (1997) Geochemical and Sr-Nd isotopic study of charnockites and related rocks in the northern Prince Charles Mountain, East Antarctica. *Precambrian Research*, **81**, 37-66.

[4] Sheraton, J.W, Tindle, A.G. and Tingey, R.J. (1996) Geochemistry, origin, and tectonic setting of granitic rocks of the Prince Charles Mountains, Antarctica. *Australian Journal of Geology & Geophysics*, **16**, 345-370.

[5] Kar, R., Bhattacharya, S. and Sheraton, J.W. (2003) Hornblende dehydration melting in mafic rocks and the link between massif-type charnockite and associated granulites, Eastern Ghats Granulite Belt, India. *Contributions to Mineralalogy and Petrology*, **145**, 707-729.

[6] Kar, R. (2010) Melting experiments in the NCFMASH system at 8 kbar: Implications for the origin of mafic granulites. *Indian Journal of Geology, Special Issue on Geodynamic Regimes, Global tectonics and evolution of Precambrian cratonic basins in India*. **80**, 71-80.

[7] Jenner, G.A., Longerich, H.P., Jackson, S.E. and Fryer, B. J. (1990) ICP-MS a powerfull tool for high-precision trace element analysis in earth science: Evidence from analysis of selected USGS reference samples, *Chemical Geology*, **83**, 133-148.

[8] Govindaraju, K. (1994) 1994 compilation of working values and sample description for 383 geostandards. *Geostandards Newsletter*, **18**, 1-158.

[9] Tarney, J., Wyborn, L.E.A., Sheraton, J.W. and Wyborn, D. (1987) Trace element differences between Archaean, proterozoic and phanerozoic crustal components: Implications for crustal growth processes. In: Ashwal, L.D. Ed., *Workshop on the growth of continental crus*t, Lunar and Planetary Institute, 139-140.

[10] Nutman, A.P., McGregor, V.R., Friend, C.R.L., Bennet, V. C. and Kinny, P.D. (1996) Itsaq gneiss complex of southern west Greenland; the world's most extensive record of early crustal evolution (3,900-3,600 Ma). *Precambrian Research*, **78**, 1-39.

[11] Santosh, M., Maruyama, S. and Sato, K. (2009) Anatomy of a Cambrian suture in Gondwana: Pacific-type orogeny in southern India? *Gondwana Research*, **16**, 321-341.

[12] Lal, R.K., Ackermand, D. and Upadhyay, H. (1987) P-T-X relationships deduced from corona textures in sapphirine-spinel-quartz assemblages from Paderu, southern India. *Journal of Petrology*, **28**, 1139-1168.

[13] Dasgupta, S., Sengupta, P., Fukuoka, M. and Bhattacharya, P.K. (1991) Mafic granulites in the Eastern Ghats, India: Further evidence for extremely high temperature crustal metamorphism. *Journal of Geology*, **99**, 124-133.

[14] Bhowmik, S.K., Dasgupta, S., Hoernes, S. and Bhattacharya, P.K. (1995) Extremely high-temperature calcareous granulites from the Eastern Ghats, India: Evidence for isobaric cooling, fluid buffering, and terminal channelized fluid flow. *Europian Journal of Mineralogy*, **7**, 689-703.

[15] Sen, S.K., Bhattacharya, S. and Acharyya, A. (1995) A multi-stage pressure-temperature record in the Chilka Lake granulites: The epitome of the metamorphic evolution of Eastern Ghats, India? *Journal of Metamorphic Geology*, **13**, 287-298.

[16] Bhattacharya, S. and Kar, R. (2002) High-temperature dehydration melting and decompressive P-T path in a granulite complex from the Eastern Ghats, India. *Contributions to Mineralogy and Petrology*, **143**,175-191.

[17] Patino Douce, A.E. and Beard, J.S. (1995) Dehydration melting of biotite gneiss and quartz amphibolite from 3 to 15 kbar. *Journal of Petrology*, **36**, 707-738.

[18] Springer, W. and Seck, H.A. (1997) Partial fusion of basic granulites at 5 to 15 kbar: Implications for the origin of TTG magmas. *Contributions to Mineralogy and Petrology*, **127**, 30-45.

[19] Lopez, S. and Castro, A. (2001) Determination of the fliud-absent solidus and supersolidus phase relationships of MORB-derived amphibolites in the range 4-14 kbar. *American Mineralogist*, **86**, 1396-1403.

[20] Sisson, T.W., Ratajeski, K. and Hankins, W.B. (2005) Voluminous granitic magmas from common basaltic sources. *Contributions to Mineralogy and Petrology*, **148**, 635-661.

[21] Rickers, K., Mezger, K. and Raith, M., (2001) Evolution of the continental crust in the Proterozoic Eastern Ghats Belt, India and new constraints for Rodinia reconstruction: Implications from Sm-Nd, Rb-Sr and Pb-Pb isotopes. *Precambrian Research*, **112**, 183-210.

[22] Bhui, U.K., Sengupta, P. and Sengupta, P. (2007) Phase relations in mafic dykes and their host rocks from Kondapalle, Andhra Pradesh, India: Implications for the time-depth trajectory of the Paleoproterozoic (late Archean?) granulites from southern Eastern Ghats Belt. *Precambrian Research*, **156**, 153-174.

[23] Taylor, S.R. and McLennan, S.M. (1985) The continental crust: Its composition and evolution. Blackwell, Oxford.

Vol.2, No.10, 1090-1103 (2010)
doi:10.4236/ns.2010.210136

Natural Science

Cell-PLoc 2.0: an improved package of web-servers for predicting subcellular localization of proteins in various organisms

Kuo-Chen Chou[1,2], Hong-Bin Shen[1,2]

[1]Gordon Life Science Institute, 13784 Torrey Del Mar Drive, San Diego, CA 92130, USA; kcchou@gordonlifescience.org
[2]Institute of Image Processing & Pattern Recognition, Shanghai Jiaotong University, 800 Dongchuan Road, Shanghai, 200240, China; hbshen@sjtu.edu.cn

Received 5 August 2010; revised 8 September 2010; accepted 12 September 2010.

ABSTRACT

Cell-PLoc 2.0 is a package of web-servers evolved from Cell-PLoc (Chou, K.C. & Shen, H.B., Nature Protocols, 2008, 2:153-162) by a top-down approach to improve the power for predicting subcellular localization of proteins in various organisms. It contains six predictors: Euk-mPLoc 2.0, Hum-mPLoc 2.0, Plant-mPLoc, Gpos-mPLoc, Gneg-mPLoc, and Virus-mPLoc, specialized for eukaryotic, human, plant, Gram-positive bacterial, Gram-negative bacterial, and virus proteins, respectively. Compared with Cell-PLoc, the predictors in the Cell-PLoc 2.0 have the following advantageous features: (1) they all have the capacity to deal with the multiplex proteins that can simultaneiously exist, or move between, two or more subcellular location sites; (2) no accession number is needed for the input of a query protein even if using the "high-level" GO (gene ontology) prediction engine; (3) the functional domain information and sequential evolution information are fused into the "*ab initio*" sequence-based prediction engine to enhance its accuracy. In this protocol, a step-to-step guide is provided for how to use the web server predictors in the Cell-PLoc 2.0 package, which is freely accessible to the public at http://www.csbio.sjtu.edu.cn/bioinf/Cell-PLoc-2/.

Keywords: Euk-mPLoc 2.0; Hum-mPLoc 2.0; Plant-mPLoc; Gpos-mPLoc; Gneg-mPLoc; Virus-mPLoc; Higher-level GO approach; Ab-initio approach; Functional domain; Sequential evolution; Multiplex proteins

1. INTRODUCTION

The localization of a protein in a cell is one of its most important attributes. It can provide useful insight about the function of the protein. It is also fundamental to system biology because knowledge of the subcellular locations of proteins is indispensable for in-depth understanding how the biological processes are regulated by the intricate pathways at the cellular level [1,2]. Particularly, the information of protein subcellular location is very useful for identifying and prioritizing drug targets [3] during the process of drug development.

Given an uncharacterized protein sequence, how can we identify which subcellular location site it resides at? Does the protein stay in a single subcellular location or can it simultaneously exist in, or move between, two and more subcellular location sites? Although the answers to these questions can be determined by means of various biochemical experiments, it is time-consuming and laborious to acquire the desired information with experimental methods alone. Particularly, in the post-genomic age, the number of newly found protein sequences has increased explosively. For instance, in 1986 the Swiss-Prot databank contained merely 3,939 protein sequence entries, but the number has since jumped to 519,348 according to the data released by the same databank on 10-Aug-2010 (www.expasy.org/sprot/relnotes/relstat.html), meaning that the number of protein sequence entries now is more than 131 times the number from about 24 years ago. Facing such an avalanche of protein sequences, it is highly desired to develop automated methods for timely identifying the subcellular locations of uncharacterized proteins based on their sequence information alone.

Actually, during the past 18 years or so, various computational methods were developed in this regard (see, e.g., [4-59].

All the aforementioned methods each have their own advantages and have indeed played a role in stimulating

the development of this area. Meanwhile, they also each have their own limitations. For example, TargetP [15] is one of the popular methods in this area. Its remarkable merit is to make the prediction of the subcellular location of a protein related to its signal peptide and hence has a clearer biological meaning and basis. But TargetP [15] can only cover four subcellular location sites. For a query protein located outside its coverage scope, TargetP would either fail to predict or the predicted result thus obtained would not make any sense. The similar problem also exists for PSORTb [33], one of the other popular methods in this area.

The other problem for the existing methods listed above is that none of them can be used to deal with multiplex proteins that may simultaneously reside at, or move between, two or more different subcellular locations. Proteins with multiple location sites or dynamic feature of this kind are particularly interesting because they may have some unique biological functions worthy of our special notice [2,3]. Particularly, as pointed out by Millar *et al*. [60], recent evidence indicates that an increasing number of proteins have multiple locations in the cell.

About two years ago, a package of web-servers called **Cell-PLoc** was published [61] that can be used to predict subcellular localization of proteins in various organisms. It contained six web-server predictors: **Euk-mPLoc** [62], **Hum-mPLoc** [63], **Plant-PLoc** [64], **Gpos-PLoc** [65], **Gneg-PLoc** [66], and **Virus-PLoc** [67], specialized for eukaryotic, human, plant, Gram-positive bacterial, Gram-negative bacterial, and virus proteins, respectively. As elucidated in the protocol article [61], each of the six predictors in **Cell-PLoc** was established by hybridizing the "higher-level" GO (gene ontology) [68] approach and the "*ab initio*" PseAAC (pseudo amino acid composition) [16] approach, and hence could yield higher success rates as well as cover much wider scope. For example, the **Euk-mPLoc** predictor can cover up to 22 subcellular location sites. Moreover, of the six predictors in the **Cell-PLoc** package [61], **Euk-mPLoc** and **Hum- mPLoc** can be also used to deal with proteins with multiple-location sites. Therefore, ever since it was published, **Cell-PLoc** has been widely and increasingly used.

However, the existing version of **Cell-PLoc** [61] has the following shortcomings. **(1)** The accession number of a query protein is indispensable as an input in order to utilize the advantage of the "higher-level" GO approach. Many proteins, such as hypothetical and synthetic proteins as well as those newly-discovered proteins that have not been deposited into databanks yet, do not have accession numbers, and hence cannot be handled with the GO approach. **(2)** Even with their accession numbers available, many proteins cannot be meaningfully formulated in a GO space because the current GO database is far from complete yet. **(3)** Although the PseAAC approach was used as a complement in **Cell-PLoc** [61] that could take some partial sequence order effects into account, the original PseAAC [16,69] did not contain the sequential evolution and functional domain information, and hence would affect the prediction quality. **(4)** Except **Euk-mPLoc** (the predictor for eukaryotic proteins) and **Hum-mPLoc** (the predictor for human proteins), all the other predictors in **Cell-PLoc** package [61] cannot be used to deal with multiplex proteins.

To address the aforementioned four problems, a top-down approach to enhance the power of **Cell-PLoc** has been implemented. The new version thus obtained is denoted by **Cell-PLoc 2.0**. Compared with the old **Cell-PLoc** [61], **Cell-PLoc 2.0** has the following advantageous features.

Input Data. By means of the "homology-based GO extraction" strategy as developed recently (see, e.g., [70]), the requirement for the accession number of a query protein is no longer needed even if using the higher-level GO approach to perform the prediction. This is especially useful for predicting the subcellular location sites of hypothetical proteins or synthetic proteins, as well as those new protein sequences without being deposited into data banks and hence having no accession numbers assigned yet.

Sequence Information. For those proteins that have no useful GO information to carry out the higher-level prediction, a hybridization approach by fusing the functional domain information and sequential evolution information as illustrated in **Figure 1** is developed to replace the simple PseAAC approach [16] in the old **Cell-PLoc** [61]. As a consequence, the success rates have been remarkably increased for those proteins without useful GO numbers.

Multiplex Proteins. In the old **Cell-PLoc** package [61], only two predictors, i.e., the one specialized for eukaryotic proteins and the one specialized for human proteins, can be used to treat proteins with multiple location sites. In **Cell-PLoc 2.0**, all the six predictors, including those specialized for plant proteins, Gram- positive bacterial proteins, Gram-negative bacterial proteins, and virus proteins, can be used to deal with the multiplex proteins.

Benchmark Datasets. With more experimental data available in Swiss-Prot database (www.ebi.ac.uk/swissprot), to update the data for training the predictors, instead of version 50.7 released on 9-Sept-2006 as used in the old **Cell-PLoc** [61], the benchmark datasets for training the

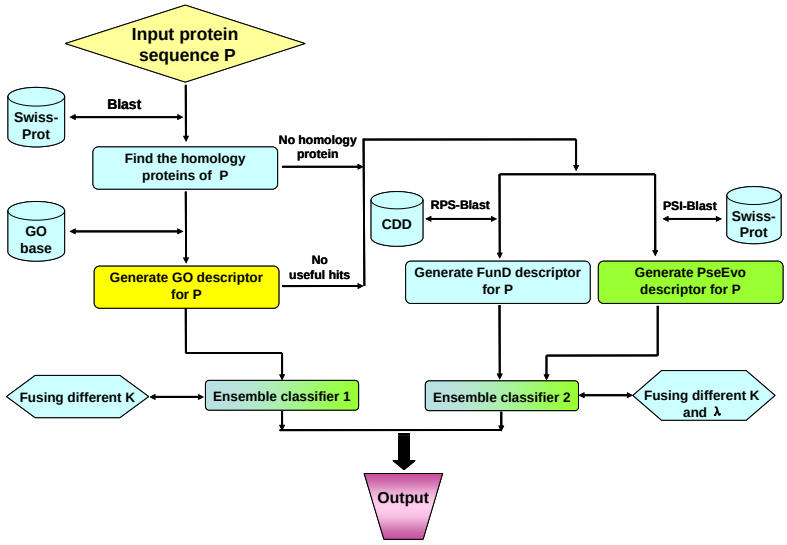

Figure 1. A flowchart to show the prediction process of the predictors in Cell-PLoc 2.0, where ensemble classifier 1 is for processing the GO descriptor samples, while ensemble classifier 2 is for the FunD (functional domain) and PseEvo (pseudo sequential evolution) descriptor samples. See [70,71] for further explanation.

predictors in **Cell-PLoc 2.0** were constructed based on version 55.3 released on 29-April-2008. Moreover, to make all the predictors in **Cell-PLoc 2.0** have the capacity to deal with the multiplex proteins as well, the sequences annotated with two or more subcellular location sites were no longer excluded even for plant proteins, Gram-positive bacterial proteins, Gram-negative bacterial proteins, and virus proteins as done previously in the old **Cell-PLoc** package [61].

Below, let us describe how to use the new **Cell-PLoc 2.0** package to get the desired results.

2. EQUIPMENT AND MATERIALS

Hardware. Same as in the old **Cell-PLoc** [61], i.e., you need a computer that is able to access to internet.

Data. Your input protein sequences should be in FASTA format. You can enter the sequence of a query protein by either typing or copying-and-pasting it into the input box. Spaces and line breaks will be ignored and will not affect the prediction result.

Programs. Cell-PLoc 2.0 contains the following programs: (1) **Euk-mPLoc 2.0** for predicting the subcellular localization of eukaryotic proteins; (2) **Hum-mPLoc 2.0** for human proteins; (3) **Plant-mPLoc** for plant proteins; (4) **Gpos-mPLoc** for Gram-positive bacterial proteins; (5) **Gneg-mPLoc** for Gram-negative bacterial proteins; (6) **Virus-mPLoc** for virus proteins. The six predictors were evolved from Euk-mPLoc [62], Hum-mPLoc [63], Plant- PLoc [64], Gpos-PLoc [65], Gneg-PLoc [66], and Virus- PLoc [67] in the original **Cell-PLoc** package [61] through a top-down approach to enhance their power, as elaborated in [70-75], respectively. Note that now all the six predictors in **Cell-PLoc 2.0** have the capacity to deal with multiplex proteins as well, as indicated by the character "m" in front of their partial name "PLoc" that stands for the first character of "multiple".

3. PROCEDURE

1) Go to the internet at http://www.csbio.sjtu.edu.cn/bioinf/Cell-PLoc-2/ and you will see the top page of the **Cell-PLoc 2.0** package on the screen of your computer, as shown in **Figure 2**.

2) You should use the relevant predictor to conduct the prediction: (1) if your query protein is an eukaryotic one, click the button Euk-mPLoc 2.0**;** (2) if it is a human protein, click Hum-mPLoc 2.0; (3) if it is a plant protein, click Plant-mPLoc; (4) if it is a Gram-positive bacterial protein, click Gpos-mPLoc; (5) if it is a Gram- negative bacterial protein, click Gneg-mPLoc; (6) if it is a viral protein, click Virus-mPLoc**.**

3) Without loss of generality, let us take **Hum-mPLoc 2.0** as an example. By clicking Hum-mPLoc 2.0, you will be prompted with the top page of the **Hum-mPLoc 2.0** web-server predictor (**Figure 3**). To find the coverage scope and caveat in using the predictor, click the Read Me button and you will see that the current **Hum-mPLoc 2.0** version can cover the following 14 human protein subcellular location sites: (1) centriole, (2) cytoplasm, (3) cytoskeleton, (4) endoplasmic reticulum, (5) endosome, (6) extracell, (7) Golgi apparatus, (8) ly-

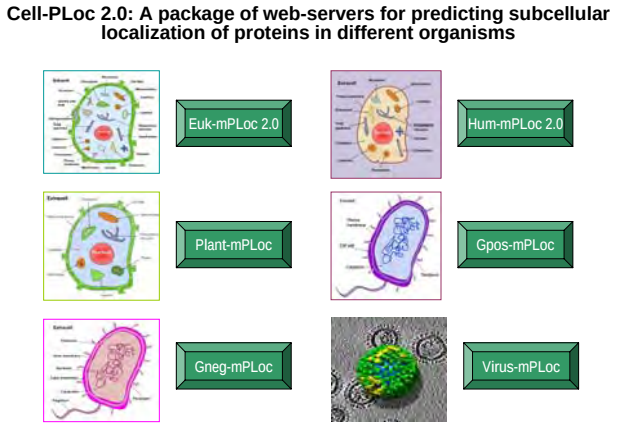

Figure 2. Illustration to show the **Cell-PLoc 2.0** web-page at http://www.csbio.sjtu.edu.cn/bioinf/Cell-PLoc-2/.

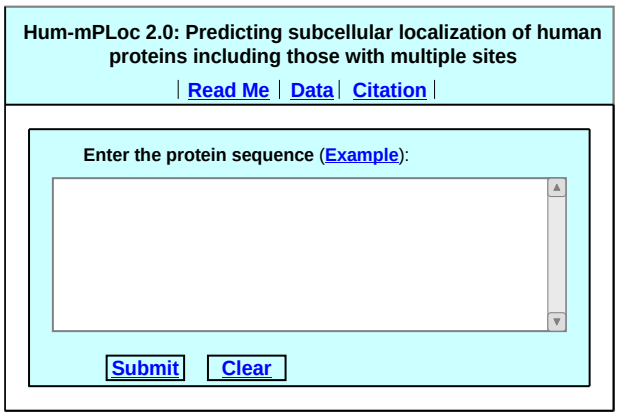

Figure 3. A semi-screenshot to show the top page of the web-server predictor **Hum-mPLoc 2.0** in the **Cell-PLoc 2.0** package.

sosome, (9) microsome, (10) mitochondrion, (11) nucleus, (12) peroxisome, (13) plasma membrane, and (14) synapse, as schematically shown in **Figure 4**. You will also see the caveat from the Read Me window how to avoid meaningless prediction. To continue the prediction, go back to the top page of the **Hum-mPLoc 2.0** web-server predictor by closing the Read Me window.

4) Enter your query protein sequence into the input box as shown at the centre of **Figure 3**. The input sequence should be in FASTA format. A sequence in FASTA format consists of a single-line description, followed by lines of sequence data. The first character of the description line is a greater-than symbol (“>”) in the first column. All lines should be shorter than 80 characters. Example sequences in FASTA format can be seen by clicking on the Example button right above the input box. For more information about FASTA format, visit http://en.wikipedia.org/wiki/Fasta_format.

5) To get the predicted result, click the Submit button.

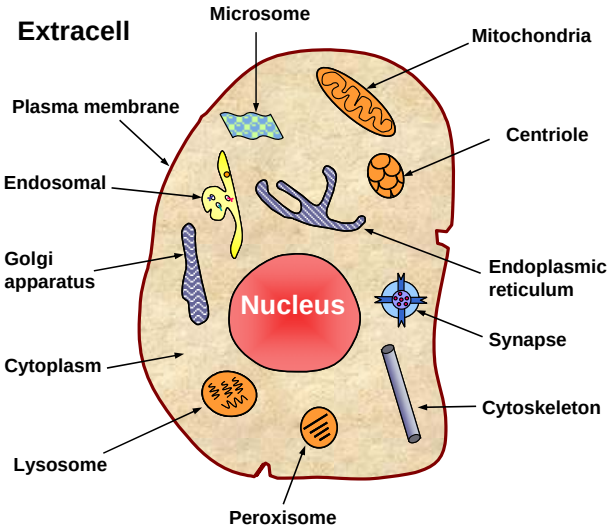

Figure 4. Schematic illustration to show the fourteen subcellular location sites of human proteins that are covered by the **Hum-mPLoc 2.0** predictor.

For example, if using the sequence of query protein 1 in the Example window as an input, you will see the input screen as shown in **Figure 5a**; after clicking the Submit button, you will see “**Cell membrane; Cytoplasm; Nucleus**” shown on the predicted location(s) window (**Figure 5b**), meaning that the query protein is a multiplex protein, which can simultaneously occur in “cell membrane”, “cytoplasm” and “nucleus” sites, fully consistent with experimental observations. However, if using the sequence of query protein 2 in the Example window as an input, you will instead see the input screen as shown in **Figure 6a**; after clicking the Submit button, you will see “**Cytoplasm**” shown on the predicted location(s) window (**Figure 6b**), meaning that the query protein is a single-location protein residing in “cytoplasm” compartment only, also fully consistent with experimental observations.

6) By clicking the Citation button, you will find the relevant papers that document the detailed development and algorithm of **Hum-mPLoc 2.0**.

7) By clicking the Data button, you will find all the benchmark datasets used to train and test the **Hum-mPLoc 2.0** predictor.

8) If your query protein sequence is from other organism, click the relevant web-server button (**Figure 2**) as elaborated in **Step 2**, and repeat **Steps 3-6**.

TIMING The computational time for each prediction is within 15 seconds for most cases. The longer the query protein sequence is, the more time it is usually needed.

4. TROUBLESHOOTING

After you click the Submit button, if the server rejects

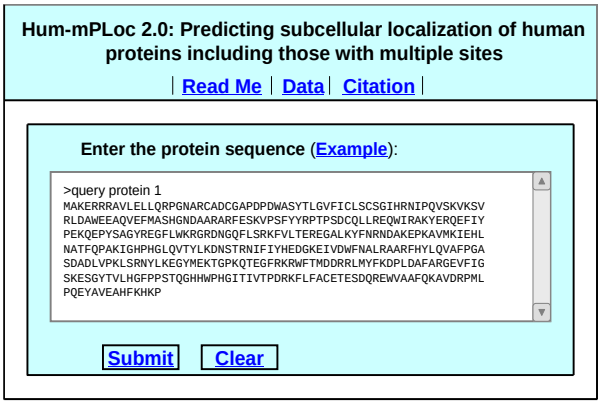

Figure 5. A semi-screenshot to show the input in the FASTA format for **(a)** the query protein 1 taken from the Example window, and **(b)** the output predicted by **Hum-mPLoc 2.0** for the query protein sequence in panel **(a)**.

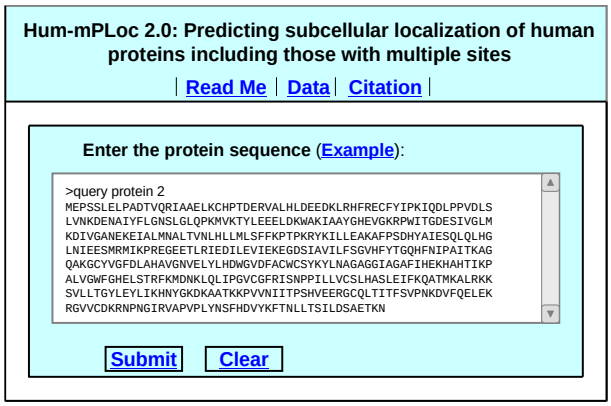

Figure 6. A semi-screenshot to show the input in the FASTA format for **(a)** the query protein 2 taken from the Example window, and **(b)** the output predicted by **Hum-mPLoc 2.0** for the query protein sequence in panel **(a)**.

your submission for prediction, consider the following points for troubleshooting.

- Check the format of your input data to make sure it complies with the FASTA format as elaborated in Step 4 of the PROCEDURE.
- Check the length of your input sequence to make sure it is at least 50 amino acids long; otherwise, it might not be a real protein but its fragment.
- Check the amino acid codes of your input sequence to make sure it does not contain any invalid characters.

You might also get meaningless result if the query protein is not among the subcellular location sites covered by the web-server predictor.

5. ANTICIPATED RESULTS

In statistical prediction of subcellular localization of proteins or their any other attributes, it would be meaningless to simply say the success rate of a predictor without specifying what method and benchmark dataset were used to test its accuracy.

The following three cross-validation methods are generally used for examining the effectiveness of a statistical prediction method: **(1)** the independent dataset test, **(2)** the sub-sampling (K-fold cross-validation) test, and **(3)** the jackknife test [76].

For the independent dataset test, although all the proteins to be tested are outside the training dataset used to train the predictor and hence can avoid the "memory" effect or bias, the way of how to select the independent proteins for testing could be quite arbitrary unless the number of independent proteins is sufficiently large. This kind of arbitrariness might lead to completely different conclusions. For instance, a predictor achieving a higher success rate than the other predictor for a given independent testing dataset might fail to keep so when tested by another independent testing dataset [76].

For the subsampling test, the concrete procedure usually used in literatures is the 5-fold, 7-fold or 10-fold

cross-validation. The problem with the K-fold cross-validation test as such is that the number of possible selections in dividing a benchmark dataset is an astronomical figure even for a very simple dataset. For example, let us consider a highly simplified dataset that consists of 300 proteins classified into five subsets, in which 60 proteins belong to subcellular location #1, 55 to location #2, 70 to location #3, 65 to location #4, and 50 to location #5. For such a simple dataset, the number of possible combinations of taking one-fifth proteins from each of the five subsets will be

$$\begin{aligned}\Omega &= \Omega_1 \cdot \Omega_2 \cdot \Omega_3 \cdot \Omega_4 \cdot \Omega_5 \\ &= \frac{60!}{(60-12)!12!} \cdot \frac{55!}{(55-11)!11!} \cdot \frac{70!}{(70-14)!14!} \\ &\quad \cdot \frac{65!}{(65-13)!13!} \cdot \frac{50!}{(50-10)!10!} > 5.45\times 10^{60}\end{aligned} \quad (1)$$

where Ω_1 is the number of possible different ways of taking $60/5=12$ proteins from subset #1, Ω_2 that of taking $55/5=11$ proteins from subset #2, Ω_3 that of taking $70/5=14$ proteins from subset #3, Ω_4 that of taking $65/5=13$ proteins from subset #4, and Ω_5 that of taking $50/5=10$ proteins from site-site-5. As we can see from **Eq.1**, even for such a simple and small dataset the number of possible ways in selecting the testing dataset for the 5-fold cross-validation would be greater than 5.45×10^{60}. It can be easily conceived that for a benchmark dataset containing over a thousand proteins that are classified into more than five subcellular location sites, the number of the possible selections for subsampling test will be even much greater. Accordingly, in any actual subsampling cross-validation tests, only an extremely small fraction of the possible selections are taken into account. Since different selections will always lead to different results even for a same benchmark dataset and a same predictor, the subsampling test (such as 5-fold cross-validation) cannot avoid the arbitrariness either. A test method unable to yield a unique outcome cannot be deemed as an ideal one.

In the jackknife test, all the proteins in the benchmark dataset will be singled out one-by-one and tested by the predictor trained by the remaining protein samples. During the process of jackknifing, both the training dataset and testing dataset are actually open, and each protein sample will be in turn moved between the two. The jackknife test can exclude the "memory" effect. Also, the arbitrariness problem as mentioned above for the independent dataset test and subsampling test can be avoided because the outcome obtained by the jackknife cross-validation is always unique for a given benchmark dataset. As for the possible overestimation in success rate by jackknife test because of only one sample being singled out at a time for testing, the answer is that as long as the jackknife test is performed on a stringent benchmark dataset in which none of proteins has $\geq 25\%$ pairwise sequence identity to any other in a same subcellular location such as those benchmark datasets specially constructed for the six predictors in **Cell-PLoc 2.0**, it is highly unlikely to yield an overestimated rate compared with the actual success rate in practical applications, as demonstrated in [72,74] and will be further discussed later. Besides, when the jackknife test was used to compare two predictors, even if there was some overestimate due to using a less stringent benchmark dataset for one predictor, the same overestimate would exist for the other as long as they were both tested by a same dataset.

Accordingly, the jackknife test has been increasingly and widely used by investigators to examine the quality of various predictors (see, e.g., [47,51,55,58,59,77- 107]).

However, even if using the jackknife approach for cross-validation, a same predictor may still generate obviously different success rates when tested by different benchmark datasets. This is because the more stringent of a benchmark dataset in excluding homologous and high similarity sequences, or the more number of subcellular location sites it covers, the more difficult for a predictor to achieve a high overall success rate, as will be shown later.

The predictors in the old **Cell-PLoc** package [61] were established by hybridizing the "higher-level" GO approach with the "*ab initio*" sequence-correlated PseAAC [16] approach. Accordingly, their overall success prediction rates are generally higher than those by the best of the existing "*ab initio*" sequence-based approaches without combining with any higher level approach, as elucidated in [61] and demonstrated in a series of previous publications [62-67,108,109], and hence there is no need to repeat here.

Now, in the new version of **Cell-PLoc 2.0**, the same high success rates will still be achieved by the "higher-level" GO prediction engine but no requirement for the accession number is needed for the input. And for those proteins without useful GO numbers, the corresponding success prediction rates will be further enhanced due to fusing the functional domain information and sequential evolution information into the "*ab initio*" prediction engine in the **Cell-PLoc 2.0** package as illustrated in **Figure 1**. Accordingly, the overall success rates by the predictors in **Cell-PLoc 2.0** are not only higher than those by the other predictors but also those by the predictors in the old **Cell-PLoc** package [61], as can be seen from the following comparisons.

Table 1. Comparison between each of the six predictors in Cell-PLoc [61] and that in Cell-PLoc 2.0 by jackknife test.

Organism	Number of subcellular locations covered	Cell-PLoc		Cell-PLoc 2.0	
		Predictor	Overall success rate[g]	Predictor	Overall success rate
Eukaryotic	22[a]	Euk-mPLoc	39.3%	Euk-mPLoc 2.0	64.2%
Human	14[b]	Hum-mPLoc	38.1%	Hum-mPLoc 2.0	62.7%
Plant	12[c]	Plant-PLoc	38.0%	Plant-mPLoc	63.7%
Gram-positive	4[d]	Gpos-PLoc	72.5%	Gpos-mPLoc	82.2%
Gram-negative	8[e]	Gneg-PLoc	71.5%	Gneg-mPLoc	85.7%
Virus	6[f]	Virus-PLoc	43.7%	Virus-mPLoc	60.3%

[a]The corresponding benchmark dataset was taken from the Supporting Information S1 of [70], in which none of protein included has $\geq 25\%$ pairwise sequence identity to any other in a same subcellular location; [b]The corresponding benchmark dataset was taken from the Online Supporting Information A of [71], in which none of protein included has $\geq 25\%$ pairwise sequence identity to any other in a same subcellular location; [c]The corresponding benchmark dataset was taken from Table S1 of [72], in which none of protein included has $\geq 25\%$ pairwise sequence identity to any other in a same subcellular location; [d]The corresponding benchmark dataset was taken from the Online Supporting Information A of [73], in which none of protein included has $\geq 25\%$ pairwise sequence identity to any other in a same subcellular location; [e]The corresponding benchmark dataset was taken from the Online Supporting Information A of [74], in which none of protein included has $\geq 25\%$ pairwise sequence identity to any other in a same subcellular location; [f]The corresponding benchmark dataset was taken from the Online Supporting Information A of [75], in which none of protein included has $\geq 25\%$ pairwise sequence identity to any other in a same subcellular location; [g]Note that in order to make the comparison under exactly the same condition, only the sequences of proteins but not their accession numbers were used as inputs during the prediction.

1) Comparison with the six predictors in **Cell-PLoc** [61]. Listed in **Table 1** are the overall success rates by **Cell-PLoc** [61] and **Cell-PLoc 2.0** using jackknife tests on six stringent benchmark datasets for eukaryotic, human, plant, Gram-positive bacterial, Gram-negative bacterial, and virus proteins, respectively. For the case of eukaryotic proteins, the comparison was made between the predictor **Euk-mPLoc** of **Cell-PLoc** [61] and the predictor **Euk-mPLoc 2.0** of **Cell-PLoc 2.0** using the benchmark dataset classified into 22 subcellular locations as given in the Supporting Information S1 of [70]. For human proteins, the comparison was made between the predictor **Hum-mPLoc** of **Cell-PLoc** [61] and the predictor **Hum-mPLoc 2.0** of **Cell-PLoc 2.0** using the benchmark dataset classified into 14 subcellular locations as given in the Online Supporting Information A of [71]. And so forth. To avoid homology bias and redundancy, none of the proteins included in the six datasets has $\geq 25\%$ pairwise sequence identity to any other in a same subcellular location. Also, to make the comparison between the two counterparts under exactly the same condition, only the sequences of proteins but not their accession numbers were used as inputs during the prediction. Meanwhile, the false positives (over-predictions) and false negatives (under-predictions) were also taken into account to reduce the scores for calculating the overall success rate. It is instructive to point out that it is much more complicated to count the over-predictions and under-predictions for a system containing both single-location and multiple-location proteins. For the detailed calculation formulation, see Eqs.43-48 as well as **Figure 4** in a comprehensive review [110]. It can be seen from **Table 1** that the overall success rates obtained by the predictors in **Cell-PLoc 2.0** are about 10-25% higher than those by their counterparts in **Cell-PLoc** [61].

2) Comparison with **PSORTb v.2.0** [33]. The predictor is widely used by biologists for predicting the subcellular locations of Gram-negative bacterial proteins. It is with a built-in training dataset covering the following five subcellular location sites: (1) cytoplasm, (2) extracellular, (3) inner membrane, (4) outer membrane, and (5) periplasm. The corresponding predictor in **Cell-PLoc 2.0** is **Gneg-mPLoc** that can cover eight subcellular locations of Gram-negative proteins; i.e., in addition to the above five locations, it also covers "fimbrium", "flagellum", and "nucleoid". In order to make the two predictors with different coverage scopes comparable, a degenerate testing dataset was generated by randomly picking testing proteins according to the following criteria: (1) the testing samples must be Gram-negative bacterial proteins; (2) to avoid the unfair "memory" effect, the testing samples must be not in the training dataset of **PSORTb v.2.0**, nor in the training dataset of **Gneg-mPLoc**; (3) the experimentally observed subcellular locations of the testing proteins are known as clearly annotated in Swiss-Prot database; (4) their location sites must be within the scope covered by **PSORTb v.2.0** for properly using it (for the proteins with multiple location sites, at least one of them should be within the scope covered by **PSORTb**

v.2.0). For the detailed information about the testing dataset thus generated, see the Online Supporting Information B of [74] that contains 759 Gram-negative proteins, of which 116 are of cytoplasm, 62 of extracellular, 397 of inner membrane, 89 of outer membrane, and 95 of periplasm. As shown in **Table 2**, the overall success rates by **Gneg-mPLoc** and **PSORTb v.2.0** [33] in identifying the subcellular locations of proteins in such a testing dataset were 98.0% and 79.3%, respectively, indicating the success rate by **Gneg-mPLoc** of **Cell-PLOc 2.0** was 19% higher than that by **PSORTb v.2.0** [33]. Furthermore, some examples are given in **Table 3** to show how the results mispredicted by **PSORTb v.2.0** were successfully corrected by **Greg-mPLoc**. It is interesting to see from the table that the first protein with accession number P62532 was predicted by **Gneg-mPLoc** belonging to two subcellular location sites, "extracellular" and "fimbrium", fully consistent with experimental observation as annotated in Swiss-Prot database (version 55.3 released on 29- April-2008).

3) Comparison with **TargetP** [15]. The predictor is widely used by biologists for predicting the subcellular locations of plant proteins. It has a web-server at http://www.cbs.dtu.dk/services/TargetP/, with a built-in training dataset covering the following four items: "mitochondria", "chloroplast", "secretory pathway", and "other". Since the "secretory pathway" is not a final destination of subcellular location as annotated in Swiss-Prot databank, and should be removed from the comparison. Also, the location of "other" is not a clear site for comparison, and should be removed too. The corresponding predictor in **Cell-PLoc 2.0** is **Plant-mPLoc** that can cover 12 subcellular locations of plant proteins; i.e., in addition to "mitochondria" and "chloroplast", it also covers "cell membrane", "cell wall", "cytoplasm", "endoplasmic reticulum", "extracellular", "Golgi apparatus", "nucleus", "peroxisome", "plastid", and "vacuole". Thus, to make the two predictors with different coverage scopes comparable, a degenerate testing dataset was generated according to the similar procedures as described in section **5.2**. For the detailed information about the testing dataset thus generated, see Table S2 of [72] that contains 1,775 plant proteins of which 1,500 are of chloroplast and 275 of mitochondrion. As reported in [72], the overall success rates by **Plant-mPLoc** on such a testing dataset was 86%, which is more than 40% higher than that by **TargetP** [15] on the same testing dataset.

4) Comparison with Predotar [111]. This is another popular predictor used by biologists for predicting the subcellular locations of plant proteins. Its web-server is at http://urgi.versailles.inra.fr/predotar/predotar.html, with a built-in training dataset covering the following four items: "endoplasmic reticulum", "mitochondrion", "plastid", and "other". Since the term "other" is not a clear description for subcellular location, and was removed from comparison. The corresponding predictor in **Cell-PLoc 2.0** is **Plant-mPLoc** that can cover 12 subcellular locations of plant proteins; *i.e.*, in addition to "endoplasmic reticulum", "mitochondria" and "plastid", it also covers "cell membrane", "cell wall", "chloroplast", "cytoplasm", "extracellular", "Golgi apparatus", "nucleus", "peroxisome", and "vacuole". Again, to make the two predictors with different coverage scopes comparable, a degenerate testing dataset was generated by following the similar procedures as described in section **5.2**. For the detailed information about the testing dataset thus generated, see Table S4 of [72], where it was also reported that the overall success rates by **Plant-mPLoc** on such a testing dataset was 70%, which is more than 30% higher than that by **Predotar** [111] on the same testing dataset.

Moreover, it was also shown in [72,74] that some proteins coexisting in two or more subcellular location sites were successfully identified by **Gneg-mPLoc** [74] and **Plant-mPLoc** [72]; cases like that are beyond the reach of **PSORTb v.2.0** [33], **TargetP** [15], or **Predotar** [111].

Table 2. A comparison of the predicted results by **Gneg-mPLoc** and **PSORTb v.2.0** [33] on the testing dataset of Online Supporting Information B of [74].

Subcellular location	Success rate	
	PSORTb v.2.0	Gneg-mPLoc
Cytoplasm	99/116=85.3%	115/116=99.1%
Extracellular	20/62=32.3%	52/62=83.9%
Inner membrane	329/397=82.9%	397/397=100%
Outer membrane	75/89=84.3%	87/89=97.8%
Periplasm	79/95=83.2%	93/95=97.9%
Total	602/759=79.3%	744/759=98.0%

Table 3. Some examples to show how the subcellular location sites mispredicted by **PSORTb v.2.0** were corrected by **Gneg-mPLoc.**

Protein accession number[a]	Experimental result annotated in Swiss-Prot database	Predicted result by PSORTb v.2.0	Predicted result by Gneg-mPLoc
P62532	Extracellular; Fimbrium	Unknown	Extracellular; Fimbrium
Q8X9H8	Cytoplasm	Unknown	Cytoplasm
P00962	Cytoplasm	Unknown	Cytoplasm
Q83LY4	Cytoplasm	Unknown	Cytoplasm
Q8DFR1	Cytoplasm	Unknown	Cytoplasm
Q84H44	Cytoplasm	Unknown	Cytoplasm
P27475	Extracellular	Unknown	Extracellular
O50319	Extracellular	Unknown	Extracellular
P31518	Extracellular	Unknown	Extracellular
Q89AD4	Cytoplasm	Unknown	Cytoplasm
Q56027	Extracellular	Unknown	Extracellular
O52623	Extracellular	Unknown	Extracellular
P26219	Cell inner membrane	Unknown	Cell inner membrane
P77293	Cell inner membrane	Unknown	Cell inner membrane
P95655	Cell inner membrane	Unknown	Cell inner membrane.
P04123	Cell inner membrane	Periplasm	Cell inner membrane
Q47879	Cell outer membrane	Unknown	Cell outer membrane
P0A935	Cell outer membrane	Unknown	Cell outer membrane
P00211	Periplasm	Cytoplasm	Periplasm
P0A182	Periplasm	Unknown	Periplasm
Q9Z4N3	Periplasm	Unknown	Periplasm
P31330	Periplasm	Cytoplasm	Periplasm

[a] Only the sequences but not the accession numbers were used as inputs during the prediction by Gneg-mPLoc. The accession numbers here are just for the usage of identification.

From the above four comparisons, we can now make the following points very clear.

- The more stringent a benchmark dataset is in excluding homologous and high similarity sequences, or the more subcellular location sites it covers, the more difficult for a predictor to achieve a high overall success rate. The impact of the coverage scope on the success rate can be easily understood by just considering the following cases. For a benchmark dataset only covering four subcellular locations each containing same number of proteins, the overall success rate by random assignments would generally be $1/4 = 25\%$; while for a benchmark dataset covering 22 subcellular locations, the overall success rate by random assignments would be only $1/25 \approx 4.5\%$. This means that the former is more than five times the latter.
- Also, a predictor examined by jackknife test is very difficult to yield a high success rate when performed on a stringent benchmark dataset in which none of proteins included has $\geq 25\%$ pairwise sequence identity to any other in a same subset (subcellular location). That is why the overall success rate achieved by **Gneg-mPLoc** was 85.7% when examined by the jackknife test on the benchmark dataset of the Online Supporting Information A of [74] but was 98.0% when examined by the independent dataset test for the proteins in the Online Supporting Information B of [74]. That is also why the overall success rate achieved by **Plant-mPLoc** was only 63.7% when examined by the jackknife test on the benchmark dataset of Table S1 of [72] but was over 86% and 70% when tested by the independent proteins of Table S2 and

Table S4 of [72], respectively. However, regardless of using what test methods or test datasets, one thing is crystal clear, i.e., the overall success rates achieved by the six predictors in **Cell-PLoc 2.0** are significantly higher than those by its counterparts.

- Meanwhile, it has also become understandable why the success rates as originally reported by **PSORTb v.2.0** [33], **TargetP** [15] and **Predotar** [111] were over-estimated. This is because none of the success rates reported for these predictors was derived by the jackknife test. Also, the benchmark datasets used to test these predictors covered much less subcellular location sites than those used in their counterparts in **Cell-PLoc 2.0**. Particularly, the benchmark datasets used by **PSORTb v.2.0** , **TargetP** and **Predotar** to estimate their success rates contained many homologous sequences. For instance, the cutoff threshold to reduce the homology bias for the benchmark dataset used in **Predotar** [111] was set at 80%, meaning that only those sequences which have $\geq 80\%$ pairwise sequence identity to any other in a same subset were excluded [111]; while for the benchmark dataset used in **TargetP** [15] and **PSORTb v.2.0** [33], even no cutoff threshold was indicated to remove homologous sequences. Compared with the benchmark datasets used in [70-75] where none of proteins included has $\geq 25\%$ pairwise sequence identity to any other in a same subset, the benchmark datasets adopted by **PSORTb v.2.0**, **TargetP**, and **Predotar** are much less stringent and hence cannot avoid homology bias and overestimation.

6. CONCLUDING REMARKS

Evolved from the old **Cell-PLoc** package [61], **Cell-PLoc 2.0** is much more flexible and powerful than the former. In addition to yielding higher success rates than the existing prediction method, all the predictors in **Cell-PLoc 2.0** have the capacity to deal with proteins with two or more subcellular location sites. Besides, the predictors in **Cell-PLoc 2.0** cover much wider scopes than most of the existing predictors in this area. For instance, **Hum-mPLoc 2.0** and **Euk-mPLoc 2.0** can cove up to 14 sites of human proteins and 22 sites of eukaryotic, respectively, which are about two to five times the number of subcellular location sites covered by most of the existing predictors.

However, **Cell-PLoc 2.0** also has the following limitations and further improvements will be needed with more experimental data available in future. **(1)** Although **Euk-mPLoc 2.0** in the **Cell-PLoc 2.0** package can cover 22 sites of eukaryotic proteins, if a query protein is outside of the 22 location sites, it would still generate meaningless result. Therefore, we shall continuously extend the coverage scope for each of the predictors in the **Cell-PLoc** series in a timely manner once more statistically significant experimental data will be available in future. **(2)** For some subcellular locations with very small numbers of proteins, the prediction success rates are still quite low. This is because there are not sufficient location-known proteins in these sites to effectively train the prediction engine. It is anticipated that with more experimental data available for these sites in the future, this kind of situation will be improved. **(3)** Since the power of **Cell-PLoc 2.0** is closely associated with the GO database [68,112,113] and functional domain database [114], with the continuous development of the GO database and functional domain database, more useful GO numbers and functional domain information will be incorporated into the prediction engine, further strengthening its prediction power.

Once further improvements are implemented, the future version of **Cell-PLoc** series will be announced via a publication or a webpage.

REFERENCES

[1] Ehrlich, J.S., Hansen, M.D., Nelson, W.J. (2002) Spatio-temporal regulation of Rac1 localization and lamellipodia dynamics during epithelial cell-cell adhesion. *Dev Cell*, **3**, 259-270.

[2] Glory, E., Murphy, R.F. (2007) Automated subcellular location determination and high-throughput microscopy. *Dev Cell*, **12**, 7-16.

[3] Smith, C. (2008) Subcellular targeting of proteins and drugs. http://www.biocompare.com/Articles/TechnologySpotlight/976/Subcellular-Targeting-Of-Proteins-And-Drugs.html

[4] Nakai, K., Kanehisa, M. (1991) Expert system for predicting protein localization sites in Gram-negative bacteria. *Proteins*: *Structure, Function and Genetics*, **11**, 95-110.

[5] Nakashima, H., Nishikawa, K. (1994) Discrimination of intracellular and extracellular proteins using amino acid composition and residue-pair frequencies. *Journal of Molecular Biology*, **238**, 54-61.

[6] Cedano, J., Aloy, P., P'erez-Pons, J.A., Querol, E. (1997) Relation between amino acid composition and cellular location of proteins. *Journal of Molecular Biology*, **266**, 594-600.

[7] Nakai, K., Horton, P. (1999) PSORT: A program for detecting sorting signals in proteins and predicting their subcellular localization. *Trends in Biochemical Science*, **24**, 34-36.

[8] Chou, K.C., Elrod, D.W. (1998) Using discriminant function for prediction of subcellular location of prokaryotic proteins. *Biochemical and Biophysical Research Communications*, **252**, 63-68.

[9] Reinhardt, A., Hubbard, T. (1998) Using neural networks for prediction of the subcellular location of proteins.

Nucleic Acids Research, **26**, 2230-2236.
[10] Chou, K.C., Elrod, D.W. (1999) Protein subcellular location prediction. *Protein Engineering*, **12**, 107-118.
[11] Yuan, Z. (1999) Prediction of protein subcellular locations using Markov chain models. *FEBS Letters*, **451**, 23-26.
[12] Nakai, K. (2000) Protein sorting signals and prediction of subcellular localization. *Advances in Protein Chemistry*, **54**, 277-344.
[13] Murphy, R.F., Boland, M.V., Velliste, M. (2000) Towards a systematics for protein subcellular location: quantitative description of protein localization patterns and automated analysis of fluorescence microscope images. *Proc. Int. Conf. Intell. Syst. Mol. Biol.*, **8**, 251-259.
[14] Chou, K.C. (2000) Review: Prediction of protein structural classes and subcellular locations. *Current Protein and Peptide Science*, **1**, 171-208.
[15] Emanuelsson, O., Nielsen, H., Brunak, S., von Heijne, G. (2000) Predicting subcellular localization of proteins based on their N-terminal amino acid sequence. *Journal of Molecular Biology*, **300**, 1005-1016.
[16] Chou, K.C. (2001) Prediction of protein cellular attributes using pseudo amino acid composition. *PROTEINS: Structure, Function, and Genetics* (*Erratum*: *ibid.*, 2001, Vol.44, 60), **43**, 246-255.
[17] Feng, Z.P. (2001) Prediction of the subcellular location of prokaryotic proteins based on a new representation of the amino acid composition. *Biopolymers*, **58**, 491-499.
[18] Hua, S., Sun, Z. (2001) Support vector machine approach for protein subcellular localization prediction. *Bioinformatics*, **17**, 721-728.
[19] Feng, Z.P., Zhang, C.T. (2001) Prediction of the subcellular location of prokaryotic proteins based on the hydrophobicity index of amino acids. *Int. J. Biol. Macromol.*, **28**, 255-261.
[20] Feng, Z.P. (2002) An overview on predicting the subcellular location of a protein. *In. Silico. Biol.*, **2**, 291-303.
[21] Chou, K.C., Cai, Y.D. (2002) Using functional domain composition and support vector machines for prediction of protein subcellular location. *Journal of Biological Chemistry*, **277**, 45765-45769.
[22] Zhou, G.P., Doctor, K. (2003) Subcellular location prediction of apoptosis proteins. *Proteins*: *Structure, Function, and Genetics*, **50**, 44-48.
[23] Pan, Y.X., Zhang, Z.Z., Guo, Z.M., Feng, G.Y., Huang, Z.D., He, L. (2003) Application of pseudo amino acid composition for predicting protein subcellular location: Stochastic signal processing approach. *Journal of Protein Chemistry*, **22**, 395-402.
[24] Park, K.J., Kanehisa, M. (2003) Prediction of protein subcellular locations by support vector machines using compositions of amino acid and amino acid pairs. *Bioinformatics*, **19**, 1656-1663.
[25] Gardy, J.L., Spencer, C., Wang, K., Ester, M., Tusnady, G.E., Simon, I., Hua, S., deFays, K., Lambert, C., Nakai, K., Brinkman, F.S. (2003) PSORT-B: Improving protein subcellular localization prediction for Gram-negative bacteria. *Nucleic Acids Research*, **31**, 3613-3617.
[26] Huang, Y., Li, Y. (2004) Prediction of protein subcellular locations using fuzzy k-NN method. *Bioinformatics*, **20**, 21-28.
[27] Xiao, X., Shao, S., Ding, Y., Huang, Z., Huang, Y., Chou, K.C. (2005) Using complexity measure factor to predict protein subcellular location. *Amino Acids*, **28**, 57-61.
[28] Gao, Y., Shao, S.H., Xiao, X., Ding, Y.S., Huang, Y.S., Huang, Z.D., Chou, K.C. (2005) Using pseudo amino acid composition to predict protein subcellular location: approached with Lyapunov index, Bessel function, and Chebyshev filter. *Amino Acids*, **28**, 373-376.
[29] Lei, Z., Dai, Y. (2005) An SVM-based system for predicting protein subnuclear localizations BMC. *Bioinformatics*, **6**, 291.
[30] Shen, H.B., Chou, K.C. (2005) Predicting protein subnuclear location with optimized evidence-theoretic K-earest classifier and pseudo amino acid composition. *Biochem. Biophys. Res. Comm.*, **337**, 752-756.
[31] Garg, A., Bhasin, M., Raghava, G.P. (2005) Support vector machine-based method for subcellular localization of human proteins using amino acid compositions, their order, and similarity search. *Journal of Biological Chemistry*, **280**, 14427-14432.
[32] Matsuda, S., Vert, J.P., Saigo, H., Ueda, N., Toh, H., Akutsu, T. (2005) A novel representation of protein sequences for prediction of subcellular location using support vector machines. *Protein Sci.*, **14**, 2804-2813.
[33] Gardy, J.L., Laird, M.R., Chen, F., Rey, S., Walsh, C.J., Ester, M., Brinkman, F.S. (2005) PSORTb v.2.0: expanded prediction of bacterial protein subcellular localization and insights gained from comparative proteome analysis. *Bioinformatics*, **21**, 617-623.
[34] Gao, Q.B., Wang, Z.Z., Yan, C., Du, Y.H. (2005) Prediction of protein subcellular location using a combined feature of sequence. *FEBS Letters*, **579**, 3444-3448.
[35] Chou, K.C., Shen, H.B. (2006) Predicting protein subcellular location by fusing multiple classifiers. *Journal of Cellular Biochemistry*, **99**, 517-527.
[36] Guo, J., Lin, Y., Liu, X. (2006) GNBSL: A new integrative system to predict the subcellular location for Gram-egative bacteria proteins. *Proteomics*, **6**, 5099-5105.
[37] Xiao, X., Shao, S.H., Ding, Y.S., Huang, Z.D., Chou, K.C. (2006) Using cellular automata images and pseudo amino acid composition to predict protein subcellular location. *Amino Acids*, **30**, 49-54.
[38] Hoglund, A., Donnes, P., Blum, T., Adolph, H.W., Kohlbacher, O. (2006) MultiLoc: prediction of protein subcellular localization using N-terminal targeting sequences, sequence motifs and amino acid composition. *Bioinformatics*, **22**, 1158-1165.
[39] Lee, K., Kim, D.W., Na, D., Lee, K.H., Lee, D. (2006) PLPD: reliable protein localization prediction from imbalanced and overlapped datasets. *Nucleic Acids Research*, **34**, 4655-4666.
[40] Zhang, Z.H., Wang, Z.H., Zhang, Z.R., Wang, Y.X. (2006) A novel method for apoptosis protein subcellular localization prediction combining encoding based on grouped weight and support vector machine. *FEBS Letters*, **580**, 6169-6174.
[41] Shi, J.Y., Zhang, S.W., Pan, Q., Cheng, Y.-M., Xie, J. (2007) Prediction of protein subcellular localization by support vector machines using multi-scale energy and pseudo mino acid composition. *Amino Acids*, **33**, 69-74.
[42] Chen, Y.L., Li, Q.Z. (2007) Prediction of apoptosis protein subcellular location using improved hybrid approach and pseudo amino acid composition. *Journal of Theoret-*

ical Biology, **248**, 377–381.
[43] Chen, Y.L., Li, Q.Z. (2007) Prediction of the subcellular location of apoptosis proteins. *Journal of Theoretical Biology*, **245**, 775-783.
[44] Mundra, P., Kumar, M., Kumar, K.K., Jayaraman, V.K., Kulkarni, B.D. (2007) Using pseudo amino acid composition to predict protein subnuclear localization: Approached with PSSM. *Pattern Recognition Letters*, **28**, 1610-1615.
[45] Emanuelsson, O., Brunak, S., von Heijne, G., Nielsen, H. (2007) Locating proteins in the cell using TargetP, SignalP and related tools. *Nature Protocols*, **2**, 953-971.
[46] Lin, H., Ding, H., Feng-Biao Guo, F.B., Zhang, A.Y., Huang, J. (2008) Predicting subcellular localization of mycobacterial proteins by using Chou's pseudo amino acid composition. *Protein & Peptide Letters*, **15**, 739-744.
[47] Shi, J.Y., Zhang, S.W., Pan, Q., Zhou, G.P. (2008) Using Pseudo Amino Acid Composition to Predict Protein Subcellular Location: Approached with Amino Acid Composition Distribution. *Amino Acids*, **35**, 321-327.
[48] Li, F.M., Li, Q.Z. (2008) Predicting protein subcellular location using Chou's pseudo amino acid composition and improved hybrid approach. *Protein & Peptide Letters*, **15**, 612-616.
[49] Tantoso, E., Li, X.B. (2008) AAIndexLoc: Predicting Subcellular Localization of Proteins Based on a New Representation of Sequences Using Amino Acid Indices. *Amino Acids*, **35**, 345-353.
[50] Jiang, X., Wei, R., Zhang, T.L., Gu, Q. (2008) Using the concept of Chou's pseudo amino acid composition to predict apoptosis proteins subcellular location: an approach by approximate entropy. *Protein & Peptide Letters*, **15**, 392-396.
[51] Zhou, X.B., Chen, C., Li, Z.C., Zou, X.Y. (2008) Improved prediction of subcellular location for apoptosis proteins by the dual-layer support vector machine. *Amino Acids*, **35**, 383-388.
[52] Ding, Y.S., Zhang, T.L. (2008) Using Chou's pseudo amino acid composition to predict subcellular localization of apoptosis proteins: an approach with immune genetic algorithm-based ensemble classifier. *Pattern Recognition Letters*, **29**, 1887-1892.
[53] Zhang, S.W., Zhang, Y.L., Yang, H.F., Zhao, C.H., Pan, Q. (2008) Using the concept of Chou's pseudo amino acid composition to predict protein subcellular localization: an approach by incorporating evolutionary information and von Neumann entropies. *Amino Acids*, **34**, 565-572.
[54] Jin, Y., Niu, B., Feng, K.Y., Lu, W.C., Cai, Y.D., Li, G.Z. (2008) Predicting subcellular localization with AdaBoost learner. *Protein & Peptide Letters*, **15**, 286-289.
[55] Lin, H., Wang, H., Ding, H., Chen, Y.L., Li, Q.Z. (2009) Prediction of Subcellular Localization of Apoptosis Protein Using Chou's Pseudo Amino Acid Composition. *Acta Biotheoretica*, **57**, 321-330.
[56] Zhang, L., Liao, B., Li, D., Zhu, W. (2009) A novel representation for apoptosis protein subcellular localization prediction using support vector machine. *Journal of Theoretical Biology*, **259**, 361-365.
[57] Zeng, Y.H., Guo, Y.Z., Xiao, R.Q., Yang, L., Yu, L.Z., Li, M.L. (2009) Using the augmented Chou's pseudo amino acid composition for predicting protein submitochondria locations based on auto covariance approach. *Journal of Theoretical Biology*, **259**, 366-72.
[58] Du, P., Cao, S., Li, Y. (2009) SubChlo: predicting protein subchloroplast locations with pseudo-amino acid composition and the evidence-theoretic K-nearest neighbor (ET-KNN) algorithm. *Journal of Theoretical Biology*, **261**, 330-335.
[59] Cai, Y.D., He, J., Li, X., Feng, K., Lu, L., Kong, X., Lu, W. (2010) Predicting protein subcellular locations with feature selection and analysis. *Protein Pept. Lett.*, **17**, 464-472.
[60] Millar, A.H., Carrie, C., Pogson, B., Whelan, J. (2009) Exploring the function-location nexus: using multiple lines of evidence in defining the subcellular location of plant proteins. *Plant Cell*, **21**, 1625-1631.
[61] Chou, K.C., Shen, H.B. (2008) Cell-PLoc: A package of Web servers for predicting subcellular localization of proteins in various organisms. *Nature Protocols*, **3**, 153-162.
[62] Chou, K.C., Shen, H.B. (2007) Euk-mPLoc: a fusion classifier for large-scale eukaryotic protein subcellular location prediction by incorporating multiple sites. *Journal of Proteome Research*, **6**, 1728-1734.
[63] Shen, H.B., Chou, K.C. (2007) Hum-mPLoc: An ensemble classifier for large-scale human protein subcellular location prediction by incorporating samples with multiple sites. *Biochemical and Biophysical Research Communications*, **355**, 1006-1011.
[64] Chou, K.C., Shen, H.B. (2007) Large-scale plant protein subcellular location prediction. *Journal of Cellular Biochemistry*, **100**, 665-678.
[65] Shen, H.B., Chou, K.C. (2007) Gpos-PLoc: An ensemble classifier for predicting subcellular localization of Gram-positive bacterial proteins. *Protein Engineering, Design, and Selection*, **20**, 39-46.
[66] Chou, K.C., Shen, H.B. (2006) Large-scale predictions of Gram-negative bacterial protein subcellular locations. *Journal of Proteome Research*, **5**, 3420-3428.
[67] Shen, H.B., Chou, K.C. (2007) Virus-PLoc: A fusion classifier for predicting the subcellular localization of viral proteins within host and virus-infected cells. *Biopolymers*, **85**, 233-240.
[68] Ashburner, M., Ball, C.A., Blake, J.A., Botstein, D., Butler, H., Cherry, J.M., Davis, A.P., Dolinski, K., Dwight, S.S., Eppig, J.T., Harris, M.A., Hill, D.P., Issel-arver, L., Kasarskis, A., Lewis, S., Matese, J.C., Richardson, J.E., Ringwald, M., Rubin, G.M., Sherlock, G. (2000) Gene ontology: Tool for the unification of biology. *Nature Genetics*, **25**, 25-29.
[69] Chou, K.C. (2005) Using amphiphilic pseudo amino acid composition to predict enzyme subfamily classes. *Bioinformatics*, **21**, 10-19.
[70] Chou, K.C., Shen, H.B. (2010) A new method for predicting the subcellular localization of eukaryotic proteins with both single and multiple sites: Euk-mPLoc 2.0. *PLoS ONE*, **5**, e9931.
[71] Shen, H.B., Chou, K.C. (2009) A top-down approach to enhance the power of predicting human protein subcellular localization: Hum-mPLoc 2.0. *Analytical Biochemistry*, **394**, 269-74.
[72] Chou, K.C., Shen, H.B. (2010) Plant-mPLoc: A top-down strategy to augment the power for predicting plant protein subcellular localization. *PLoS ONE*, **5**, e11335.

[73] Shen, H.B., Chou, K.C. (2009) Gpos-mPLoc: A top-down approach to improve the quality of predicting subcellular localization of Gram-positive bacterial proteins. *Protein & Peptide Letters*, **16**, 1478-1484.
[74] Shen, H.B., Chou, K.C. (2010) Gneg-mPLoc: A top-down strategy to enhance the quality of predicting subcellular localization of Gram-negative bacterial proteins. *Journal of Theoretical Biology*, **264**, 326-333.
[75] Shen, H.B., Chou, K.C. (2010) Virus-mPLoc: A fusion classifier for viral protein subcellular location prediction by incorporating multiple sites. *Journal of Biomolecular Structure & Dynamics*, **28**, 175-186.
[76] Chou, K.C., Zhang, C.T. (1995) Review: Prediction of protein structural classes. *Critical Reviews in Biochemistry and Molecular Biology*, **30**, 275-349.
[77] Fang, Y., Guo, Y., Feng, Y., Li, M. (2008) Predicting DNA-binding proteins: Approached from Chou's pseudo amino acid composition and other specific sequence features. *Amino Acids*, **34**, 103-109.
[78] Feng, Y.E., Luo, L.F. (2008) Use of tetrapeptide signals for protein secondary-structure prediction. *Amino Acids*, **35**, 607-614.
[79] Li, Z.C., Zhou, X.B., Dai, Z., Zou, X.Y. (2009) Prediction of protein structural classes by Chou's pseudo amino acid composition: approached using continuous wavelet transform and principal component analysis. *Amino Acids*, **37**, 415-425.
[80] Nanni, L., Lumini, A. (2008) Genetic programming for creating Chou's pseudo amino acid based features for submitochondria localization. *Amino Acids*, **34**, 653-660.
[81] Wang, Y., Xue, Z., Shen, G., Xu, J. (2008) PRINTR: Prediction of RNA binding sites in proteins using SVM and profiles. *Amino Acids*, **35**, 295-302.
[82] Zhao, X.M., Chen, L., Aihara, K. (2008) Protein function prediction with high-throughput data. *Amino Acids*, **35**, 517-530.
[83] Jahandideh, S., Abdolmaleki, P., Jahandideh, M., Asadabadi, E.B. (2007) Novel two-stage hybrid neural discriminant model for predicting proteins structural classes. *Biophys. Chem.*, 128, 87-93.
[84] Chen, K., Kurgan, L.A., Ruan, J. (2008) Prediction of protein structural class using novel evolutionary collocation-based sequence representation. *Journal of Computational Chemistry*, **29**, 1596-1604.
[85] Jahandideh, S., Sarvestani, A.S., Abdolmaleki, P., Jahandideh, M., Barfeie, M. (2007) Gamma-Turn types prediction in proteins using the support vector machines. *Journal of Theoretical Biology*, **249**, 785-790.
[86] Shao, X., Tian, Y., Wu, L., Wang, Y., L., J., Deng, N. (2009) Predicting DNA- and RNA-binding proteins from sequences with kernel methods. *Journal of Theoretical Biology*, **258**, 289-293.
[87] Yang, J.Y., Peng, Z.L., Yu, Z.G., Zhang, R.J., Anh, V., Wang, D. (2009) Prediction of protein structural classes by recurrence quantification analysis based on chaos game representation. *Journal of Theoretical Biology*, **257**, 618-626.
[88] Anand, A., Suganthan, P.N. (2009) Multiclass cancer classification by support vector machines with class-wise optimized genes and probability estimates. *Journal of Theoretical Biology*, **259**, 533-540.
[89] Chen, C., Chen, L.X., Zou, X.Y., Cai, P.X. (2008) Predicting protein structural class based on multi-features fusion. *Journal of Theoretical Biology*, **253**, 388-392.
[90] Du, P., Li, Y. (2008) Prediction of C-to-U RNA editing sites in plant mitochondria using both biochemical and evolutionary information. *Journal of Theoretical Biology*, **253**, 579-589.
[91] Jahandideh, S., Hoseini, S., Jahandideh, M., Hoseini, A., Disfani, F.M. (2009) Gamma-turn types prediction in proteins using the two-stage hybrid neural discriminant model. *Journal of Theoretical Biology*, **259**, 517-522.
[92] Lin, H. (2008) The modified Mahalanobis discriminant for predicting outer membrane proteins by using Chou's pseudo amino acid composition. *Journal of Theoretical Biology*, **252**, 350-356.
[93] Munteanu, C.B., Gonzalez-Diaz, H., Magalhaes, A.L. (2008) Enzymes/non-enzymes classification model complexity based on composition, sequence, 3D and topological indices. *Journal of Theoretical Biology*, **254**, 476-482.
[94] Rezaei, M.A., Abdolmaleki, P., Karami, Z., Asadabadi, E.B., Sherafat, M.A., Abrishami-Moghaddam, H., Fadaie, M., Forouzanfar, M. (2008) Prediction of membrane protein types by means of wavelet analysis and cascaded neural networks. *Journal of Theoretical Biology*, **254**, 817-820.
[95] Vilar, S., Gonzalez-Diaz, H., Santana, L., Uriarte, E. (2009) A network-QSAR model for prediction of genetic-component biomarkers in human colorectal cancer. *Journal of Theoretical Biology*, **261**, 449-458.
[96] Wang, T., Xia, T., Hu, X.M. (2010) Geometry preserving projections algorithm for predicting membrane protein types. *Journal of Theoretical Biology*, **262**, 208-213.
[97] Chen, Y., Han, K. (2009) BSFINDER: Finding Binding Sites of HCV Proteins Using a Support Vector Machine. *Protein & Peptide Letters*, **16**, 373-382.
[98] Kannan, S., Hauth, A.M., Burger, G. (2008) Function prediction of hypothetical proteins without sequence similarity to proteins of known function. *Protein & Peptide Letters*, **15**, 1107-1116.
[99] Nanni, L., Lumini, A. (2009) A Further Step Toward an Optimal Ensemble of Classifiers for Peptide Classification, a Case Study: HIV Protease. *Protein & Peptide Letters*, **16**, 163-167.
[100] Gu, F., Chen, H. (2009) Evaluating Long-term Relationship of Protein Sequence by Use of d-Interval Conditional Probability and its Impact on Protein Structural Class Prediction. *Protein Pept. Lett.*, **16**, 1267-1276.
[101] Ji, G., Wu, X., Shen, Y., Huang, J., Quinn Li, Q. (2010) A classification-based prediction model of messenger RNA polyadenylation sites. *Journal of Theoretical Biology*, **265**, 287-296.
[102] Yang, X.Y., Shi, X.H., Meng, X., Li, X.L., Lin, K., Qian, Z.L., Feng, K.Y., Kong, X.Y., Cai, Y.D. (2010) Classification of transcription factors using protein primary structure. *Protein & Peptide Letters*, **17**, 899-908.
[103] Gu, Q., Ding, Y.S., Zhang, T.L. (2010) Prediction of G-Protein-Coupled Receptor Classes in Low Homology Using Chou's Pseudo Amino Acid Composition with Approximate Entropy and Hydrophobicity Patterns. *Protein Pept. Lett.*, **17**, 559-567.
[104] Liu, L., He, D., Yang, S., Xu, Y. (2010) Applying chemometrics approaches to model and predict the binding

affinities between the human amphiphysin SH3 domain and its peptide ligands. *Protein Pept. Lett.*, **17**, 246- 253.
[105] Shi, R., Hu, X. (2010) Predicting enzyme subclasses by using support vector machine with composite vectors. *Protein Pept. Lett.*, **17**, 599-604.
[106] Wang, T., Yang, J. (2010) Predicting subcellular localization of gram-negative bacterial proteins by linear dimensionality reduction method. *Protein Pept. Lett.*, **17**, 32-37.
[107] Yang, J., Jiang, X.F. (2010) A novel approach to predict protein-protein interactions related to Alzheimer's disease based on complex network. *Protein Pept. Lett.*, **17**, 356-366.
[108] Chou, K.C., Shen, H.B. (2006) Hum-PLoc: A novel ensemble classifier for predicting human protein subcellular localization. *Biochemical and Biophysical Research Communications*, **347**, 150-157.
[109] Chou, K.C., Shen, H.B. (2006) Predicting eukaryotic protein subcellular location by fusing optimized evidence-theoretic K-nearest neighbor classifiers. *Journal of Proteome Research*, **5**, 1888-1897.
[110] Chou, K.C., Shen, H.B. (2007) Review: Recent progresses in protein subcellular location prediction. *Analytical Biochemistry*, **370**, 1-16.
[111] Small, I., Peeters, N., Legeai, F., Lurin, C. (2004) Predotar: A tool for rapidly screening proteomes for N-terminal targeting sequences. *Proteomics*, **4**, 1581-1590.
[112] Camon, E., Magrane, M., Barrell, D., Binns, D., Fleischmann, W., Kersey, P., Mulder, N., Oinn, T., Maslen, J., Cox, A., Apweiler, R. (2003) The gene ontology annotation (GOA) project: Implementation of GO in SWISS- PROT, TrEMBL, and InterPro. *Genome Res.*, **13**, 662-672.
[113] Barrell, D., Dimmer, E., Huntley, R.P., Binns, D., O'Donovan, C., Apweiler, R. (2009) The GOA database in 2009-an integrated Gene Ontology Annotation resource. *Nucleic Acids Research*, **37**, D396-403.
[114] Marchler-Bauer, A., Anderson, J.B., Derbyshire, M.K., DeWeese-Scott, C., Gonzales, N.R., Gwadz, M., Hao, L., He, S., Hurwitz, D.I., Jackson, J.D., Ke, Z., Krylov, D., Lanczycki, C.J., Liebert, C.A., Liu, C., Lu, F., Lu, S., Marchler, G.H., Mullokandov, M., Song, J.S., Thanki, N., Yamashita, R.A., Yin, J.J., Zhang, D., Bryant, S.H. (2007) CDD: A conserved domain database for interactive domain family analysis. *Nucleic Acids Research*, **35**, D237-D240.

Vol.2, No.10, 1104-1112 (2010)
doi:10.4236/ns.2010.210137

Natural Science

Evolution based on genome structure: the “diagonal genome universe”

Kenji Sorimachi

Educational Support Center, Dokkyo Medical University, Mibu, Japan; kenjis@dokkyomed.ac.jp.

Received 13 July 2010; revised 16 August 2010; accepted 20 August 2010.

ABSTRACT

The ratios of amino acid to the total amino acids and those of nucleotides to the total nucleotides in genes or genomes are suitable indexes to compare whole gene or genome characteristics based on the large number of nucleotides rather than their sequences. As these ratios are strictly calculated from nucleotide sequences, the values are independent of experimental errors. In the present mini-review, the following themes are approached according to the ratios of amino acids and nucleotides to their total numbers in the genome: prebiotic evolution, the chronological precedence of protein and codon formations, genome evolution, Chargaff’s second parity rule, and the origins of life. Amino acid formation might have initially occurred during prebiotic evolution, the “amino acid world”, and amino acid polymerization might chronologically precede codon formation at the end of prebiotic evolution. All nucleotide alterations occurred synchronously over the genome during biological evolution. After establishing primitive lives, all nucleotide alterations have been governed by linear formulae in nuclear and organelle genomes consisting of the double-stranded DNA. When the four nucleotide contents against each individual nucleotide content in organelles are expressed by four linear regression lines representing the diagonal lines of a 0.5 square – the “Diagonal Genome Universe”, evolution obeys Chargaff’s second parity rule. The fact that linear regression lines intersect at a single point suggests that all species originated from a single life source.

Keywords: Evolution (Prebiotic and Biological); Genome; Origin of Life; Chargaff’s Parity Rules; Organelle; Double- and Single-Strand DNA; Amino Acid; Nucleotide; Linear Formula

1. INTRODUCTION

“The Origin of Species”, written from the observations Charles Darwin made during his voyage on the HMS Beagle, was published in 1859. According to Darwin’s theory, all species have a common ancestor and a single origin. During the same period when Darwin wrote, Gregor Mendel reported “Mendel’s laws” that accorded with his observations of the inheritance of certain traits in pea plants. The former and latter are based on inter- and intra-species phenotypic expression similarities, respectively, and based on long and comparatively short lifespans, respectively. In general, interspecies changes are thought of as “evolution”, while intraspecies changes are “genetics”. These two great concepts were established by two scientists without any knowledge of DNA; although nowadays it is well known that almost all traits of organisms are based on gene characteristics. After almost a century, Oswald Avery and coworkers reported in 1944 that DNA is the material of genes and chromosomes [1].

Although it was clarified by Avery’s group that DNA is important material for the inheritance of certain traits in organisms, the structure of DNA, which has an extremely large molecular weight, was completely unknown and, therefore, the mechanisms of trait inheritance were also unknown. On the other hand, Ervin Chargaff reported in 1950 that nuclear DNA consists of four nucleotides, and that the nucleotide content relationships are: G = C, A = T, and [(G + A) = (C + T)]. This rule is well known as Chargaff’s first parity rule [2]. He and his colleagues later discovered that these relationships are applicable to the single DNA strand, and this is Chargaff’s second parity rule [3]. After Chargaff’s first parity rule, another great scientific discovery was reported in 1953 by Watson and Crick [4]. Namely, that the DNA structure is double-stranded, and C vs. G and T vs. A pairs are formed between two DNA strands. These two base-pair formations can consistently explain the inheritance of genetic traits from generation to generation. Even though this DNA structure can explain Char-

gaff's first parity rule, the second parity rule based on the single DNA strand cannot be explained by the double-stranded DNA model. Chargaff's parity rules were originally discovered from a single species and recently it was shown that Chargaff's second parity rule is applicable to interspecies evolution [5]. Nuclear nucleotide relationships were clearly expressed by linear regression lines with extremely high regression coefficients among various species. The single DNA strand which forms the double-stranded DNA has been shown, based on the huge amount of genomic data, to obey Chargaff's second parity rule [5]. Furthermore, as nucleotide relationships in the coding region are also expressed by linear formulae, 64 codons can be correctly estimated from just one nucleotide content [6].

Molecular clock research—using amino acid or nucleotide replacement rates [7] has enabled scientists to create a phylogenetic tree representing biological evolution [8-12]. However, as this method is based on sequences of certain genes among various organisms, we cannot investigate organisms without these genes. Furthermore, this method does not fit the research on whole genomes consisting of an extremely large number of nucleotides. On the other hand, by using the ratios of nucleotides to the total nucleotides or amino acids to the total amino acids after normalization, it is possible to compare certain characteristics among different genes or genomes. As this method is independent not only of sample size but also of species, the method can be recommended for comparative studies on genomes consisting of extremely large and different numbers of nucleotides. Using normalized values, each organism can be represented by simple indexes that represent whole genome characteristics. In fact, this method has been applied to genome research and its usefulness proven by using graphic representation or a diagram approach [13]. Visualization to study complicated biological systems can provide an intuitive picture and provide useful insights [14-16].

2. PREBIOTIC EVOLUTION

We have no evidence of "the origin of life", although there are two distinct ideas: one being that the origin of life was on the primitive Earth and the other that it was derived from another planet (extraterrestrial universe). Based on either idea, "the origin of life" did indeed occur somewhere after the "Big Bang". Many physical and chemical reactions occurred during prebiotic evolution and substantial materials for the formation of primitive life may have accumulated during this period. For example, Miller's experiment showed that amino acids could be formed by electric discharges in the atmosphere on the primitive Earth [17]. Furthermore, amino acids have been detected in meteorites [18,19]. Accumulation of amino acids might lead to the appearance of amino acid polymers or peptides without the codon system. As well, certain polymers or peptides might have enzyme activity that accelerates amino acid polymerization, which is reported as being able to occur in soil via heat without either enzyme or codon system [20]. The production of enzymes led to the accumulation of substantial materials for "the origin of life".

Amino acid polymers formed chemically might reflect the amino acid concentrations on the primitive Earth. Sueoka initially investigated the cellular amino acid composition of bacteria [21] and then we independently examined, not only bacterial but also plant and animal cells [22,23]. Based on amino acid composition patterns, it is clearly shown that cellular amino acid composition is very similar among organisms from bacteria to *Homo sapiens* [22], as shown in **Figure 1**. This fact led us to conclude that primitive life forms might have similar amino acid composition presumed from present organisms [24]. Based on an amino acid pattern (**Figure 1**), the ratios of the amino acids that have ultraviolet (UV) absorbance (*i.e.*, phenylalanine, tyrosine and tryptophan) to the total cellular amino acids are very low. To explain this fact, the strong irradiation of UV light might have induced their decomposition and reduced their concentration on the primitive Earth. However, the contents of glycine and alanine, which were formed easily in Miller's experiment, are relatively high [22]. In addition, the contents of hydrophobic amino acids such as leucine, isoleucine, alanine and valine are comparatively high. These amino acids might contribute to self-aggregation of amino acid polymers to form the "coacervate" proposed by Aleksandr Oparin through their hydrophobicity under low polymer concentrations.

The basic pattern of cellular amino acid compositions,

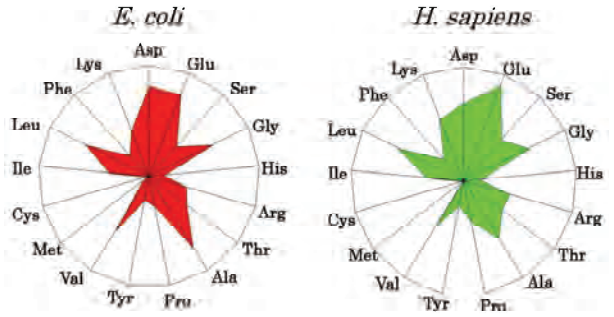

Figure 1. Cellular amino acid compositions of *Escherichia coli* and *Homo sapiens* on radar charts. Amino acid compositions are expressed as the percentage of total amino acids. Gln and Asn are combined with Glu and Asp, respectively, because the former two are converted to the latter two during hydrolysis [22].

the "star-shape", is formed with characteristic differences in amino acid contents. The fact that the basic pattern is conserved from bacteria to *Homo sapiens*, suggests that the pattern is extremely important for organisms on earth. It would be quite interesting to evaluate whether this "star-shape" is conserved on other planets with life in the future, if any is found.

3. CHRONOLOGICAL PRECEDENCE OF PROTEIN AND CODON FORMATION

Evolutionarily, it remains unclear whether protein formation preceded codon formation or codon formation preceded that of protein. However, it should be possible to judge which theory is better at explaining this theme, though it might be impossible to design a complete experiment. Amino acids, which are monomers of proteins or peptides, were easily formed by electric discharges in an atmosphere presumed from the primitive Earth [17]. In addition, their polymerizations took place in clay without the codon system [20] and certain products, protein or peptides, might possess an enzymatic activity which accelerates amino acid polymerizations. Eventually, these processes might produce various biomaterials, such as amino acids and their polymers, whereas the production of nucleic acids whose formation requires nitrogenous base and sugar synthesis, their coupling and condensation, might be difficult in the primitive Earth. Although the so-called "RNA world" has been proposed [25], the possibility of the accumulation of RNA, which has UV absorbance at around 250 nm, might be very low under the strong UV irradiation present on the primitive Earth. In general, the composition of polymerization products depends on monomer concentrations and reflects their free concentration on the primitive Earth, as mentioned above.

Simulation analysis based on random choice of amino acids showed consistent results in which amino acids were polymerized randomly without the codon system [26]. The amino acid composition obtained by a random choice of amino acids from the amino acid pool reflects each amino acid concentration in the pool. After establishing the codon system, the sequence information has been conserved until now. On the other hand, polymerization of nucleotides based on the random choice of nucleotides does not yield functional proteins [26]. Even when the codon table is considered for nucleotide polymer formation, the amino acid composition depends on the original four nucleotide contents. The nucleotide compositions differ between the coding and non-coding regions, while they are quite similar among the coding or non-coding regions [6,27,28]. Thus, the coding fragments that possessed the same characteristics might be combined through the non-coding fragments with each other like a "patchwork" in the whole genome. This structural model fits the proposed model that the formation of proteins might have preceded codon formation. At present, even though there is no experimental evidence for the process of how sequence information of amino acid polymers transfers to codon formation during a codon establishing period, protein formation might precede codon formation based on the present genome structure [26].

4. HOMOGENEITY OF GENOME STRUCTURE

The amino acid sequences of proteins differ, not only among different genes, but also among different species, and naturally, their nucleotide sequences also differ. As these differences relate to evolutionary time [7], this concept has been applied to draw phylogenetic trees [8-12]. Using the ratios of each amino acid to the total amino acids, or those of each nucleotide to the total nucleotides, it is possible to compare samples independently regarding size, kind and species, even though DNA has an extremely large number of nucleotides.

The method to analyze nucleotide sequences was established by Frederic Sanger [29], and Allan Maxam and Walter Gilbert [30], and the first complete genome analysis was carried out on *Haemophilus influenzae* in 1995 [31]. Then the complete genome analyses of species such as human (*Homo sapiens*) [32,33], mouse (*Mus musculus*) [34], rat (*Rattus norvegicus*) [35] and sea urchin (*Strongylocentrotus purpuratus*) [36] were carried out within the last two decades. Several species of Archaea were also examined and their complete genomes were determined. Based on these intriguing results, the amino acid compositions were presumed from the complete genomes. Surprisingly, the cellular amino acid compositions obtained from the whole cell lysates resemble those presumed from the complete genome [24], although the former is based on a different protein mixture and the latter is based on a different gene mixture. The coincidence of these two results in our study was not explainable until the genomic structure was fully understood [37].

The full sequence of mouse cDNA was determined in 2001 [38]. The total number of mouse cDNAs includes 10,465 genes and was divided into two equal parts and the amino acid compositions presumed from the first 5, 10, 50, 100, 500, 1,000 and 5,232 genes, according to the order listed in the data table, were compared between the two parts and within the same parts (**Figure 2**). The amino acid compositions of gene assemblies resembled those presumed from the complete genome. Of course,

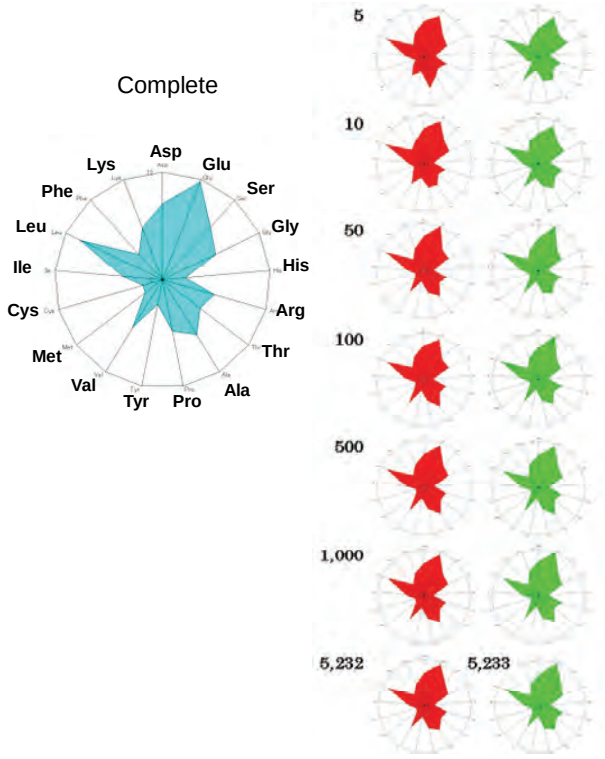

Figure 2. Amino acid compositions. Computational amino acid sequences (10,465) of FANTOM clones were divided into two equal parts; first (red) and latter (green) halves. In both parts, the first 5, 10, 50, 100, 500 and 1,000 genes were used for analyses of amino acid compositions for the units. The numbers of genes were 5,232 and 5, 233 in the first and second halves, respectively. The left side graph shows the amino acid composition based on 10,465 genes [38].

the amino acid compositions presumed from genes differ among various genes. Therefore, the genome structure is constructed homogeneously with certain similar units that encode similar amino acid compositions. The consistent result was obtained from the complete Archaeal genome (*Methanobacterium thermoautotrophicum*) [39], as shown in **Figure 3**.

When the amino acid composition presumed from the complete genome is expressed by the radar chart, the amino acid composition patterns based on a small segment, encoding 3,000-7,000 amino acid residues, represent the pattern based on the complete genome, as shown in **Figures 2** and **3**. The consistent result was obtained using the nucleotide composition [40] as well as amino acid composition of the *Saccharomyces cerevisiae* genome [37]. Additionally, the genome structure resembles the appearance of a "pearl necklace" (**Figure 4**). Based on this model, the genome is constructed with almost the same putative small units, encoding 3,000-7,000 amino acid residues, over the entire genome. This fact indicates that all nucleotide alterations occurred synchronously over the genome. In addition, based on this fact, the coincidence between the cellular amino acid composition

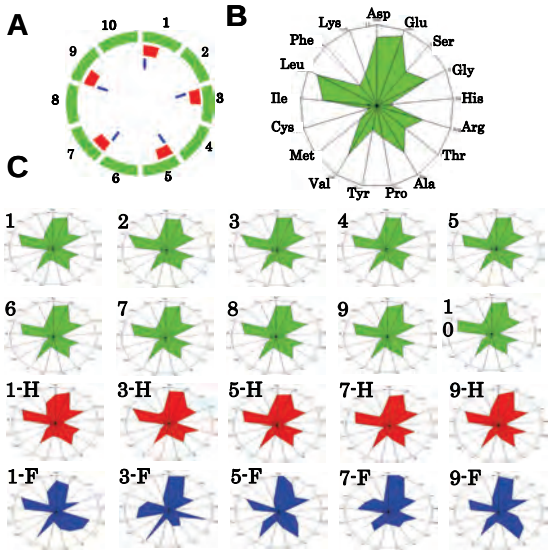

Figure 3. Radar charts of amino acid compositions calculated from various units of the complete genome of *Methanobacterium thermoautotrophicum*. **A**, the complete *M. thermoautotrophicum* genome consisting of 1,869 protein genes [39] was divided into 10 or 20 units. Ten units (1-10); based on 186 and 195 genes, half size units (1-H-9-H); based on 93 genes, single genes (1-F-9-F); based on the first single gene of each unit. Glutamine and asparagine were calculated as glutamic acid and aspartic acid, respectively, and tryptophan (< 1%) was omitted in the radar charts [22].

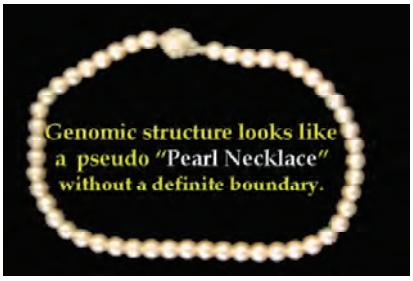

Figure 4. Model for homogeneous genome structure: a "pearl necklace" model.

obtained from cell lysates and that presumed from the complete genomes can be explained because each gene characteristics are cancelled in certain units in both different analytical systems. The genome homogeneity makes it possible to characterize the genome by the ratios of nucleotide to the total nucleotides and/or those of amino acid values. In fact, bacteria [41] and other organisms such as Archaea and eukaryotes [42] were classified based on these values. Organisms were classified into "GC-type equal to E-type" and "AT-type equal to S-type" represented by high G or C (low T or A), and high A or T (low G or C) contents, respectively, at every third codon position [42]. Similar conclusion was obtained from research that examined the content of G + C in a large number of genes [43]. Bacterial classification was carried out by another method with similar results

[44].

5. GENOME EVOLUTION

All organism's DNA consists of four nucleotides such as G, C, T and A, and it is possible to simulate their contents by a random choice of certain numbers [45]. In addition, the relationships of the four nucleotide contents can be mathematically expressed by linear formulae whether or not the four values correlate to each other. Based on the random choice of nucleotide contents, their relationships are heteroskedastic, although nucleotide content distributions are homogeneous [45]. On the other hand, for example, when plotting four nucleotide contents against certain nucleotide content in the complete chloroplast genome, their relationships were expressed by four linear regression lines with high regression coefficients [28], as shown in **Figure 5**. The lines G and C overlap, and the lines T and A overlap. This indicates that G = C and T = A in chloroplast DNA. Thus, chloroplast genome evolution is governed by Chargaff's second parity rule. Plant mitochondrial evolution was also governed by this rule, while animal mitochondrial evolution deviated from the rule [28]. These organelles were incorporated into only eukaryotes, which appeared evolutionarily later than bacteria. The contents of G or C were less than 0.25 and those of A or T were more than 0.25 [28], as shown in **Figure 5**. Thus, nucleotide contents are biased in organelle DNA because of a shorter evolutionary period compared with nuclear DNA.

6. CHARGAFF'S PARITY RULES

Chargaff's first parity rule was obtained experimentally in 1950 and the rule represents intraspecies: G = C, A = T and [(G + A) = (C + T)]. Nowadays we know that nuclear DNA structure is double-stranded [4] and the first parity rule is easily understandable. However, the second parity rule, which is applicable to the single DNA strands forming the double-stranded DNA, has been an enigma of how to make the base pairs in the single DNA strand since being published in 1968 [3]. Recently, this puzzle has been solved mathematically [46] based on genome structure homogeneity [37,40] and similarity between the forward and reverse strands [6]. To solve this puzzle, however, the double-stranded structure was necessary [46], as shown in **Figure 6**. This fact indicates that the genome structure might be double-stranded at the stage of primitive life. Both rules are intraspecies rules.

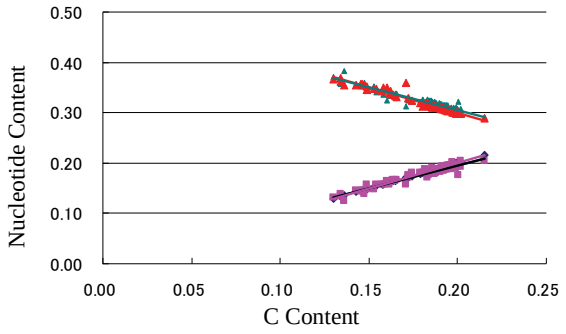

Figure 5. Nucleotide content relationships in chloroplasts. Four nucleotide contents were expressed by C content. Pink squares, C; blue diamonds, G; red triangles, T and green triangles, A. This figure has been presented in *Natural Science*, 2(5); 519-525, 2010 and reproduced with permission.

Mitchell and Bridge examined a large number of complete genomes to determine whether Chargaff's second parity rule was applicable to interspecies relationships [5] and concluded that only the single DNA strand forming the double-stranded DNA is applicable to the second parity rule [5]. This fact indicates that Chargaff's second parity rule is clearly correlated to biological evolution. In addition, although codon evolution within the coding region is expressed by a linear formula, it deviates from Chargaff's second parity rule [6]. However, when plotting nucleotide contents in the coding or non-coding region agafinst nucleotide content in the complete single DNA strand, genome evolution obeys Chargaff's second parity rule [28], as shown in **Figure 7**.

Nucleotide content relationships in the coding or non-coding regions against the nucleotide content in the complete single DNA strand between chloroplast and plant mitochondria are expressed by different regression lines [27]. According to this plotting manner, linear regression lines between chloroplast and plant mitochondria intersect forming the "V-shape" [27], and similarly, linear regression lines between the coding and non-coding regions intersect forming the "V-shape" [27]. These two cases clearly indicate that chloroplast and plant mitochondria, and the coding and non-coding regions descended from similar origins.

Furthermore, when the four nucleotide contents are

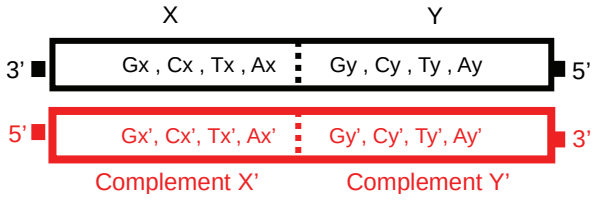

Figure 6. Double-stranded DNA model. The complete genome was divided into two fragments [46]. The contents of Gx and Cx in the fragment X are expressed via the reverse (complementary) strand by Cy and Gy, respectively, because (Gx ≈ Gy' = Cy) and (Cx ≈ Cy' = Gy). Therefore, (Gx + Gy ≈ Gx + Cx) and (Cx + Cy ≈ Cx + Gx). In both equations, as the right hand side is equal, Gx + Gy ≈ Cx + Cy. Finally, G ≈ C. Similarly, T ≈ A.

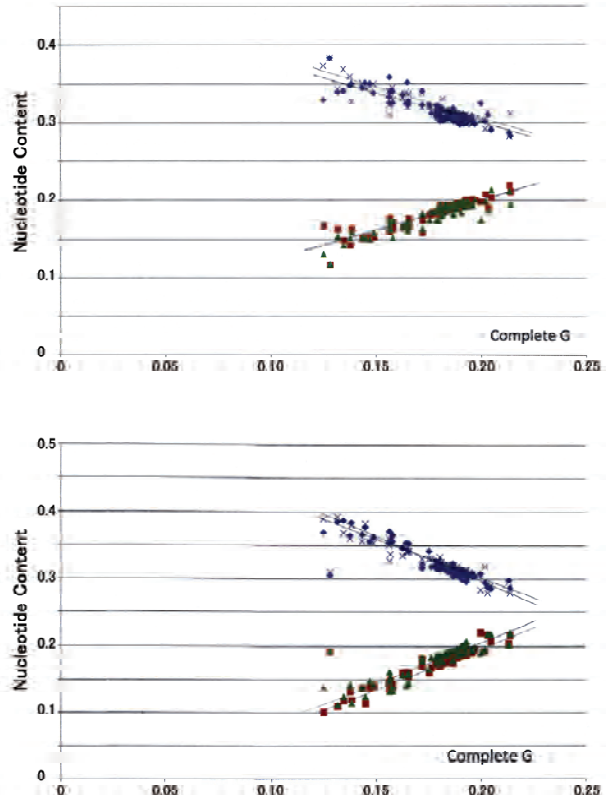

Figure 7. Nucleotide relationships in normalized chloroplast values. Upper panel, coding region; lower panel, non-coding region. Red squares, G; green triangles, C; blue diamonds, A; and shallow blue crosses, T. The composition of each nucleotide in the coding or non-coding region was plotted against the G content in the complete single DNA strand. The vertical axis represents the composition of the four nucleotides; the horizontal axis represents the G content in the complete single DNA strand. This figure has been presented in *Natural Science* 2; 2010 and is reproduced with permission.

plotted against the total nucleotide content among various species, linear regression lines with high regression coefficients are obtained: Using the normalized values, G + C + A + T = 1, Chargaff's parity rule is alternated as follows: 2G + 2A = 1, A = 0.5 – G, T = 0.5 – G, C = G and (G = G). The lines G and C overlap and the lines A and T overlap, and the former is line symmetrical to the latter against a line (y = 0.25), as shown in **Figure 8**. Namely, four nucleotide contents expressing by two duplicate nucleotide contents can be expressed by only one nucleotide content with linear formulae, as shown in **Figure 8**. The two duplicate nucleotide contents (G or C and A or T) are symmetrical. These formulae do not possess any obvious factor that is based on "Natural Selection" proposed by Charles Darwin. This fact clearly indicates that "Natural Selection" might contribute to biological evolution after genome alterations. According to Chargaff's second parity rule, the intercepts of the lines G and C are close to the origin, while those of the lines A and T are close to 0.5 at the vertical and horizontal axes. The slopes of the lines G and C, and those of A and T are 1 and − 1, respectively. All organisms from bacteria to *Homo sapiens* are located on the diagonal lines of a 0.5 square-the "Diagonal Genome Universe", using the normalized values. These formulae are not obtained from a simulation analysis using a random choice of nucleotide contents assumed to be organism nucleotide contents [45]. In this case, the nucleotide relationships are completely heteroskedastic and Chargaff's second parity rule has not been satisfied. The line A overlaps with the line T, and the line G overlaps with the line C [47]. The former overlapped line intersects with the latter overlapped line at 0.25 [47]. Thus, the exchanges of G and C or A and T never take place, while the exchanges of G or C with T or A must take place synchronously, not only within the putative small unit, but also over the entire genome according to Chargaff's second parity rule. The pair of two duplicate points, G = C and A = T, are symmetrical around y = 0.25, as shown in **Figure 8**. As a result of the synchronous nucleotide alterations over the genome, the structure of the genome has become homogeneous. Samples that are applicable to Chargaff's parity rules must satisfy these conditions. Thus, all nucleotide alterations are strictly controlled, not only by the total homo-nucleotide contents and their analog contents, but also by the total hetero-nucleotide and their analog contents, in the complete single DNA strand under Chargaff's second parity rule [28]. In animal mitochondrial evolution, which deviates from the rule, nucleotide alterations are strictly controlled by just

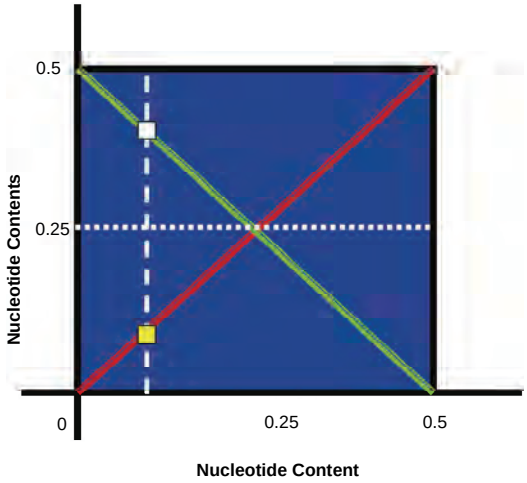

Figure 8. The "Diagonal Genome Universe". Plotting four nucleotide contents normalized to 1 against certain nucleotide content (*i.e.*, G or C content), G and G contents are expressed by (G = G) and (G = C), respectively, and T and A contents are expressed by (T = 0.5 – G) and (A = 0.5 – G), respectively. For example, if G = 0.1 (white dashed line), C = 0.1, T = 0.4 and A = 0.4. White open square, A or T; yellow closed square, C or G. White dotted line represents the line of symmetry (y = 0.25). Similarly, plotting nucleotide contents against T of A content, (T = T), (T = A), (C = 0.5 – T or A) and (G = 0.5 – T or A) are obtained.

homo-nucleotides and their analog total contents [28].

7. ORIGIN OF LIFE

Four nucleotide relationships within the coding or non-coding regions are linear; however, Chargaff's second parity rule is not satisfied [6]. On the other hand, when plotting nucleotide contents in the coding or non-coding regions against the nucleotide content in a complete single DNA strand, their relationships are expressed by linear regression lines with high regression coefficients in nuclear, chloroplast and plant mitochondrial DNA [27]. Furthermore, Chargaff's second parity rule is satisfied in both coding and non-coding regions of these DNA strands [28]. In animal mitochondrial DNA, strong regulation is observed in homo- and their analog nucleotide relationships in both coding and non-coding regions [27,28]. Mitchell and Bridge reported that the four nucleotide relationships in organelle DNA were heteroskedastic [5], while Nikolaou and Almirantis reported that mitochondria should be classified into three groups, and that chloroplast genome evolution resembled bacterial genome evolution [48]. It has been shown that classification of organelles into chloroplast, plant mitochondria, vertebrate mitochondria, invertebrate I mitochondria and invertebrate II mitochondria, makes it possible to express their genome evolution by linear formulae [47]. Thus, in respect to complete genome evolution, it is clear that all nucleotide alterations are expressed by linear formulae: y = ax + b, where "y" and "x" represent nucleotide contents, and "a" and "b" are constant values representing alteration rates and initial nucleotide contents, respectively.

When evolutionary processes are expressed by the same regression line, these evolutionary processes must be controlled by the same rule. Therefore, the fact that two linear regression lines intersect at the top of the "V-shape" indicates that the two groups diverged from the same single origin (**Figure 9(a)**). Classifying invertebrate mitochondria into two groups, I and II, two linear regression lines based on nucleotide relationships intersect forming the "V-shape" [47]. Furthermore, as mitochondria and chloroplast are derived from proteobacteria [49] and cyanobacteria [50], respectively, their regression lines intersected at a point [47]. As the origin of these organelles appears to be from bacteria, their regression lines must intersect at a point [47]. The fact that many lines intersect at the same point indicate that many groups diverged from a single origin (**Figure 9(b)**). On the other hand, many parallel regression lines indicate that there are many origins (**Figure 9(c)**), and the existence of many crossing points (**Figure 9(d)**) also indicates the existence of many origins. However, when all evolutionary processes obey the same rule, the number

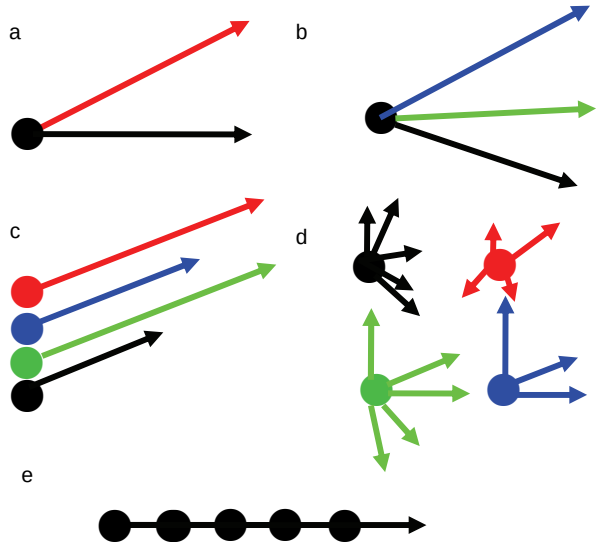

Figure 9. Assumed numbers(s) of origin of life based on nucleotide regression lines. **(a)** and **(b)**, single origin of life; **(c)**, **(d)** and **(e)**, multiple origins of life. Closed circles represent the origin of life.

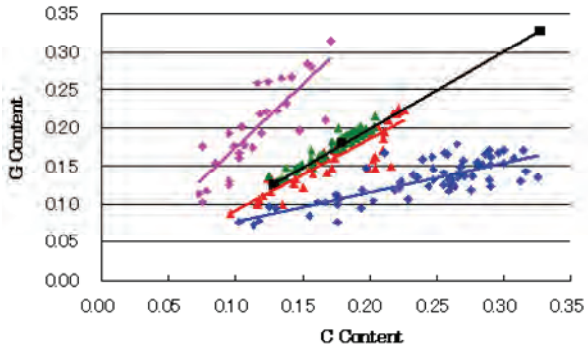

Figure 10. C content (horizontal axis) and G content (vertical axis) in nuclei and various organelles. Blue diamonds, invertebrate I and vertebrate mitochondria; pink diamonds, invertebrate II mitochondria; red squares, plant mitochondria; green triangles, chloroplasts; and black squares, nuclei. This figure has been presented in *Natural Science*, 2(5); 519-525, 2010 and reproduced with permission.

of origins cannot be determined (**Figure 9(e)**). When plotting nucleotide contents against each individual nucleotide content, linear regression lines intersect at a single point among nuclear, chloroplast and mitochondrial DNA [47], as shown in **Figure 10**. This fact clearly indicates that the origin of all species is a single life form [47]. This is the first demonstration that all species have a common ancestor and a single origin based on scientific data. Charles Darwin discussed on the evolution over the course of generation through a presence of natural selection in "On the Origin of Species by Means of Natural Selection or the Preservation of Favoured Races", while he discussed on neither "a single origin" nor "a common ancestor" of species. This concept has been presumed from Darwin's theory since being pub-

lished in 1859, and eventually phylogenetic trees, which have been drawn, represent apparently a single origin of species.

8. CONCLUSIONS

Evolution of all species, from bacteria to *Homo sapiens*, is governed by genome alterations based on simple linear formulae, including Chargaff's second parity rule, although their phenotypic expressions show immeasurable spectra over the past 3.5 billion years. Evolution based on genome alterations can be represented by two lines (G or C and A or T) that are symmetrical about y = 0.25 – the "Diagonal Genome Universe".

9. ACKNOWLEDGEMENTS

The author expresses his great thanks to Prof. Kuo-Chen Chou, Editor-in-Chief of *Natural Science*, for the opportunity to present this mini-review.

REFERENCES

[1] Avery, O.T., Macleod, C.M. and McCarty, M. (1944) Studies on the chemical nature of the substance inducing transformation of pneumococcal types: Induction of transformation isolated from pneumococcus type III. *Journal of Experimental Medicine*, **79(2)**, 137-158.

[2] Chargaff, E. (1950) Chemical specificity of nucleic acids and mechanism of their enzymatic degradation. *Experimentia*, **6(6)**, 201-209.

[3] Rudner, R., Karkas, J.D. and Chargaff, E. (1968) Separation of *B. subtilis* DNA into complementary strands. 3. Direct analysis. *Proceedings of the National Academy of Science*, **60(3)**, 921-922.

[4] Watson, J.D. and Crick, F.H.C. (1953) Genetical implications of the structure of deoxyribonucleic acid. *Nature*, **171(4361)**, 964-967.

[5] Mitchell, D. and Bridge, R. (2006) A test of Chargaff's second rule. *Biochemical and Biophysical Research Communications*, **340(1)**, 90-94.

[6] Sorimachi, K. and Okayasu, T. (2008) Codon evolution is governed by linear formulas. *Amino Acids*, **34(4)**, 661-668.

[7] Zuckerkandl, E. and Pauling, L.B. (1962) Molecular disease, evolution, and genetic heterogeneity. In: Kasha, M. and Pullman, B. Ed., *Horizons in Biochemistry*, New York Academic, New York, 189-225.

[8] Dayhoff, M.O., Park, C.M. and McLaughlin, P.J. (1977) Building a phylogenetic trees: Cytochrome C. In: Dayhoff, M.O. Ed., *Atlas of protein sequence and structure*, National Biomedical Foundation, Washington, D.C., **5**, 7-16.

[9] Sogin, M.L., Elwood, H.J. and Gunderson, J.H. (1986) Evolutionary diversity of eukaryotic small subunit rRNA genes. *Proceedings of the National Academy of Sciences*, **83(5)**, 1383-1387.

[10] DePouplana, L., Turner, R.J., Steer, B.A. and Schimmel, P. (1998) Genetic code origins: tRNAs older than their synthetases? *Proceedings of the National Academy of Sciences*, **95(19)**, 11295-11300.

[11] Doolittle, W.F. and Brown, J.R. (1994) Tempo, mode, the progenote, and the universal root. *Proceedings of the National Academy of Sciences*, **91(15)**, 6721-6728.

[12] Maizels, N. and Weiner, A.M. (1994) Phylogeny from function: Evidence from the molecular fossil record that tRNA originated in replication, not translation. *Proceedings of the National Academy of Sciences*, **91(15)**, 6729-6734.

[13] Sorimachi, K. (2009) Evolution from primitive life to *Homo sapiens* based on visible genome structures: The amino acid world. *Natural Science*, **1(2)**, 107-119.

[14] Chou, K.-C. and Zhang, C.T. (1992) Diagrammatization of codon usage in 339 HIV proteins and its biological implication. *AIDS Research and Human Retroviruses* **8(12)**, 1967-1976.

[15] Zhang, C.-T. and Chou, K.-C. (1993) Graphic analysis of codon usage strategy in1490 human proteins. *Journal of Protein Chemistry*, **12(3)**, 329-335.

[16] Qi, X.Q., Wen, J. and Qi, Z.H. (2007) New 3D graphical representation of DNA sequence based on dual nucleotides. *Journal of Theoretical Biology*, **249(4)**, 681-690.

[17] Miller, S.L. (1953) Production of amino acids under possible primitive earth conditions. *Science*, **117(3046)**, 528-529.

[18] Kvenvolden, K., Lawless, J., Pering, K., Peterson, E., Flores, J., Ponnamperuma, C., Kaplan, I.R. and Moore, C. (1970) Evidence for extraterrestrial amino-acids and hydrocarbons in the Murchison meteorite. *Nature*, **228(5275)**, 923-926.

[19] Wolman, Y., Haverland, W. and Miller, S.L. (1972) Nonprotein amino acids from spark discharges and their comparison with the Muchison meteorite amino acids. *Proceedings of the National Academy of Sciences*, **69(4)**, 809-811.

[20] Lahav, N., White, D. and Chang, S. (1978) Peptide formation in the prebiotic era: Thermal condensation of glycine in fluctuating clay environments. *Science*, **201(4350)**, 67-69.

[21] Sueoka, N. (1961) Correlation between base composition of deoxyribonucleic acid and amino acid composition in proteins. *Proceedings of the National Academy of Sciences*, **47(8)**, 1141-1149.

[22] Sorimachi, K. (1999) Evolutionary changes reflected by the cellular amino acid composition. *Amino Acids*, **17(2)**, 207-226.

[23] Sorimachi, K., Okayasu, T., Akimoto, K. and Niwa, A. (2000) Conservation of the basic pattern of cellular amino acid composition during biological evolution in plants. *Amino Acids*, **18(2)**, 193-196.

[24] Sorimachi, K., Itoh, T., Kawarabayasi, Y., Okayasu, T., Akimoto, K. and Niwa, A. (2001) Conservation of the basic pattern of cellular amino acid composition during biological evolution and the putative amino acid composition of primitive life forms. *Amino Acids*, **21(4)**, 393-399.

[25] Gilbert, W.R. (1986) The RNA world. *Nature*, **319**, 618.

[26] Sorimachi, K. and Okayasu, T. (2007) Mathematical proof of the chronological precedence of protein formation over codon formation. *Current Topics of Peptide and Protein*

Research, **8**, 25-34.
[27] Sorimachi, K. and Okayasu, T. (2008) Universal rules governing genome evolution expressed by linear formulas. *The Open Genomics Journal*, **1(11)**, 33-43.
[28] Sorimachi, K. (2010) Codon evolution in doublestranded organelle DNA: Strong regulation of homo-nucleotides and their analog alternations. *Natural Science*, **2(8)**, 846-854.
[29] Sanger, F. and Coulson, A.R. (1975) A rapid method for determing sequences in DNA by primed synthesis with DNA polymerase. *Journal of Molecular Biology*, **94(3)**, 441-446.
[30] Maxam, A.M. and Gilbert, W. (1977) A new method for sequencing DNA. *Proceedings of the National Academy of Sciences*, **74(2)**, 560-564.
[31] Fleischmann, R.D., Adams, M.D., White, O., Clayton, R. A., Kirkness, E.F., Kerlavage, A.R. *et al.* (1995) Whole-genome random sequencing and assembly of Haemophilus influenzae Rd. *Science*, **269(5223)**, 496-512.
[32] Lander, E.S., Linton, M.L., Birren, B., Nusbaum, C., Zody, M.C., Baldwin, J., *et al.* (2001) Initial sequencing and analysis of the human genome. *Nature*, **409(6822)**, 860-921.
[33] Venter, J.C., Adams, M.D., Myers, E.W., Li, P.W., Mural, R.J., Sutton, G.G., Smith, H.O., Yandell, M., Evans, C.A., Holt, R.A., *et al.* (2001) The sequence of the human genome. *Science*, **291(5507)**, 1304-1351.
[34] Waterston, R.H., Lindblad-Toh, K., Birney, E., Rogers, J., Abril, J.F., Agarwal, P. *et al.* (2002) Initial sequencing and comparative analysis of the mouse genome. *Nature*, **420(6915)**, 520-562.
[35] Gibbs, R.A., Weinstock, G.M., Metzker M.L., Muzny, D. M., Sondergren, E.J., Scherer, S., *et al.* (2004) Genome sequence of the Brown Norway rat yield insights into mammalian evolution. *Nature*, **428(6982)**, 493-521.
[36] Sodergren E., Weinstock, G.M., Davidson, E.H., Cameron, R.A., Gibbs, R.A., Angerer, L.M., *et al.* (2006) The genome of the sea urchin Strongylocentrotus purpuratus. *Science*, **314(5801)**, 941-952.
[37] Sorimachi, K. and Okayasu, T. (2003) Gene assembly consisting of small units with similar amino acid composition in the Saccharomyces cerevisiae genome. *Mycoscience*, **44(5)**, 415-417.
[38] Kawai, J. (2001) Functional annotation of a full-length mouse cDNA collection. *Nature*, **409(682)**, 685-690.
[39] Smith D.R., Doucette-Stamm, L.A., Deloughery, C., Lee, H., Dubois, J., Aldredge, T., *et al.* (1997) Complete genome sequence of Methanobacterium thermoautotrophicum delta H: Functional analysis and comparative genomics. *Journal Bacteriology*, **179(22)**, 7135-7155.
[40] Sorimachi, K. and Okayasu, T. (2004) An evolutionary theories based on genomic structures in Saccharomyces cerevisiae and Enchephalitozoon cuniculi. *Mycoscience*, **45(5)**, 345-350.
[41] Sorimachi, K. and Okayasu, T. (2004) Classification of eubacteria based on their complete genome: Where does Mycoplasmataceae belong? *Proceedings of the Royal Society of London. B* (Supplement.), **271(4)**, S127-S130.
[42] Okayasu, T. and Sorimachi, K. (2008) Organisms can essentially be classified according to two codon patterns. *Amino Acids*, **36(2)**, 261-271.
[43] Sueoka, N (1988) Directional mutation pressure and neutral molecular evolution. *Proceedings of the National Academy of Sciences*, **85(8)**, 2653-2657.
[44] Qi, Z.H., Wang, J.M. and Qi, X.Q. (2009) Classification analysis of dual nucleotides using dimension reduction. *Journal of Theoretical Biology*, **260(1)**, 104-109.
[45] Ebara, Y., Koge, T. and Sorimachi, K. (2010) Evaluation of Chargaff's parity rules using simulation analysis. *Dokkyo Journal of Medical Sciences*, **37(2)**, 139-142.
[46] Sorimachi, K. (2009) A proposed solution to the historic puzzle of Chargaff's second parity rule. *The Open Genomics Journal*, **2(3)**, 12-14.
[47] Sorimachi, K. (2010) Genomic data provides simple evidence for a single origin of life. *Natural Science*, **2(5)**, 519-525.
[48] Nikolaou, C. and Almirantis, Y. (2006) Deviations from Chargaff's second parity rule in organelle DNA insights into the evolution of organelle genomes. *Gene*, **381**, 34-41.
[49] Gray, M.W., Burger, G., Lang, B.F. (1999) Mitochondrial evolution. *Science*, **283(5407)**, 1476-1481.
[50] Raven, J.A. and Allen, J.F. (2003) Genomics and chloroplast evolution: What did cyanobacteria do for plants? *Genome Biology*, **4(3)**, 209-215.

Vol.2, No.10, 1113-1118 (2010)
doi:10.4236/ns.2010.210138

Natural Science

Assessment of a short phylogenetic marker based on comparisons of 3' end 16S rDNA and 5' end 16S-23S ITS nucleotide sequences of the *Bacillus cereus* group

Sabarimatou Yakoubou[1,2], Jean-Charles Côté[1]*

[1]Agriculture and Agri-Food Canada, Research Centre, Gouin Blvd, St-Jean-sur-Richelieu, Canada; *Corresponding Author: Jean-Charles.Cote@agr.gc.ca;
[2]Département des Sciences Biologiques, Université du Québec à Montréal, Succ."Centre-Ville" Montréal, Canada.

Received 28 May 2010; revised 30 June 2010; accepted 5 July 2010.

ABSTRACT

A short phylogenetic marker previously used in the reconstruction of the Order *Bacillales* and the genus *Bacillus* was assessed here at a lower taxa level: species in the *Bacillus cereus* group: *B. anthracis*, *B. cereus*, *B. thuringiensis* and *B. weihenstephanensis*. This maker is 220 bp in length. It is a combination of 150 bp at the 3' end of the 16S rDNA and 70 bp at the 5' end of the 16S-23S ITS sequence. Three additional *Bacillus* species, *B. halodurans*, *B. licheniformis* and *B. subtilis*, and *Clostridium tetani* were included for comparison purposes. A total of eight bacterial species and 12 strains were analyzed. A bootstrapped neighbor-joining tree was inferred from comparative analyses of all allelic sequences of the bacterial species and strains under study. Based on its topology, four major Groups were revealed at the 90% nucleotide sequence identities, Group I to IV. Group I contains all alleles of the *Bacillus cereus* group. Group II contains all alleles of *B. halodurans*. Group III contains all alleles of *B. licheniformis* and *B. subtilis*. Group IV contains all alleles of *Clostridium tetani*. The 220 bp phylogenetic marker used here could resolve different species from different genera. At the genus level, distant species could be distinguished. Very closely-related species, however, were undistinguishable. Species in the *B. cereus* group, most notably *B. cereus*, *B. anthracis* and *B. thuringiensis*, could not be distinguished. After successfully inferring the phylogenies of the Order *Bacillales* and the genus *Bacillus*, we have met the resolving limit of this short phylogenetic marker: *B. cereus*, *B. anthracis* and *B. thuringiensis*.

Keywords: *Bacillus cereus*; 16S RDNA; 16S-23S ITS; Phylogeny

1. INTRODUCTION

The *Bacillus cereus* group comprises six genetically highly related species: *B. cereus* sensu stricto, *B. anthracis*, *B. thuringiensis*, *B. weihenstephanensis*, *B. mycoides* [1] and *B. pseudomycoides* [2]. They are Gram-positive, rod-shaped, endospore-forming, either obligate or facultative aerobic bacteria [1].

Bacillus cereus is a ubiquitous soil bacterium. It can be a contaminant of a variety of foods: meats, vegetables and dairy products [3,4]. It can cause diarrheal, and emetic food poisoning syndromes [5]. It can also be the etiologic agent of some opportunistic infections [6,7]. *Bacillus anthracis* is the etiologic agent of anthrax, an acute disease in herbivorous mammals, transmissible to other animals, including humans [8]. This species has been studied and developed as a biological weapon [9]. Virulent strains of *B. anthracis* carry two plasmids, pXO1 (181 kb) and pXO2 (96 kb) which may be transmitted to others members of *Bacillus cereus* group [10]. *Bacillus thuringiensis* is an insect pathogen. It is characterized by the synthesis upon sporulation of a parasporal inclusion body. This inclusion body is made of proteins, the δ-endotoxins, which are toxic to several insect larvae [11,12] and other invertebrates [13]. *B. thuringiensis* formulations have been developed for the control of insect pests in agriculture and forestry [14-16] and for the control of insect vectors of human diseases such as malaria, yellow fever, onchocerciasis, etc [17]. *Bacillus weihenstephanensis* is a psychotolerant species characterized by the ability to grow at 7°C and the absence of growth at 43°C. It is also characterized by the presence of specific signature sequences on the 16S rRNA gene (small subunit ribosomal RNA gene) and the *cspA* gene (gene encoding the major cold shock protein) [18]. *B. mycoides* is char-

acterized by the formation of rhizoid colonies and the absence of motility [19]. *B. pseudomycoides* is phenotypically similar to *B. mycoides* and is distinguished by DNA relatedness and fatty acid composition [2].

The 16S rDNA is the macromolecule of choice in the reconstruction of bacterial phylogenies [20-24]. The 16S rDNA, however, cannot distinguish among species in the *Bacillus cereus* group [25,26]. Genomic approaches have been used in an attempt to elucidate the genetic diversity of three highly closely related species in the *B. cereus* group: *B. cereus*, *B. anthracis* and *B. thuringiensis*. They appear as a single species on the basis of genetic evidence [27].

In a previous study, a 220 bp marker was developed and used to infer the phylogeny of species in the genus *Bacillus* and closely-related genera [28]. This marker was a combination of the last 150 bp at the 3' end of the 16S rDNA and the first 70 bp at the 5' end of the 16S-23S rDNA internal transcribed spacer (ITS). More recently, we assessed the usefulness of the 220 bp marker at a higher taxonomic level, the Order *Bacillales* [29]. This marker showed several advantages over the use of 16S rDNA sequences or the generation of extensive phenotypic and genotypic data in phylogenetic analyses. First, the 150 bp at the 3' end of the 16S rDNA allowed discrimination among distantly related species. Owing to its higher rate of nucleotide substitutions, the 70 bp at the 5' end of the 16S-23S rDNA (ITS) added discriminating power among closely related species from same genus and closely related genera from same family. Because of its higher percentage of nucleotide sequence divergence than the 16S rDNA, the 220 bp marker could better discriminate among closely related *Bacillus* [28] and *Bacillales* [29] species. Second, the method was simple, rapid, suited to large screening programs and easily accessible to most laboratories. Third, the marker also revealed species which appeared misassigned and for which additional characterization appeared warranted.

In the current study, we further analyze the resolving power of this short marker in inferring phylogenies at a much lower taxa level: the *Bacillus cereus* group.

2. MATERIALS AND METHODS

2.1. Bacterial Species and Strains

Four species in the *Bacillus cereus* group: *B. anthracis*, *B. cereus*, *B. thuringiensis* and *B. weihenstephanensis* were analyzed. Three additional *Bacillus* species, *B. halodurans*, *B. licheniformis* and *B. subtilis*, and *Clostridium tetani* were included for comparison purposes. A total of eight bacterial species and 12 strains were analyzed (**Table 1**). They were selected on the basis that their complete genome sequences were freely available in GenBank at the National Center for Biotechnology Information (NCBI) completed microbial genomes database (http://www.ncbi.nlm.nih.gov/genomes/lproks.cgi,August 2009). *Bacillus mycoides* and *B. pseudomycoides* were not included because their complete genome sequences have not been determined.

Table 1. Bacterial species used in this study.

Genera	Species	Strain	GenBank accession no.
Bacillus	*anthracis*	Ames	AE016879
		Ames Ancestor	AE017334.2
		Sterne	AE017225.1
	cereus	ATCC 14579	AE016877.1
		ATCC 10987	AE017194.1
		E33L	CP000001.1
	thuringiensis serovar *konkukian*	97-27	AE017355.1
	weihenstephanensis	KBAB4	NC_010184.1
	halodurans	C-125	BA000004.3
	licheniformis	ATCC 14580	AE017333.1
	subtilis subsp. *subtilis*	168	AL009126.3
Clostridium	*tetani*	E88	AE015927.1

2.2. Sequences

The 16S rDNA and 16S-23S ITS for the 12 bacterial species and strains were retrieved from GenBank, for a total of 129 allelic sequences. The last 150 bp at the 3' end of 16S rDNA and the first 70 bp at the 5' end of 16S-23S ITS were merged into a single 220 bp sequence for each of the 129 alleles under study as described before [28]. This 220 bp sequence will be used as a phylogenetic marker for the 12 bacterial species and strains under study.

2.3. Phylogenetic Analyses

All 129 allelic sequences were aligned using ClustalW [30] (data not shown). A neighbor-joining tree was constructed [31], based on the alignment of the 129 alleles of the 220 bp sequence. The tree was bootstrapped using 1,000 random samples. The neighbor-joining tree was drawn and printed with Tree Explorer, all components of the Molecular Evolutionary Genetics Analysis (MEGA, version 3.1) software package [32].

3. RESULTS AND DISCUSSIONS

In a previous study, a 220 bp sequence was developed as a DNA marker and used to infer the phylogeny of species in the Gram-positive genus *Bacillus* and closely-related genera [28]. This marker was a combination of the last 150 bp at the 3' end of the 16S rDNA and the first 70 bp at the 5' end of the 16S-23S rDNA internal transcribed spacer (ITS). More recently, we assessed the usefulness of the 220 bp marker by extending its analyses at a higher taxonomic level, the Gram-positive Order *Bacillales* [29]. In parallel, a similar marker was used to infer the phylogeny of the Gram-negative Class γ-proteobacteria [33]. In the current study, we further analyze the resolving power of this marker in inferring the phylogeny at a much lower taxa level: the *Bacillus cereus* group.

A bootstrapped neighbor-joining phylogenetic tree was inferred from comparative analyses of the 220 bp marker from the 129 alleles from the bacterial species and strains under study (**Figure 1**). Four major Groups were revealed based on the topology of the neighbor-joining tree at the 90% nucleotide sequence identities, Group I to IV. Group I contains all alleles of the species in the *Bacillus cereus* group. Group II contains all alleles of *B. halodurans*. Group III contains all alleles of *B. licheniformis* and *B. subtilis*. Group IV contains all alleles of *Clostridium tetani*. Based on nucleotide sequence identities, sub-groups and branches can be revealed. Group I can be sub-divided into three sub-groups at the 95% nucleotide sequence identities. Sub-group I-1 encompasses 27 alleles from the *B. anthracis* strains, 36 alleles from the *B. cereus* strains, 11 alleles from *B. thuringiensis* and one allele from *B. weihenstephanensis*. Sub-group I-2 encompasses six alleles from *B. anthracis*, two alleles from *B. cereus* and one allele from *B. thuringiensis*. Sub-group I-3 encompasses 12 alleles from *B. weihenstephanensis*. A branch corresponding to an allele from *B. weihenstephanensis* is present between sub-groups I-2 and I-3. Group II contains all eight alleles from *B. halodurans*. They show at least 20% nucleotide sequence divergences with alleles from the other *Bacillus* species. Group III contains all alleles from *B. licheniformis* and *B. subtilis*. It can be sub-divided into two sub-groups at the 95% nucleotide sequence identities. Sub-group III-1 encompasses all seven alleles from *B. licheniformis*. Sub-group III-2 encompasses all ten alleles from *B. subtilis*. Group IV contains all six alleles from *Clostridium tetani*. These alleles show at least 26% nucleotide sequence divergence with alleles from species and strains in the genus *Bacillus*.

In accordance with our previous work on the Order *Bacillales*, the 220 bp sequence used as a phylogenetic marker was able to group alleles from same species for *B. halodurans*, *B. licheniformis*, *B. subtilis*, and *Clostridium tetani*, respectively. However, this 220 bp sequence could not group most alleles from same species, exclusive of alleles from others, for the *B. cereus* group. Sub-group I-1 is heterogeneous. It contains alleles from all four species from the *B. cereus* group. The close proximity of *B. cereus*, *B. anthracis* and *B. thuringiensis* is in agreement with previous works based on whole-genome DNA hybridization [34], pulsed-field gel electrophoresis (PFGE) [35], multilocus enzyme electrophoresis (MEE) [36], amplified fragment length polymorphism (AFLP) fingerprinting [37] and multilocus sequence typing (MLST) [38,39], which showed that all three species are genetically highly related. They appear as a single species on the basis of genetic evidence [27]. Sub-groups I-2 is more homogeneous. It mostly contains alleles from *B. anthracis*. Sub-groups I-3 is homogeneous. It only contains alleles from *B. weihenstephanensis*. As shown earlier, on the genus *Bacillus* [28] and the Order *Bacillales* [29], this 220 bp sequence contains 150 bp at the 3' end of 16S rDNA which allowed discrimination among distantly related species and 70 bp at the 5' end of 16S-23S ITS which, owing to its higher percentage of nucleotide sequence divergence, added resolving power among closely related species.

Here, species in the *B. cereus* group, most notably *B. cereus*, *B. anthracis* and *B. thuringiensis*, are too closely related to be discriminated with the 220 bp sequence previously used as a phylogenetic marker. Our work, however, has shown that the alleles in sub-group I-3 could distinguish *B. weihenstephanensis* from all other species.

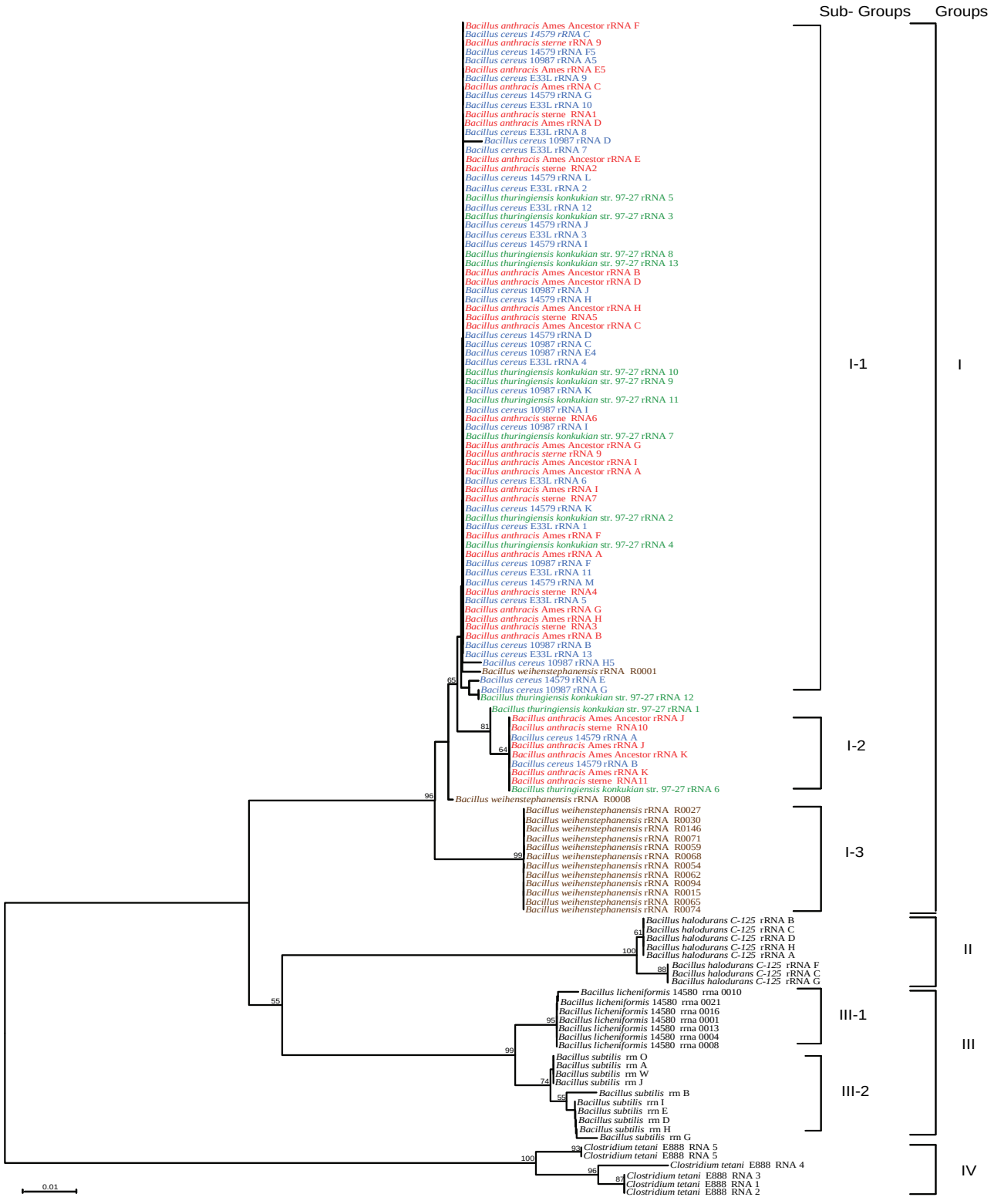

Figure 1. Bootstrapped neighbor-joining tree inferred from comparative alignment of the 220 bp marker from the 129 alleles from the 12 bacterial species and strains under study. Major groups are indicated in capital roman numerals. Sub-groups are indicated in arabic numerals. Bootstrap values higher than 50% are indicated (expressed as percentage of 1000 replication). The horizontal bar represents 1% nt difference. *Bacillus anthracis*, *B. cereus*, *B thuringiensis* and *B. weihenstephanensis*'s alleles are written in red, blue, green and brown, respectively. *B. halodurans*, *B. licheniformis*, *B. subtilis* and *Clostridium tetani*'s alleles are written in black ink.

4. CONCLUSIONS

Previous genetic analyses have shown that *B. cereus*, *B. anthracis* and *B. thuringiensis* should be regarded as a single species. We have shown here that a 220 bp marker, used to reconstruct the phylogeny of the Order *Bacillales* and the family *Bacillaceae*, was unable to discriminate between these three highly-related species. We have reached the limit of the resolving power of the 220 bp sequence as a phylogenetic marker: *B. cereus*, *B. anthracis* and *B. thuringiensis*.

REFERENCES

[1] Claus, D. and Berkeley, R.C.W. (1986) Genus *Bacillus* Cohn, 1872. In: Sneath, P.H.A., Mair, N.S., Sharpe, M.E. and Holt. J.G., Eds., *Bergey's Manual of Systematic Bacteriology*, The Williams & Wilkins Co., Baltimore, **2**, 1105-1139.

[2] Nakamura, L.K. (1998) *Bacillus pseudomycoides* sp. nov. *International Journal of Systematic Bacteriology*, **48(3)**, 1031-1035.

[3] Drobniewski, F.A. (1993) *Bacillus cereus* and related species. C*linical Microbiology Reviews*, **6(4)**, 324-338.

[4] Schoeni, J.L. and Wong, A.C.L. (2005) *Bacillus cereus* food poisoning and its toxins. *Journal of Food Protection*, **68(3),** 636-648.

[5] Kramer, J.M. and Gilbert, R.J. (1989) *Bacillus cereus* and other *Bacillus* species. In: Doyle, M.P., Ed., *Foodborne Bacterial Pathogens*, Marcel Dekker, Inc., New York, 21-50.

[6] Das, T., Choudhury, K., Sharma, S., Jalali, S., Nuthethi, R. and the Endophthalmitis Research Group (2001) Clinical profile and outcome in *Bacillus* endophthalmitis. *Ophthalmology*, **108(10)**, 1819-1825.

[7] Le Scanff, J., Mohammedi, J.I., Thiebaut, A., Martin, O., Argaud, L. and Robert, D. (2006) Necrotizing gastroenteritis due to *Bacillus cereus* in an immunocompromised patient. *Infection*, **34(2)**, 98-99.

[8] Logan, N.A. and De Vos, P. (2009) Genus I. *Bacillus* Cohn 1872, 174^{AL}. In: De Vos, P., Garrity, G.M., Jones, D., Krieg, N.R., Ludwig, W., Rainey, F.A., Schleifer, K.H. and Whitman, W.B., Eds., *Bergey's Manual of Systematic Bacteriology*, 2nd Edition, Springer, New York, **3**, 21-128.

[9] Inglesby, T.V., O'Toole, T., Henderson, D.A., Bartlett, J.G., Ascher, M.S., Eitzen, E., Friedlander, A.M., Gerberding, J., Hauer, J., Hughes, J., McDade, J., Osterholm, M.T., Parker, G., Perl, T.M., Russell, P.K. and Tonat, K. (2002) Anthrax as a biological weapon: Updated recommendations for management. *The Journal of the American Medical Association*, **287(17)**, 2236-2252.

[10] Turnbull, P.C.B. (2002) Introduction: Anthrax history, disease and ecology. In: Koehler, T., Ed., *Anthrax*, Springer-Verlag, Berlin, 1-20.

[11] Höfte, H. and Whiteley, H.R. (1989) Insecticidal crystal proteins of *Bacillus thuringiensis*. *Microbiological Reviews*, **53(2)**, 242-255.

[12] Garcia-Robles, I., Sánchez, J., Gruppe, A., Martínez-Ramírez, A.C., Rausell, C., Real, M.D. and Bravo, A. (2001) Mode of action of *Bacillus thuringiensis* PS86Q3 strain in hymenopteran forest pests. *Insect Biochemistry and Molecular Biology*, **31(9)**, 849-856.

[13] Feitelson, J.S. (1993) The *Bacillus thuringiensis* family tree. In: Kim, L., Ed., *Advanced Engineered Pesticides*, Marcel Dekker Inc., New York, 63-71.

[14] Schnepf, H.E., Crickmore, N., Van Rie, J., Lereclus, D., Baum, J., Feitelson, J., Zeigler, D.R. and Dean, D.H., (1998) *Bacillus thuringiensis* and its pesticidal crystal proteins. *Microbiology and Molecular Biology Reviews*, **62(3)**, 775-806.

[15] Otvos, I.S., Armstrong, H. and Conder, N. (2005) Safety of *Bacillus thuringiensis* var. *kurstaki*, applications for insect control to humans and large mammals. In: Côté, J.-C., Otvos, I.S., Schwartz, J.-L. and Vincent, C., Eds., *Proceedings of the* 6*th Pacific Rim Conference on the Biotechnology of Bacillus thuringiensis and its Environmental Impact*. Montréal, 30 October-3 November 2005, 45-59.

[16] Bravo, A., Gill, S.S. and Soberon, M. (2007) Mode of action of *Bacillus thuringiensis* Cry and Cyt toxins and their potential for insect control. *Toxicon*, **49(4)**, 423-435.

[17] Guillet, P., Chandre F. and Mouchet, J. (1997) L'utilisation des insecticides en santé publique: état et perspectives. *Médecine et Maladies Infectieuses*, **27(5)**, 552-557.

[18] Lechner, S., Mayr, R., Francis, K.P., Prüß, B.M., Kaplan, T., Wießner-Gunkel, E., Stewart Gordon, S.A.B. and Scherer, S. (1998) *Bacillus weihenstephanensis* sp. nov. is a new psychrotolerant species of the *Bacillus cereus* group. *International Journal of Systematic Bacteriology*, **48(4)**, 1373-1382.

[19] Nakamura, L.K. and Jackson, M.A. (1995) Clarification of the taxonomy of *Bacillus mycoides*. *International Journal of Systematic Bacteriology*, **45(1)**, 46-49.

[20] Woese, C.R., Kandler, O. and Wheelis, M.L. (1990) Towards a natural system of organisms: Proposal for the domains *Archea, Bacte*ria and *Eucarya*. *Proceedings of the National Academy of Sciences*, USA, **87(12)**, 4576-4579.

[21] Amann, R., Ludwig, W. and Schleifer, K.H. (1995) Phylogenetic identification and in situ detection of individual microbial cells without cultivation. *Microbiological Review*, **59(1)**, 143-169.

[22] Cilia, V., Lafay, B. and Christen, R. (1996) Sequence heterogeneities among 16S ribosomal RNA sequences and their effect on phylogenetic analyses at species level. *Molecular Biolology and Ecol*ogy, **13(3)**, 451-461.

[23] Goto, K., Omura, T., Hara, Y. and Sadaie, Y. (2000) Application of the partial 16S rDNA sequence as an index for rapid identification of species in the genus *Bacillus*. *Journal of General and Applied Microbiology*, **46(1)**, 1-8.

[24] Sacchi, C.T., Whitney, A.M., Mayer, L.W., Morey, R., Steigerwalt, A., Boras, A., Weyant, R.S. and Popovic, T. (2002) Sequencing of 16S rRNA gene: A rapid tool for identification of *Bacillus anthracis*. *Emerging Infectious Di*sease, **8(10)**, 1117-1123.

[25] Ash, C., Farrow, J.A. Dorsch, M. Stackebrandt, E. and Collins, M.D. (1991) Comparative analysis of *Bacillus anthracis*, *Bacillus cereus*, and related species on the basis of reverse transcriptase sequencing of 16S rRNA. *International Journal of Systematic Bacteriology*, **41(3)**, 343-346.

[26] Ash, C., Farrow, A.E., Wallbanks, S. and Collins, M.D. (1991) Phylogenetic heterogeneity of the genus *Bacillus* revealed by comparative analysis of small-subunit-ribosomal RNA sequences. *Letters in Applied Microbiology*, **13(4)**, 202-206.

[27] Vilas-Boas, G.T., Peruca, A.P. and Arantes, O.M. (2007) Biology and taxonomy of *Bacillus cereus, Bacillus anthracis*, and *Bacillus thuringiensis*. *Canadian Journal of Microbiology*, **53(6)**, 673-687.

[28] Xu, D. and Côté, J.-C. (2003) Phylogenetic relationships between *Bacillus* species and related genera inferred from comparison of 3' end 16S rDNA and 5' end 16S-23S ITS nucleotide sequences. *International Journal of Systematic and Evolutionary Microbiology*, **53(3)**, 695-704.

[29] Yakoubou, S., Xu, D. and Côté, J.-C. (2010) Phylogeny of the order *Bacillales* inferred from 3' 16S rDNA and 5' 16S-23S ITS nucleotide sequences. *Natural Science*, **2(9)**, 990-997.

[30] Thompson, J.D., Higgins, D.G. and Gibson, T.J. (1994) CLUSTAL W: Improving the sensitivity of progressive multiple sequence alignment through sequence weighting, positions-specific gap penalties and weight matrix choice. *Nucleic Acids Research*, **22(22)**, 4673-4680.

[31] Saitou, N. and Nei, M. (1987) The neighbor-joining method: A new method for reconstructing phylogenetic trees. *Molecular Biology and Evolution*, **4(4)**, 406-425.

[32] Kumar, S., Tamura, K. and Nei, M. (2004) MEGA3: Integrated software for molecular evolutionary genetics analysis and sequence alignment. *Brief Bioinformatic*, **5(2)**, 150-163.

[33] Yakoubou, S. and Côté, J.-C. (2010) Phylogeny of γ-proteobacteria inferred from comparisons of 3' end 16S rRNA gene and 5' end 16S-23S ITS nucleotide sequences. *Natural Science*, **2(6)**, 535-543.

[34] Kaneko, T., Nozaki, R. and Aizawa, K. (1978) Deoxyribonucleic acid relatedness between *Bacillus anthracis, Bacillus cereus* and *Bacillus thuringiensis*. *Microbiology and Immunology*, **22(10)**, 639-641.

[35] Carlson, C.R., Caugant, D.A. and Kolsto, A.-B. (1994) Genotypic diversity among *Bacillus cereus* and *Bacillus thuringiensis* strains. *Applied and Environmental Microbiology*, **60(6)**, 1719-1725.

[36] Helgason, E., Caugant, D.A., Olsen, I. and Kolsto, A.-B. (2000) Genetic structure of population of *Bacillus cereus* and *Bacillus thuringiensis* isolates associated with periodontitis and other human infections. *Journal of Clinical Microbiology*, **38(4)**, 1615-1622.

[37] Ticknor, L.O., Kolsto, A.B., Hill, K.K., Keim, P., Laker, M.T., Tonks, M. and Jackson, P.J. (2001) Fluorescent amplified fragment length polymorphism analysis of Norwegian *Bacillus cereus* and *Bacillus thuringiensis* soil isolates, *Applied and Environmental Microbiology*, **67(10)**, 4863-4873.

[38] Helgason, E., Tourasse, N.J., Meisal, R., Caugant, D.A. and Kolsto, A.B. (2004) Multilocus sequence typing scheme for bacteria of the *Bacillus cereus* group. *Applied and Environmental Microbiology*, **70(1)**, 191-201.

[39] Olsen, J., Skogan, G., Fykse, E., Rawlinson, E., Tomaso, H., Granum, P. and Blatny, J. (2007) Genetic distribution of 295 *Bacillus cereus* group members based on adk-screening in combination with MLST (Multilocus Sequence Typing) used for validating a primer targeting a chromosomal locus in *B. anthracis. Journal of Microbiological Methods*, **71(3)**, 265-274.

Vol.2, No.10, 1119-1129 (2010)
doi:10.4236/ns.2010.210139

Natural Science

Origin and SEM analysis of aerosols in the high mountain of Tenerife (Canary Islands)

Juan D. Delgado[1,2]*, Omaira E. García[3], Ana M. Díaz[3], Juan P. Díaz[3], Francisco J. Expósito[3], Emilio Cuevas[4], Xavier Querol[5], Andrés Alastuey[5], Sonia Castillo[5]

[1]Área de Ecología, Departamento de Sistemas Físicos, Químicos y Naturales, Universidad Pablo de Olavide, Seville, Spain;
*Corresponding Author: jddelgar@upo.es;
[2]Instituto Universitario de Enfermedades Tropicales y Salud Pública de Canarias, La Laguna, Tenerife, Canary Islands, Spain;
[3]Departamento de Física Básica, Universidad de La Laguna, E-38206 La Laguna, Tenerife, Canary Islands, Spain;
[4]Izaña Observatory, Instituto Nacional de Meteorología, INM, Santa Cruz de Tenerife, Canary Islands, Spain;
[5]Institute of Environmental Assessment and Water Research (IDÆA), CSIC, Barcelona, Spain.

Received 18 May 2010; revised 21 June 2010; accepted 24 June 2010.

ABSTRACT

Focusing on aerosolized matter of relevance to respiratory health, a major public health issue worldwide, we studied mineral and biological aerosol (bioaerosol) composition (TSP and $PM_{2.5}$) and geographical origins during dust intrusions in the Canary Islands. Seven days' backward trajectories were assessed daily during March 2004 with the ends of back trajectories being the sampling station of Izaña (high mountain, 2360 m a.s.l. at the Cañadas del Teide National Park, Tenerife island), a free troposphere site allowing characterization of dust with low influence of other pollutant sources. Scanning electron microscopy (SEM) was used to survey major types of airborne particles in the dust plumes. Control, non-intrusion conditions correspond to Atlantic oceanic middle troposphere (OMT) air masses. Of the 14 samples taken, 1 corresponded to a control (clear atmosphere conditions), and the remaining 13 to dust intrusions, with the following sources: African Dust; EAM: mixture of Europe, Africa and Oceanic; MaA: maritime aerosols. Of the air masses, 79% were directly transported to the islands from Africa, and an increase of African dust events was detected when comparing with a 52-year previous data sequence. Quartz microcristals and aggregates of quartz and platy clay were the dominant minerals identified, with marine salt and gypsum also present. Freshwater diatom tests (from two *Aulacoseira* species) represented the most important biogenic aerosols, although fungi and pollen were also detected. The diverse and complex mixture of respirable particles in large quantities in airborne dust, especially from nearby Sahara and from the Sahelian region, is of maximum interest for airway pathology in the Canaries, including the highly visited highlands in Tenerife.

Keywords: Allergens; Bioaerosols; Diatoms; High altitude; Desert dust intrusion; Public health; Scanning electron microscopy

1. INTRODUCTION

The dispersal of abiotic and biological aerosols (bioaerosols), has a growing interest in interdisciplinary research comprising epidemiology, public health and atmospheric physics. This is due to the great capacity of air masses to transport both viable organisms and inorganic dust to remote areas, where they transform local tropospheric conditions [1] and may affect human health [2]. The cell-carrying capacity of wind, long-range and high frequency transport of dust masses, aggravate the effects of seasonal peaks in local allergens through additive and synergic effects. The transport of dust might involve carrying up to 10.000 bacterial cells per gram of soil from some desert areas [3]. For example, diatoms are a large fraction of dust carried from fresh waters of the Saharo-Sahelian areas and Eurasia to remote areas such as the Caribbean [4]. Charles Darwin, on his 1845 voyage aboard the surveying ship H.M.S. Beagle, collected African dust in the Atlantic and microscopically detected the occurrence of diatoms in the dust. This same historic dust has been recently analyzed to find at least 16 different viable bacterial lineages and 2 fungal isolates [5].

Although the global amount of species of airborne pathogens is not so far clearly defined, several hundreds

of bacterial lineages, fungi and viruses can be involved in allergy, asthma and pulmonary affections, and airborne dust is a vehicle for them [6-10]. Inhaled atmospheric aerosols of any origin can be associated with a number of diseases and disorders, namely allergic airways disease (or asthma), rhinitis and rhinosinusitis, alveolitis or allergic parenchymal disease, airways or parenchymal infections, atypical thoracic pain, anxiety disorders, cardiopathy, and meningitis, among others [11-14].

The Canary Islands lay 96 km off the west of the largest dust source on Earth, the Sahara desert (> 9 million square kilometres), being comprised within the "dust-belt", where the atmospheric dust concentration is inherently very high [15]. Dust transport to the Canaries causes several-fold increase over the standard levels of particulate matter over the islands [1,16-20]. Although studies relating desert dust to "airborne" diseases in the Canary Islands are scant, dust events reach the archipelago with a high frequency, being associated with augmented prevalence, morbidity and mortality [12]. There are precedents in other regions, such as the Caribbean Sea where increase of frequency in African dust episodes reaching Barbados were associated to a seventeen-fold increase in asthma between 1973 and 1996 [21-23]. In Gran Canaria and Tenerife, type and frequency of asthma symptoms have been analyzed in a large population sample, and climatic conditions have been invoked to explain high prevalences [24].

In this paper we study aerosols from African dust intrusions at a high altitude ecosystem in Tenerife, Canarian archipelago. Specific health effects of minerogenic dust and bioaerosols have not been studied so far in the Canary Islands, and this task is difficult to approach without recognizing the type of particles involved. We thus aimed to identify and survey, through scanning electronic microscopy (SEM) analysis, the biological and mineral aerosol particles transported with dust during intrusions of African air masses and from other origins to the Canary Islands. Imaging characterization of dust particles could give us explicit information on aerosol types in relation with complementary data on origin and travelling time of air masses. We related the dust events with the air-mass origin, tracing back the dust trajectories to assess source areas. Our primary concern was on aerosolized particles with a potential interest in public health that are transported with dust plumes from Africa to the Canary Islands.

2. METHODS

2.1. Study Area

We studied air samples searching for biogenic particles (bioaerosols) during a non-intrusion episode ("clean atmosphere") and during dust invasions to Tenerife, the largest and more densely populated and visited island of this group (**Table 1**). Our sampling was focused on the

Table 1. Characteristics of air samples from filters taken at the high mountain station of Izaña in Tenerife.

Particle sampler type	Hour (GMT) and initial sampling date		Hour (GMT) and final sampling date		Cycle volume (m^3)	African dust outbreaks	Back Trajectory	
							Initial sampling	Final sampling
PM2.5	14:44	03/03/04	14:50	04/03/04	731	+	EAM	EAM
PM2.5	14:58	04/03/04	15:40	05/03/04	506	+	EAM	EAM
PM2.5	12:22	17/03/04	12:26	18/03/04	731	+	AfD	AfD
PM2.5	11:05	22/03/04	11:40	23/03/04	733	+	AfD	AfD
PM2.5	10:12	04/04/04	15:35	05/04/04	732	+	MaA	MaA
TSP	15:48	03/03/04	15:55	04/03/04	732	+	EAM	EAM
TSP	16:10	04/03/04	16:20	05/03/04	731	+	EAM	EAM
TSP	16:30	05/03/04	16:45	06/03/04	731	+	EAM	EAM
TSP	12:26	11/03/04	15:10	12/03/04	731	− (control)	OMT	OMT
TSP	12:13	17/03/04	12:17	18/03/04	731	+	AfD	AfD
TSP	12:23	18/03/04	13:30	19/03/04	732	+	AfD	EAM
TSP	11:00	22/03/04	11:35	23/03/04	731	+	AfD	AfD
TSP	11:45	23/03/04	12:20	24/03/04	731	+	AfD	AfD
TSP	10:05	04/04/04	13:40	05/04/04	732	+	MaA	MaA

Trajectory codes: OMT: Atlantic Oceanic Middle Troposphere; AfD: African Dust; EAM: mixture of Europe, Africa and Oceanic origins; MaA: maritime aerosols.

high mountain scrub, at the Teide National Park (free troposphere, over the stable inversion layer, which is found between 1000-1500 m), at the facilities of the Instituto Nacional de Meteorología (Izaña Observatory, 16º29'58" W; 28º18'32" N; 2360 m a.s.l.) (**Figure 1**).

The Izaña site is located above a sharp temperature inversion between 500 and 1500 m, thus remaining relatively apart from the contamination foci of the low areas and human settlements [25]. At Izaña, the characterization of African dust is possible with low interference of other pollutant sources [26]. The dust transport is strongly seasonal, occurring near the surface in the cold season (October to March) and above two kilometres altitude in the warm season (April to September) [27,28]. We centred the sampling effort in March-April 2004. Annual distribution of particulate matter at low areas in the Canary Islands peaks in winter and shows a minimum in summer, whereas in the Tenerife high mountain, the maximum dust incomes occur in summer. Nevertheless dust episodes are also commonly detected in springtime in both levels [19,27,28]).

2.2. Dust Trajectories and Origins

To assess the origin of the aerosols, seven days backward trajectories were calculated daily at 00 and 12 UTC during March 2004 with HYSPLIT-4 model (Draxler and Hess, 1997 in [27]). The end point of the back trajectories was the Izaña station. Physical-chemical aerosol properties can be related with the origin and trajectory of the aerosol-laden air masses. Díaz [27] and Díaz *et al.* [28] developed a methodology to characterize the source-transport paths of the aerosol over this region using multivariate clustering analysis. The back trajectories classification is based on the contribution of the main aerosol sources, considering the geographical regions, the residence time in these sectors and the altitude of the air mass during the evolution towards the island. With this technique, clusters of back trajectories can be found for different levels of transport and origins of the air masses [28].

2.3. Dust SEM Analysis

TSP (Total Suspended Particles) and $PM_{2.5}$ (Particulate Matter with 2.5 micrometers diameter or smaller) were sampled simultaneously on quartz glass filters (Schleicher and Schuell, QF20), with high volume samplers MCV CAV-A / M (30 m^3/h). Samplers operated for 24 h periods from 03 / 03 / 04 until 05 / 04 / 04, and completed 14 samples (**Table 1**). We separated part of the filters for scanning electron microscope (SEM) analysis. A small section (< 1 cm^2) of each filter was cut and glued onto an aluminium stub and processed for SEM. Complementarily, another section of the filter was gently pressed on an adhesive carbon conductive tab to transfer the filter content to the preparation, then the tab was glued to the stub and processed for SEM. Preparations

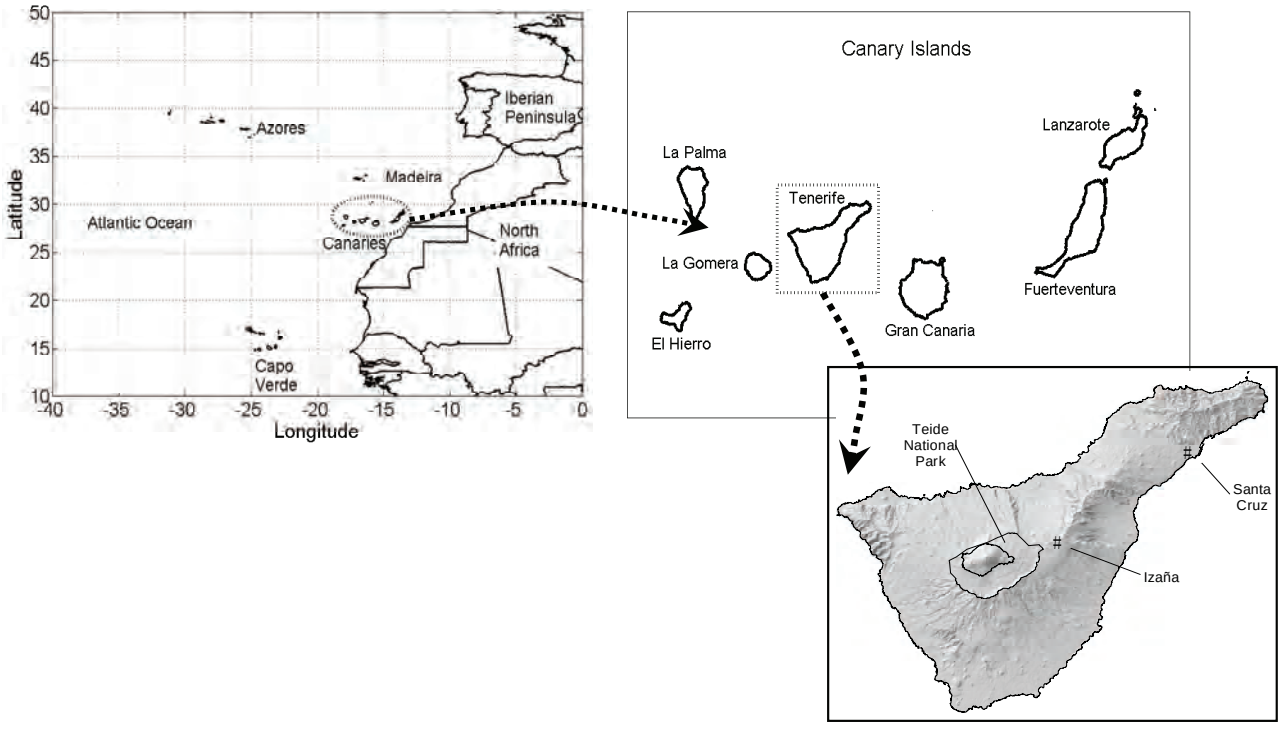

Figure 1. Study area and sampling stations.

were observed and photographed in a JEOL JSM 6300 electron microscope. We resolved the elemental composition of some particles with X-ray electron probe microanalysis (EDX) (OXFORD 6699) of selected SEM samples. The system operated at 20 kV (operation range: 0.2-30 kV) with a maximum resolution of 3.5 nm.

3. RESULTS

3.1. Dust Trajectories and Origins

Clusters of back trajectories found were: 1) representative of Atlantic oceanic middle troposphere (OMT); 2) air masses originated in the African continent (AfD); 3) mixture of aerosols from at least two of these sources: Europe, Africa and Ocean (EAM); 4) air masses with high load of maritime aerosols (MaA). The average frequencies of occurrence of these clusters on March over a 52 year period (1948-2004) were 17% AfD, 24% EAM, 40% OMT and 19% MaA.

Mean altitude for trajectories ending at Izaña was 2970.85 m (range: 0-8119.5 m) in March 2004. The back trajectories analysis for Tenerife for that month showed that air masses were 30% AfD, 24% EAM, 24% OMT and 22% MaA. These values revealed an increase in frequency of African dust events (cluster AfD) of 13% at the high mountain site compared with the average value of the 52-year period. In particular, of the 14 samples obtained at Izaña (**Table 1**), 13 corresponded to mineral dust conditions, where the 79% of the air masses were directly transported from the African continent (43% AfD and 36% EAM), whereas the remaining two represent maritime air masses with presence of dust particles. This last situation is observed most likely during the spring-summer period at Izaña [28], where the air masses cross areas with a high concentration of dust due to a Sahara-Sahel outbreak occurred in previous days. As exemplified in **Figure 2** (upper panel), the air mass in cluster AfD progressed at low altitudes while crossing the eastern Sahara desert (particularly between 0 and 15º E) and then gained altitude approaching the Atlas range, finally reaching the end point in the Tenerife high mountain at 2360 m. Furthermore, given that a 24 h sampling schedule was applied, the possibility of ascending air masses transporting coastal material up to the summit at Izaña station can not be disregarded [26].

3.2. SEM Survey of Dust Particulate Matter

In our SEM samples, most abiotic and biological or biogenic particles are within the respirable size range. Aerosols presenting a wide size range (including $PM_{2.5}$ and PM_{10}) were quartz and clay grains, gypsum rods and halite. Crustal aerosols appeared clustered, which increased average lateral dimension of particles. The main bio-

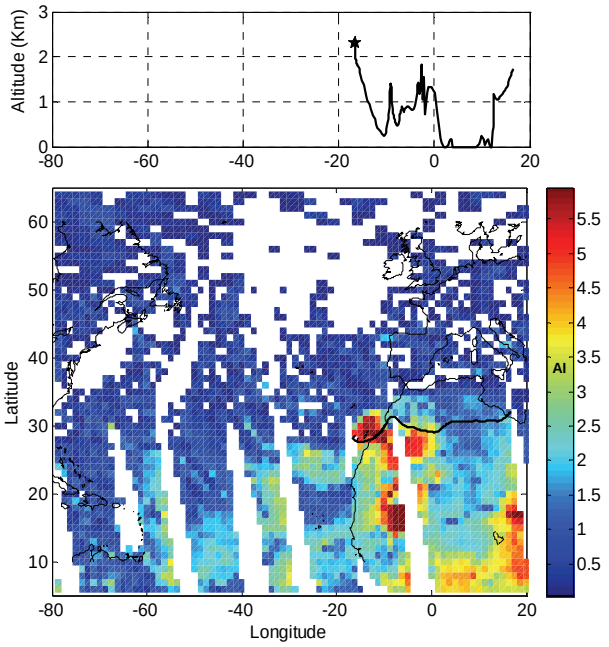

Figure 2. Values of the TOMS AI (Total Ozone Mapping Spectrometer Aerosol Index) for a back trajectory of 24 / 03 / 2004 (black line, below graphic) of African mineral dust estimated for Izaña (Tenerife, Canary Islands). The TOMS aerosol index is a relative measure of the amount of aerosol particles absorbing radiation in the atmosphere. The vertical altitude-longitude cross section of the trajectory is shown in the upper panel (maximum at ca. 2400 m a.s.l.). The white arrow points the geographic evolution of the air mass from left to right. The colour scale is adimensional and depicts the TOMS AI.

aerosols found here (diatoms) belong to the PM_{10} fraction, although a large amount of fragmented thecae were within the $PM_{2.5}$ class; pollen grains and one fungal conidium were within PM_{10}.

3.3. Aerosols of Biotic Origin

We made only an overview of major aerosol types transported with dust to the Canaries, and we did not quantify the concentration of airborne species. The most abundant biological remains identified in our SEM samples for African dust episodes were diatom siliceous tests (**Figure 3**). Two species of the genus *Aulacoseira* Thwaites (1848) (formerly *Melosira*), were identified: *A. granulata* (Ehrenb.) Simonsen 1979 and *A. islandica* (O. Müller) Simonsen (Bacillariophyta). Apart from diatom remains, other biogenic material was difficult to observe in SEM preparations, where the mineral fraction dominated. We identified only one fungal taxon, most probably *Alternaria* sp., as determined from a clavate conidium, showing the loculi under an irregular surface (**Figure 3 (A)**).

Pollen grains were found by SEM but species could

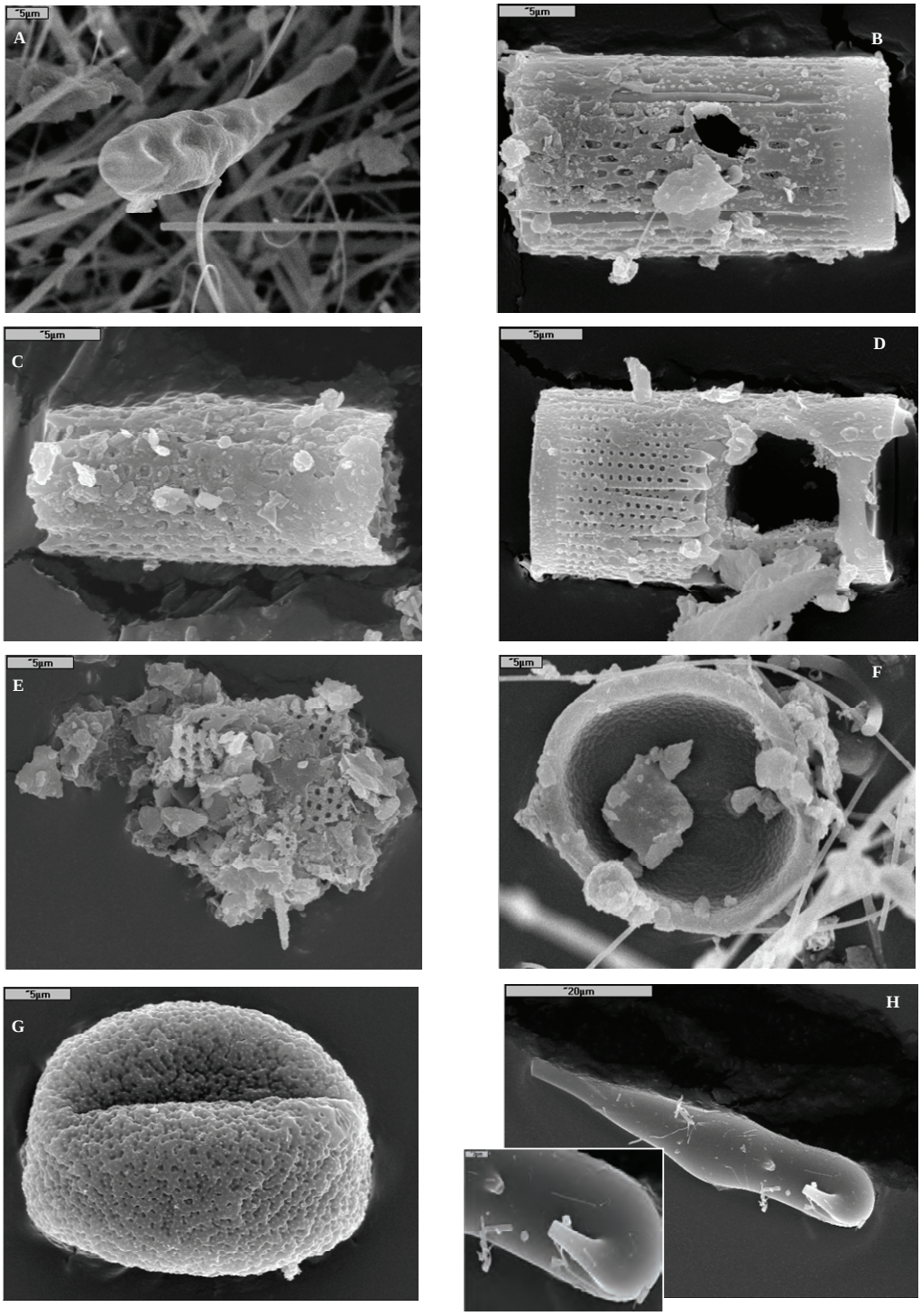

Figure 3. SEM photographs of TSP and $PM_{2.5}$, biogenic particulate matter or bioaerosols identified in dust filters from Tenerife (Canary Islands) during African dust intrusions. All samples from Las Cañadas (high mountain site), excepting F (Santa Cruz, coastal city). **(A)**: Typically club-shaped Conidium of ascomycotan fungi (*Alternaria* sp., a cause of allergic fungal sinusitis). **(B)-(D)**: Siliceous tests of freshwater diatoms (**(B)** and **(C)**: *Aulacoseira granulata*; **(D)**: *A. islandica*), heavily eroded and worn due to the transport process. **(E)**: Conglomerate of diatom test remains (presumably *Aulacoseira* spp.) with platy clay particles. **(F)**: undetermined pollen grain, cross-section, containing mineral particles (Santa Cruz). **(G)**: pollen grain, undetermined species. **(H)**: fragmentary spicule-like particle (inset: magnification), origin (either abiotic or biological) and composition uncertain.

not be assigned (**Figure 3(G)**). Pollen was very rare in filters, which operated during the early spring season when flowering period was not at its peak in the Tenerife high mountain. We failed to identify bacterial cells in filter preparations examined with SEM.

3.4. Aerosols of Abiotic Origin

Filters from the control day ("clean troposphere") showed a very different aspect when compared with filters from dust events (**Figures 4(A),4(B)**), the latter being concealed with a dense mineral-biomineral matrix (**Figure 4(C)**). The abiotic particulate aerosols identified individually included clay grades and quartz microcristals (isolated or aggregated) of crustal origin (from AfD cluster), and gypsum rods ($CaSO_4$). Halite, cubic and cube-octahedra crystals of sea salt (NaCl) were obtained from the OMT cluster correspondent to clear atmospheric conditions and incidence of marine aerosol reaching the high mountain area (compare with [26]).

Quartz (SiO_2) microcristals (particles from < 10 μm to < 2 μm) formed the dominant or background material in our filters during dust intrusions (**Figure 4**). Aerosols transported from the Sahara desert are enriched in clay material due to a high residence time in atmosphere caused by a smaller particle size and laminar habit; these clay grade grains are transported as particles of silt size forming aggregates [29,30] (**Figure 4**).

4. DISCUSSION

As suggested by our filter samples from different origins, *Aulacoseira* diatom thecae compound the dominant biogenic aerosol, and quartz is the dominant mineral fraction, which also formed up to 60% of dust material in a study from Gran Canaria [31].

The diatoms identified are dominant taxa in fresh waters from N and NW Africa, and can be found throughout the Palaearctic [32]. *A. granulata* has been recorded in the Arctic probably transported from Siberia [33]. Both *A. islandica* and *A. granulata* are typical of eutrophized and alkaline waters. As far as we know, these species have not been deemed as pathogenic to humans; on the contrary, they are used as bioindicators of freshwater quality in most studies. They can be transported as viable cells through the ocean, and their importance in the windblown diatom fraction decrease with increasing distance from the African continent [4]. The aeolian transport of diatoms and phytolyths from continental fresh water deposits in the Sahara and Sahel [4,34] should be investigated to assess relative contribution to high incidence of environmental airway diseases in the Canaries. We are not aware of detailed clinic studies relating natural (desert) diatom dust with respiratory diseases. Furthermore, concentrations of airborne diatom particles from African deserts and professional exposure to diatom dust are not comparable [35]. Diatoms transported with the dust plumes to the Canaries augment the overall silica content of the aerosols, and silicosis caused by non-crystalline forms of silica have not only occupational but environmental etiology [36]. On the contrary, non-industrial silicosis (known as "desert lung") has been reported decades ago from autopsy of Bedouine lung tissue, showing high amounts of silica dust of respirable size [37]. More study cases of non-industrial lung or environmental silicosis, have been reported for regions chronically exposed to desert dust (*i.e.* Himalaya [38]).

The Tenerife highland (> 2000 m a.s.l.) is not a populated area, but it receives > 4 million visitors/year, the most visited volcanic area of the world after Mount Fuji, Japan. There is evidence that symptoms of asthma in lowland patients improve with therapy of high-elevation stays [39,40]; however, episodic but severe dust events may imply additional health risks given the extreme conditions at these altitudes for such long permanencies (moderate hypoxia, high aridity of this area and increased sun radiation exposure, among other stressors). Origin and type of air mass and aerosol load can be predicted and used to establish and prevent potential interactions with respiratory disease in susceptible visitors to the island's National Park.

Particles of different sizes have different ability to penetrate the pulmonary system and reach the lung parenchyma [41]. Modelling of aerosol inhalation schematize the stratification of particle deposition along the human airways depending on their aerodynamic diameter [42]. Particulate matter (PM) < 10 μm (PM_{10}) penetrate the tracheobronchial region; increased deposition in the oropharynx occurs with particles larger than 6 μm, whereas central airway deposition peaks within the 4-6 μm range. Particles like those in **Figures 4(B)**, **4(D)** or **4(I)** would be able to reach the central airways. PM between 2-4 μm ($PM_{2.5}$) reach the alveolar cavities (*i.e.* lung periphery), where their damage is greater due to higher reactivity [42]. Particles like the one depicted in **Figure 4(K)** seem of potential interest in this range.

Although a great proportion of diatom remains are within or above the PM_{10} fraction (particulate matter 10 micrometers in diameter), thereby being potentially retained by the trachea and bronchia, a great amount of test fragments are within the $PM_{2.5}$ fraction, and thus could reach the lung alveolar system [35]. In addition, the role of diatom thecae as carriers of particles of health interest (e.g. bacteria, viruses, fungal or protozoan spores or cists, pollen) can be important, since: a) these remains co-dominate, along with quartz mineral, in many of the dust events of North African origin, and b)

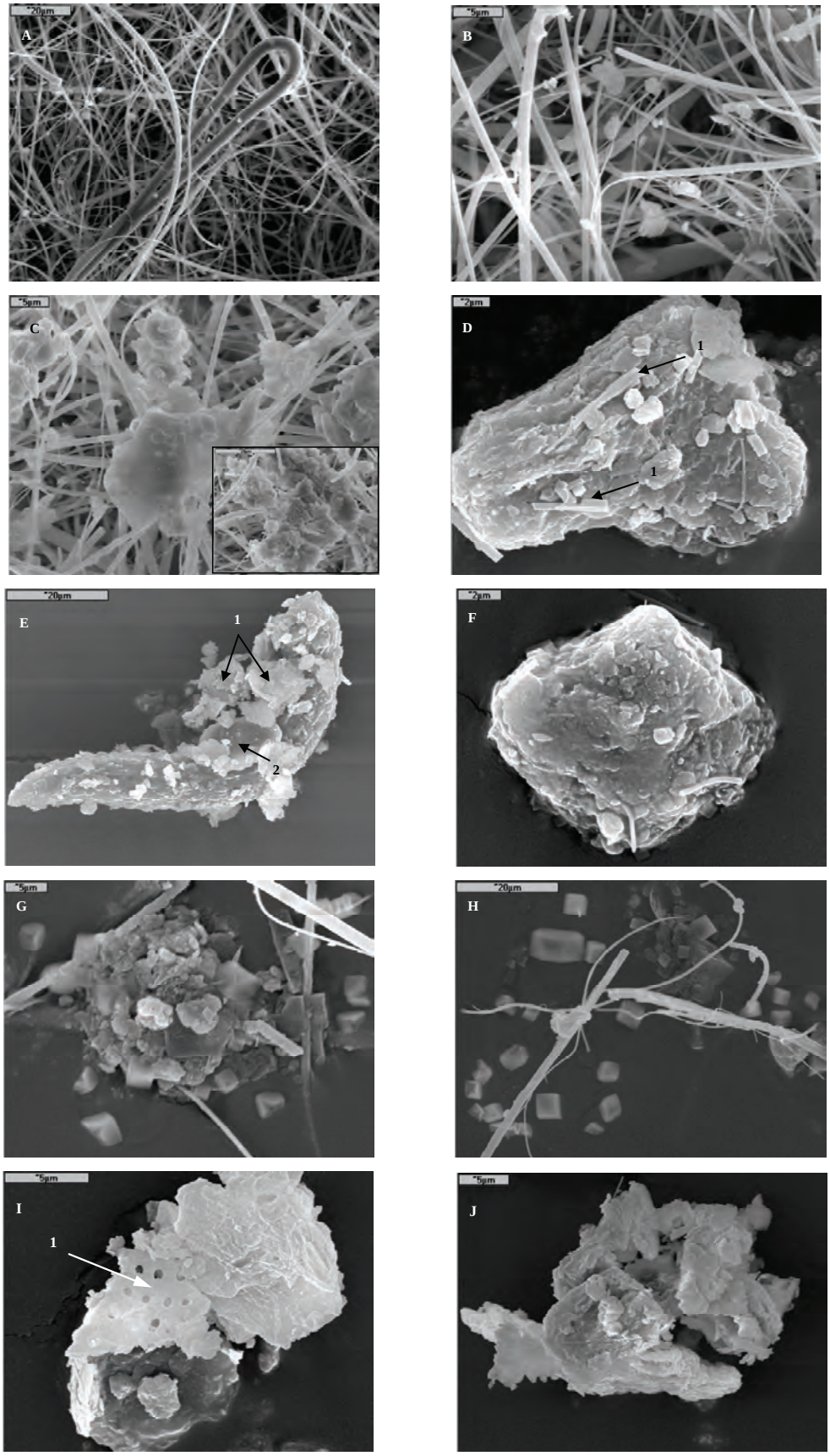

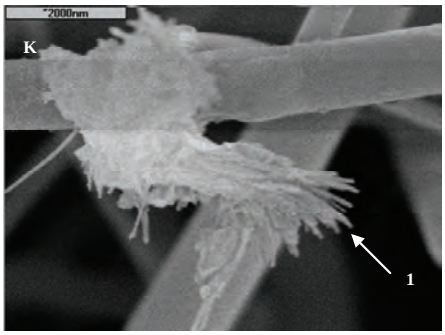

Figure 4. SEM photographs of TSP and $PM_{2.5}$, mineral aerosols of crustal, marine and anthropogenic origin identified in dust filters from Tenerife (Canary Islands) during an African dust intrusion. **(A)-(B)**: two general views of a relatively clean filter with few mineral particles (without African dust) from Izaña. **(C)**: filters with dense platy clay microcrystals typical of a dust intrusion (Santa Cruz). **(D)**: Agglomeration of clay on carbon adhesive film (EDX: Si, Al, K, Ca, Fe, Na, Mg) (Izaña); 1: elongate rectangles on the aggregate surface are gypsum rods (EDX: Ca, S, O). **(E)-(F)**: clay microcristals; 1: clay aggregates; 2: flat and rounded quartz particles adhered (Izaña). **(G)-(H)**: halite (EDX: Na, Cl), clusters of cubic crystals from marine aerosol (Santa Cruz). **(I)-(J)**: conglomerates of quartz clay grades with diatom test fragments of laminar habit (1); **(K)**: fibrous particle of unknown origin around the 2 μm size range attached to filter; note the "fringed" end (1).

due to their structural complexity, large adsorption surface and cavities for shelter of diverse particles, and lateral dimension.

We found only a fungal remain in our dust samples. However, fungal species linked to respiratory disease are surprisingly frequent from desert areas [6]. Some deserts next to urban areas behaved as differentiated sources of Basydiomycotan fungi [43]. Kellogg *et al.* [10] detected *Alternaria*, *Cladosporium* and *Aspergillus* in dust samples from Mali. *Cladosporium* was also isolated from African dust in the Virgin Islands (Caribbean) [7]. Prospero *et al*. [44] isolated more than 20 fungal taxa from North African dust in Barbados, finding low percentages of *Alternaria*. With *Cladosporium*, *Alternaria* is one of the most abundant spore-forming fungi in dry and warm regions such as the subtropical Canary Islands [6]. *Alternaria* was also a very frequent bioaerosol in a study at mid elevation on Tenerife [45]. In other dry climates (e.g. Phoenix, Arizona), *A. alternata* and *A. raphani* has been detected in PM_{10} from desert neighbouring urban areas [43], and Glikson *et al.* [46] found that fungal spores were predominant over other bioaerosols such as pollen in Brisbane (Australia). We failed to find other fungal remains through SEM, a surprising result since we expected a higher importance of this type of particles during dust events, judging from literature. However, we isolated and cultivated other common allergenic fungi (*Aspergillus*, *Penicillium* and *Cladosporium*) which were not detected by SEM from the same filter samples (unpublished data).

Apart from plant pathogen, *Alternaria* is a cosmopolitan, saprophytic soil fungus comprising several species pathogenic for immunocompromised hosts [47,48]. *A. alternata* causes environmental allergic alveolitis, and for many authors it is the most important fungi in allergy causation, especially in Mediterranean areas [49]. Allergic fungal sinusitis is due to finely dispersed fungal spores in air, and 56-95% percent of patients diagnosed with chronic rhinosinusitis presented fungus in nasal secretions [50,51]. We should investigate frequency and concentration of fungal spores in this insular region and if causes for high prevalence of allergies in areas affected by dust intrusions might be attributed to airborne fungal species.

Around 20% of the human population of the Canaries suffers from allergy or allergy-related diseases [52]. However, prevalence of diseases such as asthma or allergies has not been paid enough attention regarding associations with climatic factors, climate change or influence of atmospheric phenomena such as Saharo-Sahelian dust episodes on the archipelago [24]. The complex mixture of particles of respirable size identified by SEM in this study may play a role in sensitizing and thus preparing the road for other "opportunistic" airway diseases. Processes of aerosol particles deposition and effects in the airways depend on particle size and form, and respiratory conditions [35], but the mechanisms by which both mineral aerosols and bioaerosols act in the airway pathologies are poorly comprised.

In populated areas, mixtures amongst particulate matter of different origins are common during dust intrusions, as revealed by our SEM analysis. In many instances, allergens invade the respiratory tract in or on a different particle, and it is today clear that exposure to an

allergen on or within a carrier pollutant can substantially enhance its allergenic potential [53,54]. Many of the aerosol types overviewed here can incorporate additional pollutants from the atmosphere, and in case of bioaerosols, surface proteins can be altered and then released into the respiratory system. Synergies between anthropogenic aerosols and bioaerosols also deserve attention. Diatom tests, quartz and gypsum fiber-like particles mix to form aggregates, and pollen grains can transport those and other mineral particles (**Figures 4(B)-4(F)**, **4(J)**). Important synergies between bioaerosols (mostly pollen, fungi and soil bacteria, but perhaps also viruses) and other atmospheric pollutants (*i.e.* NOx, VOCs—volatile organic compounds—ozone, tobacco smoke) have been reported in relation with increasing asthma prevalence in urban areas [46]. Pollen secrete eicosanoid-like molecules (*i.e.* leukotriene-like) which act signaling in immunity and inflammation, and such releasing is favoured by contact of pollen with gases from traffic exhaust and petrol industry [54].

The study of the origin of the air mass through back trajectory would allow knowing the potential of remote subtropical and tropical areas for issuing other disease vectors in dust plumes to the Canary Islands and other places. This tool should be integrated along with quantitative and qualitative aerosol characterization in the creation of prevention nets [12,55]. Attention should be paid to candidate disease vectors that can be predicted, through tracing of backward trajectories, to reach the islands with dust intrusions in the next future. In fact, nearly 80% of the air masses reaching the islands have a direct North African origin. SEM analysis is useful as a complementary tool in the morphological identification of new particle types or combinations of particles of interest in disease causation [56]. Moreover, exploratory biopsy of the respiratory mucosa through SEM analysis would prove useful in identifying PM types and linking them as causal factors with atmospheric dust PM. Nevertheless, molecular and clinical characterization of the active substances associated to aerosols is a critical and unavoidable step for prevention of dust mass impact on human health [54]. In the Caribbean, relationship between asthma attendance peaks and African dust intrusions have previously been revealed [23]. For the Canary Islands, where African dust intrusions exert their effects before reaching the Caribbean, the studies dealing with problems posed by dust intrusions on public health remain anecdotic, whereas effective control of dust effects on human population is a major sanitary goal [12].

5. CONCLUSIONS

Aeolian dust reaching the high altitude areas of the Tenerife island has a larger contribution of North African air masses, and is formed by a structurally complex mixture of biogenic and abiogenic particles, of respirable size and contrasting morphology; we found that the diatom test fraction is qualitatively relevant (along with the dominant, background quartz fraction), whereas other biogenic fractions such as pollen or fungi are more scarce, or difficult to resolve, at least by means of SEM, and at these elevations within the island. Increasing aridity periods, irregular and torrential rains, changes in vegetation cover and desertification would affect the aerosol load (both biogenic and abiogenic in origin) received by these subtropical islands as dust intrusion events increase in frequency [16,17,57].

6. ACKNOWLEDGEMENTS

We thank Juan Luis González Álvarez (SEGAI facilities, ULL) and Debora Gómez for assistance with SEM. Prof. Dr. Óscar Romero (Universitaet Bremen, Germany) gently identified diatoms. We acknowledge to the MEC (Ministry of Education and Science, Spain) and F.E.D.E.R. founds (E.U.) for the economical support of the following projects: CGL2005-03428-C04-02, CGL2007-66477-C02-02/CLI, CGL2008-04740 and PI042005/033. Finally, the authors wish to express their appreciation to the operators of Izaña Atmospheric Observatory for their help on running the instruments.

REFERENCES

[1] Hernández, F., Alonso-Pérez, S., Hernández-Armasa, J., Cuevas, E., Karlsson, L. and Romero-Campos, P.M. (2005) Influence of major African dust intrusions on the ^{137}Cs and ^{40}K activities in the lower atmosphere at the Island of Tenerife. *Atmospheric Environment*, **39**, 4111-4118.

[2] Main, C.E. (2003) Aerobiological, ecological, and health linkages. *Environment International* 2003, **29**, 347-349.

[3] Kuhlman, K.R., Allenbach, L.B., Ball, C.L., Fusco, W.G., La Duc, M.T., Kuhlman, G.M., Anderson, R.C., Erickson, I.K., Stuecker, T., Benardini, J. and Crawford, R.L. (2005) Enumeration, isolation, and characterization of ultraviolet (UV-C) resistant bacteria from rock varnish in the Whipple Mountains, California. *Icarus*, **174**, 585-595.

[4] Romero, O.E., Lange, C.B., Swap, R.J. and Wefer, G. (1999) Eolian-transported freshwater diatoms and phytoliths across the equatorial Atlantic record temporal changes in Saharan dust transport patterns. *Journal of Geophysical Research*, **104(C2)**, 3211-3222.

[5] Gorbushina, A.A., Kort, R., Schulte, A., Lazarus, D., Schnetger, B., Brumsack, H.-J., Broughton, W.-J. and Favet, J. (2007) Life in Darwin's dust: Intercontinental transport and survival of microbes in the nineteenth century. *Environmental Microbiology*, **9**, 2911-2922.

[6] Lacey, J. (1991) Aerobiology and health: The role of airborne fungal spores in respiratory disease. In: Hawksworth, D.L. Ed., *Frontiers in Mycology*. C. A. B. International, Wallingford, 157-185.

[7] Griffin, D.W., Garrison, V.H., Herman, J.R. and Shinn, E.

A. (2001a) African desert dust in the Caribbean atmosphere: Microbiology and public health. *Aerobiologia*, **17**, 203-213.

[8] Griffin, D.W., Kellogg, D.A. and Shinn, E.A. (2001b) Dust in the wind: Long range transport of dust in the atmosphere and its implications for global public and ecosystem health. *Global Change & Human Health*, **2**, 20-33.

[9] Griffin, D.W., Westphal, D.L. and Gray, M.A. (2006) Airborne microorganisms in the African desert dust corridor over the mid-Atlantic ridge, Ocean Drilling Program, Leg 209. *Aerobiologia*, **22**, 211-226.

[10] Kellogg, C.A., Griffin, D.W., Garrison, V.H., Peak, K., Royall, N., Smith, R.R. and Shinn, E.A. (2004) Characterization of aerosolized bacteria and fungi from desert dust events in Mali, West Africa. *Aerobiologia*; **20**, 99-110.

[11] Salvaggio, J.E. (1994) Inhaled particles and respiratory disease. *The Journal of Allergy and Clinical Immunology*, **94**, 304-309.

[12] García Carrasco, J., Hernández Vázquez, A., Blasco de la Fuente, A., Rodríguez Hernández, B.C., Rancaño Gila, E. and Núñez Díaz, S. (2001) Invasión de viento sahariano y su impacto en la asistencia sanitaria urgente. *Emergencias*, **13**, 372-376.

[13] Pope, C.A., Burnett, R.T., Thun, M.J., Calle, E.E., Krewski, D., Ito, K. and Thurston, G.D. (2002) Lung cancer, cardiopulmonary mortality, and long-term exposure to fine particulate air pollution. *JAMA*, **287**, 1132- 1141.

[14] Lee, J.-T., Son, J.-Y. and Cho, Y.-S. (2007) A comparison of mortality related to urban air particles between periods with Asian dust days and without Asian dust days in Seoul, Korea, 2000-2004. *Environmental Research*, **105**, 409-413.

[15] Prospero, J.M. and Lamb, J.P. (2003) African droughts and dust transport to the Caribbean: Climate change and implications. *Science*, **302**, 1024-1027.

[16] Viana, M., Querol, X., Alastuey, A., Cuevas, E. and Rodríguez, S. (2002) Influence of African dust on the levels of atmospheric particulates in the Canary Islands air quality network. *Atmospheric Environment*, **36**, 5861-5875.

[17] Viana, M., Querol, X., Alastuey, A., Ballester, F., Llop, S., Esplugues, A., Fernández-Patier, R., García dos Santos, S. and Herce, M.D. (2008) Characterising exposure to PM aerosols for an epidemiological study. *Atmospheric Environment*, **42**, 1552-1568.

[18] Criado, C. and Dorta P. (2003) An unusual "blood rain" over the Canary Islands (Spain). The storm of January 1999. *Journal of Arid Environments*, **55**, 765-783.

[19] Alonso-Pérez, S., Cuevas, E., Querol, X., Viana, M. and Guerra, J.C. (2007) Impact of the Saharan dust outbreaks on the ambient levels of total suspended particles (TSP) in the marine boundary layer (MBL) of the Subtropical Eastern North Atlantic Ocean. *Atmospheric Environment*, **41**, 9468-9480.

[20] Querol, X., Alastuey, A., Moreno, T., Vian, M.M., Castillo, S., Pey, J., Rodríguez, S., Artiñano, B., Salvador, P., Sánchez M., García, S., Herce, M.D., Fernández-Patier, R., Moreno-Grau, S., Minguillón, M.C., Monfort, E., Sanz, M.J., Palomo-Marín, R., Pinilla-Gil, E., Cuevas E., De La Rosa, J. and Sánchez, A. (2008) Spatial and temporal variations in airborne particulate matter (PM10 and PM2.5) across Spain 1999-2005. *Atmospheric Environment*, **42**, 3964-3979.

[21] Prospero, J.M. (1999a) Long-term measurements of the transport of African mineral dust to the south-eastern United States: Implications for regional air quality. *Journal of Geophysical Research*, **104**, 917-927.

[22] Prospero, J.M. (1999b) Assessing the impact of advected African dust on air quality and health in the Eastern United States. *Human and Ecological Risk Assessment*, **5**, 471-479.

[23] Prospero, J.M., Blades, E., Naidu, R., Mathison, G., Thani, H. and Lavoie, M.C. (2008) Relationship between African dust carried in the Atlantic trade winds and surges in pediatric asthma attendances in the Caribbean. *International Journal of Biometeorology*, **52**, 823-832.

[24] Julià Serdà, G., Cabrera Navarro, P., Acosta Fernández, O., Martín Pérez, P., Batista Martín, J., Alamo Santana, F., Rodríguez de Castro, F. and Antó Boqué, J.M. (2005) High prevalence of asthma symptoms in the Canary Islands: climatic influence? *J. Asthma*, **42**, 507-511.

[25] Rodríguez, S. (1999) Comparación de la variaciones de ozono superficial asociadas a procesos de transporte sobre y bajo la inversión temperatura subtropical en Tenerife. Unpublished Thesis, Universidad de La Laguna, Santa Cruz de Tenerife, Spain.

[26] Alastuey, A., Querol, X., Castillo, S., Escudero, M., Avila, A., Cuevas, E., Torres, C., Romero, P.M., Expósito, F., García, O.E., Díaz, J.P., van Dingenen, R. and Putaud, J.P. (2005) Characterisation of TSP and PM2.5 at Izaña and Sta. Cruz de Tenerife (Canary Islands, Spain) during a Saharan dust episode (July 2002). *Atmospheric Environment*, **39**, 4715-4728.

[27] Díaz, A.M. (2006) Caracterización de los aerosoles atmosféricos y su influencia en los niveles de radiación UV en la región de Canarias, Ph.D. Thesis, University of La Laguna, Tenerife, Spain.

[28] Díaz, A.M., Díaz, J.P., Expósito, F.J., Hernández-Leal, P.A., Savoie, D. and Querol, X. (2006) Air masses and aerosols chemical components in the free troposphere at the Subtropical Northeast Atlantic region, *Journal of Atmospheric Chemistry*, **53**, 63-90.

[29] Pósfai, M. and Molnár, Á. (2000) Aerosol particles in the troposphere: A mineralogical introduction. In: Vaughan, D.J. and Wogelius, R.A., Eds., *Environmental Mineralogy*. Eötvös University Press, Budapest, 197-252.

[30] Thomas, D. Potter, T.D. and Colman, B.R. (2003) Handbook of weather, climate, and water. John Wiley & Sons, Hoboken.

[31] Gelado, M.D., Dorta, P., Hernández, J.J., Collado, C., Rodríguez, M.J., Cardona, P. and Siruela, V. (2004) Characterisation of African dust outbreaks in Gran Canaria (Canary Islands). *Geophysical Research Abstracts*, **6**, 05227.

[32] Gómez, N., Riera, J.L. and Sabater, S. (1995) Ecology and morphological variability of *Aulacoseira granulata* (Bacillariophyceae) in Spanish reservoirs. *Journal of Plankton Research*, **17**, 1-16.

[33] Darby, D.A., Burckle, L.H. and Clark D.L. (1974) Airborne dust on the Arctic ice pack, its composition and fallout rate. *Earth and Planetary Science Letters*, **24**, 166-172.

[34] Lange, C.B., Romero, O.E., Wefer, G. and Gabric, A. (1998) Offshore influence of coastal upwelling off Mauritania, NW Africa, as recorded by diatoms in sediment traps at 2195 m water depth. *Deep-Sea Research*, **45**, 985-

1013.
[35] Derbyshire, E. (2007) Natural minerogenic dust and human health. *AMBIO*: *A Journal of the Human Environment*, **36**, 73-77.
[36] Kusaka, Y., Hering, K. and Parker, J. (2005) International classification of HRCT for occupational and environmental respiratory diseases. Springer-Verlag, Tokyo.
[37] Bar-Ziv, J. and Goldberg, G.M. (1974) Simple siliceous pneumoconiosis in Negev Bedouins. A*rch Environ Health*, **29**, 121
[38] Norboo, T., Angchuk, P.T., Yahya, M., Kamat, S.R., Pooley, F.D., Corrin, B., Kerr, I.H., Bruce, N. and Ball, K.P. (1991) Silicosis in a Himalayan village population: Role of environmental dust. *Thorax*, **46**, 341-343.
[39] Simon, H., Grotzer, M., Nikolaizik, W., Blaser, K. and Schóni, M. (1994) High altitude climate therapy reduces peripheral blood T lymphocyte activation, eosinophilia, and bronchial obstruction in children with house-dust mite allergic asthma. *Pediatric Pulmonology*, **17**, 304-311.
[40] Schultze-Werninghaus, G. (2006) Should asthma management include sojourns at high altitude? *Chemical Immunology and Allergy*, **91**, 16-29.
[41] Silson, J.E. (1950) Dust inhalation in relation to pulmonary disease. *Chest*, **18**, 562-573.
[42] Mitchell, J.P. and Nagel, M.W. (2004) Particle size analysis of aerosols from medicinal inhalers. *KONA*, **22**, 32-65.
[43] Boreson, J., Dillner, A.M. and Peccia, J. (2004) Correlating bioaerosol load with $PM_{2.5}$ and PM_{10} concentrations: A comparison between natural desert and urban-fringe aerosols. *Atmospheric Environment*, **38**, 6029-6041.
[44] Prospero, J.M., Blades, E., Mathison, G. and Naidu, R. (2005) Interhemispheric transport of viable fungi and bacteria from Africa to the Caribbean with soil dust. *Aerobiologia*, **21**, 1-19.
[45] La Serna, I. and Domínguez, M.D. (2003) Pólenes y esporas aerovagantes en Canarias: Incidencia en alergias. Colección Materiales Didácticos Universitarios, Serie Botánica 1, SPULL, Tenerife.
[46] Glikson, M., Rutherford, S., Simpson, R., Mitchell, C. and Yago, A. (1995) The microscopic and submicron components of atmospheric particulates occurring during high asthma periods in Brisbane, Queensland, Australia. *Atmospheric Environment*, **29**, 549-562.
[47] Morrison, V.A. and Weisdorf, D.J. (1993) *Alternaria*: A sinonasal pathogen of immunocompromised hosts. *Clinical Infectious Diseases*, **16**, 265-270.
[48] Hospenthal, D.R. and Bennett, J.E. (2000) Miscellaneous fungi and Prototheca. In: Mandell, G.L., Bennet, J.E. and Dolin, R. Eds., *Principles and practice of infectious diseases*, 5th Edition, Livingstone, Philadelphia, 2772-2780.
[49] D'Amato, G., Chatzigeorgiou, G., Corsico, R., Gioulekas, D., Jäger, L., Jäger, S., Kontou-Fili, K., Kouridakis, S., Liccardi, G., Meriggi, A., Palma-Carlos, A., Palma-Carlos, M.L., Pagan, A., Parmiani, S., Puccinelli, P., Russo, M., Spieksma, F.T., Torricelli, R. and Wuthrich, B. (1997) Evaluation of the prevalence of skin prick test positivity to *Alternaria* and *Cladosporium* in patients with suspected respiratory allergy. EEACI Position Paper. *Allergy*, **52**, 711-716.
[50] Lebowitz, R.A., Waltzman, M.N., Jacobs, J.B., Pearlman, A. and Tierno, P.M. (2002) Isolation of fungi by standard laboratory methods in patients with chronic rhinosinusitis. *Laryngoscope*, **112**, 2189-2191.
[51] Braun, H., Buzina, W., Freudenschuss, K., Beham, A. and Stammberger, H. (2003) "Eosinophilic fungal Rhinosinusitis": A common disorder in Europe? *Laryngoscope*, **113**, 264-269.
[52] Gaig, P., Ferrer, M., Muñoz-Lejarazu, D., Lleonart, R., García-Abujeta, J.L., Caballero, T., Rodríguez, A., Echechipia, S., Martínez-Cocera, C., Domínguez, F.J., Gonzalo, M.A. and Olona, M. (2004) Prevalencia de alergia en la población adulta española. *Alergología e Inmunología Clínica*, **19**, 68-74.
[53] Salvaggio, J.E. and O'Neil, C.E. (1992) Pathogenetic mechanisms in occupational hypersensitivity states. *Immunology and Allergy Clinics of North America*, **4**, 711-729.
[54] Behrendt, H., Krämer, U., Schäfer, T., Kasche, A., Eberlein-König, B., Darsow, U. and Ring, J. (2001) A research concept to study the role of environmental pollutants in allergy. *Allergy and Clinical Immunology International*, **13**, 122-128.
[55] Mastalerz, M., Glikson, M. and Simpson, R.W. (1998) Analysis of atmospheric particulate matter; application of optical and selected geochemical techniques. *International Journal of Coal Geology*, **37**, 143-155.
[56] Wittmaack, K., Wehnes, H., Heinzmann, U. and Agerer, R. (2005) An overview on bioaerosols viewed by scanning electron microscopy. *Science of the Total Environment*, **346**, 244- 255.
[57] Rodríguez, S., Querol, X., Alastuey, A., Kallos, G. and Kakaliagou, O. (2001) Saharan dust contributions to PM10 and TSP levels in Southern and Eastern Spain. *Atmospheric Environment*, **35**, 2433-2447.

Vol.2, No.10, 1130-1137 (2010)
doi:10.4236/ns.2010.210140

Natural Science

The Rich-Gini-Simpson quadratic index of biodiversity

Radu Cornel Guiasu[1], Silviu Guiasu[2]

[1]Environmental and Health Studies Program, Department of Multidisciplinary Studies, Glendon College, York University, Toronto, Canada; rguiasu@glendon.yorku.ca;
[2]Department of Mathematics and Statistics, Faculty of Pure and Applied Sciences, York University, Toronto, Canada; guiasus@pascal.math.yorku.ca.

Received 6 August 2010; accepted 10 September 2010; accepted 13 September 2010.

ABSTRACT

The Gini-Simpson quadratic index is a classic measure of diversity, widely used by ecologists. As shown recently, however, this index is not suitable for the measurement of beta diversity when the number of species is very large. The objective of this paper is to introduce the Rich-Gini-Simpson quadratic index which preserves all the qualities of the classic Gini-Simpson index but behaves very well even when the number of species is very large. The additive partitioning of species diversity using the Rich-Gini-Simpson quadratic index and an application from island biogeography are analyzed.

Keywords: Rich-Gini-Simpson Index of Species Diversity; Additive Partitioning of Diversity; Island Biogeography; Biodiversity

1. INTRODUCTION

Measuring the diversity of species in a habitat has been an important area of interest in fields such as conservation biology, ecology, and biogeography for the last several decades [1]. Let us assume that there are n species and let:

$$p_i > 0, \quad (i = 1, \ldots, n), \quad \sum_i p_i = 1, \tag{1}$$

be the relative frequency distribution of these species in the respective habitat. There are three classic measures of diversity:

a) The number of species, or richness: n;

b) The Gini-Simpson quadratic index (abbreviated in this paper as GS):

$$GS = \sum_i p_i(1 - p_i) = 1 - \sum_i p_i^2, \tag{2}$$

introduced by Gini [2] and adapted for biological studies by Simpson [3];

c) The Shannon entropy (abbreviated as H):

$$H = -\sum_i p_i \ln p_i, \tag{3}$$

introduced by Shannon [4], as the discrete variant of the continuous entropy defined by Boltzmann [5] in statistical mechanics. There is an extensive literature [1,6-17] about the properties and applications of these measures of diversity.

When the number of species n and the relative abundance of species (1) are the only sources of information available, many other measures of diversity have been proposed. Recently, Jost [18,19] pleaded in favor of the "true" measure of diversity, introduced by Hill [20]:

$$N_r = \left(\sum_i p_i^r \right)^{1/(1-r)}. \tag{4}$$

For $r = 0$, we get: $N_0 = n$. For $r = 1$, N_r is not defined because the denominator of the exponent, $1 - r$, is equal to zero. However, the limit of N_r when r tends to 1 is $\exp(H)$. For $r = 2$ we get $1/(1 - GS)$. In fact, the natural logarithm of (4), *i.e.* $\ln N_r$, is just Rényi's entropy [21]. There are no sound reasons to call (4) a "true" measure of diversity. It is simply a unifying notation, as mentioned in [20]. Besides, by performing mathematical transformations on classic measures of diversity, like taking the exponential of the Shannon entropy or the reciprocal of the Gini-Simpson quadratic index, for example, we obtain other measures that lose, however, some essential features of the original measures, such as concavity, for instance. Concavity is an essential property of any measure that can be used in an additive partitioning of species diversity. Hoffmann and Hoffmann [22] are right when asking: "Is there a 'true' measure of diversity?" As noticed by Ricotta [23], there is a "jungle of measures of diversity" in the current conservation biology literature. Under the circumstances, perhaps the best strategy is to remember Occam's razor and, trying to keep things simple, it may be easier to just

go back to the classic measures of diversity mentioned before and see how they can be adjusted to address new problems under new circumstances.

The species richness n is very simple but ignores the abundance of species. Shannon's entropy has excellent properties but is difficult to estimate and maximizing it subject to linear constraints, generally gives a solution satisfying exponential equations which cannot be solved analytically. On the other hand, the Gini-Simpson quadratic index is simpler and generally seems to be preferred by ecologists. Jost [18,19,24], however, noticed a troubling anomaly related to GS. Indeed, if this measure is used in the additive partitioning of species diversity, the corresponding beta diversity approaches zero when the number of species is very large. Thus, for two habitats with no species in common, for instance, the between-habitat diversity tends to zero when the number of species in one of the habitats, or in both of them, tends to infinity, instead of becoming larger as is obviously the case in actual fact.

The objective of this paper is to show that the anomaly just mentioned can be easily fixed. The product between the species richness a) and the measure of diversity c), called here the Rich-Gini-Simpson quadratic index and abbreviated as RGS, preserves all the basic properties of GS and behaves well when the number of species is large. Therefore, RGS is suitable for use in the additive partitioning of species diversity. Subsequently, the RGS index is applied to data on the avifaunal diversity on several tropical Indian Ocean islands, using some of the numerical results obtained by Adler [25], in order to show how the alpha, beta, and gamma species diversities change when the usual equal weights for the various habitats are replaced by the relative areas and the relative elevations of the respective islands.

2. THE RICH-GINI-SIMPSON INDEX

If there are n species in a certain habitat and their relative abundance is given by (1), the Rich-Gini-Simpson quadratic index is

$$RGS = n\sum_i p_i(1-p_i) = n(1-\sum_i p_i^2). \quad (5)$$

The concavity of RGS and the maximum value of RGS are analyzed in the Appendix. Thus, we have: $0 \le RGS \le n-1$, the maximum corresponding to the uniform distribution: $p_i = 1/n$, $(i = 1,\ldots,n)$. As $GS = RGS/n$, the maximum value of GS is $\max_p GS = 1-1/n$, corresponding to the uniform distribution as well. The essential difference between these two indexes is that GS is bounded by 1 and tends to 1 when the number of species n tends to infinity, whereas RGS is not bounded and tends to infinity when the number of species n tends to infinity. Shannon's entropy, on the other hand, has the maximum $\max_p H = \ln n$, which tends to infinity when the number of species n tends to infinity, but it increases much much more slowly than $\max_p RGS = n-1$.

Pleading against the use of the GS index, Jost [24] gave the following example: "Suppose a continent has a million equally-common species, and a meteor impact kills 999,900 of the species, leaving 100 species untouched. Any biologist, if asked, would say that this meteor impact caused a large absolute and relative drop in diversity. Yet GS only decreases from 0.999999 to 0.99, a drop of less than 1%". Jost concluded that: "[The] ecologists relying on GS will often misjudge the magnitude of ecosystem changes. This same problem arises when Shannon entropy is equated with diversity. In contrast, $N_2\ldots$ drops by the intuitively appropriate 99.99%". This example shows that there is indeed a troubling anomaly in using GS when the number of species is very large. But RGS has no such a drawback. Indeed, if before the cataclysm there are $n = 1{,}000{,}000$ equally abundant species, then:

$$GS = 1-\frac{1}{n} = 0.999999; \quad H = \ln n = 13.8155105;$$

$$\exp(H) = \exp(\ln n) = n = 1000000,$$

$$N_2 = n = 1000000, \quad RGS = n-1 = 999999.$$

After the cataclysm, there are only $n = 100$ equally abundant species left. Thus:

$$GS = 1-\frac{1}{n} = 0.99; \quad H = 4.605170186;$$

$$\exp(H) = \exp(\ln n) = n = 100,$$

$$N_2 = n = 100, \quad RGS = n-1 = 99.$$

Therefore, GS indicates a decrease in diversity equal to 0.999901%, which is obviously wrong, H indicates a decrease in diversity equal to 66.6666667%, which is not good enough, whereas RGS, $\exp(H)$ and N_2 give a decrease in diversity equal to 99.9900999% and 99.9900000%, respectively, in agreement with common sense. Let us note that, practically, RGS and $\exp(H)$ have the same maximum value when the number of species n is given, but the index $\exp(H)$ is not a concave function of the relative frequency distribution of species $p = (p_1,\ldots,p_n)$ and, consequently, it is not suitable to be used in the additive partitioning of species diversity, whereas the index RGS is.

3. THE ADDITIVE PARTITIONING OF SPECIES DIVERSITY USING RGS

MacArthur [26] pointed out the need for a theory of within-habitat and between-habitat species diversities.

Identify applicable sponsor/s here. (*sponsors*)

He, together with Recher and Cody [27], proposed a measure of the difference between the species diversities of two habitats based on Shannon's entropy and using equal relative weights for habitats. This measure was also used in the influential book "The theory of island biogeography" by MacArthur and Wilson [28]. Rao [29], without mentioning the paper [27], extended the measure of the difference between the species diversities of two habitats, based also on Shannon's entropy but using arbitrary weights assigned to the two habitats. Whittaker [30,31] proposed linking diversity components between ecological scales by multiplication so that the gamma diversity, measuring the species diversity in a larger region consisting of several ecological communities taken together, is the product of the alpha diversity, which measures the mean species diversity in the local communities taken separately, and the beta diversity, representing the variation and changes in mean species diversity in a larger region which contains the local ecological communities taken together, as a whole. The beta diversity essentially measures the biogeographic changes in species diversity among various locations within a larger region. As such, the beta diversity can be important in leading to the development of geographic strategies for the conservation of species and habitats, as mentioned by Harrison and Quinn [32]. Routledge [33,34] developed Whittaker's approach. Allan [35] applied an additive linkage of species diversity components according to which the gamma diversity is partitioned into the sum of the alpha diversity and the beta diversity, using the Shannon entropy. Lande [36] dealt with an arbitrary number of habitats and arbitrary weights, using the Shannon entropy, and extended this approach to species richness and to the Gini-Simpson index, recommending the additive partitioning of species diversity as a unifying framework for measuring species diversity at different levels of ecological organization. As mentioned by Wagner, Wildi and Ewald [37], in contrast to the multiplicative model, by using the additive partitioning, all species diversity components are measured in the same way and expressed in the same units, so that they can be directly compared. Recently, it was pointed out that the additive partitioning of species diversity is an old idea which shows a new revival. According to Veech, Summerville, Crist and Gering [38], "Lande [36] appears to have been the first to place the additive partitioning of species diversity in the context of Whittaker's concepts of alpha, beta, and gamma diversities ⋯ Viewing gamma diversity as the sum of alpha and beta diversities leads to the most operational definition of beta diversity and quantifies it in a manner comensurate with the measurement of alpha and gamma diversities. In effect, the revival of additive diversity partitioning has given new meaning to beta diversity".

As RGS is a concave function, it is suitable for the additive partitioning of species diversity. Let $\{x_1,\ldots,x_n\}$ be a set of species and let $\{x_i, i\in I\}$ and $\{x_i, i\in J\}$ be the species from the habitats h_1 and h_2, respectively. The number of species from h_1 is n_1 and the number of species from h_2 is n_2. Obviously, $n_1\le n$, $n_2\le n$, and $n\le n_1+n_2$. The species $\{x_i, i\in I-J\}$ belong only to the habitat h_1, the species $\{x_i, i\in J-I\}$ belong only to the habitat h_2, whereas the species $\{x_i; i\in I\cap J\}$ belong to both habitats. We have $I\cup J=\{1,\ldots,n\}$.

Let $\{p_i, i\in I\}$ and $\{q_i, i\in J\}$ be the relative frequencies of the species from h_1 and h_2, respectively. We have:

$$p_i>0,\quad \sum_{i\in I}p_i=1;\quad q_i>0,\quad \sum_{i\in J}q_i=1.$$

In general, the beta diversity is the average between-habitat diversity, whereas the alpha diversity is the average diversity of the individual communities or the average within-habitat diversity. Using the additive partitioning of the species diversity, the gamma diversity is the sum of the alpha and beta diversities, or the average total diversity. Let $\lambda_1>0$, and $\lambda_2>0$, be two weights assigned to the habitats h_1 and h_2, respectively, such that $\lambda_1+\lambda_2=1$. We use these weights to calculate the average within-habitat species diversity, *i.e.* the alpha diversity, and the average relative frequency of the species used in the total species diversity of a larger region that includes the two individual habitats, *i.e.* the gamma diversity. If the two weights are equal, namely $\lambda_1=\lambda_2=1/2$, then the average is just the arithmetic mean. These weights, however, may represent the relative areas or the relative elevation of the two habitats, or any other quantitative characteristics of the habitats that can affect the diversity of the species. In this context, alpha diversity refers to the average species diversity in the two habitats h_1 and h_2, taken separately, gamma diversity refers to the species diversity in the habitats h_1 and h_2, averaged together, whereas beta diversity represents the average between-habitat species diversity as we move from the individual habitats h_1, h_2, averaged separately, to the larger region containing the union of h_1 and h_2, averaged together. We now use RGS to calculate the alpha, gamma, and beta species diversities. Denote by:

$$RGS(h_1)=n_1\sum_{i\in I}p_i(1-p_i)=n_1\left(1-\sum_{i\in I}p_i^2\right),$$

$$RGS(h_2)=n_2\sum_{i\in J}q_i(1-q_i)=n_2\left(1-\sum_{i\in J}q_i^2\right),$$

in which case the alpha diversity is:

$$\alpha - Div = \lambda_1 RGS(h_1) + \lambda_2 RGS(h_2).$$

The gamma-diversity is:

$$\gamma - Div = RGS(\lambda_1, h_1; \lambda_2, h_2) =$$
$$= n \sum_{i \in I \cup J} (\lambda_1 p_i + \lambda_2 q_i)(1 - \lambda_1 p_i - \lambda_2 q_i) =$$
$$= n\left[1 - \sum_{i \in I \cup J} (\lambda_1 p_i + \lambda_2 q_i)^2\right],$$

where $p_i = 0$ for $i \in J - I$, and $q_i = 0$ for $i \in I - J$.

The concavity of RGS allows the additive partition of species diversity, and the beta-diversity is:

$$\beta - Div = (\gamma - Div) - (\alpha - Div) =$$
$$= (n - \lambda_1 n_1 - \lambda_2 n_2) + \lambda_1 (n_1 - \lambda_1 n) \sum_{i \in I} p_i^2 +$$
$$+ \lambda_2 (n_2 - \lambda_2 n) \sum_{i \in J} q_i^2 - 2\lambda_1 \lambda_2 n \sum_{i \in I \cap J} p_i q_i \geq 0.$$

If both habitats contain the same species, then $I = J$, which implies $I \cap J = I$, $I \cup J = I$, $n_1 = n_2 = n$, and the beta-diversity has a simple expression:

$$\beta - Div = \lambda_1 \lambda_2 n\left(\sum_{i \in I} p_i^2 + \sum_{i \in I} q_i^2 - 2\sum_{i \in I} p_i q_i\right) =$$
$$= \lambda_1 \lambda_2 n \sum_{i \in I} (p_i - q_i)^2.$$

Clearly, if both habitats have the same species and the same abundance of these species, namely $p_i = q_i$, $(i = 1, \ldots, n)$, then $\beta - Div = 0$.

If the two habitats have no species in common, then $I \cap J = \varnothing$, $n = n_1 + n_2$, and the beta-diversity is:

$$\beta - Div = (n - \lambda_1 n_1 - \lambda_2 n_2) +$$
$$+ \lambda_1 (n_1 - \lambda_1 n) \sum_{i \in I} p_i^2 + \lambda_2 (n_2 - \lambda_2 n) \sum_{i \in J} q_i^2.$$

In particular, if the two habitats have no species in common and in each habitat the species have the same abundance, namely $p_i = 1/n_1$, $(i \in I)$, and $q_i = 1/n_2$, $(i \in J)$, then the beta-diversity is:

$$\beta - Div =$$
$$= \lambda_1 n_2\left(1 - \sum_{i \in I} p_i^2\right) + \lambda_2 n_1\left(1 - \sum_{i \in J} q_i^2\right) =$$
$$= \lambda_1 n_2\left(1 - \frac{1}{n_1}\right) + \lambda_2 n_1\left(1 - \frac{1}{n_2}\right),$$

which tends to $+\infty$ if n_1 tends to $+\infty$ or / and n_2 tends to $+\infty$.

Remark 1. The generalization of the results from this section to the case of an arbitrary number of habitats $h_1, \ldots, h_m$ is straightforward.

Remark 2. As mentioned by Lande [36], the ratio between the alpha diversity and the gamma diversity may be used as a similarity index, denoted here by Sim.

Arguing against the use of the GS index and the additive partitioning of species diversity, Jost [19] discussed the following example: "Suppose a continent with 30 million equally common species is hit by a plague that kills half the species. How do some popular diversity indices judge this drop in diversity? … The Shannon entropy only drops from 17.2 to 16.5; according to this index the plague caused a drop of only 4% in the 'diversity' of the continent. This does not agree well with our intuition that the loss of half the species and half the individuals is a large drop in diversity. The Gini-Simpson index drops from 0.99999997 to 0.99999993; if this index is equated with 'diversity', the continent has lost practically no 'diversity' when half its species and individuals disappeared". Instead of GS and H, Jost proposes the use of $\exp(H)$, which in his example has the value:

$$\exp(H) = \exp(\ln 30000000) = 30000000$$

before the plague and:

$$\exp(H) = \exp(\ln 15000000) = 15000000$$

after the plague, corresponding to a loss of 50% in diversity. However, as $\exp(H)$ is not a concave function, the additive partitioning of species diversity cannot be used and should be replaced by the multiplicative partitioning of species diversity as Whittaker [30,31] and Routledge [33,34] proposed. The situation, however, is not as hopeless as it may seem to be. In fact, it is not really hopeless at all. The additive partitioning of species diversity, so popular with some ecologists because it allows the alpha, beta, and gamma diversities to be measured in the same way and be expressed in the same units so that they can be directly compared, may in fact be preserved but GS has to be replaced by RGS. Thus, in the case just mentioned:

$$RGS = n - 1 = 30000000 - 1 = 29999999$$

before the plague and:

$$RGS = n - 1 = 15000000 - 1 = 14999999$$

after the plague, corresponding to a loss of 50% in diversity, in total agreement with common sense.

Example: If there are 30,000,000 species uniformly distributed in habitat h_1 and 15,000,000 of these species are uniformly distributed in habitat h_2, then, using the equal weights $\lambda_1 = \lambda_2 = 1/2$ and the GS index, we obtain:

$$GS(h_1) = 1 - \frac{1}{30000000} = 0.99999997,$$

$$GS(h_2) = 1 - \frac{1}{15000000} = 0.99999993,$$

which show almost no difference in species diversities. Also:

$$\alpha - Div = \frac{1}{2} GS(h_1) + \frac{1}{2} GS(h_2) = 0.99999995,$$
$$\gamma - Div = GS(\lambda_1, h_1; \lambda_2, h_2) =$$

$$= 1 - 15000000 \times \left(\frac{1}{60000000} \right)^2 -$$

$$-15000000 \times \left(\frac{3}{60000000} \right)^2 = 0.9999999,$$

$$\beta - Div = (\gamma - Div) - (\alpha - Div) = 0.0000000083,$$

which shows that the between-habitat species diversity is practically zero, in contrast to the fact that h_1 has a much higher species diversity than h_2. The similarity index is:

$$Sim = \frac{0.9999999}{0.99999995} = 0.99999995.$$

Using the Shannon entropy:

$$H(h_1) = \ln 30000000 = 17.2167,$$

$$H(h_2) = \ln 15000000 = 16.5235,$$

which show a very small difference in diversity, in fact a decrease of only 4.03% in h_2 with respect to h_1, contrary to common sense. Also:

$$\alpha - Div = \frac{1}{2} H(h_1) + \frac{1}{2} H(h_2) = 16.8702,$$

$$\gamma - Div = H(\lambda_1, h_1; \lambda_2, h_2) =$$

$$= 15000000 \times \left(-\frac{1}{60000000} \ln \frac{1}{60000000} \right) +$$

$$+ 15000000 \times \left(-\frac{3}{60000000} \ln \frac{3}{60000000} \right) = 17.0859,$$

$$\beta - Div = (\gamma - Div) - (\alpha - Div) = 0.2157,$$

a very small between-habitat species diversity. The similarity index is:

$$Sim = \frac{16.8702}{17.0859} = 0.98737756,$$

which is much too high.

Using now the equal weights $\lambda_1 = \lambda_2 = 1/2$ and the RGS diversity index, we obtain:

$$RGS(h_1) = 30000000 - 1 = 29999999,$$

$$RGS(h_1) = 15000000 - 1 = 14999999,$$

showing a decrease of 50% in species diversity in h_2 compared to h_1, in complete agreement with common sense. Also:

$$\alpha - Div = \frac{1}{2} RGS(h_1) + \frac{1}{2} RGS(h_2) = 2.25 \times 10^7,$$

$$\gamma - Div = RGS(\lambda_1, h_1; \lambda_2, h_2) =$$

$$= 30000000 \times \left[1 - 15000000 \times \left(\frac{1}{60000000} \right)^2 - \right.$$

$$\left. -15000000 \times \left(\frac{3}{60000000} \right)^2 \right] = 3 \times 10^7,$$

$$\beta - Div = (\gamma - Div) - (\alpha - Div) = 7.5 \times 10^6,$$

which show that the average between-habitat species diversity is 25% of the average total species diversity, whereas the average within-habitat species diversity is 75% of the average total species diversity. However, there are similarities between the two habitats, in the sense that h_2 contains half of the species of h_1, there are no species from h_2 that are not found in h_1, and both h_1 and h_2 have their species uniformly distributed. These features make h_2 somewhat similar to h_1. Using RGS, the similarity index is:

$$Sim = \frac{2.25 \times 10^7}{3 \times 10^7} = 0.75.$$

Remark 3. If habitat h_1 contains only one species x_1 and habitat h_2 contains only one species x_2, then, obviously:

$$RGS(h_1) = 0, \quad RGS(h_2) = 0, \quad \alpha - Div = 0,$$

$$\gamma - Div = RGS\left(\frac{1}{2}, h_1; \frac{1}{2}, h_2\right) = 2\left(1 - \frac{1}{4} - \frac{1}{4}\right) = 1,$$

$$\beta - Div = 1, \quad Sim = \frac{0}{1} = 0.$$

4. APPLICATION

There are many discussions of the role and applications of the measures of species diversity in biogeography (for instance, [15,35,39-43]). For example, MacArthur and Wilson [28] analyzed the impact of factors such as island area and the distance between the island and the mainland on the species diversity found on various islands. Some of the findings of this classic study were also applied to the study of habitat islands and nature reserves, as well as real islands, surrounded by the sea [43-45]. When MacArthur, Recher and Cody [27] introduced their measure of the average difference in species diversity between two habitats, they assigned equal weights to the respective habitats, taking into account only the relative frequencies of the species from the two habitats. More often than not, however, the habitats could be very different in other respects, and some additional factors, like area or elevation, for instance, may also have to be taken into account even when the habitats are located in the same general geographic region. These factors may be given various weights, which can be taken into account when calculating the alpha, beta, and gamma species diversities. If there are two habitats h_1, h_2, and their areas (in km^2) are a_1 and a_2, respectively, then we may attach to the two habitats the weights: $\lambda_1 = a_1/(a_1 + a_2)$ and $\lambda_2 = a_2/(a_1 + a_2)$ respectively. The same approach can be applied if the elevation (or some other factor of interest) is taken into account.

Adler [25] analyzed the birdspecies diversity on 14

different tropical archipelagoes and isolated islands in the Indian Ocean. The 139 species of resident birds, belonging to 33 families, found on these islands were grouped into three main categories: Continental, Indian Ocean (species found only on Indian Ocean islands, in general), and Endemic (species found only on a single Indian Ocean archipelago or island). **Table 1** contains the initial data set consisting of: the absolute frequencies of the Continental species (Cont), Indian Ocean species (IndOc), and Endemic species (End), the area (in km^2), and the elevation (highest peak in m), for seven archipelago / island habitats from the Indian Ocean, as given by Adler [25]. The seven archipelagoes or isolated islands (equivalent to seven distinct habitats for the purposes of this study) are: h_1: Christmas Island; h_2: Rodriguez; h_3: Mauritius; h_4: Reunion; h_5: Seychelles; h_6: Aldabra Islands; h_7: Comoro Islands. Our objective here is to calculate the numerical values of the alpha, gamma, and beta diversities, using the quadratic index RGS, when the weights assigned to the archipelagoes / islands are equal, or are the relative areas or the relative elevations of the respective archipelagoes / islands.

Table 2 contains: $p_{1,j}$, the relative frequency of Continental species in habitat h_j; $p_{2,j}$, the relative frequency of Indian Ocean species in habitat h_j; $p_{3,j}$, the relative frequency of Endemic species in habitat h_j;

Table 1. Application: The data set.

h_j	Cont	IndOc	End	Area(km^2)	Elevation(m)
h_1	7	0	2	135	361
h_2	1	0	12	119	396
h_3	7	6	15	1865	828
h_4	6	6	15	2512	3069
h_5	7	1	11	258	905
h_6	19	3	1	172	24
h_7	32	4	13	2236	2360

Table 2. Relative frequency and the RGS index.

h_j	$p_{1,j}$	$p_{2,j}$	$p_{3,j}$	$RGS(h_j)$
h_1	0.777778	0.000000	0.222222	0.691358
h_2	0.076923	0.000000	0.923077	0.284024
h_3	0.250000	0.214286	0.535714	1.813776
h_4	0.222222	0.222222	0.555556	1.777779
h_5	0.368421	0.052632	0.578947	1.578948
h_6	0.826087	0.130435	0.043478	0.896031
h_7	0.653061	0.081633	0.265306	1.489380

the RGS index of habitat h_j. We can see that Mauritius has a greater bird species diversity (RGS = 1.813776) than the other archipelagoes or islands considered here, followed by Reunion (RGS = 1.777779) and Seychelles (RGS = 1.578948). The lowest bird species diversity by far is on Rodriguez (RGS = 0.284024). These values have to be compared with the maximum value of RGS, which in this application is $n-1=3-1=2$.

Dealing with seven habitats, we calculate the alpha, gamma, and beta diversities according to the formulas:

$$\alpha - Div = \sum_{j=1}^{7} \lambda_j RGS(h_j),$$

$$\gamma - Div = RGS(\lambda_1, h_1; \ldots; \lambda_7, h_7) =$$

$$= 3 \times \left[1 - \sum_{i=1}^{3} \left(\sum_{j=1}^{7} \lambda_j \, p_{i,j} \right)^2 \right],$$

$$\beta - Div = (\gamma - Div) - (\alpha - Div),$$

where the weights are:

$$\lambda_j > 0, \quad (j = 1, \ldots, 7), \quad \sum_{j=1}^{7} \lambda_j = 1.$$

The similarity index is:

$$Sim = \frac{\alpha - Div}{\gamma - Div}.$$

Case 1. If we take all seven archipelago/island habitats together, as a group, and the weights are:

$$\lambda_j = \frac{area\ (h_j)}{area\ (h_1) + \ldots + area\ (h_7)}, (j = 1, \ldots, 7),$$

we get the corresponding relative area weights:

$$\lambda_1 = 0.018501, \lambda_2 = 0.016308, \lambda_3 = 0.255584,$$
$$\lambda_4 = 0.344251, \lambda_5 = 0.035357, \lambda_6 = 0.023571,$$
$$\lambda_7 = 0.306427,$$

for which we obtain:

$$\alpha - Div = 1.62633, \quad \gamma - Div = 1.86103,$$
$$\beta - Div = 0.234693, \quad Sim = 0.873887.$$

Case 2. If we take all seven archipelago/island habitats together, as a group, and the weights are:

$$\lambda_j = \frac{elevat\ (h_j)}{elevat\ (h_1) + \ldots + elevat\ (h_7)}, (j = 1, \ldots, 7),$$

we get the following relative elevation weights:

$$\lambda_1 = 0.045449, \lambda_2 = 0.049855, \lambda_3 = 0.104243,$$
$$\lambda_4 = 0.386378, \lambda_5 = 0.113937, \lambda_6 = 0.003022,$$
$$\lambda_7 = 0.297117,$$

for which we obtain:

$$\alpha - Div = 1.54668, \quad \gamma - Div = 1.81972,$$
$$\beta - Div = 0.273039, \quad Sim = 0.849955.$$

Case 3. If we take all seven archipelago / island habitats together, as a group, and the weights are equal:

$$\lambda_j = \frac{1}{7}, \quad (j = 1,\ldots,7),$$

we obtain the average values:

$$\alpha - Div = 1.21876, \quad \gamma - Div = 1.75528,$$

$$\beta - Div = 0.536528, \quad Sim = 0.694339.$$

Generally, for islands or habitat islands found in a similar geographic region, species diversity tends to be greater on the island or habitat island with a larger area or a higher elevation. The above numerical results obtained by using *RGS* as the main mathematical tool, show that by taking the area and elevation into account, in this order, the alpha and gamma species diversities increase whereas the beta species diversity decreases compared to what happens when we calculate the mean within-habitat and between-habitat species diversity ignoring such factors. Calculating the alpha, beta, and gamma species diversities by using the relative areas and the relative elevation as weights, we compensate for the lack of homogeneity of the habitats with respect to such essential factors which influence species diversity.

5. CONCLUSIONS

The Gini-Simpson index for species diversity is very popular with many ecologists. Recently, however, Jost [18,19,24] showed that this index does not behave well when the number of species is large and is not suitable for use in the computation of the between-habitat species diversity, also called the beta diversity. As a result, Jost pleaded in favour of abandoning the Gini-Simpson index and replacing the additive partitioning of species diversity, prefered by many ecologists, with the multiplicative partitioning. The objective of this paper is to show that the additive partitioning of species diversity may be preserved but the classic Gini-Simpson index of diversity should be replaced by the Rich-Gini-Simpson index, abbreviated as *RGS*, which behaves well when the number of species is large, while keeping the useful basic properties of the classic Gini-Simpson index unchanged. The properties of the *RGS* index and its use in the additive partitioning of the species diversity are analyzed. *RGS* is also applied to data on the avifaunal diversity on several tropical Indian Ocean islands (using some of the numerical data obtained by Adler [25]). The application shows that by using the *RGS* index as a mathematical tool and introducing weights directly proportional with the areas or elevation of the habitats (in this order), the within-habitat species diversity and the total species diversity increase while the between-habitat species diversity decreases compared to what happens when we calculate the mean within- habitat and between-habitat species diversities ignoring such important factors.

REFERENCES

[1] Sarkar, S. (2007) From ecological diversity to biodiversity. In: Hull, D.L. and Ruse, M. Eds., *The Philosophy of Biology*. Cambridge University Press, Cambridge, 388-409.

[2] Gini, C. (1912) Variabilità e mutabilità. In: Pizetti, E. and Salvemini, T. Eds., *Rome*: *Libreria Eredi Virgilio Veschi*, Memorie di metodologica statistica.

[3] Simpson, E.H. (1949) Measurement of diversity. *Nature*, **163**, 688.

[4] Shannon, C.E. (1948) A mathematical theory of communication. *Bell System Technical Journal*, **27**, 379-423, 623-656.

[5] Boltzmann, L. (1896) *Vorlesungen über Gastheorie*. J.A. Barth edition, Akademische Druck-u, Leipzig.

[6] Pielou, E.C. (1966) Shannon's formula as a measure of specific diversity: Its use and misuse. *American Naturalist*, **100**, 463-465.

[7] Pielou, E.C. (1966) Species-diversity and pattern-diversity in the study of ecological succession. *Journal of Theoretical Biology*, **10**, 370-383.

[8] Pielou, E.C. (1975) *Ecological Diversity*. Wiley, New York.

[9] Guiasu, S. (1977) *Information Theory with Applications*. McGraw-Hill, New York.

[10] Patil, G.P. and Taillie, C. (1982) Diversity as a concept and its measurement. *Journal of American Statistical Association*, **77**, 548-567.

[11] Harper, J.L. and Hawksworth, D.L. (1994) Biodiversity: Measurement and estimation. *Philosophical Transactions*: *Biological Sciences*, **345**, 5-12.

[12] Magnussen, S. and Boyle, T.J.B. (1995) Estimating sample size for inference about the Shannon-Weaver and the Simpson indices of species diversity. *Forest Ecology and Management*, **78**, 71-84.

[13] Krebs, C.J. (2001) Ecology: The experimental analysis of distribution and abundance. 5th Edition, Benjamin Cummings, San Francisco.

[14] Guiasu, R.C. and Guiasu, S. (2003) Conditional and weighted measures of ecological diversity. *International Journal of Uncertainty, Fuzziness and Knowledge-Based Systems*, **11**, 283-300.

[15] Guiasu, R.C. and Guiasu, S. (2003) Entropy in ecology and ethology. Nova Science Publishers, New York.

[16] Magurran, A.E. (2004) Measuring biological diversity. Blackwell Publishing, Malden MA.

[17] Maclaurin, J. and Sterelny, K. (2008) What is biodiversity? University of Chicago Press, Chicago and London.

[18] Jost, L. (2006) Entropy and diversity. *Oikos*, **113**, 363-375.

[19] Jost, L. (2007) Partitioning diversity into independent alpha and beta components. *Ecology*, **88**, 2427-2439.

[20] Hill, M. (1973) Diversity and evenness. A unifying notation and its consequences. *Ecology*, **54**, 427-432.

[21] Rényi, A. (1961) On measures of entropy and information. In: Neyman, J. Ed., *Fourth Berkeley Symposium on Mathematical Statistics and Probability*. Berkeley, 547-561.

[22] Hoffmann, S. and Hoffmann, A. (2008) Is there a "true" diversity? *Ecological Economics*, **65**, 213-215.
[23] Ricotta, C. (2005) Through the jungle of biological diversity. *Acta Biotheoretica*, **53**, 29-38.
[24] Jost, L. (2009) Mismeasuring biological diversity: Response to Hoffmann and Hoffmann. *Ecological Economics*, **68**, 925-928.
[25] Adler, G.H. (1994). Avifaunal diversity and endemism on tropical Indian Ocean islands. *Journal of Biogeography*, **21**, 85-95.
[26] MacArthur, R.H. (1965) Patterns of species diversity. *Biological Review*, **40**, 510-533.
[27] MacArthur, R.H., Recher, H. and Cody, M. (1966) On the relation between habitat selection and species diversity. *American Naturalist*, **100**, 319-332.
[28] MacArthur, R.H. and Wilson, E.O. (1967) The theory of island biogeography. Princeton University Press, Princeton.
[29] Rao, C.R. (1982) Diversity and dissimilarity coefficients: A unified approach. *Theoretical Population Biology*, **21**, 24-43.
[30] Whittaker, R.H. (1972) Evolution and measurement of species diversity. *Taxon*, **21**, 213-251.
[31] Whittaker, R.H. (1977) Evolution of species diversity in land communities. In: Hecht, M.K. and Steere, B.W.N.C. Eds., *Evolutionary Biology*, Plenum Press, New York, **10**, 1-67.
[32] Harrison, S. and Quinn, J. (2006) The importance of β-diversity. In: Groom, M.J., Meffe, G.K. and Carroll, C.R. Eds., *Principles of Conservation Biology*, 3rd Edition, Sinauer Associates Inc. Publishers, Sunderland, 44-45.
[33] Routledge, R.D. (1977) On Whittaker's components of diversity. *Ecology*, **58**, 1120-1127.
[34] Routledge, R.D. (1979) Niche metrics and diversity components. *Oecologia*, **43**, 121-124.
[35] Allan, J.D. (1975) Components of diversity. *Oecologia*, **18**, 359-367.
[36] Lande, R. (1996) Statistics and partitioning of species diversity and similarity among multiple communities. *Oikos*, **76**, 5-13.
[37] Wagner, H.H., Wildi, O. and Ewald, K.C. (2000) Additive partitioning of plant species diversity in an agricultural mosaic landscape. *Landscape Ecology*, **15**, 219-227.
[38] Veech, J.A., Summerville, K.S., Crist, T.O. and Gering, J.C. (2002) The additive partioning of species diversity: Recent revival of an old idea. *Oikos*, **99**, 3-9.
[39] Tramer, E.J. (1969) Bird species diversity: Components of Shannon's formula. *Ecology*, **50**, 927-929.
[40] Fager, E.W. (1972) Diversity: A sampling study. *American Naturalist*, **106**, 293-310.
[41] Brown, J.H. and Lomolino, M.V. (1998) *Biogeography*. 2nd Edition, Sinauer Associates Inc. Publishers, Sunderland, MA.
[42] Stirling, G. and Wilsey, B. (2001) Empirical relationships between species richness, evenness, and proportional diversity. *American Naturalist*, **158**, 286-299.
[43] Cox, C.B. and Moore, P.D. (2005) *Biogeography*: *An ecological and evolutionary approach*. 7th Edition, Blackwell Publishing, Oxford.
[44] Quammen, D. (1997) The song of the Dodo-Island biogeography in an Age of Extinction. Simon & Schuster Inc., New York.
[45] Powledge, F. (2003) Island biogeography's lasting impact. *BioScience*, **53**, 1032-1038.

Vol.2, No.10, 1138-1147 (2010)
doi:10.4236/ns.2010.210141

Natural Science

Correlated mutations in the four influenza proteins essential for viral RNA synthesis, host adaptation, and virulence: NP, PA, PB1, and PB2

Wei Hu

Department of Computer Science, Houghton College, Houghton, USA; wei.hu@houghton.edu.

Received 12 July 2010; revised 20 August 2010; accepted 23 August 2010.

ABSTRACT

The NP, PA, PB1, and PB2 proteins of influenza viruses together are responsible for the transcription and replication of viral RNA, and the latter three proteins comprise the viral polymerase. Two recent reports indicated that the mutation at site 627 of PB2 plays a key role in host range and increased virulence of influenza viruses, and could be compensated by multiple mutations at other sites of PB2, suggesting the association of this mutation with those at other sites. The objective of this study was to analyze the co-mutated sites within and between these important proteins of influenza. With mutual information, a set of statistically significant co-mutated position pairs (P value = 0) in NP, PA, PB1, and PB2 of avian, human, pandemic 2009 H1N1, and swine influenza were identified, based on which several highly connected networks of correlated sites in NP, PA, PB1, and PB2 were discovered. These correlation networks further illustrated the inner functional dependence of the four proteins that are critical for host adaptation and pathogenicity. Mutual information was also applied to quantify the correlation of sites within each individual protein and between proteins. In general, the inter protein correlation of the four proteins was stronger than the intra protein correlation. Finally, the correlation patterns of the four proteins of pandemic 2009 H1N1 were found to be closer to those of avian and human than to swine influenza, thus rendering a novel insight into the interaction of the four proteins of the pandemic 2009 H1N1 virus when compared to avian, human, and swine influenza and how the origin of these four proteins might affect the correlation patterns uncovered in this analysis.

Keywords: Co-mutation; Entropy; Influenza; Mutation; Mutual Information; Pandemic 2009 H1N1; Polymerase

1. INTRODUCTION

There are eight single-stranded RNA gene segments in the influenza A virus, which are present as ribonucleoprotein complexes (vRNPs) with nucleoprotein (NP) and polymerase within the virus particle. The viral polymerase itself is a heterotrimer composed of two basic subunits PB1 and PB2, and one acidic subunit PA, which catalyzes the transcription of viral RNA (vRNA) to mRNA and the replication of vRNA to complementary RNA (cRNA). The primary function of NP is to assemble the RNA gene segments into a helical nucleocapsid to provide structural support in vRNPs. After infection, vRNPs are transported into the nucleus where the transcription and replication of the viral genome take place, which means it is the vRNP, rather than the vRNA, that is utilized as the template for transcription and replication. Moreover, NP could also function as a multifunctional key adaptor for interactions between virus and host cell [1,2].

The influenza polymerase also plays an important role in host adaptation and pathogenicity, and mutations at sites 627,701, and 714 in PB2, 615 in PA, and 319 in NP could result in enhanced polymerase activity to facilitate cross species transmission and virulence [3]. A focal poultry outbreak in Manipur, India in 2007 was caused by a unique influenza A (H5N1) virus that contained two unique amino acid mutations, K116R and I411M, in the PB2 protein [4]. Additionally, several other mutations in PA, PB1, and PB2 were also shown to influence the polymerase activity [5-12]. Furthermore, the interaction of NP and PB2 with Importin α1 was found to be a determinant of host range as well [13].

The well-known mutation E627K in PB2 is a determinant marker for host shifts between avian and human

viruses and increased virulence. However, accumulating evidence demonstrated that the mutation at position 627 in PB2 could be compensated by multiple mutations at other sites of PB2 [14,15], implying that mutations in proteins tend to co-occur at different sites to compensate each other in order to maintain the structural and functional constraints. To extend our knowledge of the co-mutations in the proteins of influenza, this study employed entropy and mutual information to analyze co-varying sites in NP, PA, PB1, and PB2 and to uncover a set of statistical significant co-mutated sites to reveal and quantify the interactions of these proteins that play a key role in the life cycle of the influenza viruses.

Information theory including entropy and mutual information (MI) enjoyed wide applications in sequence analysis. Mutual information was employed to identify groups of covariant mutations in the sequences of HIV-1 protease and to distinguish the correlated amino acid polymorphisms resulting from neutral mutations and those induced by multi-drug resistance [16]. With entropy, a simple informational index was proposed in [17] to reveal the patterns of synonymous codon usage bias. Further, mutual information was utilized in the construction of site transition network based on 4064 HA1 of A/H3N1 sequences from 1968 to 2008, which was able to model the evolutionary path of the influenza virus and to predict seven possible HA mutations for the next antigenic drift in the 2009-2010 season [18]. Recently, entropy and mutual information were also applied to indentify critical positions and co-mutated positions on HA for predicting the antigenic variants [19]. In another report, sequence data of 1032 complete genomes of influenza A virus (H3N2) during 1968-2006 were used to construct networks of genomic co-occurrence to describe H3N2 virus evolutionary patterns and dynamics. It suggested that amino acid substitutions corresponding to nucleotide co-changes cluster preferentially in known antigenic regions of HA [20].

To investigate the co-mutations in the proteins of influenza, three separate tasks were performed in this study. The first task was to uncover the variation and co-variation patterns of proteins NP, PA, PB1, and PB2 by the entropy and mutual information computed from their concatenated amino acid sequences. The distributions of entropy and MI obtained reflected the unique sequence characteristics of each protein of avian, human, pandemic 2009 H1N1, and swine influenza viruses, based on which a comparative analysis could be conducted to reveal the variation signature of each influenza species. The second task was to zoom in onto each position pairs in the four proteins to identify a set of statistically significant co-mutated residue pairs (P value = 0), from which several networks of highly correlated sites could be inferred. These correlated pairs and networks of correlated sites presented, at a different scale, finer information about the co-variation of these four proteins than that from task one. In a sense, the correlation information obtained from task two was pair dependent, i.e., it was about pairs. The third task was to mine the association of these four proteins with a pair independent approach, where the locations of pairs with positive MI values were counted according to each protein or to each functional domain in a protein as described in [21]. The strength of association was measured by the averaged counts of correlated pairs located within each protein or between proteins.

2. MATERIALS AND METHODS

2.1. Sequence Data

The protein sequences of influenza A virus employed in this study were downloaded from the Influenza Virus Resource of the National Center for Biotechnology Information (NCBI). All the NP, PA, PB1, and PB2 protein sequences from the same isolates were concatenated into single sequences, and there were 1520 such concatenated sequences of avian viruses, 1928 of human viruses, 164 of pandemic 2009 H1N1, and 232 of swine viruses. These concatenated sequences, rather than the individual protein sequences, were used in our analysis. All the sequences utilized in the study were aligned with MAFFT [22].

2.2. Entropy and Mutual Information

In information theory [23,24], entropy is a measure of the uncertainty associated with a random variable. Let x be a discrete random variable that has a set of possible values $\{a_1, a_2, a_3, \ldots a_n\}$ with probabilities $p_1, p_2, p_3, \ldots p_n$ where. The entropy H of x is

$$H(x) = -\sum_i p_i \log p_i$$

The mutual information of two random variables is a quantity that measures the mutual dependence of the two variables or the average amount of information that x conveys about y, which can defined as

$$I(x,y) = H(x) + H(y) - H(x,y)$$

where $H(x)$ is the entropy of x, and $H(x,y)$ is the joint entropy of x and y. $I(x, y) = 0$ if and only if x and y are independent random variables.

In the current study, each of the N columns in a multiple sequence alignment of a set of influenza protein sequences of length N is considered as a discrete random variable x_i ($1 \le i \le N$) that takes on one of the 20 (n = 20) amino acid types with some probability. $H(x_i)$ has its minimum value 0 if all the amino acids at position i are the same, and achieves its maximum if all the 20

amino acid types appear with equal probability at position i, which can be verified by the Lagrange multiplier technique. A position of high entropy means that the amino acids are often varied at this position. While $H(x_i)$ measures the genetic diversity at position i in our current study, $I(x_i, y_j)$ measures the correlation between amino acid substitutions at positions i and j.

2.3. Mutual Information Evaluation

In order to assess the significance of the mutual information value of two positions in a multiple sequence alignment, it is necessary to show that this value is significantly higher than that based on random sequences. For each pair of positions in a multiple protein sequence alignment, we randomly permuted the amino acids from different sequences at the two positions and calculated the mutual information of these random sequences. This procedure was repeated 1000 times. The P value was calculated as the percentage of the mutual information values of the permuted sequences that were higher than those of the original sequences.

3. RESULTS

3.1. Entropy and Mutual Information of NP, PA, PB1, and PB2

To gain a global view of the sequence variation and co-variation of these four proteins, the entropy and mutual information of their concatenated sequences were calculated (**Figure 1**). The entropy distributions revealed that the swine influenza had the highest overall sequence variation and the pandemic 2009 had the least variation, with avian and human influenza being in the middle. Within each individual influenza species, it appeared that PA had the highest entropy average among the four proteins, with the exception of pandemic 2009 H1N1 (**Table 1**). Mutual information measures the correlation of the amino acids at two sites in a multiple sequence alignment. Therefore, to offer the information of how each site co-mutated with all other sites within each individual protein and between proteins, for each site, all the MI values associated with this site were summed (**Figure 1**).

These MI values represented the association between one site and all other sites in the four proteins. The patterns of MI distributions were quite different from those of entropy, where the ranking of the overall average MI values was swine (5.9533), human (3.6590), avian (0.8298), and pandemic 2009 H1N1 (0.0165), suggesting that variation and co-variation were two distinct measurements of protein sequence changes. The most co-varying protein in each influenza species was PA in avian, PB1 in human, PA in pandemic 2009 H1N1, and PA in swine (**Table 1**).

3.2. Highly Correlated Sites in NP, PA, PB1, and PB2

In order to provide more detailed information about the highly correlated sites, top 50 MI sites in the concatenated sequences from the four proteins of each influenza species were selected from the sites in **Figure 1**. Among the top 50 MI sites (**Figure 2**), there were several sites that were shared between two different influenza species indicating their significant correlation. These top 50 MI sites represented their correlation in a pair independent manner. Next, top 30 MI co-mutated residue pairs of highest MI values (P value = 0) from each influenza species were identified (**Table 2**), and a collection of highly connected networks of co-varying sites in the four proteins were established based on these 30 statistically significant pairs. There were two avian, one human, two pandemic 2009 H1N1, and one swine correlation networks (**Figure 3**). All these networks from various influenza species exhibited their preferred connectivity among the four proteins. In the two avian networks, one had only sites from PA and PB1, and the other contained only those from NP, PB1, and PB2. The human network had PA, PB1, and PB2 sites, where the most connected sites were PA_32, PB1_61, and PB1_63. In the two pandemic 2009 networks, the first had sites selected from all four proteins, while the second had only sites from PA, PB1, and PB2. The swine network had sites from all four proteins, where the most connected sites were PA_580 and PB2_661. These top 30 MI residue pairs and networks of associated sites presented their correlation in a pair dependent manner.

PB2_627 is a key site for host switches and virulence, which is also the most extensively studied site. Nevertheless, only avian viruses had it as one of their top 50 MI sites (**Figure 2**). To find those sites that related to PB2_627, a set of sites that had high MI values with

Table 1. Averaged entropy and MI of the four proteins.

Entropy	NP	PA	PB1	PB2	Overall Average
Avian	0.0407	0.0499	0.0351	0.0426	0.0420
Human	0.0476	0.0510	0.0448	0.0471	0.0476
Pandemic 2009	0.0040	0.0046	0.0039	0.0050	0.0044
Swine	0.0884	0.1056	0.0751	0.0911	0.0900
MI	**NP**	**PA**	**PB1**	**PB2**	**Overall Average**
Avian	0.7560	0.9387	0.7888	0.8358	0.8298
Human	3.3819	3.8160	4.1865	3.2518	3.6590
Pandemic 2009	0.0137	0.0189	0.0157	0.0177	0.0165
Swine	4.7358	7.5761	5.4241	6.0774	5.9533

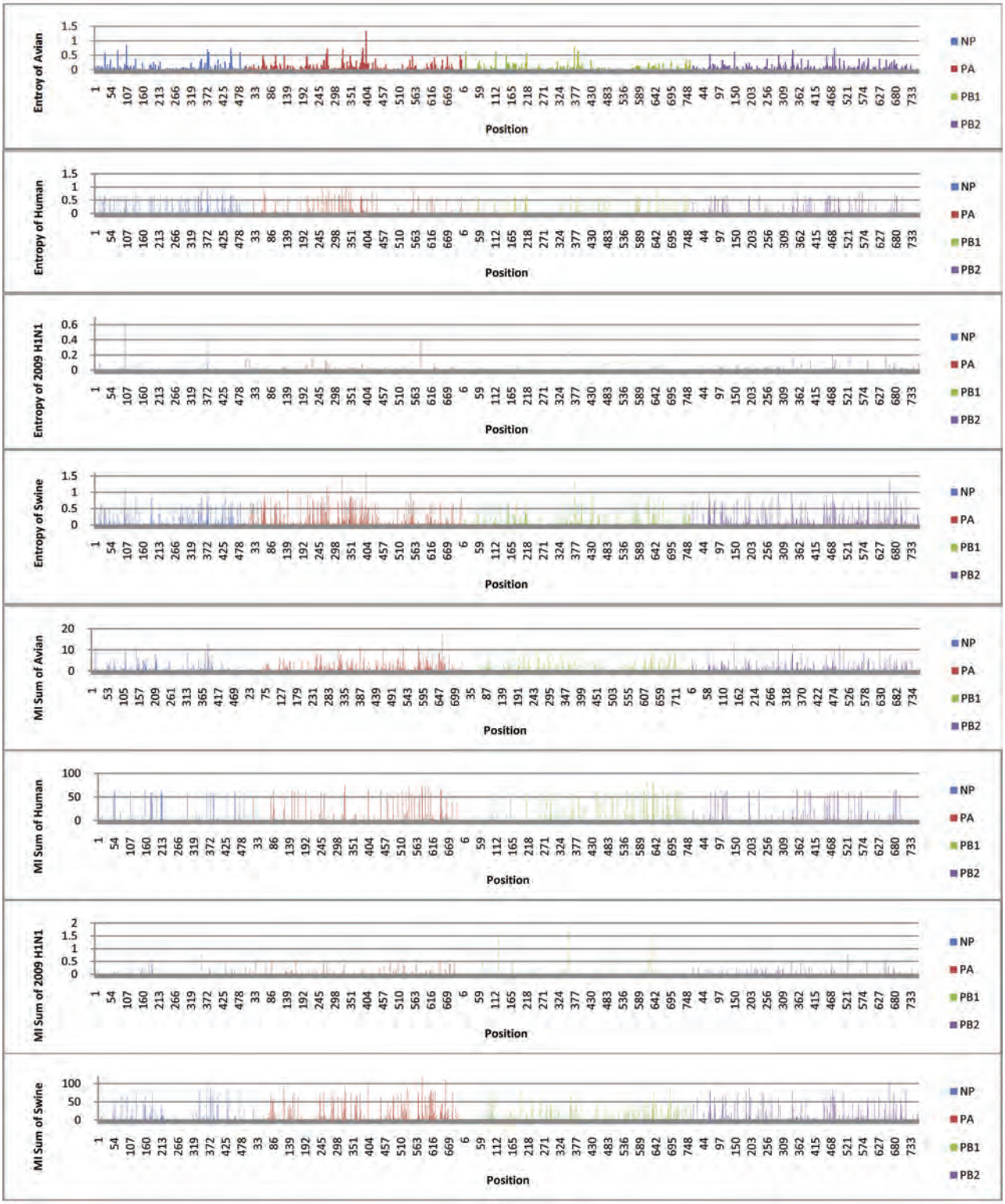

Figure 1. Entropy and MI of the four proteins.

PB2_627 (P value = 0) were included in **Table 3**, where the MI ranks were based on the MI values of all possible pairs. In swine, PB2_627 appeared to interact exclusively with sites in PA and PB2, while in avian, PB2_ 627 correlated with those in NP, PA, PB1, and PB2. The connectivity of PB2_627 with other sites in NP, PA, PB1 and

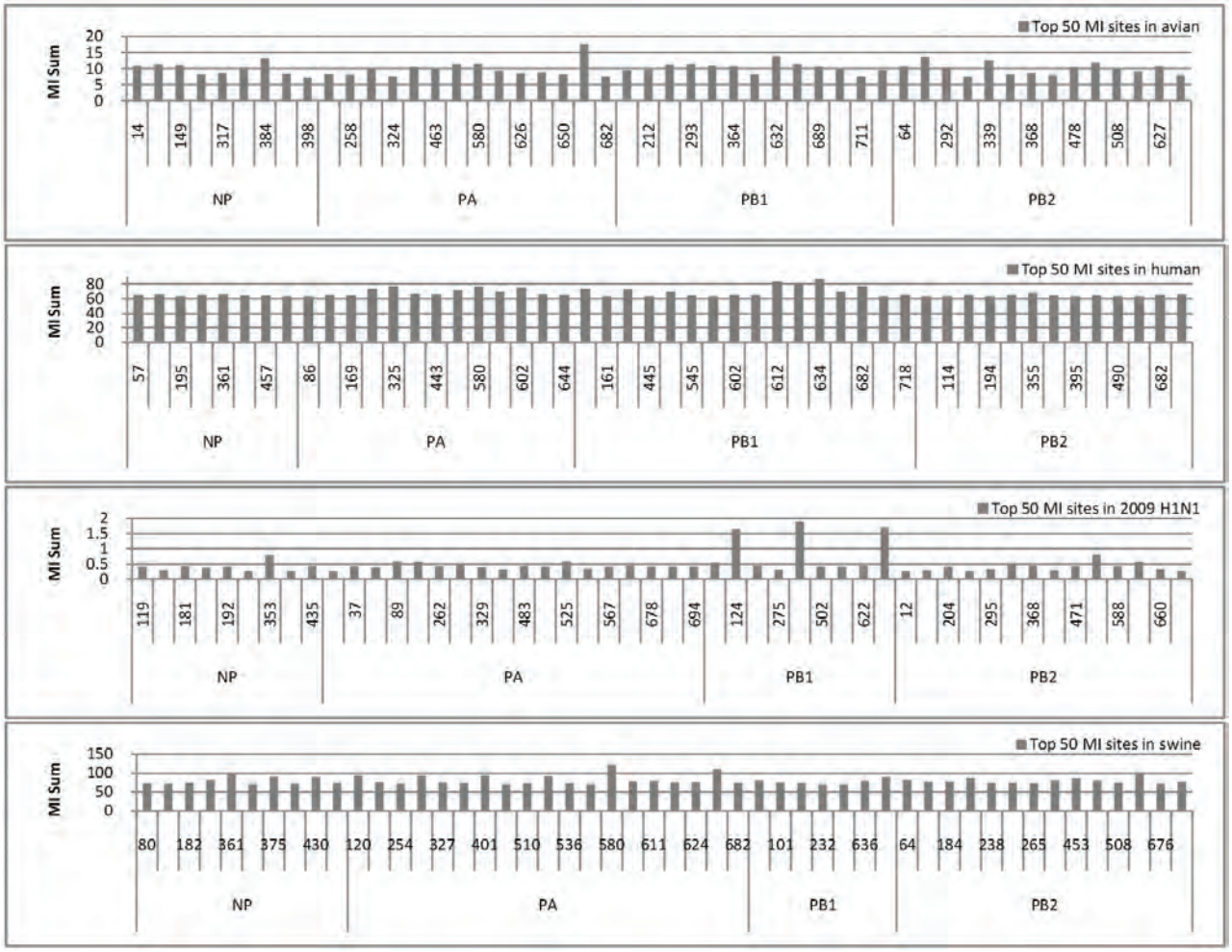

Figure 2. Top 50 MI sites from the four proteins.

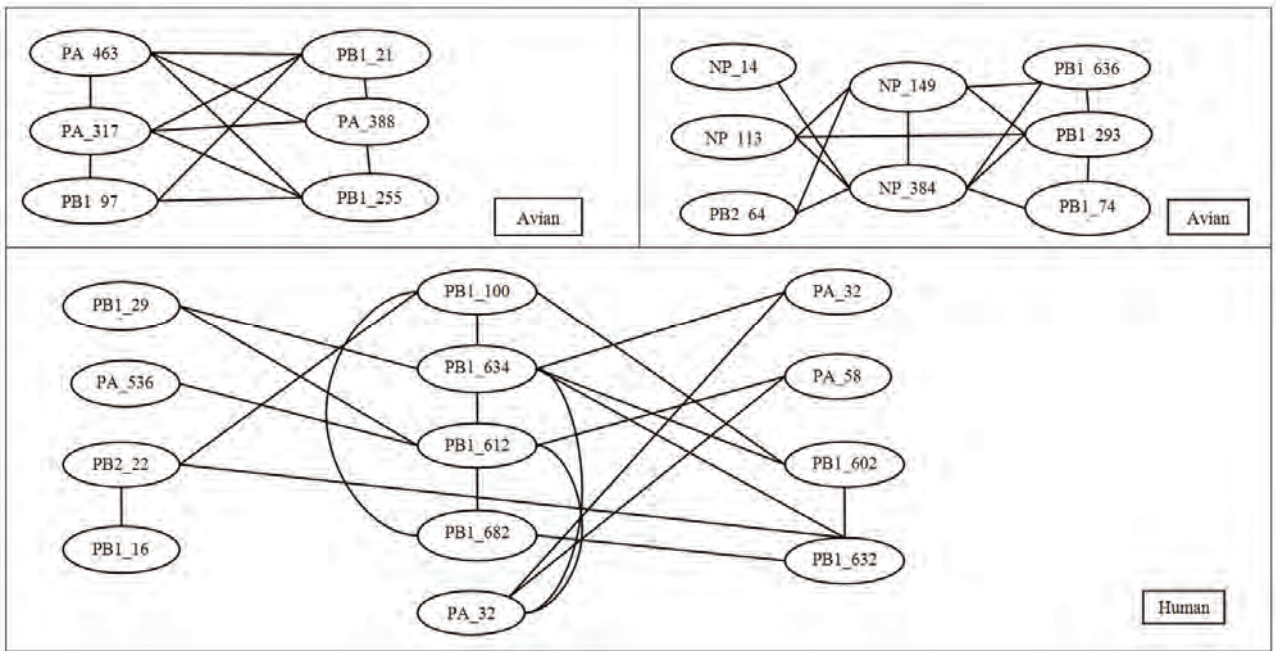

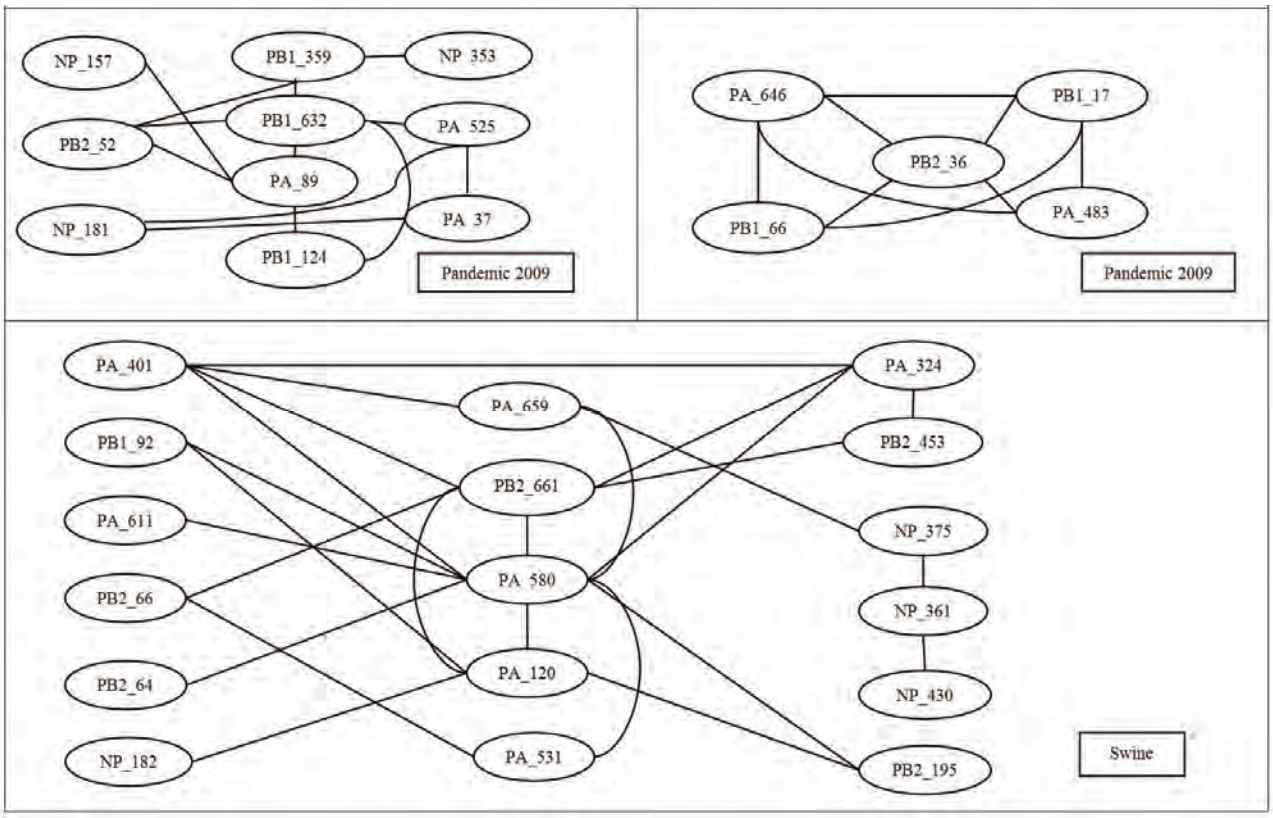

Figure 3. Networks of correlated sites from the four proteins that had high MI values (all with P value = 0).

Table 2. Top 30 MI site pairs from the four proteins (all with P value = 0).

Top 30 pairs in avian					
(NP_14,NP_384)	(NP_133,NP_149)	(NP_133,NP_384)	(NP_149,NP_384)	(NP_149,PB1_293)	(NP_149,PB1_636)
(NP_149,PB2_64)	(NP_384,PB1_636)	(NP_384,PB1_741)	(NP_113,PB1_293)	(NP_384,PB2_64)	(PA_317,PA_388)
(PA_317,PA_463)	(PA_317,PB1_97)	(PA_317,PB1_212)	(PA_317,PB1_225)	(PA_388,PA_463)	(PA_388,PB1_212)
(PA_388,PB1_255)	(PA_463,PB1_212)	(PA_463,PB1_255)	(PA_531,PA_659)	(PA_607,PB1_169)	(PA_607,PB1_169)
(PB1_97,PB1_212)	(PB1_97,PB1_255)	(PB1_212,PB1_255)	(PB1_293,PB1_636)	(PB1_293,PB1_741)	(PB1_709,PB2_478)
Top 30 pairs in human					
(PA_324,PA_325)	(PA_324,PB1_634)	(PA_325,PA_580)	(PA_325,PB1_612)	(PA_325,PB1_634)	(PA_536,PB1_612)
(PA_536,PB1_632)	(PA_580,PB1_612)	(PA_602,PB1_100)	(PA_602,PB1_632)	(PA_602,PB1_634)	(PA_602,PB2_559)
(PB1_100,PB1_277)	(PB1_100,PB1_634)	(PB1_100,PB1_682)	(PB1_161,PB1_632)	(PB1_161,PB2_227)	(PB1_293,PB1_612)
(PB1_293,PB1_643)	(PB1_324,PB1_643)	(PB1_545,PB1_632)	(PB1_602,PB1_718)	(PB1_602,PB2_682)	(PB1_612,PB1_634)
(PB1_612,PB1_682)	(PB1_632,PB1_634)	(PB1_632,PB1_682)	(PB1_632,PB2_227)	(PB1_667,PB2_355)	(PB1_718,PB2_682)
Top 30 pairs in 2009 H1N1					
(NP_157,PA_89)	(NP_181,PA_37)	(NP_181,PA_525)	(NP_353,PA_68)	(NP_353,PB1_359)	(PA_37,PA_525)
(PA_68,PB2_471)	(PA_89,PB1_124)	(PA_89,PB1_632)	(PA_89,PB2_526)	(PA_169,PB2_649)	(PA_262,PB2_677)
(PA_483,PA_646)	(PA_483,PB1_171)	(PA_483,PB1_368)	(PA_525,PB1_124)	(PA_525,PB1_632)	(PA_646,PB1_171)
(PA_646,PB1_622)	(PA_646,PB2_368)	(PB1_124,PB1_359)	(PB1_124,PB1_632)	(PB1_124,PB2_526)	(PB1_171,PB1_622)
(PB1_171,PB2_368)	(PB1_359,PB1_632)	(PB1_359,PB2_526)	(PB1_622,PB2_368)	(PB1_632,PB2_526)	(PB2_109,PB2_588)

Top 30 pairs in swine					
(NP_182,PA_120)	(NP_361,NP_375)	(NP_361,NP_430)	(NP_375,PA_659)	(PA_120,PA_580)	(PA_120,PB1_92)
(PA_120,PB2_195)	(PA_324,PA_401)	(PA_324,PA_580)	(PA_324,PB2_453)	(PA_324,PB2_661)	(PA_401,PA_580)
(PA_401,PA_659)	(PA_401,PB2_661)	(PA_531,PA_580)	(PA_531,PA_659)	(PA_531,PB2_66)	(PA_580,PA_611)
(PA_580,PA_659)	(PA_580,PB1_92)	(PA_580,PB2_64)	(PA_580,PB2_195)	(PA_580,PB2_661)	(PA_611,PB2_66)
(PB1_92,PB2_195)	(PB2_184,PB2_243)	(PB2_184,PB2_265)	(PB2_243,PB2_265)	(PB2_453,PB2_661)	(PB2_475,PB2_627)

Table 3. Pearson correlation coefficients of the pair counts between different influenza species in **Figures 4** and **5**.

	(Avian, Human)	(Avian,2009 H1N1)	(Avian, Swine)	(Human,2009 H1N1)	(Human, Swine)	(2009 H1N1, Swine)
Averaged counts in proteins	0.986644	0.852749	0.974158	0.893431	0.977686	0.78265
Averaged counts in domains	0.63857	0.3873	0.8716	0.7614	0.3893	0.0976

PB2 in human and pandemic 2009 H1N1 viruses was weak, and therefore no such sites were included in this report.

3.3. Correlation within Each Individual Protein and between Proteins

The correlated residue pairs that had a positive MI value were counted according to their location in the four proteins (**Figure 4**). In general, the inter protein correlation from (NP, PA), (NP, PB1), (NP, PB2), (PA, PB1), (PA, PB2), (PB1, PB2) was stronger than the intra protein correlation (NP, NP), (PA, PA), (PB1, PB1) and (PB2, PB2), with (NP, NP) correlation being the weakest. **Figure 4** also indicated that the correlation between PA and PB2 was the strongest in avian, human, and pandemic 2009 H1N1, and the correlations of PA and PB2, PA and PB1, and PB1 and PB2 were the strongest in swine. Similarly, **Figure 5** showed that the correlation of nuclear localization signals (NLS) of PB2 was the strongest in avian, human, and pandemic 2009 H1N1, and the correlation of the RNA cap binding domain of PB2 was the strongest in swine. To further quantify the correlation of these four proteins, the averaged counts of positions in the functional domains of the four proteins that had a positive MI value with other positions were calculated, based on the domain boundary information given in [21] (**Figure 5**). Comprehensive phylogenetic analysis suggested that the genes of 2009 pandemic H1N1 were derived from avian (PB2 and PA), human H3N2 (PB1), classical swine (HA, NP and NS), and

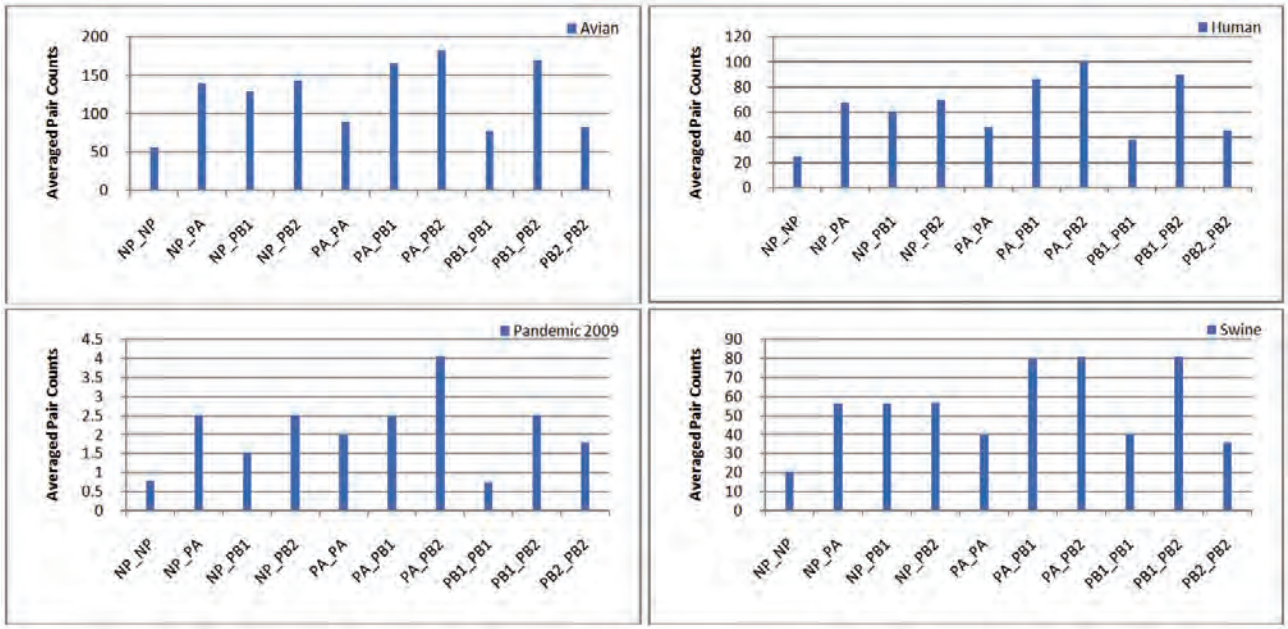

Figure 4. Averaged correlated pair counts in each individual protein and between proteins.

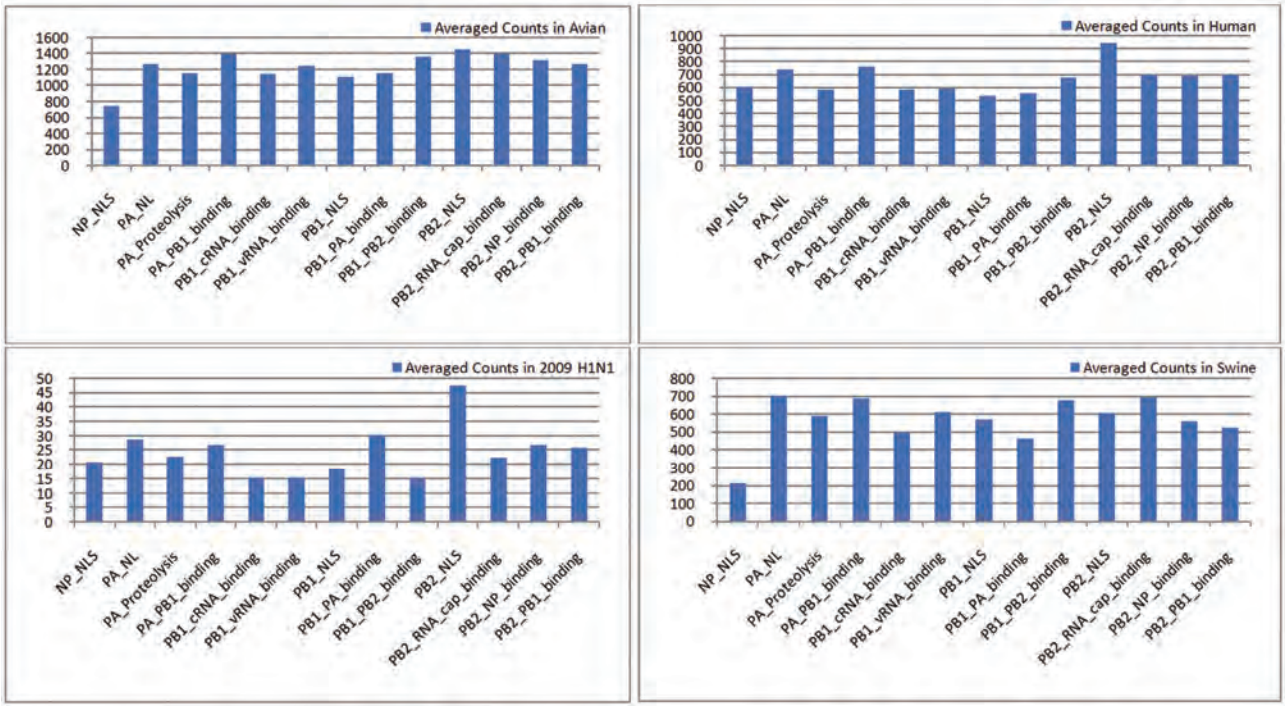

Figure 5. Averaged counts of sites in the functional domains of the four proteins that had a positive MI value with other sites.

Table 4. Sites from the four proteins of avian and swine influenza that had high MI values with PB2_627.

Avian Sites	MI Rank	P value	Avian Sites	MI Rank	P value	Swine Sites	MI Rank	P value
PA_258	163	0.0	PB1_667	332	0.0	PB2_485	21	0.0
PB2_451	207	0.0	NP_211	395	0.0	PB2_199	242	0.0
PA_626	210	0.0	PB2_339	396	0.0	PA_580	331	0.0
PA_596	220	0.0	NP_390	414	0.0	PA_401	338	0.0
PB1_292	226	0.0	PA_445	421	0.0	PA_314	364	0.0
NP_353	256	0.0	PB2_543	424	0.0	PB2_64	412	0.0
PB2_649	262	0.0	NP_178	428	0.0	PA_615	472	0.0
PB2_368	299	0.0	PB2_147	434	0.0	PA_324	473	0.0
PB1_632	307	0.0	PA_399	449	0.0			
PB1_196	323	0.0	PB1_255	491	0.0			
PB2_390	331	0.0						

Eurasian avian-like swine H1N1 (NA and M) lineages [25]. With Pearson correlation coefficients (**Table 4**), both **Figures 4** and **5** consistently illustrated that the correlation patterns of pandemic 2009 H1N1 were more similar to those of avian and human influenza than to swine, thus offering a new insight into the interaction of the four proteins of the pandemic 2009 H1N1 virus when compared with avian, human, and swine influenza and how the origin of these four proteins might contribute to the correlation patterns revealed in this analysis.

4. DISCUSSION

Development of our knowledge about the molecular mechanism of host range restriction and the adaptation of influenza viruses to a new host species remains a central topic in flu research. The four proteins NP, PA, PB1,

and PB2 are crucial components in viral RNA synthesis, and are also implicated in host adaptation and pathogenicity. Therefore, clear revelation of the function and action of these four proteins is required. Sequence survey implied that the common host shift markers in the proteins of avian or swine influenza are not present in the pandemic 2009 H1N1 virus. Moreover, introduction of known virulence markers into 2009 H1N1 does not increase its virulence [26,27]. The combination of its pandemic potential and absence of traditional host markers has remained a source for concern and justifies the search for its own host markers outside of the space of classical host markers [28,29].

The PB2 of 2009 H1N1 had a glutamic acid at position 627, reflecting its avian origin. Typically avian viruses have a glutamic acid (E) at position 627, while human viruses usually have a lysine (K) at this position. Additionally, the presence of a glutamic acid at position 627 in PB2 contributed to the cold sensitivity of polymerase derived from avian viruses in mammalian cells [3]. However, the clinical experience in 2009 demonstrated that this novel virus was able to transmit and replicate in humans efficiently. A natural assumption was that some amino acids at other sites in PB2 might be responsible for its efficiency in reproduction and transmission. It turned out that two amino acids, serine (S) at site 590 and arginine (R) at site 591, in PB2, termed SR polymorphism, compensate the lack of amino acid lysine at site 627 in PB2 [15].

Although our mutual information analysis illustrated the connectivity was low between PB2_627, PB2_591, PB2_590, and other sites in pandemic 2009 H1N1, this study discovered three sites correlating with PB2_590, which were NP_480 (MI = 0.0219, P value = 0.033, MI rank = 370), PB1_359 (MI = 0.0060, P value = 0.338, MI rank = 611), and PB1_124 (MI = 0.0011, P value = 0.0, MI rank = 1093). With the same approach, associations with other critical sites such as PB2_701 and PB2_271 could also be detected.

Host range and virulence of influenza viruses are multigenically determined through interactions between the proteins involved, which could be, in part, elucidated with identification of mutations and co-mutations that might confer increased pathogenicity or transmissibility. The absence of familiar host switch markers in 2009 H1N1 added a new dimension in this effort, and motivated the extensive search for other mutations or strategies that influenza viruses evolved to develop and adapt. To move this direction, this report revealed and quantified the interactions of NP, PA, PB1, and PB2 of avian, human, pandemic 2009 H1N1, and swine influenza, and identified a collection of statistically significant covarying sites, not only in each individual protein but also between proteins, for further investigation of their integrative biological relevance experimentally.

5. ACKNOWLEDGEMENT

We thank Houghton College for its financial support.

REFERENCES

[1] Neumann, G., Brownlee, G.G., Fodor, E. and Kawaoka, Y. (2004) Orthomyxovirus replication, transcription, and polyadenylation. *Curr Top Microbiol Immunol*, **283**, 121-143.

[2] Ng, A.K., Zhang, H., Tan, K., *et al.* (2008) Structure of the influenza virus A H5N1 nucleoprotein: Implications for RNA binding, oligomerization, and vaccine design. *The FASEB Journal*, **22(10)**, 3638-3647.

[3] Jürgen, S., (2008) Influenza A virus polymerase: A determinant of host range and pathogenicity. In: Klenk H.D., Matrosovich M.N. and Stech J. Eds., *Avian Influenza*. Monogr Virol. Basel, Karger, **27**, 187-194.

[4] Mishra, A.C., Cherian, S.S., Chakrabarti, A.K., *et al.* (2009) A unique influenza A (H5N1) virus causing a focal poultry outbreak in 2007 in Manipur, India. *Journal of Virology*, **6(1)**, 26.

[5] Yuan, P.W., Bartlam, M., Lou, Z.Y., *et al.* (2009) Crystal structure of an avian influenza polymerase PAN reveals an endonuclease active site, *Nature*, **458**, 909-913.

[6] Fodor, E., Crow, M., Mingay, L.J., *et al.* (2002) A single amino acid mutation in the PA subunit of the influenza virus RNA polymerase inhibits endonucleolytic cleavage of capped RNAs. *Journal of Virology*, **76(18)**, 8989-9001.

[7] Hara, K., Schmidt, F.I., Crow, M. and Brownlee, G.G. (2006) Amino acid residues in the N-terminal region of the PA subunit of influenza A virus RNA polymerase play a critical role in protein stability, endonuclease activity, cap binding, and virion RNA promoter binding. *Journal of Virology*, **80(16)**, 7789-7798.

[8] Kerry, P.S., Willsher, N. and Fodor, E. (2008) A cluster of conserved basic amino acids near the C-terminus of the PB1 subunit of the influenza virus RNA polymerase is involved in the regulation of viral transcription. *Virology*, **373(1)**, 202-210.

[9] Dias, A., Bouvier, D., Crépin, T., McCarthy, A.A., *et al.* (2009) The cap-snatching endonuclease of influenza virus polymerase resides in the PA subunit. *Nature*, **458 (7240)**, 914-918.

[10] Rolling, T,, Koerner, I,, Zimmermann, P,, Holz, K,, *et al.* (2009) Adaptive mutations resulting in enhanced polymerase activity contribute to high virulence of influenza A virus in mice. *Journal of Virology*, **83(13)**, 6673-6680.

[11] Bussey, K.A., Bousse, T.L., Desmet, E.A., Kim, B. and Takimoto, T. (2010) PB2 residue 271 plays a key role in enhanced polymerase activity of influenza A viruses in mammalian host cells. *Journal of Virology*, **84(9)**, 4395-4406.

[12] Zhu, H., Wang, J., Wang, P., Song, W., Zheng, Z., Chen, R., Guo, K., Zhang, T., Peiris, J.S., Chen, H. and Guan, Y. (2010) Substitution of lysine at 627 position in PB2 protein does not change virulence of the 2009 pandemic

H1N1 virus in mice. *Virology*, **401(1)**, 1-5.

[13] Gabriel, G., Herwig, A. and Klenk, H.D. (2008) Interaction of polymerase subunit PB2 and NP with importin α1 is a determinant of host range of influenza A virus. *PLoS Pathog*, **4(2)**, e11

[14] Li, J., Ishaq, M., Prudence, M., *et al.* (2009) Single mutation at the amino acid position 627 of PB2 that leads to increased virulence of an H5N1 avian influenza virus during adaptation in mice can be compensated by multiple mutations at other sites of PB2. *Virus Research*, **144 (1-2)**, 123-129.

[15] Mehle, A., Doudna, J.A. (2009) Adaptive strategies of the influenza virus polymerase for replication in humans, Proceedings of the National Acad*emy of Sciences*, **106(50)**, 21312-21316.

[16] Liu, Y., Eyal, E. and Bahar, I. (2008) Analysis of correlated mutations in HIV-1 protease using spectral clustering. Bioinformatics, **24(10)**, 1243-1250.

[17] Colman, P.M., Hoyne, P.A. and Lawrence, M.C. (1993) Sequence and structure alignment of paramyxovirus hemagglutinin-neuraminidase with influenza virus neuraminidase. *Journal of Virology*, **67**, 2972-2980.

[18] Xia, Z., Jin, G.L., Zhu, J. and Zhou, R.H. (2009) Using a mutual information-based site transition network to map the genetic evolution of influenza A / H3N2 virus. *Bioinformatics*, **25(18)**, 2309-2317.

[19] Huang, J.-W., King, C.-C. and Yang, J.-M. (2009) Coevolution positions and rules for antigenic variants of human influenza A / H3N2 viruses. *BMC Bioinformatics*, **10**, S41.

[20] Du, X.J., Wang, Z., Wu, A.P., *et al.* (2008) Networks of genomic co-occurrence capture characteristics of human influenza A (H3N2) evolution. *Genome Research*, **18**, 178-187.

[21] Miotto, O., Heiny, A.T., Albrecht, R., García-Sastre, A., *et al.* (2010) Complete-proteome mapping of human influenza A adaptive mutations: Implications for human transmissibility of zoonotic strains, *PLoS One*, **5(2)**, e9025

[22] Katoh, K., Kuma, K., Toh, H. and Miyata, T. (2005) MAFFT version 5: Improvement in accuracy of multiple sequence alignment. *Nucleic Acids Research*, **33**, 511-518.

[23] Cover, T.A. and Thomas, J.A. (1991) Elements of information theory. John Wiley and Sons, New York.

[24] MacKay, D. (2003) Information theory, inference, and learning algorithms. Cambridge University Press.

[25] Smith, G.J.D., Vijaykrishna, D., *et al.* (2009) Origins and evolutionary genomics of the 2009 swine-origin H1N1 influenza A epidemic, *Nature*,**459**, 1122-1125.

[26] Jagger, B.W., Memoli, M.J., Sheng, Z.-M., *et al.* (2010) The PB2-E627K mutation attenuates viruses containing the 2009 H1N1 influenza pandemic polymerase. *mBio* **1 (1),** e00067-10.

[27] Herfst, S., Chutinimitkul, S., Ye, J.Q., *et al.* (2010) Introduction of virulence markers in PB2 of pandemic swine-origin influenza virus does not result in enhanced virulence or transmission, *Journal of Virology*, **84(8)**, 3752-3758.

[28] Hu, W. (2010) Novel host markers in the 2009 pandemic H1N1 influenza A virus. *Journal of Biomedical Science and Engineering*, **3(6)**, 584-601

[29] Hu, W. (2010) Nucleotide host markers in the influenza a viruses. *Journal of Biomedical Science and Engineering*, **3**, 684-699.

Vol.2, No.10, 1148-1154 (2010)
doi:10.4236/ns.2010.210142

Effect of abiotic factors on the molluscicidal activity of oleoresin of *Zingiber officinale* against the snail *Lymnaea acuminata*

Vijya Singh, Pradeep Kumar, V. K. Singh, D. K. Singh

Malacology Laboratory, Department of Zoology, D. D. U., Gorakhpur University, Gorakhpur, India; dksingh_gpu@yahoo.co.in.

Received 28 April 2010; revised 30 May 2010; accepted 3 June 2010.

ABSTRACT

Earlier it has been observed that oleoresin of *Zingiber officinale* is a potent molluscicide against *Lymnaea acuminata*. This snail is the vector of *Fasciola* species, which cause endemic fascioliasis in eastern Uttar Pradesh. As this snail breeds and maintain their population constant through out the year, so that the present study has been designed to find out the effect of variations in some environmental factors in different seasons, on the molluscicidal activity of oleoresin of *Zingiber officinale* and its relative effect on certain enzymes viz., acetylcholinesterase, acid and alkaline phosphatases in the nervous tissue of the snail *Lymnaea acuminata*. In this study temperature, pH, dissolve oxygen, free carbon dioxide, conductivity of the water in control, as well as molluscicide treated water, was measured simultaneously. LC_{50} value of oleoresin was determined in each month of the year. Toxicity of oleoresin in June-July (24 h LC_{50} 16.54-14.28 mgL^{-1}) is highest. Acetylcholinesterase, acid and alkaline phosphatases activity in the nervous tissue of the snails treated with sub-lethal concentration of oleoresin was simultaneously measured. Significant positive rank correlation, in between the acetylcholinesterase or acid phosphatase activity and LC_{50} of oleoresin was observed. The present study conclusively shows that variant abiotic factors can significantly alter the toxicity of oleoresin of *Z. officinale* in *L. acuminata*. The most suitable period for control of *L. acuminata* is June-July.

Keywords: Environmental factors; Acetylcholinesterase; Oleoresin; Temperature; pH

1. INTRODUCTION

It has been reported that, oleoresin of *Zingiber officinale* is a potent molluscicide [1,2]. Fresh water snail *Lymnaea acuminata* is the intermediate host of liver fluke *Fasciola gigantica*, causing an endemic fascioliasis in the cattle population of eastern region of the state of Uttar Pradesh in India [3,4]. An effective method to reduce the incidence of fascioliasis is to control the population of vector snails and, thereby, break the life cycle of these flukes [5-8]. Earlier studies have shown that oleoresin of *Zingiber officinale* has a powerful molluscicidal action on the snail *L. acuminate* [1,2]. It has also been conclusively shown that acetylcholinesterase (AChE), acid and alkaline phosphatase (ACP and ALP) in the nervous tissue of *L. acuminata* are very sensitive parameters influenced by molluscicides [7-10]. The aim of the present study was to explore the possibility whether seasonal changes in abiotic factors, *viz* temperature, pH, dissolved oxygen and carbon dioxide, and conductivity of test water can influence the level of AChE, ACP and ALP assayed in each month of the year 2006-2007 following exposure to sublethal concentrations (40% and 80%) of 24 h LC_{50} of oleoresin of *Z. officinale*.

2. MATERIALS AND METHODS

2.1. Test Materials

Oleoresin was obtained by extraction of prepared dried rhizomes of *Z. officinale* with alcohol. The removal of the solvent under vacuum yields oleoresin of *Z. officinale* [1,11]. Temperature, pH and conductivity of water were measured by thermometer and digital pH and conductivity meters, respectively. Dissolved O_2 and CO_2 were estimated according to the methods prescribe by APHA [12].

2.2. Bioassays for LC_{50}

Adult *L. acuminata* (length 2.25 ± 0.2 cm) were collected from Ramgarh Lake, located in almost adjacent to this university campus. Snails were acclimatized in de-chlorinated tap water for 72 h. The snails were exposed to different concentrations of oleoresin in glass aquaria containing 3 litres of de-chlorinated water. Ten experimental animals were kept in each aquarium. Control animals were kept in equal volumes of de-chlorinated tap water under similar conditions. Mortality of snails was observed after 24, 48, 72, 96 h. No response to a needle probe was taken as evidence of death. Dissolved O_2, CO_2 and conductivity, temperature and pH of treated and control group of water was measured simultaneously with toxicity test at every 24 h of period to 96. Bioassays for the determination of LC_{50} value was performed in each month of the year. Lethal concentration (LC_{50}) values, lower and upper confidence limits (LCL and UCL) and slopes value were calculated by the method of POLO computer program of Robertson *et al.* [13]. The Product moment correlation coefficient was determined between LC_{50} and temperature / pH / conductivity / dissolved O_2 / CO_2, of water in each of the twelve months in order to observe any significant correlation according to the method of Sokal and Rohlf [14].

2.3. Enzyme Assays

Twenty snails, kept in glass aquaria containing 5 litres of dechlorinated water, were exposed to 40% and 80% of 24 h LC_{50} of oleoresin in each month. Six such aquaria were set up for each concentration. After 24 h treatment, the snails were washed with water and the nervous tissue was dissected out from the buccal mass for the measurement of enzyme AChE, ACP and ALP activities.

2.3.1. Acetylcholinesterase

Acetylcholinesterase (AChE) activity was measured according to the method of Ellman *et al.* [15] as modified by Singh *et al.* [16]. Fifty mg of nervous tissue was homogenized in 1.0 ml of 0.1 M phosphate buffer pH 8.0 for 5 minute in an ice bath and centrifuged at 1000 g for 30 minute at 4°C. Supernatant was used as enzyme source. The change in optical density at 412 nm was recorded for 3 minute after every 30 second interval. Enzyme activity was expressed as µ mol "SH" hydrolyzed / min / mg protein.

2.3.2. Phosphatases

Acid (ACP) and alkaline (ALP) phosphatases activities were measured by the method of Bergmeyer [17] as modified by Singh and Agarwal [18]. Tissue homogenate (2% w/v) was prepared in ice cold 0.9 % NaCl and centrifuged at 5000 g for 20 minute at 4°C. The 4-nitrophenyl phosphate disodium was used as substrate. The acid (ACP) and alkaline phosphatases (ALP) activity has been expressed as µmole substrate hydrolyzed /30 min/ mg protein.

2.3.3. Protein Estimation

Protein was estimated by the method of Lowry *et al.* [19].

2.4. Statistical Analysis

Results have been expressed as mean ± SE of six replicates. Rank correlation was applied in between control and corresponding changes in the enzyme activity in different months of the year [14].

3. RESULTS

There was a significant ($P < 0.05$) time dependent variation in the toxicity of oleoresin *Z. officinale* in different months of the year against *L. acuminata* (**Table 1**); highest toxicity was observed in months of June and July (24 h LC_{50} 14.28-16.54 mgL^{-1}) and lowest (24 h LC_{50} 124.09-126.27 mgL^{-1}) during January and February. A significant positive correlation ($r = 0.89$; $P = 0.001$) between LC_{50} and water pH was noted for each month and at each interval of 24 h exposure (**Table 1**). A similar finding between LC_{50} and dissolved O_2 ($r = 0.82$; $P = 0.001$) was found. Contrastively, significant negative correlation between LC_{50} and dissolved CO_2 ($r = 0.86$; $P = 0.001$) and with water temperature ($r = 0.91$; $P = 0.001$) was noted. No marked correlation was observed between the LC_{50} and conductivity of water. High temperature (36 °C), and free CO_2 (30.0 ppm), low pH (7.11) and dissolved oxygen (1.0 ppm) increases the toxicity of oleoresin against *L. acuminata*. The slope values were steep and separate estimations of LC_{50} based on each of the six replicates were found to be with in the 95% confidence limits of LC_{50}. The t-ratio is greater than 1.96 and the heterogeneity factor is less than 1.0. The g value was less than 0.5 at all probability levels.

There was significant positive rank correlation ($\tau = 0.666$; $P = 0.02$ - 40% of 24 h $LC_{50,}$ $\tau = 0.636$ $P = 0.02$ - 80% of 24 h $LC_{50,}$) between LC_{50} of different months and corresponding anti AChE activity in the sub-lethal treatment (40% and 80% of 24 h LC_{50}) of nervous tissue of snail *L. acuminata*. Maximum inhibition in AChE activity (56.09% of control) was observed in snails exposed to 80% of 24 h LC_{50} of oleoresin in month of July (**Table 2**). There was no significant positive rank correlation between LC_{50} of different months and alkaline phosphatase activity in the sub-lethal treatment (40% and 80% of 24 h LC_{50}) of nervous tissue of snail *L. acuminata* (**Table 3**). Like AChE, there was significant positive rank correlation between LC_{50} and acid phosphatas

Table 1. Alterations in toxicity (LC_{50} mL^{-1}) of oleoresin of Z. *officinale* against *L. acuminata* and different environmental factors in different months of the year 2006-07.

24 h												
Parameters	Aug.	Sep.	Oct.	Nov.	Dec.	Jan.	Feb.	Mar.	Apr.	May	Jun.	Jul.
LC_{50} (mgL^{-1})	39.67	54.54	55.92	58.79	62.18	126.27	124.09	74.93	24.88	21.67	16.54	14.28
Temp (°C) **	30 ± 0.37	30 ± 0.55	29 ± 0.55	26 ± 0.50	22 ± 0.36	17 ± 0.44	20 ± 0.55	22 ± 0.34	34 ± 0.30	29 ± 0.30	35 ± 0.50	36±0.30
pH +	7.09 ± 0.06	8.00 ± 0.05	8.07 ± 0.05	8.09 ± 0.05	8.76 ± 0.05	9.00 ± 0.04	8.90 ± 0.06	8.79 ± 0.05	7.81 ± 0.03	7.50 ± 0.06	7.39 ± 0.04	7.11±0.04
DO(ppm) +	1.5 ± 0.06	2.3 ± 0.05	3.0 ± 0.06	5.0 ± 0.05	5.0 ± 0.05	6.0 ± 0.04	5.0 ± 0.06	4.0 ± 0.03	3.0 ± 0.05	2.5 ± 0.05	1.8 ± 0.04	1.0±0.02
DCO_2(ppm)*	25.0 ± 0.55	20.0 ± 0.45	20.0 ± 0.70	20.0 ± 0.53	15.0 ± 0.50	15.0 ± 0.52	15.0 ± 0.55	15.0 ± 0.40	25.0 ± 0.43	25.0 ± 0.55	25.0 ± 0.50	30.0±0.50
Conductivity (μ mhos/cm)	45.0 ± 0.5	54.0 ± 0.6	46.8 ± 0.5	40.1 ± 0.56	50.0 ± 0.6	57.5 ± 0.6	40.3 ± 0.7	33.2 ± 0.5	52.6 ± 0.7	70.0 ± 0.6	30.3 ± 0.6	40.0±0.4
48 h												
LC_{50} (mgL^{-1})	34.13	20.70	34.79	40.35	42.30	72.79	88.20	61.38	19.21	18.72	11.76	11.62
Temp (°C) **	31 ± 0.40	30 ± 0.55	28 ± 0.60	26 ± 0.23	22 ± 0.36	17 ± 0.44	20 ± 0.50	21 ± 0.36	35 ± 0.35	30 ± 0.33	35 ± 0.50	36±0.33
pH +	7.45 ± 0.05	8.43 ± 0.04	8.45 ± 0.05	8.69 ± 0.04	9.08 ± 0.05	9.33 ± 0.05	9.31 ± 0.56	9.18 ± 0.06	8.00 ± 0.01	7.90 ± 0.05	7.88 ± 0.05	7.50±0.03
DO(ppm) +	1.0 ± 0.02	2.0 ± 0.01	2.5 ± 0.04	4.5 ± 0.03	4.0 ± 0.03	5.0 ± 0.05	4.0 ± 0.05	3.0 ± 0.04	2.5 ± 0.04	2.0 ± 0.04	1.0 ± 0.03	1.0±0.02
DCO_2(ppm)*	32.0 ± 0.20	19.0 ± 0.44	18.0 ± 0.3	18.0 ± 0.45	18.0 ± 0.53	17.0 ± 0.56	18.0 ± 0.54	18.0 ± 0.44	20.0 ± 0.56	20.0 ± 0.45	30.0 ± 0.46	35.0±0.54
Conductivity (μ mhos/cm)	40.2 ± 0.04	45.0 ± 0.05	43.7 ± 0.4	40.0 ± 0.6	45.0 ± 0.5	47.0 ± 0.4	38.7 ± 0.5	33.3 ± 0.6	42.0 ± 0.7	50.3 ± 0.7	30.7 ± 0.3	34.2±0.6
72 h												
LC_{50} (mgL^{-1})	28.72	15.29	24.56	25.59	27.33	43.32	44.87	38.56	13.92	13.96	8.46	8.15
Temp (°C) **	31 ± 0.40	30 ± 0.55	28 ± 0.56	26 ± 0.20	22 ± 0.36	17 ± 0.30	20 ± 0.50	21 ± 0.36	35 ± 0.33	30 ± 0.47	35 ± 0.55	36±0.32
pH +	8.35 ± 0.06	8.25 ± 0.06	8.42 ± 0.04	8.66 ± 0.03	9.15 ± 0.05	9.34 ± 0.04	9.18 ± 0.04	9.10 ± 0.07	7.97 ± 0.4	8.47 ± 0.03	7.82 ± 0.03	8.00±0.08
DO(ppm) +	1.0 ± 0.02	2.0 ± 0.01	2.5 ± 0.04	4.0 ± 0.02	4.0 ± 0.03	4.5 ± 0.04	4.0 ± 0.05	3.0 ± 0.04	2.2 ± 0.06	2.0 ± 0.04	0.8 ± 0.09	0.5±0.01
DCO_2(ppm)*	32.0 ± 0.20	21.0 ± 0.40	22.0 ± 0.6	21.0 ± 0.43	20.0 ± 0.56	18.0 ± 0.54	20.0 ± 0.30	18.0 ± 0.44	25.0 ± 0.43	25.0 ± 0.45	35.0 ± 0.37	40.0±0.67
Conductivity (μ mhos/cm)	35.2 ± 0.05	35.4 ± 0.6	33.7 ± 0.6	33.4 ± 0.67	32.0 ± 0.6	40.3 ± 0.5	40.7 ± 0.5	30.3 ± 0.6	33.0 ± 0.3	40.3 ± 0.6	32.0 ± 0.4	34.2±0.7
96 h												
LC_{50} (mgL^{-1})	24.25	11.79	19.13	18.87	19.49	22.44	24.34	25.76	11.35	11.36	7.03	7.27
Temp (°C) **	30 ± 0.30	30 ± 0.55	29 ± 0.40	26 ± 0.10	22 ± 0.36	17 ± 0.30	20 ± 0.50	21 ± 0.30	34 ± 0.21	30 ± 0.44	36 ± 0.65	35±0.40
pH +	9.35 ± 0.07	8.25 ± 0.06	8.32 ± 0.03	8.69 ± 0.03	9.00 ± 0.04	9.49 ± 0.03	9.40 ± 0.03	9.50 ± 0.04	7.95 ± 0.02	8.00 ± 0.02	7.84 ± 0.05	8.43±0.05
DO(ppm) +	1.0 ± 0.02	2.0 ± 0.01	2.3 ± 0.07	2.1 ± 0.03	2.5 ± 0.04	3.0 ± 0.03	3.5 ± 0.06	3.0 ± 0.04	1.8 ± 0.04	2.0 ± 0.04	0.5 ± 0.04	0.5±0.01
DCO_2(ppm)*	30.0 ± 0.25	30.0 ± 0.56	25.0 ± 0.5	21.0 ± 0.48	20.0 ± 0.62	19.0 ± 0.55	20.0 ± 0.30	18.0 ± 0.44	30.0 ± 0.50	30.0 ± 0.37	40.0 ± 0.35	38.0±0.66
Conductivity (μ mhos/cm)	34.2 ± 0.06	35.4 ± 0.70	23.7 ± 0.5	33.2 ± 0.5	22.0 ± 0.7	31.3 ± 0.3	32.7 ± 0.6	30.3 ± 0.5	32.0 ± 0.7	40.3 ± 0.4	30.0 ± 0.5	30.2±0.8

Each experiment was replicated six times and values are the mean of six replications. Temperature, pH, dissolved oxygen, free carbon dioxide and conductivity were measured intervals of 24 h to 96 h. Product moment correlation coefficient in between the LC_{50} and different parameters indicate significant ($P < 0.05$) (+) positive/ (*) negative correlation.

Table 2. Effect of 24 h exposure of 40% and 80% of 24 h LC_{50} of oleoresin of *Z. officinale* in different months of the year 2006-07 on acetylcholinesterase activity in the nervous tissue of *L. acuminata.*

Months	24 h LC_{50} mgL^{-1}	AChE-µ mole "SH" hydrolyzed / min / mg protein		
		Control [a]	40% of 24h LC_{50}	80% of 24h LC_{50}
August	39.67	0.093 ± 0.01 (100)	0.091 ± 0.01 (97.84)	0.088 ± 0.01 (94.62)
September	54.54	0.139 ± 0.01 (100)	0.136 ± 0.01 (97.84)	0.132 ± 0.01 (94.96)
October	55.92	0.101 ± 0.02 (100)	0.099 ± 0.01 (98.02)	0.097 ± 0.02 (96.04)
November	58.79	0.106 ± 0.01 (100)	0.103 ± 0.02 (97.17)	0.101 ± 0.01 (95.28)
December	62.18	0.109 ± 0.00 (100)	0.107 ± 0.01 (98.17)	0.105 ± 0.01 (96.33)
January	126.27	0.190 ± 0.00 (100)	0.189 ± 0.01 (99.47)	0.186 ± 0.01 (97.89)
February	124.09	0.176 ± 0.01 (100)	0.175 ± 0.00 (99.43)	0.171 ± 0.00 (97.16)
March	74.93	0.147 ± 0.02 (100)	0.142 ± 0.01 (96.60)	0.134 ± 0.01 (91.16)
April	24.88	0.141 ± 0.02 (100)	0.137 ± 0.01 (93.66)	0.133 ± 0.01 (84.51)
May	21.67	0.104 ± 0.01 (100)	0.101 ± 0.02 (75.92)	0.099 ± 0.03 (70.37)
June	16.54	0.087 ± 0.03 (100)	0.083 ± 0.02 (62.19)	0.074 ± 0.02 (59.75)
July	14.28	0.082 ± 0.02 (100)	0.073 ± 0.01 (63.41)	0.071 ± 0.01 (56.09)

Values are mean ± SE of six replicates. Value in parenthesis indicates % enzyme activity with untreated control taken as 100%. Rank correlation coefficient in between LC_{50} and AChE activity in treated group indicate significant ($P < 0.05$) positive (+) correlation. a, Significant ($P < 0.05$) when one way of ANOVA was applied in between the enzyme activity in different months of the year in control group without treatment.

Table 3. Effect of 24 h exposure of 40% and 80% of 24 h LC_{50} of oleoresin of *Z. officinale* in different months of the year 2006-07 on alkaline phosphatase activity in the nervous tissue of *L. acuminata.*

Months	24 h LC_{50} mgL^{-1}	ALP-µ moles/ 30 min / mg protein		
		Control	40% of 24 h LC_{50}	80% of 24 h LC_{50}
August	39.67	2.27 ± 0.01 (100)	2.17 ± 0.01 (95.59)	2.14 ± 0.01 (94.27)
September	54.54	3.34 ± 0.01 (100)	3.31 ± 0.01 (99.10)	3.27 ± 0.01 (97.90)
October	55.92	3.27 ± 0.01 (100)	3.23 ± 0.02 (98.77)	3.19 ± 0.02 (97.55)
November	58.79	3.36 ± 0.02 (100)	3.32 ± 0.02 (98.80)	3.27 ± 0.00 (97.32)
December	62.18	3.11 ± 0.00 (100)	3.06 ± 0.02 (98.39)	3.02 ± 0.02 (97.10)
January	126.27	2.89 ± 0.01 (100)	2.85 ± 0.00 (98.62)	2.81 ± 0.01 (97.23)
February	124.09	3.07 ± 0.01 (100)	3.02 ± 0.01 (98.37)	2.98 ± 0.01 (97.06)
March	74.93	3.10 ± 0.00 (100)	3.07 ± 0.00 (99.03)	3.02 ± 0.01 (97.41)
April	24.88	3.45 ± 0.01 (100)	3.42 ± 0.02 (99.13)	3.37 ± 0.02 (97.68)
May	21.67	2.94 ± 0.02 (100)	2.89 ± 0.00 (98.29)	2.86 ± 0.03 (97.28)
June	16.54	1.86 ± 0.03 (100)	1.74 ± 0.02 (93.55)	1.64 ± 0.02 (88.17)
July	14.28	2.36 ± 0.01 (100)	2.23 ± 0.01 (94.49)	2.16 ± 0.02 (91.52)

Values are mean ± SE of six replicates. Value in parenthesis indicates % enzyme activity with untreated control taken as 100%. Rank correlation coefficient in between LC_{50} and ALP activity in treated group indicate non significant ($P < 0.05$) positive correlation. a, Significant ($P < 0.05$) when one way of ANOVA was applied in between the enzyme activity in different months of the year in control group without treatment.

(ACP) (τ = 0.606; P= 0.05 - 40% of 24 h LC_{50}, τ = 0.606; P = 0.05 - 80% of 24 h $LC_{50,}$) activity in the nervous tissue of *L. acuminata* exposed to sub-lethal treatments of oleoresin in different months. Maximum inhibition in ACP activity (91.00% of control) was observed in snails exposed to 80% of 24 h LC_{50} in July (**Table 4**).

4. DISCUSSION

It is clear from result section that toxicity of oleoresin varies with changes in abiotic environmental factors in the water. Effect of abiotic variants in aquatic environment *i.e.* pH [20], Temperature [21] on the toxicity of different pesticides have been reported. The temperature of water is a significant factor, which alters the toxicity of oleoresin in each month of the year. When the water temperature is higher in summer season June-July, the toxicity of oleoresin is maximum. Contrarily, in winter season, the temperature of water is low and toxicity of oleoresin is less as evident by higher LC_{50} value. Temperature of environment in which the animal resides is a crucial factor, when toxicity of pesticides is determined [22-25]. Osterauer and Kohler [26] reported that the toxicity of diazinon against zebra fish strongly increased at elevated temperature. Dissolved oxygen is also one of the factors, which alter the toxicity of oleoresin. Water in winter season holds more oxygen [27] and as a result, less mortality of snails occurs during this period. At higher water temperature dissolved oxygen concentration decreases which is reflected by higher mortality of the snails. Dissolved oxygen is one of the major components, which is required by snails during metabolic activity [28,29]. Consequently, at higher temperature, increasing rate of metabolism in snail body may release more CO_2, which affects the pH of water [30,31] As the time duration increases concentration of CO_2 increases in the water (released by snails) and it also affects the pH of water. Murphy [32] reported that pesticides belonging to organophosphate and carbamate groups are very sensitive to change in pH. Earlier Vasconcellos [33] observed the influence of pH variation on the molluscicidal activity of *Euphorbia splendens* latex. According to them molluscicidal activity was maximum at pH 5.0 - 6.0 and minimum at pH 7.0 - 8.0. Toxicity of oleoresin is highest at high temperature, CO_2 of water as well as low pH, dissolved O_2 of water. The low concentration of dissolved O_2 act as physical stressor on aquatic animals [34] and in the absence of sufficient dissolved O_2; the snails appear to become more sensitive against the molluscicide. The pungent moieties of oleoresin are gingerol, zingirone and shogaol [35]. It is conceivable that, the active molluscicidal component, present in the oleoresin might get converted into a more toxic form in

Table 4. Effect of 24h exposure of 40% and 80% of 24h LC_{50} of oleoresin of *Z. officinale* in different months of the year 2006-07 on acid phosphatase activity in the nervous tissue of *L. acuminata.*

Months	24 h LC_{50} mgL^{-1}	ACP-µ moles/ 30min / mg protein		
		Control	40% of 24 h LC_{50}	80% of 24 h LC_{50}-
August	39.67	3.15 ± 0.00 (100)	3.04 ± 0.01 (95.51)	2.91 ± 0.01 (92.38)
September	54.54	3.64 ± 0.01 (100)	3.58 ± 0.01 (98.35)	3.52 ± 0.01 (96.70)
October	55.92	3.31 ± 0.01 (100)	3.29 ± 0.01 (99.40)	3.24 ± 0.00 (97.89)
November	58.79	3.34 ± 0.02 (100)	3.32 ± 0.02 (99.40)	3.28 ± 0.01 (98.20)
December	62.18	3.28 ± 0.01 (100)	3.23 ± 0.01 (98.48)	3.19 ± 0.01 (97.26)
January	126.27	3.29 ± 0.01 (100)	3.27 ± 0.00 (99.70)	3.21 ± 0.02 (97.87)
February	124.09	3.40 ± 0.00 (100)	3.39 ± 0.01 (99.70)	3.33 ± 0.01 (97.94)
March	74.93	3.46 ± 0.01 (100)	3.40 ± 0.00 (98.27)	3.34 ± 0.01 (96.53)
April	24.88	3.26 ± 0.01 (100)	3.19 ± 0.01 (97.85)	3.09 ± 0.02 (94.79)
May	21.67	3.45 ± 0.02 (100)	3.38 ± 0.02 (97.97)	3.31 ± 0.02 (95.94)
June	16.54	2.95 ± 0.03 (100)	2.86 ± 0.01 (96.95)	2.72 ± 0.03 (92.20)
July	14.28	3.00 ± 0.01 (100)	2.82 ± 0.01 (94.00)	2.73 ± 0.01 (91.00)

Values are mean ± SE of six replicates. Value in parenthesis indicates % enzyme activity with untreated control taken as 100%. Rank correlation coefficient in between LC_{50} and ACP activity in treated group indicate significant ($P < 0.05$) positive (+) correlation. a, Significant ($P < 0.05$) when one way of ANOVA was applied in between the enzyme activity in different months of the year in control group without treatment.

the aquarium water or in the snail body due to variant environmental factors in the month of June and July. Earlier, it has been shown that the treatment of oleoresin of *Z. officinale* caused significant inhibition of AChE, ALP and ACP activity in the nervous tissue of *L. acuminata* [9]. The high anti AChE and ACP activity of oleoresin of *Z. officinale* was observed in months of June-July. The enzyme ALP plays a critical role in protein synthesis, [36] and secretary activity, [37] is comparatively less inhibited than AChE, Acid phosphatase (ACP), a lysosomal enzyme, [38] plays an important role in autolysis and phagocytosis, pathological necrosis, and overall catabolism, [8,10,39] was reduced significantly. Earlier, it has been observed that increased activity of ACP causes breakdown of existing protein in *L. acuminata* [18], but inhibition of ACP activity in this study indicates that it is not used in breakdown of cellular protein. The rank correlation coefficient applied between the LC_{50} values of different months and the corresponding inhibition in enzyme activity, point out a positive correlation between the LC_{50} and the inhibition of AChE and ACP. Whereas there was no correlation in between LC_{50} and ALP activity indicate that ALP is not altered by action of oleoresin in different months.

Accurate prediction of molluscicide fate and toxicity in aqueous environment against snails are hindered due to lack of information that how abiotic factors of aqueous environment affect the biological activity and related toxicity of molluscicides. Abiotic factors are not only correlated with the lethality of molluscicide, but with each other also. The present study conclusively shows that variant abiotic factors can significantly alter the toxicity of oleoresin of *Z. officinale* in *L. acuminata*. It is also obvious that the most suitable period for the control of this snail in India is the month of June, July. It is suggested that the treatment of a water body with oleoresin of *Z. officinale* for the control of *L. acuminata* and ultimately fascioliasis, is not only more potent and cost effective during these months than spending more money by using higher concentrations of this molluscicide during the rest ten months of the year.

REFERENCES

[1] Singh, S., Singh, V.K. and Singh, D.K. (1997) Molluscicidal activity of some common spice plants. *Biology, Agriculture and Horticulture*, **14**, 237-249.

[2] Shukla, S., Singh, V.K. and Singh, D.K. (2006) The effect of single, binary, tertiary, combination of few plant derived molluscicides alone or in combination with synergist on different enzymes in the nervous tissues of the freshwater snail *Lymnaea* (Radix) *acuminata* (Lamark). *Pesticide Biochemistry and Physiology*, **85**, 167-173.

[3] Singh, O. and Agarwal, R.A. (1981) Toxicity of certain pesticides to two economic species of snails in northern India. *Journal of Economic Entomology*, **74**, 568-571.

[4] World Health Organization. (2006) Report of the WHO informal meeting on use of triclabendazole in fascioliasis control, WHO headquarters, Geneva, Switzerland, 17-18 October 2006.

[5] Singh, P., Singh, V.K. and Singh, D.K. (2005) Effect of binary combination of some plant-derived molluscicides with MGK-264 or piperonyl butoxide on the reproduction of the snail *Lymnaea acuminata*. *Pest Management Science*, **61**, 204-208.

[6] Kumar, P. and Singh, D.K. (2006) Molluscicidal activity of *Ferula asafoetida*, *Syzygium aromaticum* and *Carum carvi* and their active components against the snail *Lymnaea acuminata*. *Chemo* **63**, 1568-1574.

[7] Kumar, P., Singh, V.K. and Singh, D.K. (2009) Kinetics of enzyme inhibition by active molluscicidal agents ferulic acid, umbelliferone, eugenol and limonene in the nervous tissue of snail *Lymnaea acuminata. Physiological Research*, **23**, 172-177.

[8] Jaiswal, P., Singh, V.K. and Singh, D.K. (2008) Enzyme inhibition by molluscicidal component of *Areca catechu* and *Carica papaya* in the nervous tissue of vector snail *Lymnaea acuminata*. *Pesticide Biochemistry and Physiology*, **92**, 164-168.

[9] Singh, K. and Singh, D.K. (2000) Toxicity to the snail *Lymnaea acuminata* of plant-derived molluscicides in combination with synergists. *Pest Management Science*, **56**, 889-898.

[10] Tripathi, S.M., Singh, V.K., Singh, S. and Singh, D.K. (2004) Enzyme inhibition by the molluscicidal agent *Punica granatum* Linn. bark and *Canna indica* Linn. root. *Physiological Research*, **18**, 501-506.

[11] Gunther, E. (1975) The essential oils. Robert, E Krieger Publishing Company, NewYork.

[12] American Public Health Association (APHA), (2005) Standard methods for the examination of water and waste water. 21st Edition, Washington, D.C.

[13] Robertson, J.L., Russell, R.M., Preisler, H.K. and Savin, N.E. (2007) *Bioassay with Arthropods* POLO computer programme for analysis of bioassay data. 2nd Edition, Talor and Francis, CRC Press, 1-224.

[14] Sokal, R.R. and Rohlf, F.J. (1973) Introduction to biostatistics. W. H. Freeman & Co., Ltd., San Francisco.

[15] Ellman, G.L., Courtney, K.D., Andres, V. and Featherstone, R.M. (1961) A new and rapid colorimetric determination of acetylcholinesterase activity. *Bio Pharmacol*, **7**, 88-95.

[16] Singh, D.K., Singh, O. and Agarwal, R.A. (1982) Comparative study of cholinesterase in two snails. *Pila globosa* and *Lymnaea acuminata. The Journal of Physiology*, **78**, 467-472.

[17] Bergmeyer, U.H. (1967) Methods of enzymatic analysis. Academic Press, New York, 1129.

[18] Singh, D.K. and Agarwal, R.A. (1989) Toxicity of piperonyl butoxide carbaryl synergism on the snail Lymnaea acuminata. *Internationale Revue der gesamten Hydrobiologie und Hydrographie*, **74**, 689-699.

[19] Lowry, O.H., Rosebrough, N.J., Farr, A.L. and Randall R.J. (1951) Protein measurement with folin phenol reagent. *The Journal of Biological Chemistry*, **193**, 265- 275.

[20] Watson, S.J. and Maly, E.J. (1987) Thiocyanate toxicity

to Daphina magna: Modified by pH and temperature. *Aquatic Toxicol*, **10**, 1-8.

[21] Sogorb, A., Andreu-Moliner, E.S., Almar, M.M., del Ramo, J. and Nunez, A. (1988) Temperature-toxicity relationship of fluvalinate (synthetic pyrethroid) on *Procambarus clarkia* (Girard) under laboratory conditions. *Bull Environ Cantam Toxicol*, **40**, 13-17.

[22] Schott, J.G. and Georghion, G.P. (1984) Influence of temperature on knockdown, toxicity and resistance to pyrethroids in the house fly, *Musca domestica*. *Pesticide Biochemistry and Physiology*, **21**, 53-62.

[23] Ferrando, M.D., Andreu-Moliner, E.S., Almar, M.M., Cerebrian, C. and Nunez, A. (1987) Acute toxicity of organochlorine pesticides to the European eel, *Anguilla anguilla*. The dependency on exposure time and temperature. *Bulletin of Environmental Contamination and Toxicology*, **39**, 365-369.

[24] Schott, J.G. (1995) Effects of temperature on insecticides toxicity. In: Roe, R.M. and Kuhr, R.J. Eds., *Reviews in Pesticide Toxicology*, North Carolina State University, Raleigh, 111-135.

[25] Young, C. (1996) Metal chelates as stomach poison molluscicides for introduced pests, *Helix aspersa*, *Theba pisana*, *Cernuella virgata* and *Deroceras reticulatum* in Australia. In: Henderson, I.F. Ed., *Slug and Snail Pests in Agriculture*. British Crop Protection Council, Farnham, 237-243.

[26] Osterauer, R. and Kohler, H.R. (2008) Temperature-dependent effects of the pesticides thiacloprid and diazinon on the embryonic development of zebra fish (*Danio rerio*). *Aquatic Toxicol*, **86**, 485-494.

[27] Waterwatch Australia. (2002) National Technical Manual. Module 4: Physical and chemical parameters. Waterwatch Australia Steering Committee Environment Australia, http://www.waterwatch.org.au

[28] Ishak, M.M. and Mohamed, A.M. (1975) Effect of sublethal doses of copper sulphate and bayluscide on survival and oxygen consumption of the snail *Biomphalaria alexandrina*. *Hydrobiol*, **47**, 499-512.

[29] Watten, B.J. (2004) Method and apparatus for control of aquatic vertebrate and invertebrate invasive species. US Patent No. 6821442, 23 November 2004.

[30] Toews, K.L., Shroll, R.M., Wai, C.M. and Smart, N.G. (1995) pH – Defining equilibrium between water and supercritical CO_2– influence on SFE of organics and metal chelates. *Analytical Chemistry*, **67**, 4040-4043.

[31] Berge, J.A., Bjerkeng, B., Pettersen, O., Schaanning, M.T. and Oxnevad, S. (2006) Effects of increased sea water concentrations of CO_2 on growth of the bivalve *Mytilus edulis* L. *Chemo*, **62**, 681-687.

[32] Murphy, G. (2004) Water pH and its Effect on Pesticides. Ministry of Agriculture and Food Ontario, Canada. http://www.gov.on.ca/OMAFRA/english/crops/hort/news/grower/2004/08gn04a1.htm

[33] Vasconcellos, M.C. and Amorim, A. (2003) Molluscicidal action of the latex of *Euphorbia splendens* var. *hislopii* NEB (Christ Crown) (Euphorbiaceae) against *Lymnaea columella* (Say, 1817) (Pulmonata; Lymnaeidae), Intermediate host of *Fasciola hepatica* (Linn. 1758) (Trematode: Fasciolidae). 1-Test in laboratory. *Mem Inst Oswaldo Cruz, Rio de Janeiro*, **98**, 557-563.

[34] Irving, E.C., Lowell, R.B., Culp, J.M., Liber, K., Xie, Q. and Kerrich, R. (2008) Effects of arsenic speciation and low dissolved oxygen condition on the toxicity of the arsenic to a lotic Mayfly. *Environmental Toxicology & Chemistry*, **27**, 593-590.

[35] Mustafa, T., Srivastava, K.C. and Jensen, K.B. (1993) Drug development report (9) Pharmacology of ginger *Zingiber officinale*. *Journal of Drug Development*, **6**, 25-39.

[36] Pilo, B., Asnani, M.B. and Shah, R.V. (1972) Studies on wound healing and repair in pigeon liver III. Histochemical studies on acid and alkaline phosphatase activity during the process. *J Ani Mor Phy*, **19**, 205-212.

[37] Ibrahim, A.M., Migazi, M.G. and Dexian, E.S. (1974) Histochemical localization of alkaline phosphatase activity in the alimentary tract of the snail *Marisa coruarielis* (1). *Bul Zoo Soc Egy*, **26**, 95-105.

[38] Aruna, P., Chetty, C.S., Naidu, R.C. and Swami, K.S. (1979) Acid phosphatase activity in the Indian apple snail *Pila globosa* (Swainsen) during aestivation and starvation stress. *Proceedings of Indian Academy Science (India)*, **88**, 363-365.

[39] Abou-Donia, M.B., (1978) Increased acid phosphatase activity in hens following oral dose of Leptophos. *Toxicology Letters*, **2**, 199-203.

Vol.2, No.10, 1155-1163 (2010)
doi:10.4236/ns.2010.210143

Natural Science

Distribution of polychaetes in the shallow, sublittoral zone of Admiralty Bay, King George Island, Antarctica in the early and late austral summer

Letícia de Souza Barbosa[1], Abílio Soares-Gomes[1], Paulo Cesar Paiva[2]*

[1]Department of Marine Biology, Fluminense Federal University, Niterói, Brazil; leticiadsb@gmail.com; abiliosg@vm.uff.br;
[2]Department of Zoology, Federal University of Rio de Janeiro, Rio de Janeiro, Brazil; *Corresponding Author: paulo.paiva@gmail.com.

Received 20 July 2010; revised 25 August 2010; accepted 28 August 2010.

ABSTRACT

This study assessed the spatial distribution pattern of soft-sediment polychaetes on the nearshore of Admiralty Bay, King George Island, Antarctica. In the early and late summer of 2003 /04, seven sites at three different depths (20,30 and 60 meters) were sampled using a van Veen grab. 8,668 individuals all told, belonging to 67 species and 23 families, were identified. The families Terebellidae, Syllidae and Maldanidae were the most speciose. Mean densities ranged from 45.2 to 388.1 ind. 0.1 m^{-2} in the early summer, and from 29 to 183 ind.0.1m^{-2} in the late. The species *Aphelochaeta cincinnata*, *Levinsenia gracilis* and *Rhodine antarctica* were the most frequent and abundant. Initially, mean biomass ranged from 0.11 to 5.27 g.0.1 m^{-2}, in the early season and from 0.35 to 5.86 g.0.1 m^{-2} towards the end. *Aglaophamus trissophyllus*, *Eupolymnia* sp. and *Barrukia cristata* were the species with the highest biomass. Polychaete taxocoenosis structure remained similar in both periods. In the early summer, mean densities, biomass and number of species were lower at 30 meters and higher at 60, whereas in the late, these differences were higher among transects. Ice impacts, mainly anchor-ice, in the early summer, as well as icebergs later on, most likely caused the differences encountered.

Keywords: Polychaeta; Soft-Sediment; Benthic Structure; South Shetland Islands; Antarctic Peninsula

1. INTRODUCTION

The Antarctic benthos is characterized by pronounced endemism and a marked dependence on physical conditions, such as sediment patterns, waves and ice effects [1]. Distribution of the benthic community in shallow waters (up to 100 m) could be influenced by depth [2]. According to Sahade *et al.* [3], benthic density is the highest at 25 meters. From here down to 50 meter depth, there is a decrease [4]. Below this, the community is free from the impacts of icebergs and storms, thereby reaching an advanced stage in development. Besides depth, distribution is also influenced by habitat heterogeneity, bottom topography and hydrodynamics, among other factors [2]. Low and stable water temperatures, low fluctuations in salinity during the summer, reduced terrigenous sediment input and the seasonality of food resources, could also exert an influence on both the structure and distribution of the Antarctic fauna [1]. Nevertheless, according to Barnes & Conlan [5], ice remains as one of the foremost agents of disturbance in shallow water benthos.

The benthic fauna of the Southern Ocean is well known, the polychaetes being one of the most representative groups in soft-sediment habitats [6-8]. The group can account for over 50% of the macrofauna in several Antarctic areas, such as Chile Bay, Greenwich Island [9], Port Foster, Deception Island [10], Arthur Harbour, Anvers Island [11], McMurdo Sound [12] and Admiralty Bay, King George Island [6]. Polychaete composition and distribution in Admiralty Bay was already studied by several authors [6,13-19] and can be summarized in the following zonation patterns: the dominance of *Leitoscoloplos kerguelensis*, *Ophryotrocha notialis* and *Microspio* cf. *moorei* on shallow bottoms (down to 12 m) and higher densities of *Aphelochaeta cincinnata*, *Apistobranchus glacierae*, *Rhodine antarctica* and *Levinsenia gracilis* further down. According to Conlan *et al.* [20], certain polychaetes, such as *Ophryotrocha notialis*, *Capitella perarmata*, *Aphelochaeta* sp. and *Leitoscoloplos kerguelensis*, are dominant in areas under the impact of sea-waste disposal, besides being capable of coloniz-

ing ice-disturbed areas [21,22].

The aim of this survey was to investigate polychaete spatial distribution in the nearshore soft-sediments at three depths in Admiralty Bay, during the early and late austral summer.

2. STUDY AREA

Admiralty Bay, the largest bay in King George Island, is approximately 122 km², with depths exceeding 500 meters [23]. The fjord-like shaped bay has three inlets, Mackellar and Martel located in the northern portion, and Ezcurra located in the western [17]. The bay receives water from the Bransfield Strait through a 500-meters-deep channel. Coarse sediments mixed with fine mud occur down to a depth of 50 meters, the rest consisting mainly of fine mud [24]. The sediment in front of the Brazilian Antarctic station contained high concentrations of trace metals (B, Mo, Pb, V, Zn, Ni, Cu, Mg and Mn), organic matter and oil contaminants. However, despite the evidence of contamination, the low bioavailability of these pollutants is an indication of low environmental risk [25]. Variation in temperature and salinity is slight, ranging from −0.4°C to 0.9°C and 33.8 to 33.4, respectively, at the bottom [24]. The phytoplankton from Admiralty Bay is dominated by diatoms, under the influence of benthic species from sediment resuspension or ice defrosting [26].

3. MATERIAL AND METHODS

Seven transects located in the Mackellar and Martel inlets were sampled (**Figure 1**): Research Station "Comandante Ferraz" (CFA, CFB and CFC), Botany Point (BP), Hennequin Point (HE), Machu Picchu (MP) and Thomas Point (AR), during the austral summer of 2003-2004. At each site, samples were collected at three depths (20, 30 and 60 meters) with a van Veen grab (0.056 m²). In the early summer (November and December, 2003) three replicates were collected, whereas four were in the late season (February and March, 2004). Samples were sieved through a 0.5 mm mesh. Specimens were fixed in 4% formaldehyde and preserved in 70% alcohol. The polychaetes were identified at the species level. Unidentifiable individuals were included in the analysis as morphotypes. Biomass was estimated by the measurement of wet-weight (± 0.01 mg). Dry-sieve and pipette methodologies were used for grain-size analysis, as described by Suguio [27]. Calcium carbonate content was determined by dry-weight difference after HCl 10% attack, and that of total carbon and nitrogen by using an Elemental Analyser CHNS/O Perkin Elmer (2400 Series II), with a detection limit of 0.02% for C and 0.03% for N [28]. Species densities (ind. 0.1 m² ± standard-error) were used to calculate species dominance, according to the formula:

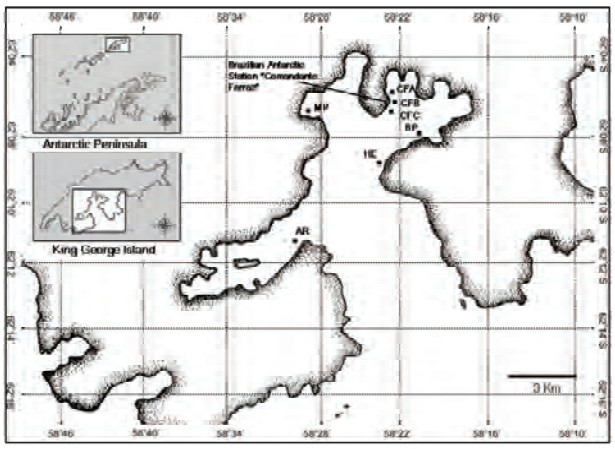

Figure 1. Sampling sites at Admiralty Bay.

Do = (Na/N) * 100

where Do = dominance of species A, Na = density of species A and N = sum of all species densities.

Species occurrence frequencies were calculated by using the following formula:

Fa = (Pa/P) * 100

where Fa = frequency of species A, Pa = number of samples in which species A occurred, and P = total of samples.

Species with higher than 50% occurrence were considered constant, those between 50% and 10%, common, and those with less than 10%, rare. Density data were transformed (square root), and Two-way ANOVA employed to check differences between early and late summer surveys. Cluster analysis was with the UPGMA algorithm using a Bray Curtis similarity index calculated by densities. Diagrams of ordination were produced through non-metric Multi-Dimensional Scaling (nMDS) analysis. The significance of differences among depths during early and late summer was tested by One-Way Analysis of Variance by Similarities-ANOSIM [29].

Canonical Correspondence Analysis (CCA) was applied with a matrix of 10 abiotic variables (gravel, coarse sand, medium sand, fine sand, silt, clay, carbonate, total carbon, organic carbon and total nitrogen), together with the most frequent species in each of the summer periods. The transect AR 60 m was not considered, due to the lack of grain-size data. Statistical analysis was undertaken with the Statistica 6.0 program, multivariate analysis with the Primer 6, program, and CCA by using the Biplot 1.1 add-in routine for Excel [30].

4. RESULTS

4.1. Abiotic Variables

The sediment consisted mainly of silt and clay (more

than 60%) at most transects and depths, although the percentages of fine sand were higher (ca. 30%) in some stations like HE and AR. At 60 meters, slightly lower percentages of both gravel and coarse sand were observed, when compared to shallower transects. Calcium carbonate content was slightly higher in the late summer (more than 12%), whereas in the early season, this was lower at 20 and 30 meters, with the lowest (6.5%) at MP. Carbon and nitrogen content were very low (< 1%). CFA, CFB and CFC presented the highest percentages of carbon content (0.54 to 0.75%), and MP the lowest (0.28 to 0.46%). There was no apparent variation of either variable with the increase in depth.

4.2. Polychaete Composition

A total of 8,668 individuals were collected throughout the period. The set of samples yielded 67 species and four morphotypes (Cirratulidae gen. sp.1, Cirratulidae gen. sp.2, Maldanidae gen. sp. and Terebellidae gen. sp.), belonging to 23 families (**Table 1**). 21 species were collected in each sampling survey. The most speciose families were Terebellidae and Syllidae with seven species each, and Maldanidae with six. The families Glyceridae and Sabellidae were exclusive to the early summer, whereas Nereididae and Serpulidae were to the late summer. The families Nereididae, Serpulidae and Glyceridae were each represented by only one species, viz., *Nicon ehlersi*, *Helicosiphon biscoensis* and *Glycera capitata*, respectively. The sabellids were represented by three species: *Euchone pallida*, *Perkinsiana litorallis* and *Perkinsiana milae*, all somewhat scarce during the summer.

4.3. Dominance and Frequency

In terms of density, the species *Aphelochaeta cincinnata*, *Levinsenia gracilis*, Cirratulidae gen. sp. 1, *Apistobranchus glacierae* and *Rhodine antarctica* dominated, throughout the whole period studied. The exceptions were Cirratulidae gen. sp. 1 and *A. glacierae*, dominant only at the beginning. Throughout, *Aphelochaeta cincinnata* was the most frequent species, with 93.55% in the early summer and 85.71% in the late. The species *Levinsenia gracilis* and *Rhodine antarctica* were also constant during the whole study period, with 69.35% and 56.45%, respectively, in the first part, and both 65,48% towards the end. These three species were responsible for 33.7% of total polychaetes in the early summer and 34.7% in the late. *Aricidea (Acmira) strelzovi*, *Leitoscloplos geminus*, *Brada villosa*, *Apistobranchus glacierae*, *Barrukia cristata* and *Cirrophorus brevicirratus* were considered common throughout. *Scalibregma inflatum*, besides being a low-frequency species during the whole period (8.06% in the early part and 5.95% in the late), occurred only at 60 meters (**Table 1**).

4.4. Density and Biomass

Polychaete density ranged from 45.24 to 388.10 ind.0.1 m^{-2} in the early summer. *Apistobranchus glacierae*, with the highest score all told, was also responsible for the high result observed at CFC (20 m) (173.21 ± 76.79 ind. 0.1 m^{-2}). The species *Aphelochaeta cincinnata* at CFB (60 m), *Rhodine antarctica* at CFC (20 m) and *Levinsenia gracilis* at CFC (60 m) also presented high values (**Figure 2**). In the late summer, polychaete density varied from 29.02 to 183.93 ind.0.1 m^{-2}. The highest densities, attributed to *R. antarctica*, were observed at the MP transect at 20 and 30 meters (**Figure 3**).

During sampling, a significant variation in density among depths was observed (ANOVA, $p < 0.002$) (**Table 2**), with lower densities at 30 meters when compared to both 20 and 60 (Tukey test, $p < 0.005$), although no differences among transects were detected ($p = 0.599$). Nevertheless, this pattern seems to be rather complex, since the interaction between transect and depth was significant ($p < 0.02$). This interaction occurred at transects CFA and CFC, with no clear bathymetric pattern. On the contrary, in late summer, significant differences were found only among transects ($p < 0.002$), but not depths (**Table 2**), with MP and AR presenting higher densities than CFA and CFC (Tukey test, $p < 0.05$). These differences occurred due to the high densities of cirratulids (*Aphelochaeta cincinnata* and Cirratulidae gen. sp.1), paraonids (*Levinsenia gracilis*, *Aricidea (Acmira) strelzovi* and *Cirrophorus brevicirratus*) and the maldanid *Rhodine antarctica*, at MP and AR. On the other hand, biomass encountered at both CFA and CFC was low. Surprisingly, polychaete density at CFB was similar to that observed at MP and AR.

In the early summer, biomass means (± standard-error) ranged from 5.27 ± 4.19 g.0.1 m^{-2} at CFC-20 m, to 0.11 ± 0.06 g.0.1 m^{-2} at BP-30 m (**Figure 4**). In the late season, the highest biomass mean was observed at CFB-30 m (5.86 ± 4.72 g.0.1 m^{-2}) and the lowest at BP-30 m (0.35 ± 0.27 g.0.1 m^{-2}) (**Figure 5**). The species *Aglaophamus ornatus*, *Eupolymnia* sp. and *Barrukia cristata* presented the highest values. Although *Rhodine antarctica* biomass was not high, it remained constant at MP, all through the later part of summer, this constancy probably contributing to the proximity of values found at all depths.

4.5. Multivariate Analysis

In the early summer, the samples were grouped through cluster analysis, according to depth. The results indicated that in the first group, composed of transects MP, BP, AR at 20 meters, and MP and AR at 30 meters, the

Table 1. Frequency (Fo) and dominance (Do) of polychaete species in early and late summer, and species codes used in canonical correspondence analysis.

Species	Code	Family	Early summer		Late summer	
			Fo (%)	*Do*	*Fo* (%)	*Do*
Levinsenia gracilis	Lev	Paraonidae	69.35	17.51	65.48	28.64
Aricidea (*Acmira*) *strelzovi*	Ari		35.48	4.45	33.33	4.45
Cirrophorus brevicirratus	Aph		12.90	0.85	23.81	3.94
Leitoscoloplos kerguelensis	Lek	Orbiniidae	22.58	1.02	16.67	0.95
Leitoscoloplos geminus	Leg		29.03	1.76	21.43	1.13
Scoloplos (*Leodamas*) *marginatus*			3.23	0.04	2.38	0.08
Orbinia minima			-	-	2.38	0.08
Scalibregma inflatum		Scalibregmatidae	8.06	0.38	5.95	0.43
Ophelina syringopyge		Ophellidae	4.84	0.22	4.76	0.33
Ophelina breviata			3.23	0.07	1.19	0.03
Ophelina sp.			1.61	0.09	2.38	0.08
Capitella sp.1		Capitellidae	1.61	0.02	4.76	0.13
Capitella sp. 2			-	-	1.19	0.08
Asychis ampliglypta	Asy	Maldanidae	11.29	0.44	21.43	1.21
Maldane sarsi antarctica	Mal		11.29	0.58	11.90	0.60
Lumbriclymenella robusta	Lur		1.61	0.02	10.71	0.38
Rhodine antarctica	Rho		56.45	9.50	65.48	20.30
Praxillella sp.			1.61	0.02	-	-
Maldanidae gen. sp.	Mas		24.19	0.76	19.05	0.98
Austrolaenilla antarctica			4.84	0.07	5.95	0.13
Barrukia cristata	Bar	Polynoidae	22.58	0.47	21.43	0.73
Harmothoe sp.			-	-	1.19	0.03
Glycera capitata		Glyceridae	1.61	0.02	-	-
Eulalia varia			-	-	2.38	0.05
Eulalia sp.			-	-	4.76	0.13
Eteone sculpta		Phyllodocidae	1.61	0.02	2.38	0.05
Genetyllis polyphylla			3.23	0.07	3.57	0.15
Anaitides sp.			1.61	0.04	1.19	0.03
Sphaerodoropsis arctowskyensis			6.45	0.20	2.38	0.05
Sphaerodoropsis sp.		Sphaerodoridae	1.61	0.02	-	-
Ephesiella muelenhardte			1.61	0.04	1.19	0.05
Aglaophamus ornatus	Agl	Nephtyidae	11.29	0.18	8.33	0.23
Nicon ehlersi		Nereididae	-	-	1.19	0.03
Exogone heterosetosa			4.84	0.20	-	-
Exogone minuscula			1.61	0.04	-	-
Exogone heterosetoides			4.84	0.11	8.33	0.30
Exogone sp.		Syllidae	4.84	0.16	1.19	0.03
Syllis sp.			1.61	0.02	-	-
Branchiosyllis sp.			8.06	0.18	1.19	0.05
Syllides liouvillei			-	-	2.38	0.05
Pettiboneia kerguelensis	Pet	Dorvilleidae	17.74	1.69	1.19	0.03
Ophryotrocha notialis			-	-	1.19	0.03
Lumbrineris kerguelensis	Lum	Lumbrineridae	8.06	0.11	15.48	0.35
Augeneria sp.			1.61	0.02	2.38	0.05
Apistobranchus glacirae	Api	Apistobranchidae	24.19	10.03	15.48	0.73
Spiophanes tcherniai			1.61	0.04	4.76	0.15
Laonice antarcticae			1.61	0.02	-	-
Microspio sp.		Spionidae	1.61	0.33	1.19	0.03
Scolelepis eltaninae			1.61	0.04	-	-
Pygospiopis dubia			-	-	1.19	0.05
Aphelochaeta cf. cincinnata	Aph	Cirratulidae	93.55	30.57	85.71	21.71
Cirratulidae gen. sp. 1	Cir 1		32.26	13.59	19.05	6.11
Cirratulidae gen. sp. 2	Cir 2		16.13	2.38	5.95	1.76
Brada villosa	Bra	Flabelligeridae	25.81	0.62	25.00	1.18
Pherusa kerguelarum			-	-	1.19	0.08
Ampharete kerguelensis		Ampharetidae	3.23	0.04	4.76	0.10
Amphicteis gunneri antarctica	Amp		6.45	0.09	15.48	0.70
Anobothrus cf. *patagonicus*			1.61	0.04	2.38	0.05
Phyllocomus crocea			-	-	1.19	0.03
Hauchiella tribullata			1.61	0.02	-	-
Proclea cf. *graffii*			3.23	0.09	1.19	0.03
Amphitrite kerguelensis			-	-	1.19	0.03
Eupolymnia sp.	Eup	Terebellidae	8.06	0.20	21.43	0.53
Terebellides stroemii kerguelensis			8.06	0.24	5.95	0.25
Pista cristata			6.45	0.13	4.76	0.13
Trichobranchus sp.			-	-	1.19	0.03
Terebelidae gen sp.			1.61	0.02	-	-
Euchone palida		Sabellidae	1.61	0.02	-	-
Perkinsiana milae			1.61	0.02	-	-
Perkinsiana littoralis			1.61	0.02	-	-
Helicosiphon biscoensis		Serpulidae	-	-	1.19	0.05

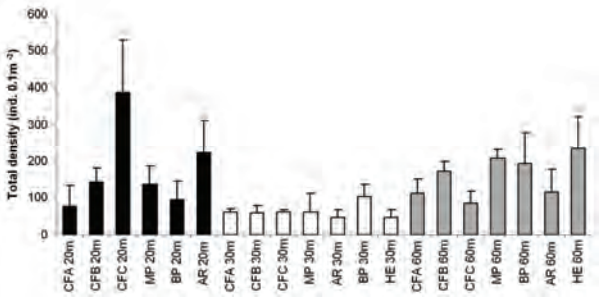

Figure 2. Mean densities (± stardard-error) of Polychaeta at the transects in early summer. Depths: 20 m = black bars; 30 m = white bars; 60 m = gray bars.

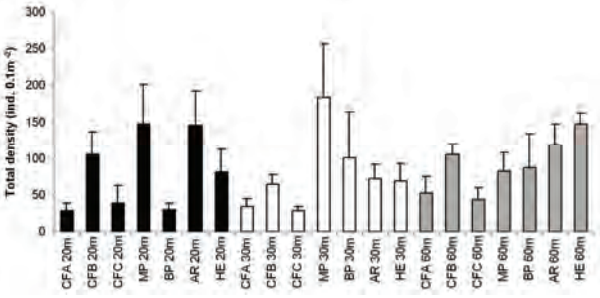

Figure 3. Mean densities (± stardard-error) of Polychaeta at the transects in late summer. Depths: 20 m = black bars; 30 m = white bars; 60 m = gray bars.

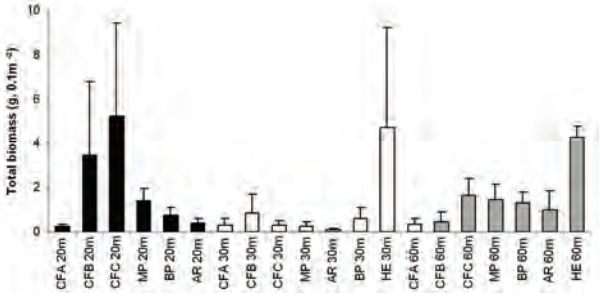

Figure 4. Mean biomass (± stardard-error) of Polychaeta at the transects in early summer. Depths: 20 m = black bars; 30 m = white bars; 60 m = gray bars.

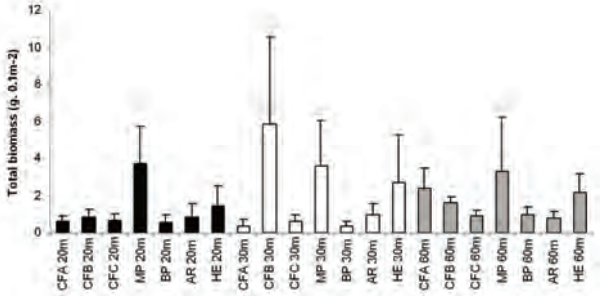

Figure 5. Mean biomass (± stardard-error) of Polychaeta at the transects in late summer. Depths: 20 m = black bars; 30 m = white bars; 60 m = gray bars.

Table 2. Results of Two-way ANOVA in early and late summer.

Factors	Early summer		Late summer	
	p	F	*p*	F
Transect	0.599	0.737	0.001	4.286
Depth	0.001	11.716	0.581	0.547
Transect * Depth	0.015	1.554	0.583	0.867

density of Cirratulidae gen. sp. 1 was high, whereas both *Branchiosyllis* sp. and *S. arctowskyensis* were absent. In the second group (CFB and CFC at 20 m, HE at 30 m, and MP and HE at 60 m), both *R. antarctica* and *A. glacirae* were the most abundant. In the third group, formed by CFA at 20 meters, and CFA, CFB, CFC and BP, all at 30 meters, richness and densities were low in *R. antarctica*, *A. amphiglypta* and *A. cincinnata*. In the last group, *A. cincinnata*, *L. gracilis* and Cirratulidae gen. sp. 2 were abundant, and both *S. inflatum* and *A. strelzovi* present (**Figure 6**). The results from cluster analysis were confirmed through nMDS. In the late summer, no clear pattern of clustering, in relation to either transects or depths, was apparent.

When using ANOSIM, no differences were detected in the polychaete community between the periods sampled (R global = 0.031; p = 20.5%), although the contrary was the case as regards depths. In the early summer, communities at 60 meters differed from those found at 20 and 30 meters, whereas in the late season, the only difference was between 20 and 60 meters (**Table 3**).

Results through Canonical Correlation Analysis (CCA) were rather similar, in both early and late summer. The first axis was responsible for 45.9% of the variance in early summer and 42.8% in late and was positively related to gravel, coarse and fine sand and negatively so to silt, clay, carbonate, carbon and nitrogen contents. The sediment in all transects at 20 meters was coarser, whereas that at 60 meters was characterized by the dominance of silt and clay fractions, and that at 30 meters an intermediate pattern between the former two. The second axis accounted for 25.5% and 20.8% of the variance in early and late summer, respectively (**Figures 7** and **8**). In both summer periods, most species appeared to be associated with gravel, and coarse and fine sand. The maldanids *Maldane sarsi antarctica* and *Asychis amphiglypta* were related to stations at 60 meters. The species *L. geminus*, *L. kerguelensis*, *A. glacirae* and *C. brevicirratus* and Cirratulidae gen sp.1 were positively related with gravel, and coarse and fine sand.

5. DISCUSSION

The number of polychaete species found in the present study was higher than that presented by Sicinski & Ja-

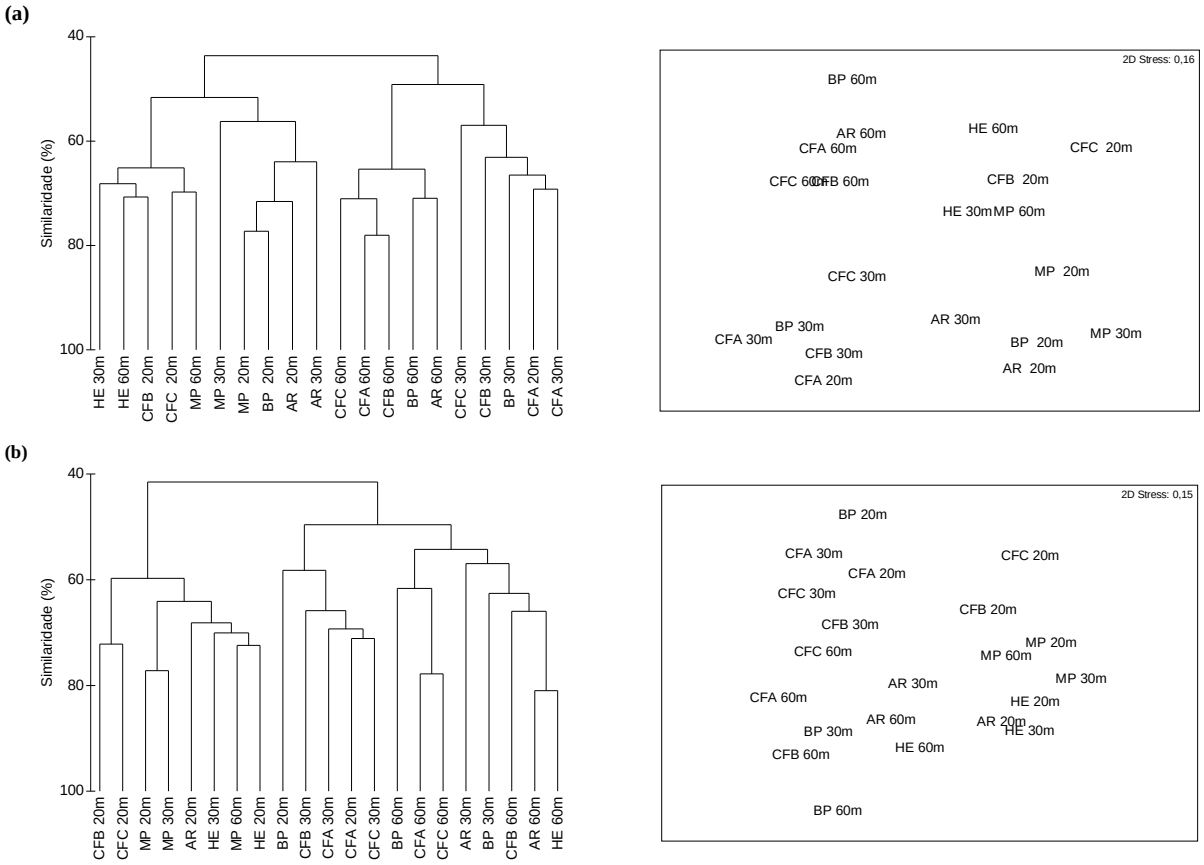

Figure 6. Cluster analysis and nMDS from the transects. **(a)** polychaete density in early summer; **(b)** polychaete density in late summer.

Table 3. Results of One-way ANOSIM for effect of depth (20, 30 and 30 m) on polychaete abundance data.

Groups	Early summer		Late summer	
	R-value	Significance level (%)	R-value	Significance level (%)
All depths	0.43	0.1	0.25	1.8
20,30	0.21	8.2	0.15	11.1
20,60	0.60	0.1	0.48	0.3
30,60	0.49	0.1	0.13	13.7

nowska [16] and Bromberg [17], in Admiralty Bay, at similar depths. However, this richness was low when compared with that in other Antarctic areas, such as Arthur Harbor on Anvers Island [31], Chile Bay on Greenwich Island [32], Terra Nova Bay [33], Livingston Island and Port Foster on Deception Island [34], the Weddell Sea continental shelf and slope, and the Antarctic Peninsula [35]. The relatively low richness found in the present study might be related to differences in sampling effort, seeing that in the aforementioned studies, different sampling techniques were used. The dominance of *Aphelochaeta cincinnata* is in accordance with the results obtained by Sicinski [6], Gambi *et al*. [33] and Bromberg [17]. The high density of *Rhodine antarctica*

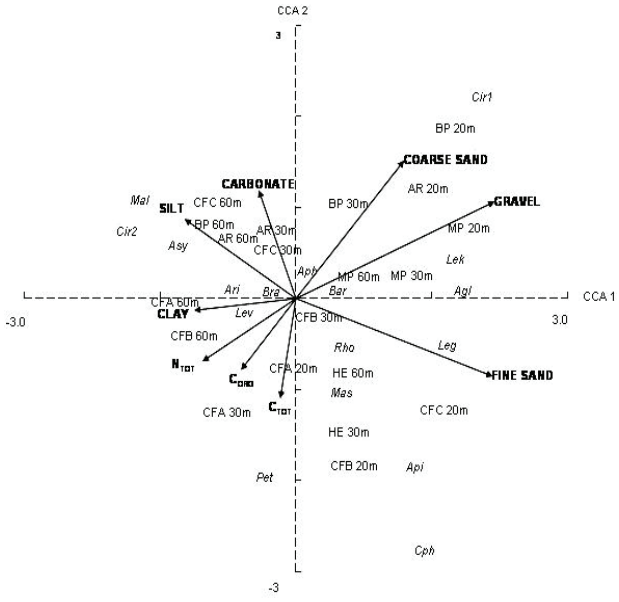

Figure 7. Graphic representation of the two axis of canonical correspondence analysis for early summer. For species codes see **Table 1**.

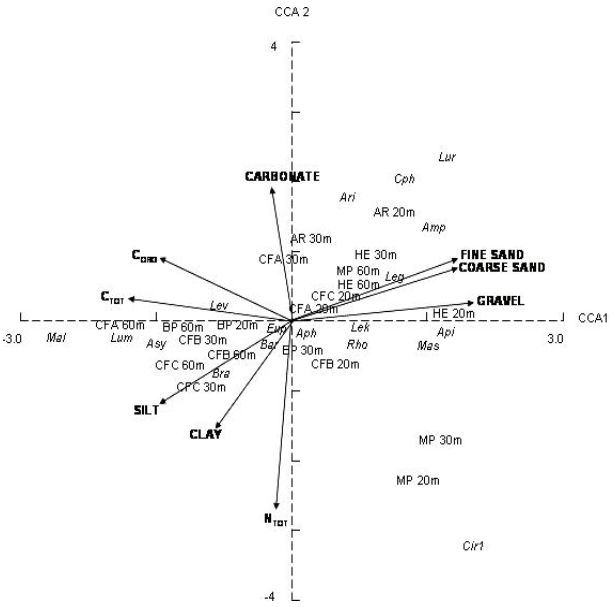

Figure 8. Graphic representation of the two axis of canonical correspondence analysis for late summer. For species codes see **Table 1**.

at the MP transect could be related to its life cycle. According to Dayton & Oliver [12], in McMurdo Sound, the individuals of the family Maldanidae may have evolved asexual reproduction in response to high predation and juvenile mortality. The dominance of maldanids was also reported by Gallardo *et al*. [9], who found a benthic community dominated by *Maldane sarsi antarctica* (Maldane assembly) in Chile Bay. Jazdzewski *et al*. [24] and Sicinski [6,13] also observed typical maldanid communities at depths over 100 meters.

The highest mean density observed in the early summer was similar to that reported by Sicinski [14]. On the other hand, mean density itself, although in accordance to that observed by Sicinski & Janowska [16], was lower than that reported by other authors [17,33-35]. These differences may reflect variations in sampling design, depth and seasonality. The mean values of biomass were similar to those observed in Admiralty Bay by Sicinski & Janowska [16], and were within the range reported by Gambi *et al*. [33]. According to Sicinski [13], polychaete biomass at 50 m may vary from 30 to 40 g.m^{-2} and might be responsible for 15% of the local zoobenthic biomass itself. The species responsible for the increase in biomass values, *Aglaophamus ornatus* and *Eupolymnia* sp. occurred mainly at 20 and 30 meters, respectively. This may be related to the deposition of organic matter from phytoplankton bloom, which occurs in the early summer [36].

Polychaete taxocoenosis structure remained the same throughout the period under study, possibly as a result of the prevailing sedimentary conditions (grain-size percentages) remaining invariable between transects. Nevertheless, certain differences were observed during the early and late summer, separately. During the early summer, polychaete mean density, biomass and richness declined at the 30 meters level and increased at the 60. An increase in density related to depth had been previously reported in the Martel inlet [16]. The results in early summer may be an outcome of ice impact. According to Sahade *et al*. [3], ice impacts (icebergs and anchor-ice) seem to be the major regulating factor of benthic assemblages in shallow waters. Although actually not observed in this study, but based mainly on underwater observations, anchor-ice impacts have been imputed as promoting winter structuring in benthic communities. The displacement of established fauna in their area of influence may be attributed to these phenomena, thereby accounting for the low diversity in early summer [37]. According to Dayton *et al*. [38], the influence of anchor-ice impacts extends down to 33 meters, thus constituting the main cause of low diversity in shallow waters. Anchor-ice usually occurs during the winter, but its influence might have extended throughout the early summer of 2003/04, with consequential superficial sediment defaunation, thus making it difficult for the community to recover within a few months.

The increase in temperature in the late summer promotes the formation of icebergs. Echeverría & Paiva [39] reported the presence of one in the summer of 2001 at the CFB 25 meter station, where it remained for over 20 days. Iceberg impacts are likely to affect benthic communities down to 20 meters. Below this, conditions are more stable, with higher densities, biomass and richness, the area below 30 meters thus presenting a substantial change in benthic megafauna structure, composition and diversity [37]. In both summer periods, most of the species which appear to be related to coarser sediment fractions are motile or discretely motile polychaetes. On the other hand, the maldanids (sessile polychaetes) related to higher percentages of silt and clay, appear mostly at 60 meters. Further analysis of polychaete feeding guilds is necessary to better evaluate their distribution in Admiralty Bay.

The possible environmental impacts related to activities of the Brazilian research station (Cmte. Ferraz) were not revealed in this survey, since variability among those transects under the influence of the station itself (CFA, CFB and CFC) was higher than among all the others. Furthermore, the slight variation between early and late summer seems to be more related to natural impacts than to the more intense activities at the research station itself.

6. ACKNOWLEDGEMENTS

The authors would like to thank the staff of the Brazilian Antarctic Station "Comandante Ferraz" and the Brazilian Antarctic Programm (PROANTAR) for logistical support, Laboratorio de Ciências Ambientais/UENF for the abiotic data, Lucia Campos (GEAMB/UFRJ) for providing biological material, and Rafael Moura for the map. This work was supported by grant from CNPq/MCT/MMA (PROANTAR), and a MSC fellowship from Coordenadoria de Aperfeiçoamento de Pessoal de Nível Superior (CAPES) for first author and research fellowships from Conselho Nacional de Desenvolvimento Científico e Tecnológico (CNPq) for second and third author.

REFERENCES

[1] Arntz, W.E., Brey, T. and Gallardo, V.A. (1994) Antarctic zoobenthos. *Oceanography and Marine Biology - An Annual Review*, **32**, 241-304.

[2] Clarke, A. (1996) The distribution of Antarctic marine benthic communities. In: Ross, R.M., *et al.*, Eds., *Foundations for Ecological Research West of the Antarctic Peninsula*. *Antarctic Research Series*, **70**, 219-230.

[3] Sahade, R., Tatian, M., Kowalke, J., Kuhne, S. and Esnal, G.B. (1998) Benthic faunal associations on soft substrates at Potter Cove, King George Island, Antarctica. *Polar Biology*, **19(2)**, 85-91.

[4] Parulekar, A.H. Ansari, Z.A. and Harkantra, S.N. (1983) Benthic fauna of the Antarctic Ocean: Quantitative aspects. In: Iyenger, R.V. and Rajaram, R., Eds., *Scientific Report of First Indian Expedition to Antarctica*, Department of Ocean Development, New Delhi, 213-218.

[5] Barnes, D.K.A. and Conlan, K.E. (2007) Disturbance, colonization and developmentof Antarctic benthic communities. *Philosophical Transactions of the Royal Society B*, **362(1477)**, 11-38.

[6] Sicinski, J. (1986) Benthic assemblages of polychaeta in chosen regions of Admiralty Bay (King George Island, South Shetlands Island). *Polish Polar Research*, **7(1-2)**, 63-78.

[7] Arnaud, P.M., Jazdzewski, K., Presler, P. and Sicinski, J. (1986) Preliminary survey of benthic invertebrates collected by Polish Antarctic Expeditions in Admiralty Bay, King George Island, South Shetland Islands, Antarctica. *Polish Polar Research*, **7(1-2)**, 7-24.

[8] Clarke, A. and Johnston, N.M. (2003) Antarctic marine benthic diversity. *Oceanography and Marine Biology*: *An Annual Review*, **41**, 47-114.

[9] Gallardo, V.A., Castillo, J.C., Retamal, A.Y., Moyano, H. I. and Hermosilla, J.G. (1977) Quantitative studies on the soft-bottom macrobenthic animal communities of shallow Antarctic Bays. In: Llano, G.A., Ed., *Adaptations within Antarctic Ecosystems*, Gulf Publishing, Houston, 361-387.

[10] Retamal, M.A., Quintana, R. and Neira, E. (1982) Analisis cualiy cuantitativo de las comunidades bentonicas en Bahia Foster (Isla Decepción) (XXXV Expedición Antartica Chilena, enero 1981). *Série Científica Instituto Antártico Chileno*, **29**, 5-15.

[11] Lowry, J.K. (1975) Soft bottom macrobenthic community of Arthur Harbor, Antarctica. *Antarctic Resesarch Series*, **23(1)**, 1-19.

[12] Dayton, P.K. and Oliver, J.S. (1977) Antarctic soft-bottom benthos in oligotrophic and eutrophic environments. *Science*, **197(4298)**, 55-58.

[13] Sicinski, J. (1993) Polychaeta. In: Racuksa-Suszczewski, S., Ed., *The Maritime Antartic Coastal Ecosystem of Admiralty Bay*, Department of Antarctic Biology, Polish Academy of Sciences, Warsaw, 101-107.

[14] Sicinski, J. (2000) Polychaeta (Annelida) of Admiralty Bay: Species richness, diversity, and abundance. *Polish Polar Research*, **21(3-4)**, 153-169.

[15] Wägele, J.W. and Brito, T.A.S. (1990) Die sublitorale fauna der maritimen Antarktis, Erste unterwasserbiobachtungen in der Admiralitasbucht. *Natur und Museum*, **120(7)**, 269-282.

[16] Sicinski, J. and Janowska, E. (1993) Polychaetes of the shallow sublittoral of Admiralty Bay, King-George Island, South Shetland Islands. *Antarctic Science*, **5(2)**, 161-167.

[17] Bromberg, S., Nonato, E.F., Corbisier, T.N. & Petti, M.A. V. (2000) Polychaetes distribution in the nearshore zone of Martel Inlet, Admiralty Bay (King George Island, Antarctica). *Bulletin of Marine Science*, **67(1)**, 175-188.

[18] Echeverría, C.A., Paiva, P.C. and Alves, V.C. (2005) Composition and biomass of shallow benthic megafauna during an annual cycle in Admiralty Bay, King George Island, Antarctica. *Antarctic Science*, **17(3)**, 312-318.

[19] Petti, M.A.V., Nonato, E.F., Skowronski, R.S.P. and Corbisier, T.N. (2006) Bathymetric distribution of the meiofaunal polychaetes in the nearshore zone of Martel intel, King George Island, Antarctica. *Antarctic Science*, **18(2)**, 163-170.

[20] Conlan, K.E., Kim, S.L., Leninhan, H.S. and Oliver, J.S. (2004) Benthic changes during 10 years of organic enrichment by McMurdo Station, Antarctica. *Marine Pollution Bulletin*, **49(1-2)**, 43-60.

[21] Conlan, K.E., Leninham, H.S. Kvitek, R.G. and Oliver, J. S. (1998) Ice scour disturbance to benthic communities in the Canadian high arctic. *Marine Ecology Progress Series*, **166(1)**, 1-16.

[22] Gerdes, D., Hilbig, B. and Montiel, A. (2003) Impact of iceberg scouring on macrobenthic communities in the high-Antarctic Weddell Sea. *Polar Biology*, **26(5)**, 295-301.

[23] Lipski, M. (1987) Variations of physical conditions, nutrients and chlorophyll a content in Admiralty Bay (King George, South Shetland Islands, 1979). *Polish Polar Research*, **8(4)**, 307-332.

[24] Jazdzewski, K., Jurasz, W., Kittel, W., Presler, E., Presler P. and Sicinski, J. (1986) Abundance and biomass estimates of the benthic fauna in Admiralty Bay, King George Island, South Shetland Islands. *Polar Biology*, **6(1)**, 5-16.

[25] Santos, I.R., Silva-Filho, E.V., Schaefer, C.E.G.R., Albuquerque-Filho, M.R. and Campos, L.S. (2005) Heavy metal contamination in coastal sediments and soils near the Brazilian Antarctic Station, King George Island. *Marine Pollution Bulletin*, **50(2)**, 185-194.

[26] Lange, P.K., Tenenbaum, D.R., Braga E.S. and Campos, L.S. (2007) Micro phytoplankton assemblages in shallow waters at Admiralty Bay (King George Island, Antarctica) during the summer 2002-2003. *Polar Biology*, **30(11)**,

1438-1492.
[27] Suguio, K. (1973) Introdução à sedimentologia. Editora da Universidade de São Paulo, São Paulo, 317.
[28] Skoog, D.A. and Leary, J.J. (1992) Principles of instrumental analysis. 4th Edition, Saunders College Publishing, Forth Worth, 801.
[29] Clarke, K.R. and Warwick, R.W. Change in marine communities: An aproach to statistical analysis and interpretation. Plymouth Marine Laboratory, Bourne Press, Bournemouth, 1994.
[30] Lipkovich, I. and Smith, E.P. (2002) Biplot and singular value decomposition macros for Excel. *Journal of Statistical Software*, **7(5)**, 1-15.
[31] Richardson, M.D. and Hedgpeth, J.W. (1977) Antarctic soft-bottom macrobenthic community adaptations to a cold stable, highly, productive, glacially affected environment. In: Llano, G.A., Ed., *Adaptations within Antarctic Ecosystems*, Gulf Publishing, Houston, 181-196.
[32] Gallardo, V., Medrano, S.A. and Carrasco, F.D. (1988) Taxonomic composition of the sublittoral soft-bottom polychaetes of Chile Bay (Greenwich Island, South Shetland Islands, Antarctica). *Serie Científica Instituto Antártico Chileno*, **37(1)**, 49-67.
[33] Gambi, M.C., Castelli A. and Guizzardi, M. (1997) Polychaete populations of the shallow soft bottoms off Terra Nova Bay (Ross Sea, Antarctica): Distribution, diversity and biomass. *Polar Biology*, **17(3)**, 199-210.
[34] San Martin, G., Parapar, J., García F.J. and Redondo, M. S. (2000) Quantitative analysis of soft-bottoms infaunal macrobenthic polychaetes from South Shetland Islands (Antarctica). *Bulletin of Marine Science*, **67(1)**, 83-102.
[35] Hilbig, B., Verdes, D. and Montiel, A. (2006) Distribution patterns and biodiversity in polychaete communities of the Weddell Sea and Antarctic Peninsula area (Southern Ocean). *Journal of Marine Biological Association of the U.K.*, **86(4)**, 711-725.
[36] Mincks, S. and Smith, C.R. (2007) Recruitment patterns in Antarctic Peninsula shelf sediments: Evidence of decoupling from seasonal phytodetritus pulses. *Polar Biology*, **30(5)**, 587-600.
[37] Nonato, E.F., Brito, T.A.S., Paiva, P.C., Petti, M.A.V. and Corbisier, T.N. (2000) Benthic megafauna of the nearshore zone of Martel Inlet (King George Island, South Shetland Islands, Antarctica): Depth zonation and underwater observations. *Polar Biology*, **23(8)**, 580-588
[38] Dayton, P.K., Robilliard, G.A., Paine R.T. and Dayton, L. B. (1974) Biological accommodation in the benthic community at McMurdo Sound, Antarctica. *Ecological Monographs*, **44(1)**, 105-128.
[39] Echeverría, C.A and Paiva, P.C. (2006) Macrofaunal shallow benthic communities along a discontinuous annual cycle at Admiralty Bay, King George Island, Antarctica. *Polar Biology*, **29(3)**, 263-269.

Vol.2, No.10, 1164-1170 (2010)
doi:10.4236/ns.2010.210144

Natural Science

The factorial structure of self-reported androgen-promoted physiological traits

Lee Ellis[1], Shyamal Das[2]

[1]University Malaya, Department of Anthropology, Kuala Lumpur, Malaysia; lee.ellis@hotmail.com;
[2]Elizabeth City State University, North Carolina, USA; sdas@mail.ecsu.edu.

Received 27 June 2010; revised 29 July 2010; accepted 4 August 2010.

ABSTRACT

Androgens make major contributions to average sex differences in anatomy, physiology, and behavior. Despite having established their crucial role in sexual differentiation, much remains to be learned about how androgens coordinate their influences. The present study was undertaken to shed light on androgenic effects on the body using self-reported survey data. We analyzed the ratings provided by over 11,000 college students on the magnitude of eleven traits that previous research has shown to be influenced by testosterone or other androgens. Predictably, the average values for all eleven traits were significantly greater in males than in females. Nevertheless, when data were analyzed separately according to sex of the respondents, some of the traits failed to positively correlate with one another, suggesting that not all androgen-influenced traits differentiate in a simple fashion. Factor analysis of these eleven traits by sex reinforced this view by identifying four factors. In men, the primary factor loaded most heavily on: masculine body build, masculine mannerisms, overall physical strength, upper body strength, and lower body strength. The primary factor for women was limited to: upper body strength, lower body strength, and overall physical strength. In both sexes, the primary factor was interpreted as reflecting the influence of perinatal and postpubertal testosterone exposure. The other three factors may reflect the effects of other androgens (e.g., androstenediol), or the influence of female hormones such as estradiol. Findings were discussed in terms of future use of self-reported physiological measures for assessing androgenic effects on the human body.

Keywords: Androgen-promoted physical traits; Testosterone; Masculinization; Physical strength; Factorial structure; Sex differences

1. INTRODUCTION

A recent literature review provided evidence that the sexes differ in a mired of ways, ranging from easy-to-measure traits (e.g., birth weights and adult body size) to many complex characteristics (e.g., susceptibility to numerous diseases, detailed biochemistry, neurology, perceptual sensitivities, motor coordination, and even many cognitive and behavioral patterns) [1]. This evidence raises questions about how sex differences are produced. Although the details are still far from fully understood, numerous studies have implicated bodily exposure to androgens as primarily responsible for sex differences in traits [2-5].

In broad terms, the sexual differentiation of animals occurs as follows: The default sex at least for mammals, is female, meaning that males are a genetic variant on the female sex [6-9]. Early in the gestation process of nearly all males, the would-be ovaries are made to begin differentiating into testes instead by genes located on the Y-chromosome [10]. As this occurs in humans during the first five months of gestation, the genitals of males gradually take on a masculine rather than a feminine appearance [11-12].

The gestational aspects of sexual differentiation are referred to as its organizational stage, a stage in humans extending from the first month of gestation into about the fourth month following birth [13]. The second phase of sexual differentiation is known as the activational (or postpubertal) stage. It is marked by the appearance of so-called secondary sex characteristics, but also includes enlargement of the penis and testes in males [14-17].

The traits that are masculinized by bodily exposure to androgens are numerous. They include the following:

- Growth of body hair [18-20]
- Darkening of the iris of the eye [21,22]
- Facial acne [23-25]

- Darkening of hair color [26,27]
- Increase in height [28-32]
- Lowering of the voice [33-37]
- Increase in upper body strength [15,38,39]
- Increase in lower body strength [40,42]
- Increase in masculine body appearance [43-44]
- Increase in masculine mannerisms [45,46]

Despite the abundant evidence that androgens masculinize many aspects of human development, the details are still only vaguely understood. The purpose of the present study was to examine the eleven androgen-influenced traits listed above using self-ratings, with the following three questions in mind. First, are all of these traits in fact sexually dimorphic? Second, within each sex, how well do the eleven traits correlate with one another? Third, do the within-sex expressions of these traits cluster together, thereby suggesting that they may be resulting from a limited number of similar androgenic regimens?

2. METHODS

As part of a broad-ranging investigation, a standardized questionnaire was completed by a large sample of college students at twenty United States and two Canadian universities between 1988 and 1998 involving 3,786 males and 7,697 females [47]. Subjects ranged in age from 18 to 56, with a mean of 22 for both sexes. In terms of race and ethnicity, the subjects were 85% white, 4% black, 2% Native American, 2% Asian / Pacific Islander, 1% Hispanic, and 6% providing no answer.

Eight of the androgen-promoted physiological traits were measured by asking subjects to rate themselves regarding each trait using a 1 to 100 scale, with 100 representing maximum expression of each trait. These eight traits were: masculine mannerisms, masculine body appearance, physical strength, low deep voice, upper body strength, lower body strength, body-hair development, and facial acne. Height was measured simply in terms of feet and inches (converted to inches). Eye color and hair color were measured, first, by asking subjects to give a one- or two-word description of their eye color and natural hair color. These descriptions were then interpreted and transcribed into four categories. From highest to lowest values, eye color was coded as being Black, Brown, Hazel / Green, and Blue. For hair color, the four categories were Black, Dark Brown, Light Brown, and Blond. (A copy of the questionnaire is available upon request.)

Analysis was carried out in three stages. First, the sexes were compared regarding their average scores on all eleven traits using a *t*-test. Second, to determine how well the eleven traits correlated with one another, a correlation matrix was created for the sexes separately. Third, factorial analysis was performed on the eleven traits to assess whether or not some of the traits would form into clusters.

3. RESULTS

Table 1 shows that all eleven androgen-promoted traits are significantly more pronounced in men than in women, with $p = 0.000$ in all cases except for eye color (which attained significance only at the 0.05 level). This is entirely predictable, given that the levels of testosterone (and other androgens) are higher for males than for females throughout both the organizational and activational stages of sexual differentiation ([1], pp. 89-93).

Table 2, however, reveals that *within* each sex, some of the androgen-promoted traits are not positively correlated with one another. Such a rather surprising finding can be interpreted as suggesting that the enhancement of androgen-promoted traits does not occur through a unitary process. Most notably, the variables of eye color and especially adolescent facial acne correlate negatively with many of the other androgen-influenced traits among both sexes.

The results for factor analyzing responses regarding the eleven androgen-promoted traits are presented in **Table 3** for each sex separately. Regarding males (**Table 3(a)**), the first factor to emerge was named *masculinity / strength* since it was comprised of masculine mannerisms, masculine body build, and all three of the physical strength measures. We named the second factor *pigment* because it only loaded strongly on hair color and eye color. Body hair development and adolescent facial acne loaded most heavily on the third factor (with some secondarily strong loadings on upper and lower body strength), which was named *dark pigmentation*. Finally, height and low-deep voice comprised a fourth factor, which we named *physical prowess* since both height and low-deep voice are likely to have evolved primarily to intimidate rivals (and possibly impress prospective mates).

Turning to females (**Table 3(b)**), four factors also emerged. The first factor had to do with *strength*. Masculine mannerisms and body build loaded along with low-deep voice onto a second factor; therefore, we called it *female masculinity*. The remaining two female factors were identical to those in males, a *dark pigmentation* factor and a *skin-hair* factor. It is interesting to note that height loaded heavily on the physical prowess factor in males but failed to load on any factor among females.

4. CONCLUSIONS

While there is no doubt that androgens play a pivotal role in differentiating males from females, much remains

Table 1. Descriptive statistics for androgen-promoted physical traits by comparing males with females.

Traits	N	Mean	Std. Dev	Effect Size (d)	Variance Explained	Std. Error Mean	t-Test Results for Equality of Means
Masculine Mannerisms							
Female	7,456	21.84	21.89	2.59	0.62	0.254	132.748***
Male	3,757	74.88	74.88			0.309	
Masculine Body Appearance							
Female	7,447	12.90	19.27	3.32	0.74	0.223	165.808***
Male	3,767	76.82	19.29			0.314	
Physical Strength							
Female	7,697	60.48	18.89	0.52	0.06	0.215	26.473***
Male	3,786	70.00	17.72			0.288	
Height							
Female	6,655	65.15	2.70	2.05	0.51	0.033	95.150***
Male	3,282	70.88	2.88			0.050	
Low Deep Voice							
Female	6,540	21.22	24.84	1.38	0.32	0.307	64.699***
Male	3,217	54.98	23.92			0.422	
Upper Body Strength							
Female	5,016	52.46	22.12	0.41	0.04	0.314	16.698***
Male	2,483	61.57	22.23			0.446	
Lower Body Strength							
Female	5,834	57.91	21.19	0.38	0.03	0.279	16.136***
Male	2,827	65.72	21.01			0.395	
Body-Hair Development							
Female	5,806	46.56	21.64	0.24	0.01	0.285	10.304***
Male	2,828	52.06	23.96			0.451	
Facial Acne							
Female	5,793	29.88	25.73	0.17	0.008	0.338	7.699***
Male	2,816	34.39	25.42			0.479	
Hair Color							
Female	6,399	2.47	1.01	0.21	0.01	0.013	9.762***
Male	3,128	2.68	0.99			0.018	
Eye Color							
Female	3,881	1.84	0.90	0.05	0.003	0.014	2.249*
Male	2,002	1.89	0.92			0.021	

Notes: $p < 0.001$ = ***, $p < 0.01$ = **, and $p < 0.05$ = *; d = Cohen's d

Table 2. Inter-correlation matrix for androgen-promoted traits by sex. The coefficients for males (bolded) appear in the upper right quadrant; those for females (italicized) are in the lower left quadrant (the sample sizes used in calculating each correlation are represented in parentheses).

	Masculine Mannerism	Masculine Body Build	Physical Strength	Height in inches	Low-Deep Voice	Upper Body Strength	Lower Body Strength	Body Hair	Facial Acne	Hair-color	Eye-color
Masculine Manner-isms	1	**0.737** (3,751)	**0.464** (3,756)	**0.053** (3,246)	**0.190** (3,193)	**0.326** (2,458)	**0.285** (2,804)	**0.129** (2,813)	**–0.121** (2,794)	**0.026** (3,100)	**0.062** (1,980)
Masculine Body Build	0.676** (7,423)	1	**0.550** (3,766)	**0.062** (3,255)	**0.206** (3,201)	**0.398** (2,468)	**0.327** (2,812)	**0.149** (2,813)	**–0.098** (2,802)	**0.029** (3,108)	**0.065** (1,987)
Physical Strength	0.194** (7,447)	0.158** (7,436)	1	**0.052** (3,273)	**0.215** (3,216)	**0.563** (2,478)	**0.390** (2,822)	**0.102** (2,823)	**–0.123** (2,812)	**0.007** (3,125)	**0.049** (2,001)
Height in inches	0.087** (6,394)	0.089** (6,384)	0.096** (6,629)	1	**0.131** (2,738)	**0.036** (2,381)	**0.039** (2,375)	**0.005** (2,376)	**–0.014** (2,364)	**–134** (2,707)	**–0.076** (1,949)
Low-Deep Voice	0.314** (6,332)	0.284** (6,321)	0.144** (6,528)	0.087** (5,496)	1	**0.184** (2,470)	**0.152** (2,815)	**0.149** (2,816)	**0.012** (2,806)	**0.014** (3,115)	**0.058** (1,994)
Upper Body Strength	0.172** (4,814)	0.140** (4,806)	0.476** (5,006)	0.063** (4,844)	0.130** (4,961)	1	**0.588** (2,477)	**0.288** (2,475)	**–0.030** (2,463)	**0.007** (2,408)	**0.060*** (1,704)
Lower Body Strength	0.170** (5,632)	0.100** (5,624)	0.401** (5,824)	0.083** (4,837)	0.113** (5,783)	0.648** (5,002)	1	**0.282** (2,823)	**–0.008** (2,811)	**0.014** (2,741)	**0.033** (1,700)
Body Hair	0.073** (5,607)	0.060** (5,597)	0.049** (5,796)	-0.019 (4,808)	0.086** (5,756)	0.266** (4,969)	0.279** (5,791)	1	**0.066** (2,811)	**0.058** (2,742)	**0.035** (1,701)

Facial Acne	0.080** (5,592)	0.046** (5,585)	–0.026* (5,783)	0.016 (4,796)	0.052** (5,743)	0.082** (4,947)	0.089** (5,772)	0.211** (5,745)	1	**–0.015 (2,730)**	**–0.073** (1,693)**
Hair-color	–0.039** (6,153)	–0.021 (6,141)	–0.028* (6,382)	–0.075** (5,489)	0.022 (6,331)	–0.035* (4,858)	–0.040** (5,663)	0.081** (5,636)	–0.028* (5,622)	1	**0.440** (1,998)**
Eye-color	–0.023 (,3739)	0.001 (3,731)	–0.008 (3,871)	–0.085** (3,824)	0.017 (3,847)	–0.014 (3,298)	–0.010 (3,297)	0.052** (3,277)	–0.017 (3,267)	0.442** (3,880)	1

Note: * $p < 0.05$ ** $p < 0.01$

Table 3(a). Factor Loadings for Androgen-Promoted Traits for Males.

Items	Factor 1	Factor 2	Factor 3	Factor 4
Masculine Mannerism	**0.806**	–0.001	–0.125	0.056
Masculine Body Build	**0.845**	0.011	–0.064	0.071
Height	0.002	–0.158	–0.145	**0.835**
Low Deep Voice	0.178	0.157	0.290	**0.633**
Overall Physical Strength	**0.780**	0.059	0.043	0.082
Upper Body Strength	**0.679**	0.046	0.445	0.026
Lower Body Strength	**0.592**	0.023	*0.481*	0.028
Body Hair	0.172	0.081	**0.692**	0.066
Facial Acne	–0.263	–0.154	**0.566**	–0.022
Hair Color	0.004	**0.832**	0.018	–0.064
Eye Color	0.046	**0.829**	–0.042	0.036

Table 3(b). Factor Loadings for Androgen-Promoted Traits for Females.

Items	Factor 1	Factor 2	Factor 3	Factor 4
Masculine Mannerism	0.091	**0.856**	–0.057	0.050
Masculine Body Build	0.025	**0.860**	–0.015	0.000
Height	0.132	0.206	–0.212	–0.254
Low Deep Voice	0.119	**0.589**	0.063	0.017
Overall Physical Strength	**0.746**	0.164	–0.012	–0.216
Upper Body Strength	**0.858**	0.096	–0.024	0.134
Lower Body Strength	**0.825**	0.047	–0.013	0.195
Body Hair	0.299	0.017	0.123	**0.677**
Facial Acne	–0.054	0.101	–0.121	**0.775**
Hair Color	0.004	0.002	**0.835**	0.009
Eye Color	–0.010	0.028	**0.830**	0.003

to be learned about which androgens are involved in particular traits and when they have their greatest influences. The present study sheds light on the process by suggesting that in both sexes, four independent factors emerge when eleven androgen-promoted physiological traits are measured. The structures of these four factors are slightly different for males and for females.

In males, the primary factor loads most heavily on masculinity and strength, whereas in females, the loading is strictly on strength. We hypothesize that in both sexes this primary factor is the result of perinatal and postpubertal exposure to testosterone. This hypothesis is consistent with studies showing that testosterone is by far the most consequential sex hormone regarding both masculine mannerisms [46] and muscular strength [15, 41]. To explain why mannerisms in females would not be masculinized by testosterone, we suspect that the levels of this hormone to which most females are exposed

are insufficient to significantly affect this trait while muscular strength responds to even low amounts of testosterone. Another possibility is that high (female-typical) exposure to estradiol or other female hormones may counteract the effects of testosterone on masculine mannerisms.

The fact that the same factors for the dark pigmentation factor and the skin-hair factor emerged in both sexes suggests that these traits are (a) the result of androgens other than testosterone, and (b) that the androgen(s) primarily responsible for hair growth and facial acne is different from those influencing hair and eye color.

Regarding the three questions posed in the introduction, one can conclude the following: First, all eleven traits that other studies have shown to be androgen-promoted are, as expected, more pronounced in males than in females. Second, within each sex, most of the eleven traits are positively correlated. The fact that there are exceptions leads one to expect that different androgens are operating in somewhat different ways within each sex. Third, factor analysis supports this expectation by demonstrating that there are four clusters of androgen-promoted traits amongst the eleven traits examined in the present study. We named these four factors and hypothesized that testosterone is responsible for the first (and most prominent) factor for both sexes. In males, this primary factor involved both strength and masculine mannerisms, while in females it only involved strength.

Research is needed to verify these four factors and to look for other androgen-promoted traits within each sex. In future studies, direct measurement would almost certainly provide more reliable data than self-reports. However, the time required for obtaining direct measures with a sufficiently large sample of subjects needed for factor analysis could be prohibitive. It can also be said that the extent to which people can provide accurate information about themselves may surpass expectations. In this regard, we compared the average heights of our subjects to estimates recently given by the Center for Disease Control based on direct measurements [48]. The results were very similar: 70.88 inches or 5’ 9.1” tall in our male sample compared to 5’ 9.2” for the national sample, and 65.15 inches or 5’ 4.3” tall in our female sample compared to 5’ 3.8” for the national sample.

If the four factor structure of androgen-promoted traits revealed in the present study can be replicated, the next phase in this line of research would be to identify each of their specific causes. In other words, what are the actual androgens involved in producing each factor and what is the developmental timing involved?

REFERENCES

[1] Ellis, L., Hershberger, S., Field, E., Wersinger, S., Pellis, S., Geary, D., Palmer, C., Hoyenga, K., Hetsroni, A. and Karadi, K. (2008). Sex differences: Summarizing more than a century of scientific research. Psychology Press, New York.

[2] Alexander, G.M., Welcox, T. and Farmer, M.E. (2009). Hormone-behavior associations in early infancy. *Hormones and Behavior*, **56**, 498-502.

[3] Cooke, B., Hegstrom, C.D., Villeneuve, L.S. and Breedlove, S.M. (1998). Sexual differentiation of the vertebrate brain: Principles and mechanisms. *Frontiers in Neuroendocrinology*, **19**, 323-362.

[4] Lutchmaya, S., Baron-Cohen, S., Raggatt, P., Knickmeyer, R. and Manning, J. (2004). 2nd to 4th digit ratios, fetal testosterone and estradiol. *Early Human Development*, **77**, 23-28.

[5] Zucker, K.J., Beaulieu, N., Bradley, S.J., Grimshaw, G.M. and Wilcox, A. (2001). Handedness in boys with gender identity disorder. *Journal of Child Psychology and Psychiatry*, **42**, 767-776.

[6] Dennis, C. (2004). Brain development: The most important sexual organ. *Nature*, **427**, 390-392.

[7] Goodfellow, P.N. and Lovell-Badge, R. (1993). SRY and sex determination in mammals. *Annual Review of Genetics*, **27**, 71-92.

[8] Jost, A., Price, D. and Edwards, R.G. (1970). Hormonal factors in the sexual differentiation of the mammalian foetus. *Transactions of the Royal Society of London*, **259**, 119-130.

[9] Woodson, J.C. and Gorski, R.A. (2000). Structural sex differences in the mammalian brain: Reconsidering the male / female dichotomy. In: Malsumoto, A. Ed., *Sexual differentiation of the brain*, CRC Press, Boca Raton, pp. 229-239.

[10] Vergnaud, G., Page, D.C., Simmler, M.C., Brown, L., Rouyer, F., Noel, B., *et al.* (1986) A deletion map of the human Y chromosome based on DNA hybridization. *American Journal of Human Genetics*, **38**, 109-124.

[11] Jost, A. (1983). Genetic and hormonal factors in sex differentiation of the brain. *Psychoneuroendocrinology*, **8**, 183-193.

[12] Carruth, L.L., Reisert, I. and Arnold, A.P. (2002). Sex chromosome genes directly affect brain sexual differentiation. *Nature Neuroscience*, **5**, 933-934.

[13] Ellis, L. (1996). The role of perinatal factors in determining sexual orientation. In: Savin-Williams, R. C. and Cohen, K. M. Eds., *The Lives of Lesbians, Gays, and Bisexuals*: *Children to Adults*, Harcourt Brace, New York, pp. 35-70.

[14] Cohen-Bendahan, C.C., van de Beek, C. and Berenbaum, S.A. (2005). Prenatal sex hormone effects on child and adult sex-typed behavior: Methods and findings. *Neuroscience and Biobehavior Review*, **29**, 353-384.

[15] Fink, B., Thanzami, V., Seydel, H. and Manning, J.T. (2006). Digit ratio and hand-grip strength in German and Mizos men: Cross-cultural evidence for an organizing effect of prenatal testosterone on strength. *American Journal of Human Biology*, **18**, 776-782.

[16] Seale, J.V., Wood, S.A., Atkinson, H.C., Lightman, S.L. and Harbuz, M.S. (2001). Organizational role for testosterone and estrogen on adult hypothalamic-pituitary- adrenal axis activity in the male rat. *Endocrinology*, **146**, 1973-1982.

[17] Sisk, C.L. and Zehr, J.L. (2005). Pubertal hormones organize the adolescent brain and behavior, *Frontiers in Neuroendocrinology*, **26**, 163-174.
[18] Marshall, W.A. and Tanner, J.M. (1970). Variations in the pattern of pubertal changes in boys. *Archives of Disease in Childhood*, **45**, 13-23.
[19] Lookingbill, D.P., Demers, L.M., Wang, C., Leung, A., Rittmaster, R.S. and Santen, R.J. (1991). Clinical and biochemical parameters of androgen action in normal healthy caucasian versus chinese subjects. *Journal of Clinical Endocrinology and Metabolism*, **72**, 1242-1248.
[20] Giltay, E.J. and Gooren, L.J. (2000). Effects of sex steroid deprivation / administration on hair growth and skin sebum production in transsexual males and females. *Journal of Clinical Endocrinology & Metabolism*, **85**, 2913-2921.
[21] Morejohn, G.V. and Genelly, R.E. (1961). Plumage differentiation of normal and sex-anomalous ring-necked pheasants in response to synthetic hormone implants. *The Condor*, **63**, 101-110.
[22] Coplan, R.J., Coleman, B. and Rubin, K.H. (1998). Shyness and little boy blue: Iris pigmentation, gender, and social wariness in preschoolers. *Developmental Psychobiology*, **32**, 37-44.
[23] Farthing, M., Mattei, A.M., Edwards, C.R.W. and Dawson, A.M. (1982). Relationship between plasma testosterone and dihydrotestosterone concentrations and male facial hair growth. *British Journal of Dermatology*, **107**, 559-564.
[24] de Waal, W.J., Torn, M., de Muinck Keizer-Schrama, S. M. P. F., Aarsen, R.S.R. and Drop, S.L.S. (1995). Long term sequelae of sex steroid treatment in the management of constitutionally tall stature. *Archives of Disease in Childhood*, **73**, 311-315.
[25] Thiboutot, D. (2003). Acne: Hormonal concepts and therapy. *Clinics in Dermatology*, **22**, 419-428.
[26] Bubenik, G.A. and Bubenik, A.B. (1985). Seasonal variations in hair pigmentation of white-tailed deer and their relationship to sexual activity and plasma testosterone. *Journal of Experimental Zoology*, **235**, 387-395.
[27] Toro, J., Turner, M. and Gahl, W.A. (1999). Dermatologic manifestations of hermansky-pudlak syndrome in patients with and without a 16- base pair duplication in the hps1 gene. *Archives of Dermatology*, **135**, 774-780.
[28] Cassorla, F.G., Skerda, M.C., Valk, I.M., Hung, W., Cutler, G.B. and Loriaux, D.L. (1984). The effects of sex steriods on ulnar growth during adolescence. *Journal of Clinical Endocrinology and Metabolism*, **58**, 717-720.
[29] Bourguignon, J.P., Vandeweghe, M., Vanderschueren-Lodeweyckx, M., Malvaux, P., Wolter, R., Du Caju, M., *et al.* (1986). Pubertal growth and final height in hypo-pituitary boys: A minor role of bone age at onset of puberty. *Journal of Clinical Endocrinology and Metabolism*, **63**, 376-382.
[30] Zemel, B.S. and Katz, S.H. (1986). The contribution of adrenal and gonadal androgens to the growth in height of adolescent males. *American Journal of Physical Anthropology*, **71**, 459-466.
[31] Martin, M.M., Martin, A.L. and Mossman, K.L. (1986). Testosterone treatment of constitutional delay in growth and development: Effect of dose on predicted versus definitive height. *Acta Endocrinology Supplement*, **279**, 147-152.
[32] Jassal, S.K., Barrett-Connor, E. and Edelstein, S.L. (1995). Low bioavailable testosterone levels predict future height loss in postmenopausal women. *Journal of Bone and Mineral Research*, **10**, 650-654.
[33] Butler, G., Walker, R.F., Walker, R.V., Teague, P., Riad-Fahmy and Ratcliffe, S. (1989). Salivary testosterone levels and the progress of puberty in the normal boy. *Clinical Endocrinology*, **30**, 487-596.
[34] Harries, M., Hawkins, S., Hacking, J. and Hughes, I.A. (1998). Changes in the male voice at puberty: Vocal fold length and its relationship to the fundamental frequency of the voice. *Journal of Laryngology and Otology*, **112**, 451-454.
[35] Dabbs, J. M. and Mallinger, A. (1999). High testosterone levels predict low voice pitch among men. *Personality and Individual Differences*, **27**, 801-804.
[36] Nieschlag, E. and Zitzmann, M. (2001). Testosterone levels in healthy men and the relation to behavioural and physical characteristics: Facts and constructs. *European Journal of Endocrinology*, **144**, 183-197.
[37] Bruckert, L., Lienard, J.-S., Lacroix, A., Kreutzer, M. and Leboucher, G. (2006). Women use voice parameters to assess men's characteristics. *Proceedings of the Royal Society B*, **273**, 83-89.
[38] Hamilton, J.B. (1948). The role of testicular secretions as indicated by the effects of castration in man and by studies of pathological conditions and the short lifespan associated with maleness. *Recent Progress of Hormonal Research*, **3**, 257-322.
[39] Wang, C., Eyre, D.R., Clark, R., Kleinberg, D., Newman, C., Iranmanesh, A., *et al.* (1996). Sublingual testosterone replacement improves muscle mass and strength, decreases bone resorption, and increases bone formation markers in hypogonadal men—a clinical research center study. *Journal of Clinical Endocrinology and Metabolism*, **81**, 3654-3662.
[40] Joubert, Y., Tobin, C. and Lebart, C. (1994). Testosterone-induced masculinization of the rat levator ani muscle during puberty. *Developmental Biology*, **162**, 104-110.
[41] Perry, H.M., Miller, D.K., Patrick, P., & Morley, J.E. (2000). Testosterone and leptin in older African-American men: Relationship to age, strength, function, and season. *Metabolism*, **49**, 1085-1091.
[42] Iannuzzi-Sucich, M., Prestwood, K.M. and Kenny, A.M. (2002). Prevalence of sarcopenia and predictors of skeletal muscle mass in healthy, older men and women. *Journals of Gerontology Series A*: *Biological Sciences and Medical Sciences*, **57**, M772-M777.
[43] Bosinski, H.A.G., Schroder, I., Peter, M., Arndt, R., Wille, R. and Sippell, W.G. (1997). Anthropometrical measurements and androgen levels in males, females, and hormonally untreated female-to-male transsexuals. *Archives of Sexual Behavior*, **26**, 143-157.
[44] Wang, C., Swerdloff, R.S. and Iranmanesh, A. (2000). Transdermal testosterone gel improves sexual function, mood, muscle strength, and body composition parameters in hypogonadal men. *Journal of Clinical Endocrinology and Metabolism*, **85**, 2839-2853.
[45] Whalen, R.E. and Edwards, D.A. (1967). Hormonal determinants of the development of masculine and feminine behavior in male and female rats. *Anatomical Record*,

157, 173-180.

[46] Goy, R.W., Bercovitch, F.B. and McBrair, M.C. (1988). Behavioral masculinization is independent of genital masculinization in prenatally androgenized female rhesus macaques. *Hormones and Behavior*, **22**, 552-571.

[47] Ellis, L. and Cole-Harding, S. (2001). The effects of prenatal stress, and of prenatal alcohol and nicotine exposure, on human sexual orientation. *Physiology and Behavior*, **74**, 213-226.

[48] Ogden, C.L., Fryar, C.D., Carroll, M.D. and Flegal, K.M. (2004). Mean body weight, Height, and body mass index, United States 1960-2002. *Advance Data from Vital and Health Statistics*, (**347)**, 1-18.

Vol.2, No.10, 1171-1179 (2010)
doi:10.4236/ns.2010.210145

Natural Science

Transient response of multilayered hollow cylinder using various theories of generalized thermoelasticity

Daoud S. Mashat[1], Aahraf M. Zenkour[1,2]*, Khaled A. Elsibai[3]

[1]Department of Mathematics, Faculty of Science, King AbdulAziz University, Jeddah, Saudi Arabia; *Corresponding author: zenkour@kau.edu.sa;
[2]Department of Mathematics, Faculty of Science, Kafrelsheikh University, Kafr El-Sheikh, Egypt;
[3]Department of Mathematics, Faculty of Applied Science, Umm Al-Qura University, Holy Makkah, Saudi Arabia.

Received 7 March 2010; revised 12 April 2010; accepted 16 April 2010.

ABSTRACT

The present paper deals with thermoelastic problems of finitely long hollow cylinder composed of two different materials with axial symmetry. The medium is traction-free, with negligible body forces and with internal and external heat generations. The governing equations for different theories of the generalized thermoelasticity are written in terms of displacement and temperature increment. The exact solution of the problem; using different theories of generalized thermoelasticity; has been deduced. The analytical expressions for displacements, temperature and stresses are found in final forms, and a numerical example has been taken to discuss the effect of the relaxation times. Finally, the results have been illustrated graphically to find the responses of different theories.

Keywords: Multilayered Hollow Cylinder; Generalized Theories of Thermoelasticity; Relaxation Times

1. INTRODUCTION

The governing equations for displacement and temperature fields in the linear dynamical theory of classical thermoelasticity consist of the coupled partial differential equation of motion and Fourier's law of heat conduction equation. The equation for displacement field is controlled by a wave type hyperbolic equation, whereas that for the temperature field is a parabolic diffusion type equation. This amounts to the remark that the classical thermoelasticity predicts a finite speed for predominantly elastic disturbances but an infinite speed for predominantly thermal disturbances, which are coupled together. This means that a part of every solution of the equations extends to infinity.

Biot [1] formulated the theory of coupled thermoelasticity (named as C-D theory) to eliminate the paradox inherent in the classical uncoupled theory of thermoelasticity that the elastic changes have no effect on the temperature. But, the classical dynamical coupled theory of thermoelasticity still based on a parabolic heat equation, which predicts an infinite speed for the propagation of heat wave, contradicts the physical facts. Generalized theories of thermoelasticity have been developed that are free from this paradox. Lord and Shulman [2] (L-S theory) introduced the theory of generalized thermoelasticity based on a new law of heat conduction by incorporating a flux rate term and involved a hyperbolic type of heat transport equation (called the generalized thermoelasticity with one relaxation time). The L-S theory was extended by Dhaliwal and Sherief [3] to the case of anisotropic media. Uniqueness of the solution for the generalized thermoelasticity with one relaxation time under a variety of conditions was proved by Ignaczak [4] and Sherief and Dhaliwal [5]; respectively. Generalized theory of thermoelasticity with two relaxation time parameters has also been proposed. Based on a generalized inequality of thermodynamics, Green and Lindsay [6] developed the theory of thermoelasticity with two relaxation time parameters (named as G-L theory). The G-L theory doesn't violate the Fourier's law of heat conduction when the body under consideration has a center of symmetry. In this theory, both the equations of motion and heat conduction are hyperbolic but the equation of motion is modified and differs from that of the classical dynamical coupled theory of thermoelasticity.

The axisymetric multilayered hollow cylinder problems have been discussed by some researchers in the uncoupled, coupled and generalized thermoelasticity in the recent years. Jane and Lee [7] considered the thermoelasticity of multilayered cylinders subjected to known temperatures at traction-free boundaries by using Laplace transform and the finite difference method. Kandil

[8] studied the effect of steady-state temperature and pressure gradient on compound cylinders fitted together by shrink fit. Sherief and Anwar [9] discussed the problem of an infinitely long elastic circular cylinder; whose inner and outer surfaces are subject to known temperature and traction free. Yang and Chen [10] discussed the transient response of one-dimensional quasi- static coupled thermoelasticity problems of an infinitely long annular cylinder composed of two different materials. Lee [11] solved the two-dimensional, quasi-static coupled, thermoelastic problem of finitely long hollow cylinder composed of two different materials with axial symmetry. Chen *et al*. [12,13] discussed also the transient response of one-dimensional quasi static coupled and uncoupled thermoelasticity problems of multilayered hollow cylinder. Allam *et al.* [14] solved the problem of an infinite body with a circular cylindrical hole in a harmonic field in the context of the generalized theory of thermoelasticity. In a recent article, Zenkour *et al.* [15] presented the static bending response for a simply supported functionally graded rectangular plate subjected to a through-the-thickness temperature field under the effect of various theories of generalized thermoelasticity with relaxation times.

In the present article, the analytical expressions for displacements, temperature and stresses of finitely long hollow cylinder composed of two different materials with axial symmetry are found in final forms. Numerical examples have been taken to discuss the effect of the relaxation times. Finally, the results have been illustrated graphically to find the differences between the different generalized theories of thermoelasticity.

2. FORMULATION OF THE PROBLEM

Through this area of research, we consider the following boundary value problem. We deal with a problem of finitely long hollow cylinder composed of three layered of two different materials with axial symmetry. The length of the multilayered hollow cylinder is L, and; the inner and outer radii of the cylinder are denoted by r_i and r_o, respectively (see **Figure 1**).

We assume that, the hollow cylinder is taken to be heated suddenly at the inner and outer surface under temperature ϕ_i and ϕ_o, respectively. We take into account that the body forces are absent, and then the fundamental equations of the boundary value problem in the context of the different theories of generalized thermoelasticity; in the case of quasi-static; can be written as:

1) Equilibrium equations for the cylinder along r and z directions:

$$\sigma_r + r\frac{\partial \sigma_r}{\partial r} + r\frac{\partial \sigma_{rz}}{\partial z} - \sigma_\theta = 0, \tag{1}$$

$$\sigma_{rz} + r\frac{\partial \sigma_z}{\partial z} + r\frac{\partial \sigma_{rz}}{\partial r} = 0. \tag{2}$$

where σ_{ij} are the components of stress tensor and (r,θ,z) are the cylindrical coordinate system.

2) General heat conduction equation in the context of generalized thermo-elasticity theories:

$$\kappa_r\frac{\partial^2\overline{\Theta}}{\partial r^2} + \frac{\kappa_\theta}{r}\frac{\partial\overline{\Theta}}{\partial r} + \kappa_z\frac{\partial^2\overline{\Theta}}{\partial z^2} = \rho c_v\frac{\partial}{\partial t}\left(1+t_2\frac{\partial}{\partial t}\right)\overline{\Theta} + \Theta_o\left[\beta_r\frac{\partial}{\partial t}\left(1+t_3\frac{\partial}{\partial t}\right)\varepsilon_r + \beta_\theta\frac{\partial}{\partial t}\left(1+t_3\frac{\partial}{\partial t}\right)\varepsilon_\theta + \beta_z\frac{\partial}{\partial t}\left(1+t_3\frac{\partial}{\partial t}\right)\varepsilon_z\right], \tag{3}$$

in which $\overline{\Theta} = \Theta - \Theta_0$ is the temperature and Θ_0 is the reference temperature; ε_i are the components of strain tensor; t_2 and t_3 are the second and third thermal relaxation times; κ_r, κ_θ and κ_z are the thermal conductivity; ρ is the density; and c_v is the specific heat at constant deformation. The components of the thermoelastic tensor are given by

$$\beta_r = \frac{1}{\Delta}\left[E_r(1-\nu_{\theta z}\nu_{z\theta})\alpha_r + E_\theta(\nu_{r\theta}+\nu_{\theta z}\nu_{rz})\alpha_\theta + E_z(\nu_{rz}+\nu_{r\theta}\nu_{z\theta})\alpha_z\right],$$

$$\beta_\theta = \frac{1}{\Delta}\left[E_\theta(\nu_{r\theta}+\nu_{\theta z}\nu_{rz})\alpha_r + E_\theta(1-\nu_{rz}\nu_{zr})\alpha_\theta + E_z(\nu_{\theta z}+\nu_{r\theta}\nu_{rz})\alpha_z\right],$$

$$\beta_z = \frac{1}{\Delta}\left[E_z(\nu_{rz}+\nu_{r\theta}\nu_{\theta z})\alpha_r + E_z(\nu_{\theta z}+\nu_{r\theta}\nu_{rz})\alpha_\theta + E_z(1-\nu_{r\theta}\nu_{\theta r})\alpha_z\right],\ \Delta = 1-\nu_{r\theta}\nu_{\theta r}-\nu_{z\theta}\nu_{\theta z}-\nu_{zr}\nu_{rz}-2\nu_{\theta r}\nu_{z\theta}\nu_{rz}. \tag{4}$$

where $\nu_{rz}, \nu_{r\theta}$ and $\nu_{\theta z}$ are Poisson's ratios; E_r, E_θ and E_z are Young's moduli; and α_r, α_θ and α_z are linear thermal expansion coefficients.

3) Duhamel-Neumann's relations for layer number k:

$$\sigma_r = c_{11}\frac{\partial U_r}{\partial r} + c_{12}\frac{U_r}{r} + c_{13}\frac{\partial U_z}{\partial z} - \beta_r\left(1+t_1\frac{\partial}{\partial t}\right)\overline{\Theta}, \tag{5}$$

$$\sigma_\theta = c_{12}\frac{\partial U_r}{\partial r} + c_{22}\frac{U_r}{r} + c_{23}\frac{\partial U_z}{\partial z} - \beta_\theta\left(1+t_1\frac{\partial}{\partial t}\right)\overline{\Theta}, \tag{6}$$

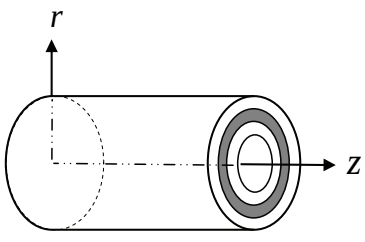

Figure 1. The three-layer hollow cylinder and its coordinate system.

$$\sigma_z = c_{13}\frac{\partial U_r}{\partial r} + c_{23}\frac{U_r}{r} + c_{33}\frac{\partial U_z}{\partial z} - \beta_z\left(1+t_1\frac{\partial}{\partial t}\right)\overline{\Theta}, \quad (7)$$

$$\sigma_{rz} = c_{55}\left(\frac{\partial U_z}{\partial r} + \frac{\partial U_r}{\partial z}\right), \quad (8)$$

where t_1 is the first thermal relaxation time and U_i are the components of displacement vector. The elastic constants c_{ij} are given by

$$c_{11} = \frac{E_r(1-\nu_{\theta z}\nu_{z\theta})}{\Delta}, \quad c_{22} = \frac{E_\theta(1-\nu_{rz}\nu_{zr})}{\Delta},$$

$$c_{33} = \frac{E_z(1-\nu_{r\theta}\nu_{\theta r})}{\Delta},$$

$$c_{12} = \frac{E_\theta(\nu_{r\theta}+\nu_{z\theta}\nu_{rz})}{\Delta} = \frac{E_r(\nu_{\theta r}+\nu_{\theta z}\nu_{zr})}{\Delta} = c_{21}, \; c_{55} = G_{rz},$$

$$c_{13} = \frac{E_r(\nu_{zr}+\nu_{z\theta}\nu_{\theta r})}{\Delta} = \frac{E_z(\nu_{rz}+\nu_{r\theta}\nu_{\theta z})}{\Delta} = c_{31},$$

$$c_{23} = \frac{E_z(\nu_{z\theta}+\nu_{\theta r}\nu_{zr})}{\Delta} = \frac{E_\theta(\nu_{\theta z}+\nu_{rz}\nu_{r\theta})}{\Delta} = c_{32}. \quad (9)$$

The full system equations for the different theories of generalized thermoelasticity will appear by the following instructions:

1) $t_1 = t_2 = t_3 = 0$, C-D theory,
2) $t_1 = 0$, $t_2 = t_3 \neq 0$, L-S theory,
3) $t_1 \neq 0$, $t_2 \neq 0$, $t_3 = 0$, G-L theory.

3. SOLUTION OF THE PROBLEM

Substituting **Eqs.5-8** into **Eqs.1-3**, we get the following system of partial differential equations:

$$c_{11}\frac{\partial^2 U_r}{\partial r^2} + c_{11}\frac{1}{r}\frac{\partial U_r}{\partial r} - c_{22}\frac{U_r}{r^2} + c_{55}\frac{\partial^2 U_r}{\partial z^2} + (c_{13}+c_{55})\frac{\partial^2 U_z}{\partial r\partial z} + (c_{13}-c_{23})\frac{1}{r}\frac{\partial U_z}{\partial z} - \beta_r\frac{\partial}{\partial r}\left(1+t_1\frac{\partial}{\partial t}\right)\overline{\Theta} - (\beta_r-\beta_\theta)\frac{1}{r}\left(1+t_1\frac{\partial}{\partial t}\right)\overline{\Theta} = 0, \quad (10)$$

$$c_{55}\frac{\partial^2 U_z}{\partial r^2} + (c_{13}+c_{55})\frac{\partial^2 U_r}{\partial r\partial z} + c_{55}\frac{1}{r}\frac{\partial U_z}{\partial r} + c_{33}\frac{\partial^2 U_z}{\partial z^2} + (c_{23}+c_{55})\frac{1}{r}\frac{\partial U_r}{\partial z} - \beta_z\frac{\partial}{\partial z}\left(1+t_1\frac{\partial}{\partial t}\right)\overline{\Theta} = 0, \quad (11)$$

$$\left[\kappa_r\frac{\partial^2}{\partial r^2} + \frac{\kappa_\theta}{r}\frac{\partial}{\partial r} + \kappa_z\frac{\partial^2}{\partial z^2}\right]\overline{\Theta} = \rho c_\nu\frac{\partial}{\partial t}\left(1+t_2\frac{\partial}{\partial t}\right)\overline{\Theta} + \Theta_o\left[\beta_r\frac{\partial^2}{\partial r\partial t}\left(1+t_3\frac{\partial}{\partial t}\right)U_r + \beta_\theta\frac{1}{r}\frac{\partial}{\partial t}\left(1+t_3\frac{\partial}{\partial t}\right)U_r + \beta_z\frac{\partial^2}{\partial z\partial t}\left(1+t_3\frac{\partial}{\partial t}\right)U_z\right]. \quad (12)$$

Eqs.10 and **11** represent the equations of equilibrium for the hollow cylinder along the *r* and *z* directions, respectively, while **Eq.12** represents the coupled transient heat conduction equation for the *k*th layer of the axisymmetric hollow cylinder. The boundary and interface conditions of the present composite hollow cylinder are given by:

3.1. Boundary Conditions

$$\begin{aligned} &U_r = U_z = 0, \quad \overline{\Theta} = \eta_1 \quad \text{at} \quad r = r_i, \\ &U_r = U_z = 0, \quad \frac{\partial\overline{\Theta}}{\partial r} = 0 \quad \text{at} \quad r = r_o, \\ &\sigma_{rz} = U_z = 0, \quad \overline{\Theta} = \eta_2 \quad \text{at} \quad z = 0, \\ &\sigma_{rz} = U_z = 0, \quad \overline{\Theta} = \eta_3 \quad \text{at} \quad z = L. \end{aligned} \quad (13)$$

3.2. Interface Conditions

$$(U_r, U_z, \overline{\Theta}, \sigma_r, \sigma_\theta, \sigma_z, \sigma_{rz})_k = (U_r, U_z, \overline{\Theta}, \sigma_r, \sigma_\theta, \sigma_z, \sigma_{rz})_{k+1}. \quad (14)$$

3.3. Initial Conditions

$$\overline{\Theta} = \tfrac{1}{2}\Theta_0 \quad \text{at } t = 0. \quad (15)$$

To solve the above equations, we introduce the following dimensionless quantities:

$$R = \frac{r}{r_o}, \quad Z = \frac{z}{L}, \quad \tau = \frac{t}{r_o^2}\left(\frac{\kappa_r}{\rho c_\nu}\right)_1, \quad t_i^* = \frac{t_i}{r_o^2}\left(\frac{\kappa_r}{\rho c_\nu}\right)_1,$$

$$i = 1,2,3, \quad U_r^* = \frac{U_r}{r_o}\left(\frac{\beta_r}{\rho c_\nu}\right)_1, \quad U_z^* = \frac{U_z}{r_o}\left(\frac{\beta_r}{\rho c_\nu}\right)_1,$$

$$\sigma_{ij}^* = \frac{\sigma_{ij}}{(\beta_r)_1}, \quad R_i = \frac{r_i}{r_o}, \quad T^* = \frac{\overline{\Theta}}{\Theta_0}, \quad \beta_r^* = \frac{\beta_r}{(\beta_r)_1},$$

$$\beta_\theta^* = \frac{\beta_\theta}{(\beta_r)_1}, \quad \beta_z^* = \frac{\beta_z}{(\beta_r)_1}, \quad c_{ij}^* = \frac{c_{ij}}{(c_{11})_1},$$

$$\kappa_r^* = \frac{\kappa_r}{(\kappa_r)_1}, \quad \kappa_\theta^* = \frac{\kappa_\theta}{(\kappa_r)_1}, \quad \kappa_z^* = \frac{\kappa_z}{(\kappa_r)_1}, \quad \rho c_\nu^* = \frac{\rho c_\nu}{(\rho c_\nu)_1},$$

$$B_r = \beta_r\left(\frac{\beta_r}{\rho c_\nu c_{11}}\right)_1\Theta_0, \quad B_\theta = \beta_\theta\left(\frac{\beta_r}{\rho c_\nu c_{11}}\right)_1\Theta_0, \quad .$$

$$B_z = \beta_z \left(\frac{\beta_r}{\rho c_v c_{11}} \right)_1 \Theta_0$$

Note that, the index "1" represents the thermomechanical properties of layer 1. Substituting the above dimensionless quantities into **Eqs.10-12**, we get

$$c_{11}^* \frac{\partial^2 U_r^*}{\partial R^2} + c_{11}^* \frac{1}{R} \frac{\partial U_r^*}{\partial R} - c_{22}^* \frac{U_r^*}{R^2} + c_{55}^* \left(\frac{r_o}{L} \right)^2 \frac{\partial^2 U_r^*}{\partial Z^2} + (c_{13}^* + c_{55}^*) \frac{r_o}{L} \frac{\partial^2 U_z^*}{\partial R \partial Z} + (c_{13}^* - c_{23}^*) \frac{r_o}{L} \frac{1}{R} \frac{\partial U_z^*}{\partial Z} - B_r \frac{\partial}{\partial R} \left(1 + t_1^* \frac{\partial}{\partial \tau} \right) T^* - (B_r - B_\theta) \frac{1}{R} \left(1 + t_1^* \frac{\partial}{\partial \tau} \right) T^* = 0, \tag{16}$$

$$c_{55}^* \frac{\partial^2 U_z^*}{\partial R^2} + (c_{13}^* + c_{55}^*) \frac{r_o}{L} \frac{\partial^2 U_r^*}{\partial R \partial Z} + c_{55}^* \frac{1}{R} \frac{\partial U_z^*}{\partial R} + c_{33}^* \left(\frac{r_o}{L} \right)^2 \frac{\partial^2 U_z^*}{\partial Z^2} + (c_{23}^* + c_{55}^*) \frac{r_o}{L} \frac{1}{R} \frac{\partial U_r^*}{\partial Z} - B_z \frac{r_o}{L} \frac{\partial}{\partial Z} \left(1 + t_1^* \frac{\partial}{\partial \tau} \right) T^* = 0, \tag{17}$$

$$\left[\kappa_r^* \frac{\partial^2}{\partial R^2} + \frac{\kappa_\theta^*}{R} \frac{\partial}{\partial R} + \kappa_z^* \left(\frac{r_o}{L} \right)^2 \frac{\partial^2}{\partial Z^2} \right] T^* = \rho c_v^* \frac{\partial}{\partial \tau} \left(1 + t_2^* \frac{\partial}{\partial \tau} \right) T^* + \beta_r^* \frac{\partial^2}{\partial R \partial \tau} \left(1 + t_3^* \frac{\partial}{\partial \tau} \right) U_r^* + \beta_\theta^* \frac{1}{R} \frac{\partial}{\partial \tau} \left(1 + t_3^* \frac{\partial}{\partial \tau} \right) U_r^* + \beta_z^* \frac{r_o}{L} \frac{\partial^2}{\partial Z \partial \tau} \left(1 + t_3^* \frac{\partial}{\partial \tau} \right) U_z^*. \tag{18}$$

The dimensionless stresses are also given by

$$\sigma_r^* = \bar{c}_{11} \frac{\partial U_r^*}{\partial R} + \bar{c}_{12} \frac{U_r^*}{R} + \bar{c}_{13} \frac{r_o}{L} \frac{\partial U_z^*}{\partial Z} - \beta_r^* \left(1 + t_1^* \frac{\partial}{\partial \tau} \right) T^*, \tag{19}$$

$$\sigma_\theta^* = \bar{c}_{12} \frac{\partial U_r^*}{\partial R} + \bar{c}_{22} \frac{U_r^*}{R} + \bar{c}_{23} \frac{r_o}{L} \frac{\partial U_z^*}{\partial Z} - \beta_\theta^* \left(1 + t_1^* \frac{\partial}{\partial \tau} \right) T^*, \tag{20}$$

$$\sigma_z^* = \bar{c}_{13} \frac{\partial U_r^*}{\partial R} + \bar{c}_{23} \frac{U_r^*}{R} + \bar{c}_{33} \frac{r_o}{L} \frac{\partial U_z^*}{\partial Z} - \beta_z^* \left(1 + t_1^* \frac{\partial}{\partial \tau} \right) T^*, \tag{21}$$

$$\sigma_{rz}^* = \bar{c}_{55} \left(\frac{\partial U_z^*}{\partial R} + \frac{r_o}{L} \frac{\partial U_r^*}{\partial Z} \right), \tag{22}$$

where

$$\bar{c}_{ij} = \frac{c_{ij}}{\Theta_0} \left(\frac{\rho c_v}{\beta_r^2} \right)_1. \tag{23}$$

The solution of **Eqs.16-18** may be given by using the following substitutions of T^*, U_r^* and U_z^* that satisfy the boundary conditions given in **Eq.13**:

$$\begin{aligned} T^* &= \varphi(\tau) f_1(R) \cos(\pi Z), \\ U_r^* &= u(\tau) f_2(R) \cos(\pi Z), \\ U_z^* &= w(\tau) f_2(R) \sin(\pi Z), \end{aligned} \tag{24}$$

where the functions f_1 and f_2 are given, respectively, by:

$$\begin{aligned} f_1 &= (R-1)^2 - (R_i - 1)^2 + \Omega, \\ f_2 &= (R - R_i)(R-1). \end{aligned} \tag{25}$$

Using **Eq.23** into **Eqs.15-17**, one can get

$$\begin{aligned} &A_1 \left(1 + t_1^* \frac{\mathrm{d}}{\mathrm{d}\tau} \right) \varphi + A_2 u + A_3 w = 0, \quad A_4 \left(1 + t_1^* \frac{\mathrm{d}}{\mathrm{d}\tau} \right) \varphi + A_5 u + A_6 w = 0, \\ &A_7 \varphi = A_8 \frac{\mathrm{d}}{\mathrm{d}\tau} \left(1 + t_3^* \frac{\mathrm{d}}{\mathrm{d}\tau} \right) u + A_9 \frac{\mathrm{d}}{\mathrm{d}\tau} \left(1 + t_3^* \frac{\mathrm{d}}{\mathrm{d}\tau} \right) w + A_{10} \frac{\mathrm{d}}{\mathrm{d}\tau} \left(1 + t_2^* \frac{\mathrm{d}}{\mathrm{d}\tau} \right) \varphi, \end{aligned} \tag{26}$$

where

$$A_1 = B_2 \frac{f_1}{R} - B_1 \left(\frac{1}{R} + \frac{\mathrm{d}}{\mathrm{d}R} \right) f_1, \quad A_2 = c_{11}^* \left(\frac{1}{R} \frac{\mathrm{d}}{\mathrm{d}R} + \frac{\mathrm{d}^2}{\mathrm{d}R^2} \right) f_2 - c_{22}^* \frac{f_2}{R} - c_{55}^* \left(\frac{r_o \pi}{L} \right)^2 f_2,$$

$$A_3 = -\frac{r_o \pi}{L} \left[c_{13}^* \left(\frac{1}{R} + \frac{\mathrm{d}}{\mathrm{d}R} \right) - c_{23}^* \frac{1}{R} + \frac{\mathrm{d}}{\mathrm{d}R} c_{55}^* \right] f_2, \quad A_4 = -\frac{r_o \pi}{L} B_3 f_1,$$

$$A_5 = \frac{r_o \pi}{L} \left[c_{55}^* \left(\frac{1}{R} + \frac{\mathrm{d}}{\mathrm{d}R} \right) + c_{23}^* \frac{1}{R} + \frac{\mathrm{d}}{\mathrm{d}R} c_{13}^* \right] f_2, \quad A_6 = c_{55}^* \left(\frac{1}{R} \frac{\mathrm{d}}{\mathrm{d}R} + \frac{\mathrm{d}^2}{\mathrm{d}R^2} \right) f_2 - c_{33}^* \left(\frac{r_o \pi}{L} \right)^2 f_2,$$

$$A_7=\left(\kappa_r^*\frac{\mathrm{d}^2}{\mathrm{d}R^2}+\kappa_\theta^*\frac{1}{R}\frac{\mathrm{d}}{\mathrm{d}R}-\kappa_z^*\left(\frac{r_o\pi}{L}\right)^2\right)f_1,\quad A_8=\left(\beta_r^*\frac{\mathrm{d}}{\mathrm{d}R}+\beta_\theta^*\frac{1}{R}\right)f_2,\quad A_9=-\frac{r_o\pi}{L}\beta_z^*f_2,\quad A_{10}=\rho c_v^*f_1. \tag{27}$$

The solution of the above system of first-order differential equations may be easily given for all theories. The corresponding solutions for C-D, L-S and G-L theories are also obtained from the general one.

4. NUMERICAL EXAMPLES

In order to illustrate the results graphically, the geometry and thermoelastic constants for the two materials of the hollow cylinder are given in **Table 1**. The cylinder is composed of three layers of two distinct materials with the same thickness of each layer. Layers 1 and 3 have properties of the same material. So, the two interfaces are given at $R = 0.5$ and $R = 0.75$, respectively. The various non-dimensional parameters used are:

$$u_1=10^2U_r^*=\frac{U_r}{r_o}\left(\frac{\beta_r}{\rho c_v}\right)_1,\quad u_3=U_z^*=\frac{U_z}{r_o}\left(\frac{\beta_r}{\rho c_v}\right)_1,$$

$$T=T^*=\frac{\overline{\Theta}}{\Theta_0},\quad \sigma_1=\sigma_r^*=\frac{\sigma_r}{(\beta_r)_1},\quad \sigma_2=\sigma_\theta^*=\frac{\sigma_\theta}{(\beta_r)_1},$$

$$\sigma_3=\sigma_z^*=\frac{\sigma_z}{(\beta_r)_1},\quad \sigma_5=\sigma_{rz}^*=\frac{\sigma_{rz}}{(\beta_r)_1}.$$

The numerical results are plotted in **Figures 2-17**. The values of Θ_0 and Ω are taken to have the same value as $\Theta_0=\Omega=5$. The values of ϕ_i and ϕ_o and η_1, η_2, and η_3 are given, respectively, in terms of Θ_0 and Ω. The ratio of the outer radius of the cylinder to its length is given by $r_o/L=0.2$. In addition, the * is dropped, for simplicity, from the dimensionless relaxation times.

Figure 2 illustrates the variation of dimensionless temperature T through axial parameter Z, for value of the dimensionless time namely $\tau=8$ and at the second interface of the dimensionless radial direction ($R = 0.75$). The computations were carried out for C-D, L-S and G-L theories of thermoelasticity. **Figure 3** shows the variation of dimensionless radial stress σ_1 through the axial parameter Z. The values of dimensionless time and radial direction are chosen to be 8 and 0.75, respectively. The results were calculated for L-S and G-L theories.

In what follows, we restrict our attention to the results of L-S theory. **Figures 4**,**6**,**8**,**10**,**12**,**14** and **16** illustrate, respectively, the variation of dimensionless radial and axial displacements, u_1 and u_3; the dimensionless temperature T; and the dimensionless stresses σ_1, σ_2,σ_3, and σ_5 through the radial direction of the multilayered hollow cylinder for different values of the dimensionless time $\tau=5,7,$ and 9 with the relaxation time $t_3=t_2=20$. Similar results are plotted in **Figures 5**,**7**,**9**,**11**,**13**,**15**, and **17** through the radial direction of the

Table 1. The geometry and material constants of a finitely long hollow cylinder.

	Material 1	Material 2
$E_r\left(\frac{N}{m^2}\right)$	50×10^6	58×10^6
$E_\theta\left(\frac{N}{m^2}\right)$	15×10^6	22×10^6
$E_z\left(\frac{N}{m^2}\right)$	15×10^6	18×10^6
$G_{rz}\left(\frac{N}{m^2}\right)$	15×10^5	20×10^6
$\kappa_r\left(\frac{\text{watt}}{\text{m.K}}\right)$	18	22
$\kappa_\theta\left(\frac{\text{watt}}{\text{m.K}}\right)$	12	15
$\kappa_z\left(\frac{\text{watt}}{\text{m.K}}\right)$	15	20
$\nu_{r\theta}=\nu_{\theta r}$	0.2	0.2
$\nu_{rz}=\nu_{zr}$	0.1	0.1
$\nu_{z\theta}=\nu_{\theta z}$	0.15	0.15
$\alpha_\theta=\alpha_z\left(\frac{1}{\text{K}}\right)$	3×10^{-6}	3×10^{-6}
$\alpha_r\left(\frac{1}{\text{K}}\right)$	4×10^{-6}	4×10^{-6}
$\rho\left(\frac{\text{kg}}{\text{m}^3}\right)$	0.095	0.095
$c_v\left(\frac{\text{kj}}{\text{kg}K}\right)$	0.31	0.31

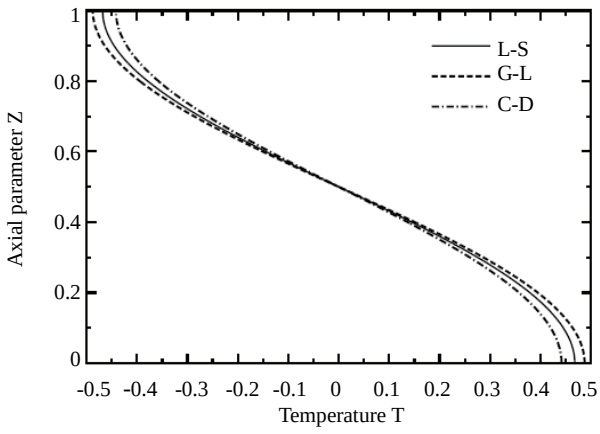

Figure 2. Variation of dimensionless temperature T through the axial direction of the hollow cylinder for various thermoelasticity theories ($\tau = 8$; $R = 0.75$).

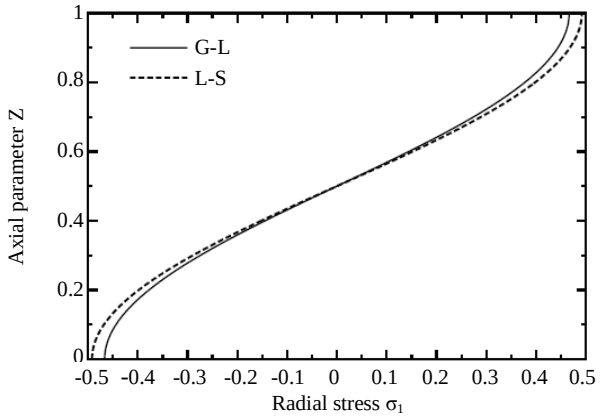

Figure 3. Variation of dimensionless radial stress σ_1 through the axial direction of the hollow cylinder for L-S and G-L theories (τ = 8; R = 0.75).

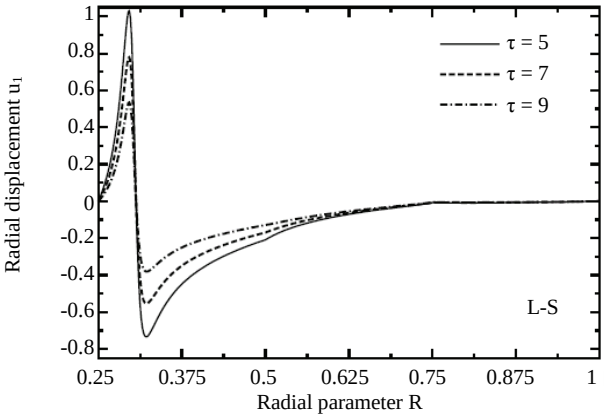

Figure 4. Variation of dimensionless radial displacement u_1 through the radial direction of the hollow cylinder for different values of the time parameter τ ($t_2 = t_3 = 20$).

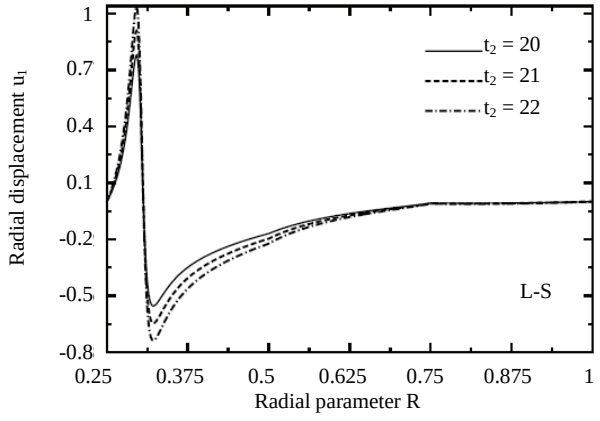

Figure 5. Variation of dimensionless radial displacement u_1 through the radial direction of the hollow cylinder for different values of the relaxation time ($t_2 = t_3$, $\tau = 7$).

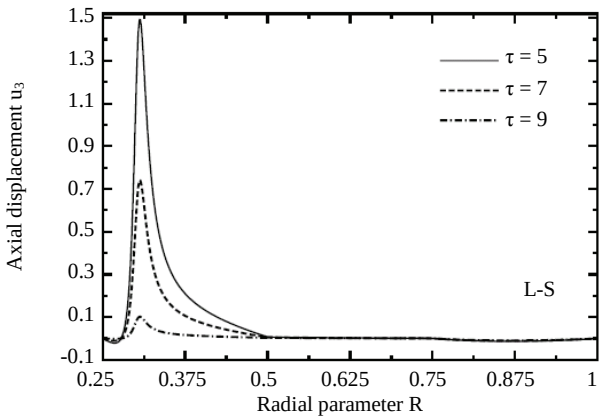

Figure 6. Variation of dimensionless axial displacement u_3 through the radial direction of the hollow cylinder for different values of the time parameter τ ($t_2 = t_3 = 20$).

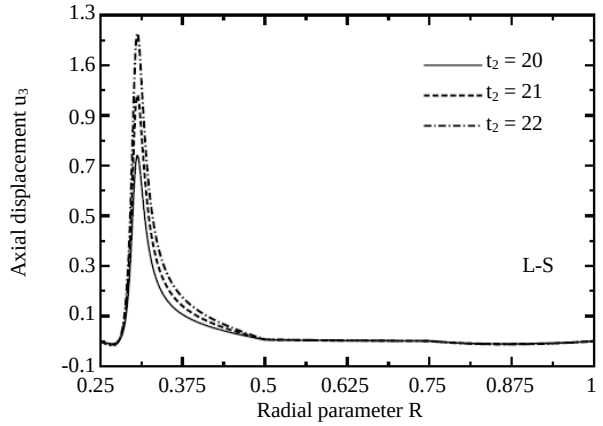

Figure 7. Variation of dimensionless axial displacement u_3 through the radial direction of the hollow cylinder for different values of the relaxation time ($t_2 = t_3$, $\tau = 7$).

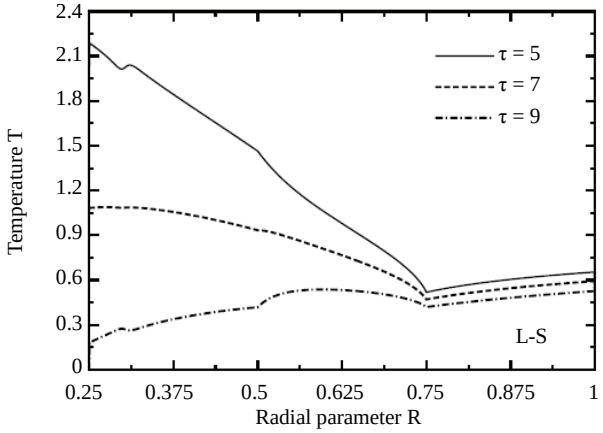

Figure 8. Variation of dimensionless temperature T through the radial direction of the hollow cylinder for different values of the time parameter τ ($t_2 = t_3 = 20$).

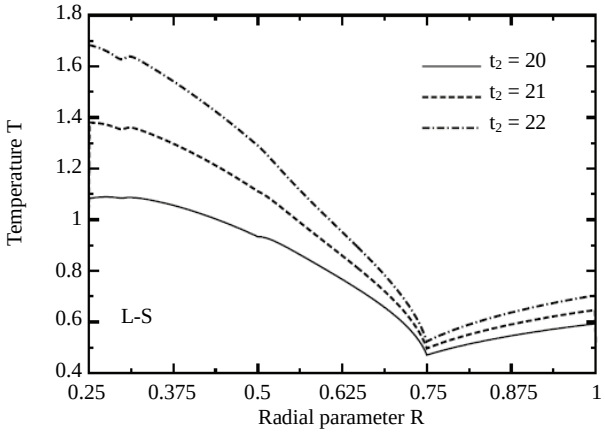

Figure 9. Variation of dimensionless temperature T through the radial direction of the hollow cylinder for different values of the relaxation time ($t_2 = t_3$, $\tau = 7$).

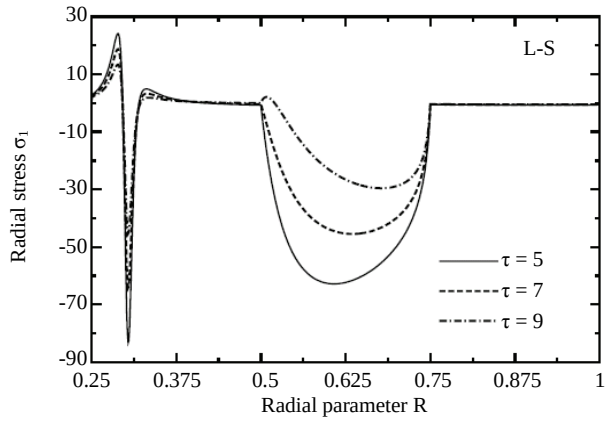

Figure 10. Variation of dimensionless radial stress σ_1 through the radial direction of the hollow cylinder for different values of the time parameter τ ($t_2 = t_3 = 20$).

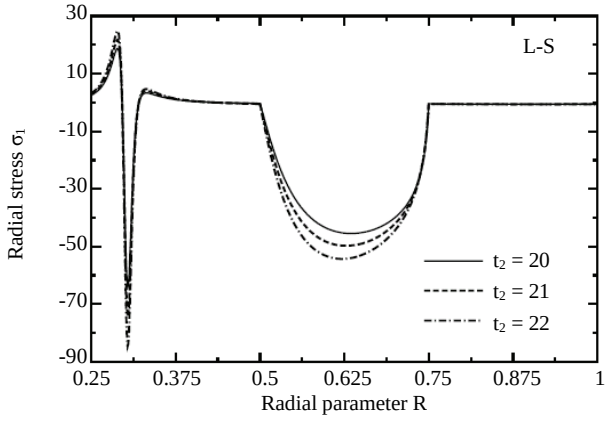

Figure 11. Variation of dimensionless radial stress σ_1 through the radial direction of the hollow cylinder for different values of the relaxation time ($t_2 = t_3$, $\tau = 7$).

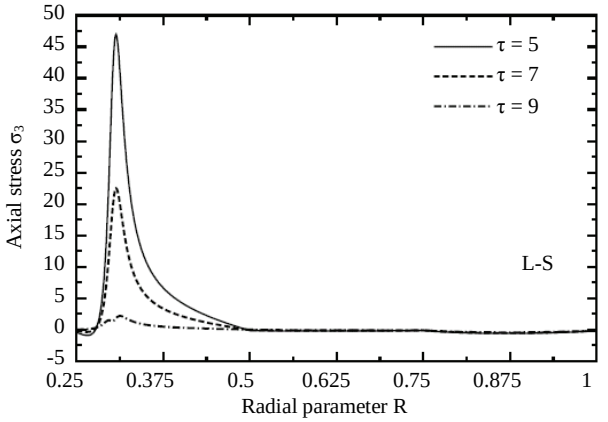

Figure 12. Variation of dimensionless axial stress σ_3 through the radial direction of the hollow cylinder for different values of the time parameter τ ($t_2 = t_3 = 20$).

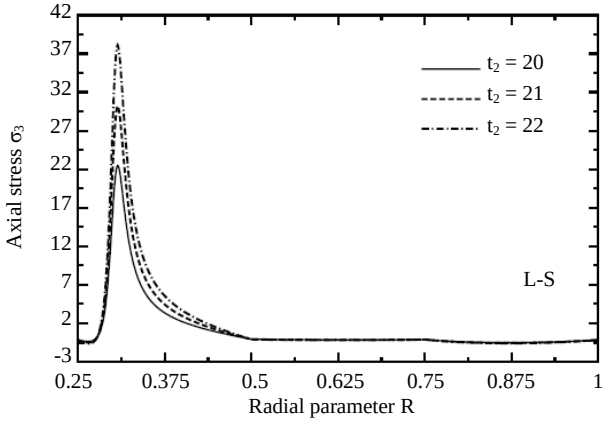

Figure 13. Variation of dimensionless axial stress σ_3 through the radial direction of the hollow cylinder for different values of the relaxation time ($t_2 = t_3$, $\tau = 7$).

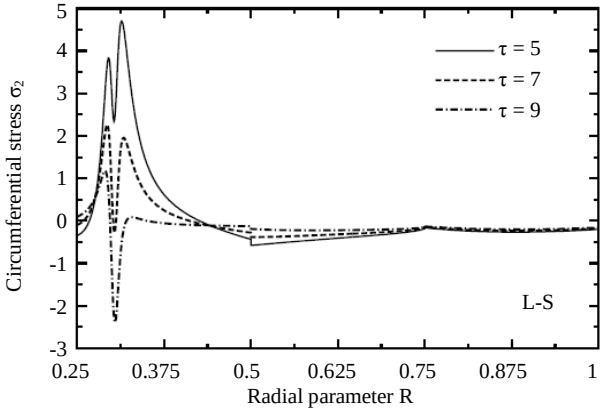

Figure 14. Variation of dimensionless circumferential stress σ_2 through the radial direction of the hollow cylinder for different values of the time parameter τ ($t_2 = t_3 = 20$).

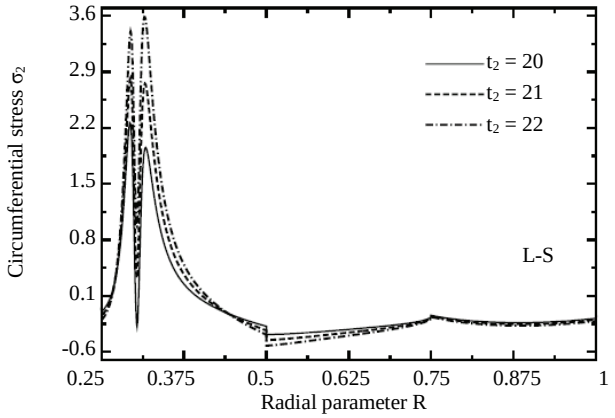

Figure 15. Variation of dimensionless circumferential stress σ_2 through the radial direction of the hollow cylinder for different values of the relaxation time ($t_2 = t_3$, $\tau = 7$).

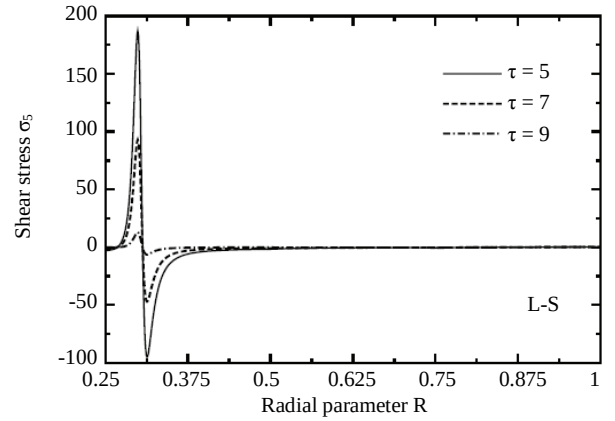

Figure 16. Variation of dimensionless shear stress σ_5 through the radial direction of the hollow cylinder for different values of the time parameter τ ($t_2 = t_3 = 20$).

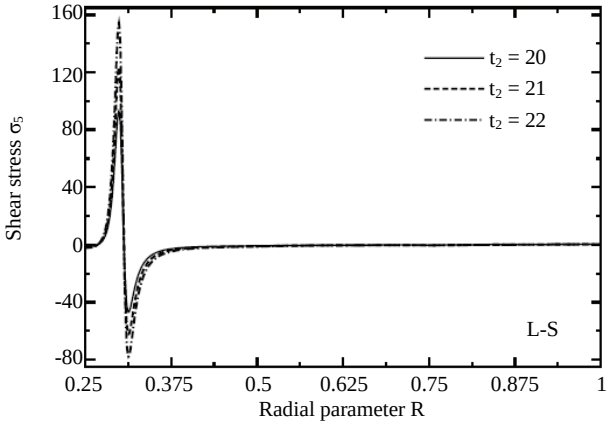

Figure 17. Variation of dimensionless shear stress σ_5 through the radial direction of the hollow cylinder for different values of the relaxation time ($t_2 = t_3$, $\tau = 7$).

multilayered hollow cylinder for different values of the relaxation time ($t_3 = t_2 = 20, 21, 22$) when the dimensionless time $\tau = 7$.

5. CONCLUSIONS

The conclusion of the above results may be given as:

1) **Figure 2** illustrates that the dimensionless temperature is slightly changed and the differences between C-D, L-S, and G-L are very small (tiny). The coupled theory (C-D) may give results with small relative error compared with those given by Lord and Shulman's (L-S) and Green and Lindsay's (G-L) theories. However, the results of L-S and G-L are much closed to each other (see **Figure 3**).
2) The plots of results given by Lord and Shulman's theory show that the effect of the dimensionless time is slightly clear in the first layer, but in the second and third layers the effect is not declared. This happened for dimensionless radial and axial displacements (see **Figures 4-7**), and axial, circumferential, and shear stresses (see **Figures 12-17**).
3) However, for dimensionless temperature and radial stress, the effects of dimensionless time is very clear in the first layer and start to decrease with the increase of radial direction in the second and third layer (see **Figures 8-11**).
4) The effect of the relaxation time of Lord and Shulman's theory in all physical waves (displacements, temperature and stresses) is clear in the first layer, but is less considerable in the second and third layers. This revealed that the effect of the relaxation time has no effect when the dimensionless radius is increasing.

6. ACKNOWLEDGEMENTS

This paper is fully supported by the Deanship of Scientific Research at King AbdulAziz University, Grant No. 181/428.

REFERENCES

[1] Biot, M. (1956) Thermoelasticity and irreversible thermo-dynamics. *Journal of Applied Physics*, **27**, 240-253.
[2] Lord, H.W. and Shulman, Y.A. (1967) A generalized dynamical theory of thermoelasticity. *Jornal of Mechanics and Physics of Solids*, **15**, 299-309.
[3] Dhaliwal, R.S. and Sherief, H.H. (1980) Generalized thermoelasticity for anisotropic media. *Quarterly of Applied Mathematics*, **38**, 1-8.
[4] Ignaczak, J. (1979) Uniqueness in generalized thermoelasticity. *Journal of Thermal Stresses*, **2**, 171-175.
[5] Sherief, H.H. and Dhaliwal, R. (1980) A uniqueness theorem and a variational principle for generalized thermoelasticity. *Journal of Thermal Stresses*, **3**, 223-230.

[6] Green, A. and Lindsay, K. (1972) Thermoelasticity. *Journal of Elasticity*, **2**, 1-7.
[7] Jane, K.C. and Lee, Z.Y. (1999) Thermoelasticity of multilayered cylinder. *Journal of Thermal Stresses*, **22**, 57-74.
[8] Kandil, A. (1975) Investigation of stress analysis in compound cylinders under high pressure and temperature. M.Sc. Thesis, CIT Helwan.
[9] Sherief, H.H. and Anwar, M.N. (1988) A problem in generalized thermoelasticity for an infinitely long annular cylinder. *International Journal of Engineering Science*, **26**, 301-306.
[10] Yan, Y.C. and Chen, C.K. (1986) Thermoelastic transient response of an infinitely long annular cylinder composed of two different materials. *International Journal of Engineering Science*, **24**, 569-581.
[11] Lee, Z.-Y. (2006) Generalized coupled transient response of 3-D multilayered hollow cylinder. *International Communications in Heat and Mass Transfer*, **33**, 1002-1012.
[12] Chen, C.K., Hung, C.I. and Lee, Z.Y. (2001) Transient thermal stresses analysis of multilayered hollow cylinder. *Acta Mechanica*, **151**, 75-88.
[13] Chen, C.K., Hung, C.I. and Lee, Z.Y. (2001) Thermoelastic transient response of multilayered hollow cylinder with initial interface pressure. *Journal of Thermal Stresses*, **24**, 987-1006.
[14] Allam, M.N., Elsibai, K.A. and Abouelregal, A.E. (2002) Thermal stresses in a harmonic field for an infinite body with a circular cylindrical hole without energy dissipation. *Journal of Thermal Stresses*, **25**, 57-67.
[15] Zenkour, A.M., Mashat, D.S. and Elsibai, K.A. (2009) Bending analysis of functionally graded plates in the context of different theories of thermoelasticity. *Mathematical Problems in Engineering*, **2009**, Article ID 962351, 1-15.

Call for Papers

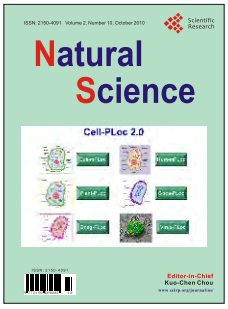

Natural Science

A Journal Published by Scientific Research Publishing, USA
www.scirp.org/journal/ns

Natural Science is an international journal dedicated to the latest advancement of natural sciences. The goal of this journal is to provide a platform for scientists and academicians all over the world to promote, share, and discuss various new issues and developments in different areas of natural sciences. All manuscripts must be prepared in English, and are subject to a rigorous and fair peer-review process. Accepted papers will immediately appear online followed by printed hard copy. The journal publishes original papers including but not limited to the following fields:

- **Astronomy & Space Sciences**
  - Astronomy
  - Astrophysics
  - Atmospheric Science
  - Space Physics
- **Earth Science**
  - Geography
  - Geology
  - Geophysics/Geochemistry
  - Oceanography
- **Chemistry**
  - Analytical Chemistry
  - Biochemistry
  - Computational Chemistry
  - Inorganic Chemistry
  - Organic Chemistry
  - Physical Chemistry
- **Life Science**
  - Cell Biology
  - Computational Biology
  - Genetics
  - Immunology
  - Medicine/Diseases
  - Microbiology
  - Molecular Biology
  - Neuroscience
  - Pharmacology/Toxicology
  - Physiology
  - Psychology
  - Virology
- **Physics**
  - Applied Physics
  - Atomic, Molecular, and Optical Physics
  - Biophysics
  - High Energy/Particle Physics
  - Material Science
  - Plasma Physics
- **Others**
  - Education
  - History of Science
  - Science and Innovations

We are also interested in: 1) Short Reports—2-5 page papers where an author can either present an idea with theoretical background but has not yet completed the research needed for a complete paper or preliminary data; 2) Book Reviews—Comments and critiques.

Notes for Intending Authors

Submitted papers should not be previously published nor be currently under consideration for publication elsewhere. Paper submission will be handled electronically through the website. For more details, please access the website.

Website and E-Mail

http://www.scirp.org/journal/ns ns@scirp.org

Natural Science, 2010, 2, 1057-1179
Published Online October 2010 in SciRes (http://www.scirp.org/journal/ns).

TABLE OF CONTENTS

Volume 2 Number 10 **October 2010**

ASTRONOMY & SPACE SCIENCES

CHEMISTRY

EARTH SCIENCE

LIFE SCIENCE

PHYSICS

